



POLITECNICO DI MILANO  
DEPARTMENT OF CIVIL AND ENVIRONMENTAL ENGINEERING  
DOCTORAL PROGRAMME IN  
STRUCTURAL SEISMIC AND GEOTECHNICAL ENGINEERING

---

ENVIRONMENTAL APPLICATIONS OF AMBIENT SEISMIC  
NOISE FOR MONITORING SITES WITH HIGH  
HYDROGEOLOGICAL RISK

Doctoral Dissertation of:

**Marco Taruselli**

Supervisor:

**Prof.ssa Laura Longoni**  
**Prof.ssa Monica Papini**  
**Prof. Luigi Zanzi**

Tutor:

**Prof. Della Vecchia Gabriele**

The Chair of the Doctoral Program:

**Prof. Umberto Perego**

XXXIII Cycle – 2021



# Table of contents

Acknowledgements .....	vii
Abstract .....	viii
CHAPTER 1.....	1
The ambient seismic noise.....	1
1.    Introduction to the Ambient Seismic Noise .....	1
2.    Sources of the Ambient Seismic Noise.....	2
2.1.    Microtremors ( $F > 1$ Hz).....	3
2.2.    Microseisms & Hum ( $F < 1$ Hz).....	4
3.    Composition of the Seismic Noise .....	5
4.    Geophysical methods in landslide investigation.....	6
5.    Ambient seismic noise for monitoring site with high-hydrogeological risk: State-of-the-art.....	6
6.    Conclusion.....	10
7.    Bibliography.....	10
CHAPTER 2 .....	16
Ambient seismic noise processing methods .....	16
1.    Introduction .....	16
2.    Spectral analysis .....	16
2.1.    Welch's Periodogram .....	16
2.2.    Multitaper spectral estimation.....	18
2.3.    Spectrogram.....	19
3.    HVSR Analysis .....	20
4.    Polarization analysis .....	21
4.1.    Hodogram.....	21
4.2.    HVSR-Rotate.....	21
4.3.    Principal Component Analysis (PCA) .....	22
5.    Passive Seismic interferometry.....	24
5.1.    Single-station data pre-processing.....	25
5.2.    Computation of the cross-correlations .....	27
5.3.    Estimation of the relative velocity changes ( $dV/V$ ).....	28
6.    Conclusion.....	30
7.    Bibliography .....	30
Appendix A .....	33
Appendix B .....	34
CHAPTER 3 .....	36
Raspberry Shake sensor laboratory and field tests for shallow passive seismic applications....	36

1.	Introduction .....	36
2.	Method.....	36
2.1.	Sensors description.....	36
2.2.	Laboratory tests.....	37
2.3.	Field application.....	39
3.	Results And Discussions.....	40
3.1.	Laboratory test .....	40
3.2.	Field application.....	41
4.	Conclusions.....	45
5.	Bibliography .....	46
<b>CHAPTER 4</b>	<b>.....</b>	<b>48</b>
	<b>Seismic noise monitoring of unstable rock blocks.....</b>	<b>48</b>
1.	Introduction .....	48
2.	Small rock block collapse test.....	50
2.1.	Field test.....	51
2.2.	Methods.....	53
2.2.1.	Spectral analysis.....	53
2.2.2.	Polarization analysis.....	53
2.3.	Numerical modelling.....	53
2.4.	Results.....	54
2.4.1.	Seismic monitoring.....	54
2.4.2.	Numerical modelling .....	59
2.5.	Discussion.....	60
2.6.	Conclusions .....	61
3.	Torrioni di Rialba .....	63
3.1.	Case study .....	63
3.1.1.	Geological investigations .....	64
3.1.2.	Geoelectrical investigations.....	65
3.2.	Methods.....	67
3.3.	Results and discussions .....	67
3.4.	Conclusions .....	72
4.	Bismantova Rock Cliff .....	74
4.1.	Case study .....	74
4.2.	Methods.....	75
4.3.	Results and discussions .....	76
4.4.	Conclusions .....	79
5.	Unstable rocks blocks at Malta .....	80
5.1.	Case study .....	80

5.2. Method .....	81
5.3. Results and discussions.....	82
5.4. Conclusions .....	85
6. General conclusions .....	87
7. Bibliography.....	88
Appendix.....	92
<b>CHAPTER 5 .....</b>	<b>96</b>
<b>A preliminary test to monitor the Cà Lita landslide using the ambient seismic noise.....</b>	<b>96</b>
1. Introduction.....	96
2. Case study .....	96
3. Methods.....	98
4. Results & discussions.....	98
5. Conclusions .....	100
6. Bibliography.....	101
<b>CHAPTER 6 .....</b>	<b>103</b>
<b>Seismic passive interferometry to monitor groundwater level variations. ....</b>	<b>103</b>
1. Introduction .....	103
2. The Crépieux–Charmy water exploitation field test.....	104
2.1. Site description.....	104
2.2. Methods.....	106
2.3. Results and discussion.....	107
3. The experimental test in the Campastrino aquifer.....	111
3.1. Site description.....	111
3.2. Methods.....	112
3.3. Results and discussions .....	113
4. Conclusions .....	115
5. Bibliography .....	116
<b>Conclusions .....</b>	<b>118</b>
<b>Appendix: PassiveBarinda Guide.....</b>	<b>121</b>



## **Acknowledgements**

I am sincerely grateful and I wish to express my deepest gratitude to everyone who made this PhD experience memorable.

Firstly, I would like to express my sincere gratitude to Diego for the continuous support of my PhD study and related research, for his patience and motivation.

I also want to thank my supervisors, Laura, Luigi and, Monica for their invaluable support and guidance. I would like to thank my PhD colleagues, for every smile or funny time we spent together, which surely helped to reduce the stress of the bad days.

I would like to acknowledge Stèphane and Christophe that hosted me for the second time at ISTerre lab.

I thank all the people I met in France who made those days unforgettable.

Finally, I want to thank my family and friends for their constant support and encouragement throughout my whole life.

## Abstract

The assessment and management of landslide hazard and related risk have always been widely studied topics in the scientific community due to their destructive nature and the consequent socio-economic impacts. The occurrence of such events is strongly conditioned by both natural and anthropogenic factors and the definition of adequate prevention and mitigation measures is still a challenging task. One of the current challenges in the academic world is to provide reliable techniques able to forecast and monitor these phenomena in real-time, hence, reducing the adverse nature of their consequences. In order to achieve this objective, in the past decade, geophysical techniques have been integrated into multidisciplinary approaches to monitor slope instability as well as to design early-warning monitoring systems.

This PhD project is directed towards the analysis, development and experimentation with novel geophysical technologies and sensors for the monitoring of sites prone to slope stability issues. In detail, the research is focused on the detection of ambient seismic noise to retrieve features that can provide valuable information concerning slope stability over time and thus, to support already existing technologies for geohazard monitoring. Among the available passive geophysical methods, three types of analysis were chosen due to their capability to yield the variation of the recorded signals' features over time: 1) spectral analysis; 2) polarization analysis; 3) monitoring of seismic wave velocity changes. These methodologies have been used to study the dynamic response of unstable rock blocks, both in terms of resonance frequencies and preferential vibrational directions, as well as to deduce whether ambient seismic noise allows retrieving information concerning the stability and water content of landslides. The combination of all these techniques aims to provide significant progress in the realization of an effective monitoring tool for slope stability phenomena. In addition, in this work, a low-cost seismometer (Raspberry Shake 3D) was tested through both laboratory and field experiments to assess whether it can be used for ambient seismic noise applications, thus, to perform long-term monitoring. Finally, this thesis was completed through the development of user-friendly software for organising, visualizing, and processing seismic signals.

Dealing with ambient seismic noise strategy, this thesis yielded the following results which can supply further perspectives for monitoring sites prone to slope stability issues:

- With regards to the monitoring of unstable rock blocks, a controlled collapse test confirmed that both spectral and polarization features of seismic noise recordings are strictly dependent on the evolving constraints of the unstable rock blocks and thus, on their stability. It was observed that rock bridges breakage leads to a drop of resonance frequencies. However, it was additionally noticed that they can bring to a new dynamic response if the monitored rock undergoes an abrupt change of its initial stability condition.
- Different methodologies have been tested for the analysis of the seismic noise recordings. As far as the spectral analysis is concerned, the implementation of the Multitaper method was proposed for the estimate of structures' vibrational modes allowing for a reduction of the bias and variability with respect to the traditional techniques used in seismic methods. In terms of polarization features, the experimented spectral Singular Value Decomposition (SVD) approach proved to be the most exhaustive method to study 3D motion characteristics of rock structures, both for the description of their vibration modes and to track their variation over time.
- Concerning water content in a landslide body, two pilot tests confirmed the potential of the ambient seismic noise cross-correlation method in retrieving water content variations in both confined and unconfined aquifers.
- With regards to the cross-correlation of ambient seismic noise technique, different signals' length was tested, revealing the possibility to increase the temporal resolution of seismic velocity

variations down to one minute. This result is of crucial importance in view of building early warning systems since it allows to promptly predict the landslide occurrence.

- Concerning landslide monitoring, the use of polarization analysis and passive interferometry revealed that both techniques can provide useful information to characterize the dynamic conditions of the unstable slopes, thus, to improve our capabilities of landslides forecasting.
- Both laboratory and field experimental tests demonstrated that the RaspberryShake-3D seismometers could be a valuable alternative to the high-cost broadband sensors in the evaluation of unstable rock dynamic response, provided that the vibrational frequencies are within the RS flat frequency response.

The thesis is divided into six chapters. The first chapter introduces the reader to the ambient seismic noise providing the definition, a description of the passive sources and explaining the composition of the ambient vibration in terms of frequency bands. Further, it contains a literature review focused on the applications of ambient seismic noise for geohazard monitoring. The second chapter describes the different methodologies that have been used within this work. A distinction among spectral analysis, polarization analysis and passive interferometry is outlined. The third chapter describes the testing procedures and the results of the laboratory and field test carried out to evaluate the performances of the low-cost seismometer. Finally, the fourth, fifth and sixth chapters integrate the results of the unstable rock blocks monitoring, the landslide case study and underground water monitoring, respectively.



# CHAPTER 1

## The ambient seismic noise

The ambient seismic noise is an enormous dataset containing precious information. Even though this seismic wavefield has not been considered for a long time, the research carried out in the last decades highlights that the ambient vibration is far from useless and it contains valuable information about the properties of the hosting media. Indeed, the emerging of new techniques allowed us to retrieve explicit signals from the ambient wavefield providing information about the Earth's properties. This chapter of the manuscript aims to present an overview of ambient seismic noise and its application for monitoring site with high hydrogeological risks. This section opens with a definition of ambient seismic noise. It then goes into detail providing the reader with information about the seismic noise spectrum, the sources that cause this ground vibration worldwide and its composition in terms of seismic waves. In the second part, state-of-the-art of ambient seismic noise-based techniques that are used to monitor slopes stability is provided.

### 1. Introduction to the Ambient Seismic Noise

The Earth's surface is continuously subjected to acting forces caused by human activities and natural phenomena. The seismic radiation that arises due to these forces has been historically called microseisms and it constitutes the seismic background vibration of the Earth. The ambient tremor is omnipresent, independent of geographic location, and it appears even during seismically quiet days. These characteristics immediately attracted the scientific community. However, the quasi-random nature of this wavefield (an example is shown in Figure 1) prevents the identification of distinct arrivals, which are instead well-defined when dealing with earthquakes, explosions, or other active sources that are usually used for seismological investigations. The absence of an identifiable and deterministic signal made it difficult to use this input in seismic applications and it has led to defining the ambient vibration as **ambient seismic noise**.

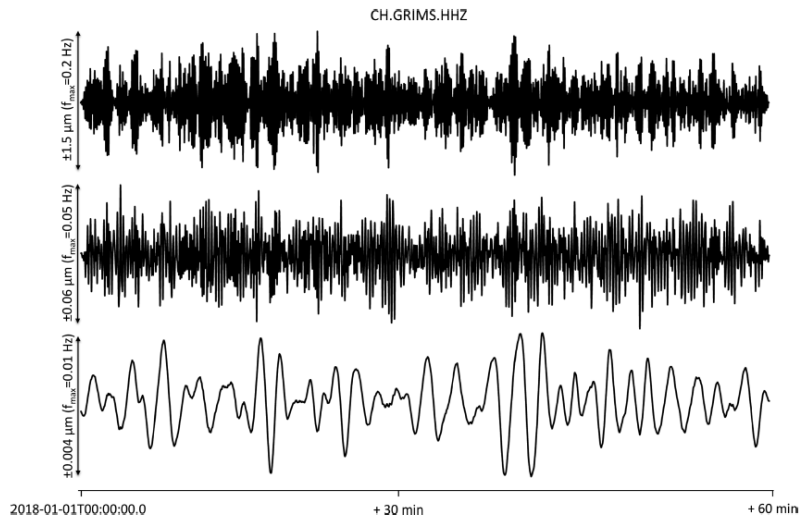


Figure 1 Example of ambient seismic noise records.

Despite being quasi-random, the ambient vibration obeys the laws of physics, which imprint coherent information into the apparent disorder. However, the appearance of seismic ambient noise-based techniques had to await improvements of seismic sensors (with low instrument self-noise), the development of processing techniques to suppress large-amplitude transients and the deployment of seismic arrays to enable the detection of coherent signals (Figure 2).

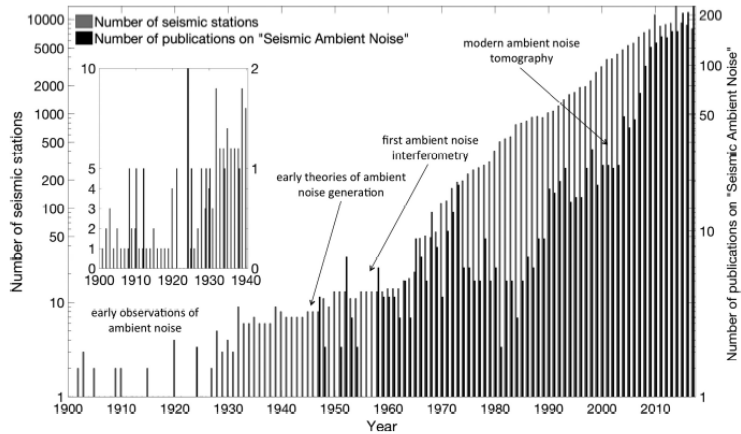


Figure 2 Histograms showing the number of seismic stations in the IRIS data (Nakata et al. 2019)

Indeed, the presence of instrumental noise and transient signals, for instance from earthquakes, may hide the weak amplitude of the ambient seismic noise. Since the beginning, it has been therefore important to quantify the power distribution of the seismic vibration and distinguish, within the records, the different sources of noise. The standard method to analyse the Earth seismic noise consists in the computation of the Power Spectral Density (PSD) which provides a measurement of how the average power of a waveform is distributed as a function of frequency. Based on this methodology, in 1993, Peterson proposed the Earth noise models that are used as baselines for evaluating instruments quality, site characteristics and environmental seismic noise sources. In detail, using 75 long-term broadband records from the Global Seismographic Network (GSN) and by removing earthquakes and other transient signals, he defined the New High and Low Noise Models (NHNM, NLNM) which graphically (Figure 3) and numerically represent the lowest and highest vertical seismic noise levels observed worldwide (Peterson 1993). Nowadays, these thresholds are considered the standard by which the noise level at a seismic station is evaluated.

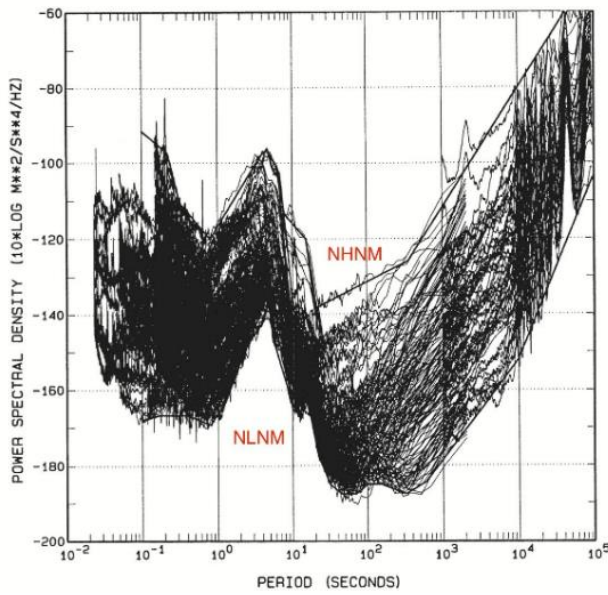


Figure 3 Overlay of network spectra with straight-line segments fitted to the high-noise and low-noise envelopes of the overlay (Peterson 1993).

## 2. Sources of the Ambient Seismic Noise

The theoretical understanding of the seismic ambient noise achieved over the recent decades, as well as the development of a worldwide seismic network, brought to better identification of the main physical mechanisms able to transfer energy into the solid Earth in the form of seismic waves. Generally, the sources able to generate the ground motion can be classified based on the frequency at which they occur. However, due to the large Spatio-temporal variability of the noise spectra, the boundaries between different types of ambient noise are not well

defined. Thus, the definition of the frequency bands for the classifications of seismic noise is still vague in the literature. Nevertheless, based on the frequency content, many authors separate noise sources into microseisms/hum (frequency waves  $< 1\text{Hz}$ ) and microtremors (frequency waves  $> 1\text{ Hz}$ ), generally dominated by ocean waves and by human activities, respectively (Table 1). These mechanisms generate a stationary stochastic process having an undefined phase spectrum (Bormann & Wielandt 2013), an amplitude that is typically in the orders of  $0.1\text{-}10\text{ }\mu\text{m}$ , and with a time-dependent and site-dependent frequency content.

Seismic noise	Source	Frequency band
Seismic hum	Ocean infra-gravity waves	1–20 mHz
Primary microseisms	Ocean gravity waves	0.02–0.1 Hz
Secondary microseisms	Ocean gravity waves	0.1–1 Hz
Microtremors	Mainly human activities	$> 1\text{ Hz}$

Table 1 Sources of the ambient seismic noise

### 2.1. Microtremors ( $F > 1\text{ Hz}$ )

The most common source of short-period seismic noise comes from the human activities carried out at the Earth' surface. This is often referred to as “cultural noise” and originates primarily from traffic and work machinery which transfers vibrations to the solid Earth. Human activities mainly produce mid-high frequency surface waves (1-10 Hz) that propagate at the local level, attenuating within several kilometres in distance and depth. Due to its origin, cultural noise is bimodal and thus it changes throughout the day following the human lifestyle. Therefore, power levels of noise are higher during the daytime hours when people are actively driving vehicles and working. Whereas, the energy content decreases during the night, as well as on weekends and holidays. If it may be considered that the major source of microtremors radiates from cars, trains and machinery it must not forget that there are also natural phenomena able to generate short-period seismic noise. For instance, it has been observed that the interaction of wind with trees or artificial structures can transfer energy to the solid Earth in the form of seismic waves (Withers *et al.* 1996). Even though rarer and not worldwide spread, another source of short-period seismic noise has been associated with the calving events. Indeed, it has been discovered that this phenomenon generates energy in the 2 Hz band (Walter *et al.* 2010).

The distinction between human and natural-generated seismic noise has been a challenging task for a long time. Nevertheless, due to the emergency measures adopted worldwide to reduce the coronavirus (COVID-19) pandemic, it has been possible to differentiate anthropogenic sources of noise from those generated by natural phenomena. From the first analysis of worldwide seismic network recordings, it has been observed (Figure 4) that the global median high-frequency ambient seismic noise (from 4 to 14 Hz) dropped down by 50% in the period between March and May 2020 (Lecocq *et al.* 2020). This behaviour highlights the contribution of human activities to ambient seismic noise.

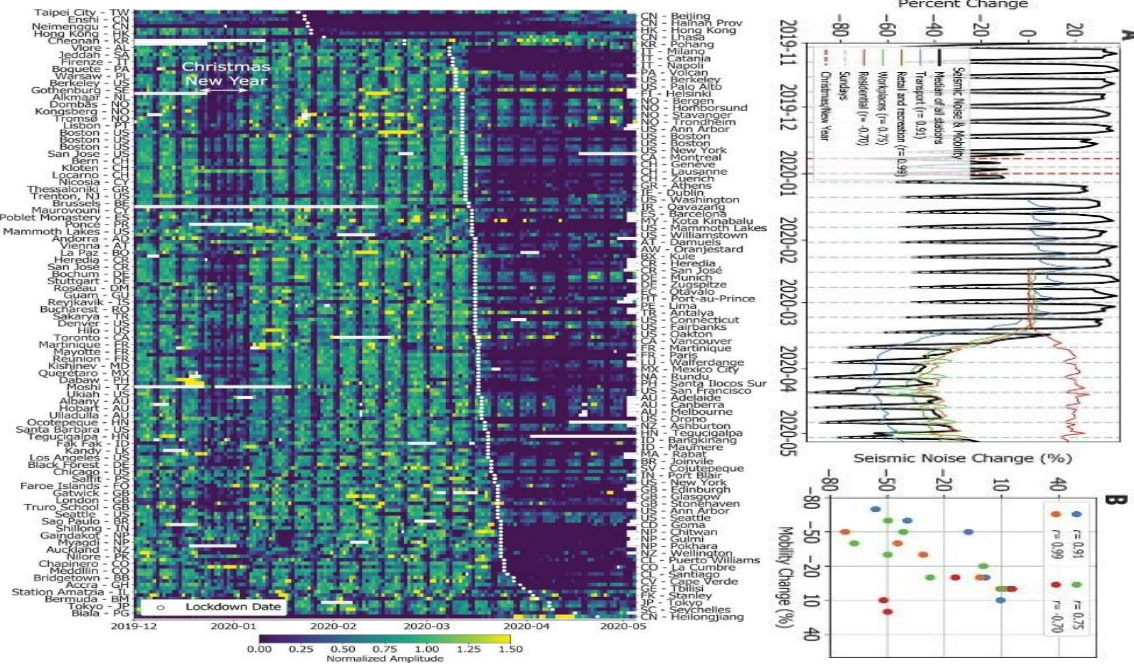


Figure 4 Global median high-frequency ambient seismic noise during Covid pandemic (Lecocq et al. 2020).

## 2.2. Microseisms & Hum ( $F < 1 \text{ Hz}$ )

For a long time, recording the low-frequency ambient seismic noise and identifying its triggering causes have been a challenge for scientists. Indeed, the longest periods of seismic vibration were difficult to record since they require both high-quality broadband sensors as well as a well-built seismic station. Nevertheless, the advances in instrumentations have reduced noise levels in the low-frequency bands and allowed to record the Earth' vibration characterized by very low power levels, almost close to the NLNM. Even though the research on this topic is still ongoing, the scientific community agrees to the fact that the ambient seismic noise with a frequency content lower than 1 Hz is dominated by ocean gravity waves which include ocean swell, wind waves, and ocean infragravity waves. Based on the frequency band of these wavefields, scientists distinguish these Earth' oscillations into seismic hum (1–20 mHz), primary microseisms (0.02–0.1 Hz), and secondary microseisms (0.1–1 Hz), as shown in Figure 5 (Nishida 2017)(Nishida 2017).

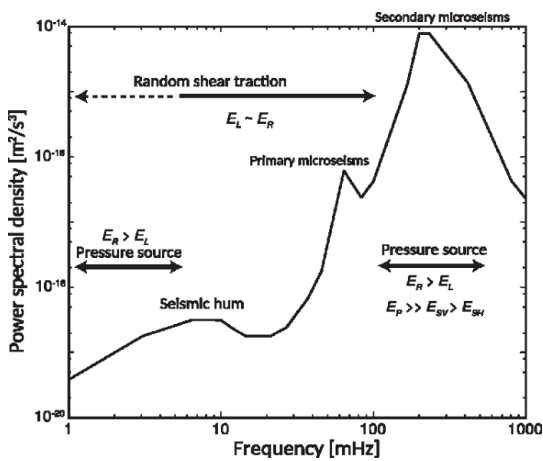


Figura 5 Seismic noise composition (Nishida 2017).

It must be highlighted that in the scientific literature, the microseisms and the seismic hum are often considered together although they refer to different parts of the seismic spectrum and are generated by different physical phenomena.

Primary microseisms are generated via direct pressure of both breaking and/or shoaling ocean waves into the seafloor while approaching shallower water (Figure 6) (Hasselmann 1963). The secondary microseisms occur when standing waves, in the open ocean, interact with coastal reflections of the same frequency travelling in the opposite direction (Figure 6) (Longuet-Higgins 1950, Kedar *et al.* 2008, L. Gaultier *et al.* 2013, 2014, Ardhuin *et al.* 2015). The superimposition of both standing and reflected waves is the reason why the secondary microseisms show a higher energetic content with respect to the primary ones. However, whether this process occurs in deep or shallow water, or in both environments is still a matter of debate. Due to their origin, microseisms power is affected by any process that alters ocean wave intensity. For example, it has been observed that the microseisms amplitude and bandwidth is strictly linked to the thickness of the sea ice due to the fact that it prevents large ocean waves formation (Grob *et al.* 2011, Tsai & McNamara 2011, Anthony *et al.* 2015).

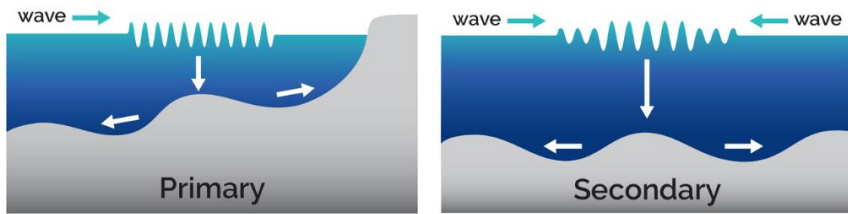


Figure 6 Distinction between primary and secondary microseisms waves ('Sounding Out Earth's Hum' 2019).

The seismic hum can be defined as the Earth's background free oscillations (Webb 2007, Uchiyama & McWilliams 2008, Bromirski & Gerstoft 2009). Even though the origin of this seismic source is not yet clear, many authors state that the seismic hum is linked to atmospheric and/or oceanic disturbances and it is produced by low-frequency surface waves that are generated by the so-called infragravity waves, which are a combination of wind waves and swell (Webb 2007, Ardhuin *et al.* 2015). These surface gravity waves find their triggering factor in distant weather systems, where the wind blows for a duration of time over a fetch of water (Tanimoto & Um 1999, Roult & Crawford 2000). This may be the case, for example, of the intense cyclonic low-pressure storm systems whose steep pressure gradients cause strong surface winds that transfer atmospheric energy into ocean swell which finally produce seismic vibration (Ebeling & Stein 2011). Given the link with these weather systems, the hum power levels are strongly affected by climate factors, seasonal variations and geographic location (Bromirski *et al.* 2005, Lucia Gaultier *et al.* 2018). An interesting low-frequency signal (0.005-0.01Hz) has been observed in the Panama Canal (Figure 1.1b). Even though this signal is in the hum period band, it does not show seasonal-related variations but rather a diurnal distribution. Indeed, it has the highest power content during daytime hours, and it is essentially absent in the early morning. This observation led to the hypothesis that this low-frequency signal is related to the ship traffic. Indeed, even though the canal is always open, the long-period signal primarily arises when major shipping operations occur (McNamara *et al.* 2011). This seismic noise results from a seiche wave that generates in the canal channel because of the constructive interference of the wakes of passing ships and wind-forced waves reflecting off the nearby shorelines.

### 3. Composition of the Seismic Noise

Considering that most of the cultural and natural sources of ambient noise are distributed on the Earth's crust, many scientists assumed that the seismic noise wavefield is dominated by surface waves (Bonnefoy-Claudet *et al.* 2006, Larose *et al.* 2006). Nevertheless, using seismic arrays it has been observed that seismic vibration also contains a small portion of body waves, including both P and S-waves (Gerstoft *et al.* 2008, Keith D. Koper *et al.* 2009, Pyle *et al.* 2015, Nishida 2017). The contribution of the different types of waves (P and S waves, Love and Rayleigh waves, fundamental and higher modes) is indefinite and time and space-dependent (Bonnefoy-Claudet *et al.* 2006, L. Gaultier *et al.* 2015). It is commonly assumed that the Rayleigh waves are the most energetic surface waves making up the microseismic wavefield. Indeed, Gaultier *et al.* (2013) demonstrated that the main characteristics of vertical component microseism amplitude spectrum can be reproduced by the fundamental Rayleigh waves. However, many studies showed counter-examples with more Love-waves energy than Rayleigh one (Bonnefoy-

Claudet *et al.* 2006, Tanimoto *et al.* 2016) or, at short periods (0.25 to 2.5 sec), P waves that dominate compare to the Rayleigh waves (K.D. Koper *et al.* 2010).

#### 4. Geophysical methods in landslide investigation

In the last decades, geophysics has been widely used for landslide investigations. This has been evinced in many publications which highlighted the potential of geophysical techniques in the characterisation of slope stability (Bogoslovsky & Ogilvy 1977, McCann & Forster 1990, Hack 2000, Jongmans & Garambois 2007). Indeed, these methodologies make it possible to investigate the medium properties involved in landslide processes such as dimension, geometry, physical parameters, water content and dynamic behaviour. Moreover, geophysics presents several practical advantages that make this discipline appropriate for slope stability analysis. In particular, the surveys are generally easy and quick to perform under almost all circumstances. This makes it possible to investigate large areas in a relatively short time. In addition, geophysical techniques provide information on the soil or rock mass properties through non-invasive surveys allowing to perform investigations in different environments. These characteristics, as well as the technological and scientific advancement, created a breeding ground for the employment of geophysics in landslide investigations. For instance, considering translational or rotational landslides, geophysics is helpful to identify the contrast that arises between the slide and the unaffected mass. This information allows defining the dimension, the water content and the movement of the unstable mass (McCann & Forster 1990). In this perspective, technicians generally make use of electrical and seismic surveys. The electrical resistivity tomography method is one of the most used for shallow investigations. It provides 2D and 3D maps of the soil electrical resistivity (Telford *et al.* 1990) which is sensitive to several factors such as the water content and conductivity, the nature of the material and the rock weathering. These variables are useful for the identification of the rupture surface within a landslide. It is therefore clear why this method is generally applied for landslide investigation purposes (Bichler *et al.* 2004, Lapenna *et al.* 2005, Lebourg *et al.* 2005, Wisén *et al.* 2005). On the other hand, seismic active methods are based on the analysis of the elastic waves travelling through the medium. Indeed, the different physical properties of the weakened layer (landslide body) and the surrounding intact material influence the velocities of the seismic waves making it possible to locate the surface of rupture (Caris & Van Asch 1991). By means of seismic methods, such as seismic refraction and tomography, it is, therefore, possible to characterize the landslide body by defining its dimensions, geometry and slip surface (Caris & Van Asch 1991, Glade *et al.* 2005, Meric *et al.* 2005, Jongmans & Garambois 2007). Even though these geophysical methods are a useful tool to provide 2D or 3D images of the landslide inner structure, they are not appropriate to be implemented in monitoring systems. The problems that make the application of these methodologies unsustainable to monitor landslides are primarily two. First, these geophysical techniques do not include the time variable. Thus, they do not track over time the stability of the unstable slopes. For ERT surveys some solutions to overcome this problem have been proposed in the literature (Chambers *et al.* 2009), however, the deployment of these automatic systems is economically expensive and thus not always affordable. The second important problem of both the aforementioned methods is that they do not provide a direct measure of slope stability. Indeed, the measured parameters are not linked to the displacement rate of the landslide, thus is not possible to check whether the weakened layer is getting more unstable. These problems shifted the researchers' attention to the passive seismic methodologies. The substantial difference with the active methods regards the source of the seismic waves. In the active methods, the seismic waves are artificially generated by an operator through a controlled source (e.g. hammer, explosive, ...). Whereas the passive techniques make use of the ambient seismic noise which is generated by random and uncontrolled sources. This makes the noise-based methods cheaper and convenient to implement with respect to the active ones. Moreover, the characteristic of being an omnipresent signal which does not require the presence of an operator, make the ambient vibration the ideal candidate for investigating and monitoring the time evolution of landslides.

In the following paragraph, we will present an overview of the emerging seismic noise-based techniques for monitoring and analyse the landslide phenomenon.

#### 5. Ambient seismic noise for monitoring site with high-hydrogeological risk: State-of-the-art

The idea to extract useful signals from the ambient noise is not thoroughly new. The first methods for analysing seismic noise records back to the second half of the last century. In 1957, Aki developed the Spatial Autocorrelation (SPAC) method to estimate the phase velocity dispersion of surface waves (Aki 1957). A few years later, Capon introduced the Frequency-Wavenumber analysis (f-k) which is used to find the apparent velocity and back azimuth of an incoming wavefront (Capon 1969). Both these two methods are part of the so-called seismic array methods which are based on simultaneous and combined analysis of recordings derived by several seismic sensors deployed

in a specific geometry. On the contrary, single-station techniques are performed using independent seismic sensors. Among this group, the most common methodology is the Horizontal-to-Vertical Spectral Ratio (HVS), which has been introduced in 1989 by Nakamura with the objective to study the ground motion amplification (Nakamura 1989).

It is from 1970 that the number of publications concerning seismic noise analysis went through a strong increment. This trend is surely linked to the fact that passive seismic techniques have been rapidly employed in a wide variety of application areas. With the global growth of climate-related disasters, passive techniques have been also used to investigate and monitor unstable slopes (Havenith *et al.* 2002, Danneels *et al.* 2008, V. Del Gaudio *et al.* 2008, Moore *et al.* 2011, Burjánek *et al.* 2012a, Mainsant *et al.* 2012, Vincenzo Del Gaudio *et al.* 2014, Pazzi *et al.* 2017) and unstable rock blocks (Got *et al.* 2010, Lévy *et al.* 2010, Panzera *et al.* 2012, Pierre Bottelin *et al.* 2013, P. Bottelin *et al.* 2014, 2017, Colombero *et al.* 2017a, Valentin *et al.* 2017). Among the available methods used for this purpose, the HVS has gained a lot of popularity due to the fact that this technique can be applied in almost all situation because it requires only a 3-component seismometer. Moreover, the acquisition time is relatively short, and the data processing is easy to be performed. This methodology was initially developed to map the site effects of the territory, to identify the thickness of the soft covering and so the depth of the seismic bedrock. It also provides information on the mean seismic wave velocity of the resonant layers by means of the following relation:

$$f_0 = \frac{V_s}{4h}$$

where  $f_0$  represents the resonance frequency,  $V_s$  the mean S-wave velocity and  $h$  the total thickness.

Due to the similar sedimentary condition (i.e. homogeneous and sub-horizontal strata), the HVS method has been then applied for investigating landslides where a marked impedance contrast exists between the slip surface and the unstable body which is considered as the resonant layer (Havenith *et al.* 2002, Danneels *et al.* 2008, V. Del Gaudio *et al.* 2008, Bozzano *et al.* 2011, Torgoev *et al.* 2012, Vincenzo Del Gaudio *et al.* 2014, IMPOSA *et al.* 2017). Recently, the HVS analysis has been also used to monitor rock slopes involved in gravity-induced instability processes whose evolution produce unstable rock blocks (Bottelin *et al.* 2013, P. Bottelin *et al.* 2017, Valentin *et al.* 2017, Taruselli *et al.* 2018). In this perspective, a frequency domain analysis is generally performed by resorting to periodograms, spectrograms and the horizontal-to-vertical spectral ratios (HVS) technique. The goal of these analyses is to identify the vibration modes of the investigated structure and monitor their evolution in time by borrowing an approach generally used to detect the change in building stiffness during their progressive damage (Doebling *et al.* 1996, Kim & Stubbs 2003, Clinton 2006, MICHEL *et al.* 2010). The key assumption is that every structure, either man-made or natural, has its own set of natural frequencies that can be identified by spectral peaks in ambient vibration records (Clinton 2006, Burjánek *et al.* 2012b). Given that the shape, density and elastic moduli of potentially unstable rock structures generally stay constant or change only a little over time (Bottelin *et al.* 2013), the variations of the vibrational modes occur when the contact stiffness between stable and unstable compartments change. In detail, when a rock compartment partially detaches from the stable cliff, the stiffness of the structure itself decreases, resulting in a drop of the natural frequencies (Lévy *et al.* 2010). Recent studies have pointed out that resonance frequencies can also change due to irreversible rock behaviours ruled by meteorological parameters, such as temperature and thaw/freeze cycles (Lévy *et al.* 2010, Colombero *et al.* 2017b). The HVS technique is generally used to identify the vibrational modes of unstable rock blocks because these structures often present a column-like shape. In this particular case, the horizontal oscillation of the rock pillar is bigger than the vertical one and thus, by computing the ratio between the vertical and horizontal components, it is possible to highlight the first vibrational mode of the structure (Bottelin *et al.* 2017, Colombero *et al.* 2017a).

With the aim of assessing the effectiveness of the spectral analysis in monitoring unstable rock structures, Got *et al.* (2010) and Lévy *et al.* (2010, 2011) collected the ambient seismic noise on the Chamrousset (Vercors Massif - French Alps), an unstable rock block of 21000 m<sup>3</sup> that collapsed in November 2007. The seismometers were installed four months before the collapse both on the stable compartment and on the top of the unstable rock. The obtained continuous recordings were processed with the objective of identifying possible variations of the unstable rock block resonance frequencies. The obtained results evinced a significant drop in the fundamental frequency as well as a decrease in amplitude of the base noise level preceding the collapse (Got *et al.* 2010, Lévy *et al.* 2010). While processing the continuous noise dataset, the authors also noticed the presence of a high number of events similar to weak earthquakes (Got *et al.* 2010, Lévy *et al.* 2010). Such micro-earthquakes are known in the literature as micro-seismic events and are strictly connected to the progressive failure and detachment of the rock block. For this reason, they can be considered as the micro-seismic precursor of the landslide event (Amitrano 2005, D. Arosio *et al.* 2009). However, this technique is not included among the seismic noise methods because it specifically concerns the detection and analysis of micro-seismic events only. In other words, microseismic

monitoring relies on events triggered by fracture propagation and slope failures and not on the analysis of the ambient vibrations. For this reason, we do not include the microseismic analysis within this manuscript.

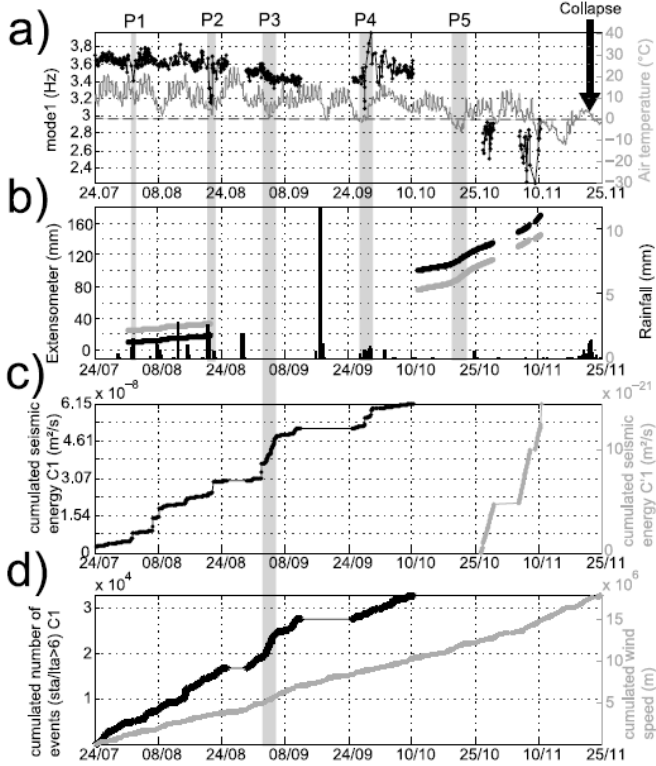


Figure 7 Comparison of seismic data measured for the Chamouset rock column with the meteorological data measured at the ‘Jardin du Roi’ station (Lévy *et al.* 2010).

Although spectral analysis proved to be a valuable tool to monitor unstable rock blocks, this technique is less adapted when considering soft-soil landslides. Indeed, for these landslides types is necessary to study the changes occurring within the material since one of the main triggering mechanisms of earth flows is the partial or total liquefaction of the unstable mass resulting from pore water pressure increasing. Given the fact that the medium properties have a strong impact on seismic velocities, the researchers moved their attention to another family of methods based on cross-correlation of the ambient noise (also called passive interferometry). The principle of this method consists of calculating the noise cross-correlation functions (NCFs) between two sensors by cross-correlating the acquired ambient noise signals as if an active source had been placed at one of them (Rickett & Claerbout 1996). The NCFs approximate the Green’s function which represents the impulse response of the medium comprises between the two seismometers. When changes in the subsurface occur, they may be observed in the reconstructed GFs and quantified as seismic velocity variations by using either the moving-window cross-spectral analysis or the stretching method (Poupinet *et al.* 1984, Sens-Schönfelder & Wegler 2006, Wapenaar *et al.* 2010). On these grounds, methods based on cross-correlation of the ambient seismic noise were firstly tested with an ultrasonic laboratory demonstration performed on a solid block using two ultrasonic receivers and a pulse generator (Lobkis and Weaver, 2001), then applied at a crustal-scale using the coda-waves of an earthquake (Campillo and Paul, 2003). The approximation of Green’s function was then improved and made more stable exploiting the diffused ambient seismic noise from multiple sources (Shapiro and Campillo, 2004). In 2006, Sens-Schönfelder and Wegler demonstrated that the GFs at large lapse times contain deterministic information about the propagation medium providing the basis for passive seismic imaging with non-ballistic waves. In detail, over a year of monitoring their study showed that the hydrological conditions can change the seismic velocities by more than 10% (Sens-Schönfelder and Wegler, 2006). Later, many other interesting discoveries from the application of PII in different environments have been carried on. Apparent velocity was observed to decrease before volcanic eruption (Brenguier *et al.*, 2011, 2008b, 2016; Obermann *et al.*, 2013a; Nakata *et al.*, 2016) and even earthquakes (Brenguier *et al.*, 2014; Taira and Brenguier, 2016, Wegler and Sens-Schönfelder, 2007; Brenguier *et al.*, 2008a; Rivet *et al.*, 2011; Hobiger *et al.*, 2016). On a smaller-scale, seismic velocity drop was observed during seasonal

thawing of permafrost (James et al., 2017). In complement to these studies, the passive seismic interferometry can detect structural changes of a material (e.g., Obermann et al., 2013a, b; Walter et al., 2015; Preiswerk and Walter, 2018), which may also be used to monitor landslides. Indeed, in this contest, a drop in the rigidity of the material constituting a landslide, due for instance to heavy rainfalls, may induce a variation of the seismic velocity propagation ( $dV/V$ ). This has been evinced for the first time by Mainsant (2015) who observed a clear velocity drop five days before the catastrophic activation of a shallow clayey landslide, at Pont-Bourquin (Mainsant et al., 2012b). The significant drop (7%) in Rayleigh wave velocity before the landslide occurrence has been interpreted as a consequence of the decay in clay mechanical properties, thus to a reduction of the material rigidity during partial fluidization at the base of the moving layer caused by water pore pressure increasing. The shear-wave velocity variation depends on the density  $\rho$  and the rigidity  $\mu$  of the medium, following the equation:

$$V_s = \sqrt{\frac{\mu}{\rho}}$$

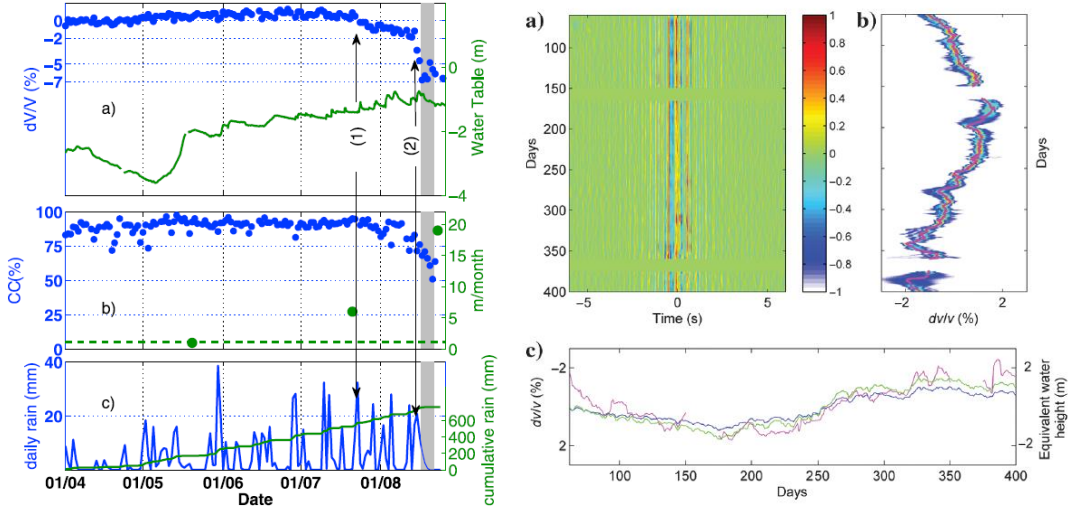


Figure 8 Examples of seismic velocity variation curves (Mainsant et al., 2012b, Voisin et al. 2016)

This phenomenon was replicated in a laboratory experiment where it has been demonstrated that the pore saturation decreases the shear-wave velocity as the clay medium progressively fluidized (Mainsant et al., 2012a, 2015; Dong and Lu, 2016; Carrière et al., 2018a, 2018b). Since then, passive seismic interferometry has been used in a wide range of landslide types, including deep-seated landslides (Bontemps et al., 2020), a rock glacier (Guillemot et al., 2020), and a rockfall/slide (Colombero et al., 2018). However, since these landslides remained relatively stable over the monitored period, it has not been possible to detect precursory velocity changes before disaster events. Another example of the passive interferometry application for landslide monitoring purposes has been proposed by Voisin et al. 2016. In this study, the ambient seismic noise recorded on the Utiku landslide (New Zealand) revealed seismic velocity variations ( $dV/V$ ) limited to a specific frequency band (6-8 Hz). The authors proved that the Rayleigh waves limited in the 6-8 Hz band have a maximum penetration depth of 2-3 m below the surface. This depth-sensitivity resulted to be coherent with the water table level measured in the piezometers, revealing that the seismic noise correlations may also use to monitor water table oscillations through saturation changes which is considered to be one of the main factors affecting the stability of landslides. A more recent study proofed the potential of the relative change in seismic velocity ( $dV/V$ ) in providing precursory information about earthflow stability (Bertello et al., 2018). Indeed, it has been observed that Rayleigh wave velocity decreased four days before the landslide collapse. Moreover, in the Harmalière rotational landslide, a clear decrease of the correlation coefficient was observed 20 days before the failure of an earth column (Folleau et al., 2020). While monitoring landslides throughout the ambient seismic noise recordings, the researcher realized that also the polarization features of these signals can provide useful insights to track the kinematic behaviour of the mass movement over time (Diego Arosio et al. 2019). In this contest, it has been shown a preferential polarization of

the ambient vibrations consistent with the direction of slope movement and/or major discontinuities (Gaudio & Wasowski 2007, Burjanek *et al.* 2010, Diego Arosio *et al.* 2019). Burjanek *et al.* (2010) and Moore *et al.* (2011) monitored an unstable rock slope above the village of Randa (Swiss Alps), which experienced two disastrous failure in April and May 1991. The collected ambient noise did not present any polarization outside the unstable area, whereas the seismic wavefield of the stations installed within the unstable body was polarized in the main direction of active rock slope movement (Moore *et al.* 2011). This different response of the stable and unstable areas suggested that the ambient noise recordings could be useful to map other instabilities. Two years later, a seismic array was deployed at a potentially unstable slope in the same area (Burjánek *et al.* 2012b). The data analysis showed that the wavefield was dominated by standing waves with horizontal spectral amplification oriented perpendicular to near-vertical deep fractures. The polarization analysis has been also applied to the unstable rock slopes. In this context, Bottelin *et al.* (2013) studied the dynamic response of four prone-to-fall rock compartments showing that every single site exhibited well-defined polarized spectral peaks at distinct frequencies. In particular, he highlighted that the predominant spectral peaks, corresponding to the first vibrational mode of the studied rocks, had a polarization perpendicular to the rear fracture.

## 6. Conclusion

This chapter was written with the intent to introduce the reader to the ambient seismic noise providing a clear definition of this still little known seismic wavefield and a list of the sources that cause the Earth' background vibration. This part is then followed by an overview of the existing literature on the topic of landslide monitoring by means of ambient vibration. Since the use of the ambient seismic noise for geo-hazard monitoring seems promising, the core of the following work will be the investigation of the potentiality of such wavefield in monitoring both unstable rock blocks and water table level variations.

## 7. Bibliography

- Aki, K. (1957) Space and Time Spectra of Stationary Stochastic Waves, with Special Reference to Microtremors. *Bulletin of the Earthquake Research Institute*, **35**, 415–456.
- Amitrano, D. (2005) Seismic precursory patterns before a cliff collapse and critical point phenomena. *Geophysical Research Letters*, **32**. doi:10.1029/2004GL022270
- Anthony, R.E., Aster, R.C., Wiens, D., Nyblade, A., Anandakrishnan, S., Huerta, A., Winberry, J.P., *et al.* (2015) The Seismic Noise Environment of Antarctica. *Seismological Research Letters*, **86**, 89–100. doi:10.1785/0220140109
- Ardhuin, F., Gualtieri, L. & Stutzmann, E. (2015) How ocean waves rock the Earth: Two mechanisms explain microseisms with periods 3 to 300 s. *Geophys. Res. Lett.*, **42**, 765–772. doi:10.1002/2014GL062782
- Arosio, D., Longoni, L., Papini, M., Scaioni, M., Zanzi, L. & Alba, M. (2009) Towards rockfall forecasting through observing deformations and listening to microseismic emissions. *Nat. Hazards Earth Syst. Sci.*, **9**, 1119–1131. doi:10.5194/nhess-9-1119-2009
- Arosio, Diego, Longoni, L., Papini, M., Bièvre, G. & Zanzi, L. (2019) Geological and geophysical investigations to analyse a lateral spreading phenomenon: the case study of Torrioni di Rialba, northern Italy. *Landslides*. doi:10.1007/s10346-019-01176-w
- Bertello, L., Berti, M., Castellaro, S., Squarzoni, G., 2018. Dynamics of an Active Earthflow Inferred From Surface Wave Monitoring. *Journal of Geophysical Research: Earth Surface* **123**, 1811–1834. <https://doi.org/10.1029/2017JF004233>
- Bichler, A., Bobrowsky, P., Best, M.E., Douma, M., Hunter, J., Calvert, T. & Burns, R. (2004) Three-dimensional mapping of a landslide using a multi-geophysical approach: The Quesnel Forks Landslide. *Landslides*, **1**, 29–40. doi:10.1007/s10346-003-0008-7
- Bogoslovsky, V.A. & Ogilvy, A.A. (1977) Geophysical methods for the investigation of landslides. *Geophysics*, **42**, 562–571, GeoScienceWorld. doi:10.1190/1.1440727
- Bonnetfond-Claudet, S., Cotton, F. & Bard, P.-Y. (2006) The nature of noise wavefield and its applications for site effects studies: A literature review. *Earth-Science Reviews*, **79**, 205–227. doi:10.1016/j.earscirev.2006.07.004
- Bontemps, N., Lacroix, P., Larose, E., Jara, J., Taipe, E., 2020. Rain and small earthquakes maintain a slow-moving landslide in a persistent critical state. *Nat Commun* **11**, 1–10. <https://doi.org/10.1038/s41467-020-14445-3>

- Bormann, P. & Wielandt, E. (2013) Seismic Signals and Noise. New Manual of Seismological Observatory Practice 2 (NMSOP2), 1–62, Deutsches GeoForschungsZentrum GFZ. doi:10.2312/GFZ.NMSOP-2\_ch4
- Bottelin, P., Baillet, L., Larose, E., Jongmans, D., Hantz, D., Brenguier, O., Cadet, H., et al. (2017) Monitoring rock reinforcement works with ambient vibrations: La Bourne case study (Vercors, France). *Engineering Geology*, **226**, 136–145. doi:10.1016/j.enggeo.2017.06.002
- Bottelin, P., Jongmans, D., Daudon, D., Mathy, A., Helmstetter, A., Bonilla-Sierra, V., Cadet, H., et al. (2014) Seismic and mechanical studies of the artificially triggered rockfall at Mount Néron (French Alps, December 2011). *Natural Hazards and Earth System Sciences*, **14**, 3175–3193. doi:10.5194/nhess-14-3175-2014
- Bottelin, Pierre, Jongmans, D., Baillet, L., Lebourg, T., Hantz, D., Levy, C., Roux, O., et al. (2013) Spectral Analysis of Prone-to-fall Rock Compartments using Ambient Vibrations. *Journal of Environmental & Engineering Geophysics*, **18**, 205–217. doi:10.2113/JEEG18.4.205
- Bozzano, F., Lenti, L., Martino, S., PACIELLO, A. & Mugnochza, G. (2011) Evidences of landslide earthquake triggering due to self-excitation process. *International Journal of Earth Sciences*, **100**, 861–879. doi:10.1007/s00531-010-0514-5
- Brenguier, F., Campillo, M., Hadzioannou, C., Shapiro, N.M., Nadeau, R.M., Larose, E., 2008a. Postseismic Relaxation Along the San Andreas Fault at Parkfield from Continuous Seismological Observations. *Science* 321, 1478–1481. <https://doi.org/10.1126/science.1160943>
- Brenguier, F., Shapiro, N.M., Campillo, M., Ferrazzini, V., Duputel, Z., Coutant, O., Nercessian, A., 2008b. Towards forecasting volcanic eruptions using seismic noise. *Nature Geoscience* 1, 126–130. <https://doi.org/10.1038/ngeo104>
- Brenguier, F., Clarke, D., Aoki, Y., Shapiro, N.M., Campillo, M., Ferrazzini, V., 2011. Monitoring volcanoes using seismic noise correlations. *Comptes Rendus Geoscience* 343, 633–638. <https://doi.org/10.1016/j.crte.2010.12.010>
- Brenguier, F., Campillo, M., Takeda, T., Aoki, Y., Shapiro, N.M., Briand, X., Emoto, K., Miyake, H., 2014. Mapping pressurized volcanic fluids from induced crustal seismic velocity drops. *Science* 345, 80–82. <https://doi.org/10.1126/science.1254073>
- Brenguier, F., Rivet, D., Obermann, A., Nakata, N., Boué, P., Lecocq, T., Campillo, M., Shapiro, N., 2016. 4-D noise-based seismology at volcanoes: Ongoing efforts and perspectives. *Journal of Volcanology and Geothermal Research* 321, 182–195. <https://doi.org/10.1016/j.jvolgeores.2016.04.036>
- Bromirski, P.D., Duennbier, F.K. & Stephen, R.A. (2005) Mid-ocean microseisms: MID-OCEAN MICROSEISMS. *Geochem. Geophys. Geosyst.*, **6**, n/a-n/a. doi:10.1029/2004GC000768
- Bromirski, P.D. & Gerstoft, P. (2009) Dominant source regions of the Earth’s “hum” are coastal. *Geophys. Res. Lett.*, **36**, L13303. doi:10.1029/2009GL038903
- Burjanek, J., Gassner-Stamm, G., Poggi, V., Moore, J. & Fäh, D. (2010) Ambient vibration analysis of an unstable mountain slope. *Geophysical Journal International - GEOPHYS J INT*, **180**, 820–828. doi:10.1111/j.1365-246X.2009.04451.x
- Burjánek, J., Moore, J.R., Yugsi Molina, F.X. & Fäh, D. (2012) Instrumental evidence of normal mode rock slope vibration: Evidence of normal mode rock slope vibration. *Geophysical Journal International*, **188**, 559–569. doi:10.1111/j.1365-246X.2011.05272.x
- Burjánek, J., Moore, J.R., Yugsi Molina, F.X. & Fäh, D. (2012) Instrumental evidence of normal mode rock slope vibration. *Geophysical Journal International*, **188**, 559–569. doi:10.1111/j.1365-246X.2011.05272.x
- Dong, Y., Lu, N., 2016. Dependencies of Shear Wave Velocity and Shear Modulus of Soil on Saturation. *Journal of Engineering Mechanics* 142, 04016083. [https://doi.org/10.1061/\(ASCE\)EM.1943-7889.0001147](https://doi.org/10.1061/(ASCE)EM.1943-7889.0001147)
- Campillo, M., Paul, A., 2003. Long-Range Correlations in the Diffuse Seismic Coda. *Science* 299, 547–549. <https://doi.org/10.1126/science.1078551>.
- Capon, J. (1969) High-resolution frequency-wavenumber spectrum analysis. doi:10.1109/PROC.1969.7278
- Caris, J.P.T. & Van Asch, Th.W.J. (1991) Geophysical, geotechnical and hydrological investigations of a small landslide in the French Alps. *Engineering Geology*, **31**, 249–276. doi:10.1016/0013-7952(1)90011-9
- Carrière, S.R., Bièvre, G., Jongmans, D., Chambon, G., Bellot, H., Lebourg, T., 2018a. Measurement of geophysical parameters on clay samples at the solid–fluid transition. *Near Surface Geophysics* 16, 1–15. <https://doi.org/10.3997/1873-0604.2017039>
- Chambers, J., Meldrum, P., Gunn, D.A., Wilkinson, P.B., Kuras, O., Weller, A. & Ogilvy, R.D. (2009) Hydrogeophysical Monitoring of Landslide Processes Using Automated Time-Lapse Electrical Resistivity Tomography (ALERT). *Near Surface 2009 - 15th European Meeting of Environmental and Engineering Geophysics*. doi:10.3997/2214-4609.20147066

- Clinton, J.F. (2006) The Observed Wander of the Natural Frequencies in a Structure. *Bulletin of the Seismological Society of America*, **96**, 237–257. doi:10.1785/0120050052
- Colombero, C., Baillet, L., Comina, C., Jongmans, D. & Vinciguerra, S. (2017) Characterization of the 3-D fracture setting of an unstable rock mass: From surface and seismic investigations to numerical modeling: Fracture Settings of an Unstable Cliff. *Journal of Geophysical Research: Solid Earth*, **122**, 6346–6366. doi:10.1002/2017JB014111
- Colombero, C., Baillet, L., Comina, C., Jongmans, D., Larose, E., Valentin, J., Vinciguerra, S., 2018. Integration of ambient seismic noise monitoring, displacement and meteorological measurements to infer the temperature-controlled long-term evolution of a complex prone-to-fall cliff. *Geophys J Int* 213, 1876–1897. <https://doi.org/10.1093/gji/ggy090>
- Danneels, G., Bourdeau, C., Torgoev, I. & Havenith, H.-B. (2008) Geophysical investigation and dynamic modelling of unstable slopes: case-study of Kainama (Kyrgyzstan). *Geophysical Journal International*, **175**, 17–34. doi:10.1111/j.1365-246X.2008.03873.x
- Del Gaudio, V., Coccia, S., Wasowski, J., Gallipoli, M.R. & Mucciarelli, M. (2008) Detection of directivity in seismic site response from microtremor spectral analysis. *Natural Hazards and Earth System Sciences*, **8**, 751–762, Copernicus GmbH. doi:<https://doi.org/10.5194/nhess-8-751-2008>
- Del Gaudio, Vincenzo, Muscillo, S. & Wasowski, J. (2014) What we can learn about slope response to earthquakes from ambient noise analysis: An overview. *Engineering Geology*, **182**. doi:10.1016/j.enggeo.2014.05.010
- Doebling, S.W., Farrar, C.R., Prime, M.B. & Shevitz, D.W. (1996) Damage identification and health monitoring of structural and mechanical systems from changes in their vibration characteristics: A literature review (No. LA-13070-MS), Los Alamos National Lab., NM (United States). doi:<https://doi.org/10.2172/249299>
- Ebeling, C.W. & Stein, S. (2011) Seismological Identification and Characterization of a Large Hurricane. *Bulletin of the Seismological Society of America*, **101**, 399–403. doi:10.1785/0120100175
- Fiolleau, S., Jongmans, D., Bi`evre, G., Chambon, G., Baillet, L., Vial, B., 2020. Seismic characterization of a clay-block rupture in Harmali`ere landslide, French Western Alps. *Geophysical Journal International* 221, 1777–1788. <https://doi.org/10.1093/gji/ggaa050>
- Gaudio, V.D. & Wasowski, J. (2007) Directivity of slope dynamic response to seismic shaking. *Geophysical Research Letters*, **34**. doi:<https://doi.org/10.1029/2007GL029842>
- Gerstoft, P., Shearer, P.M., Harmon, N. & Zhang, J. (2008) Global P, PP, and PKP wave microseisms observed from distant storms. *Geophysical Research Letters*, **35**. doi:<https://doi.org/10.1029/2008GL036111>
- Glade, T., Stark, P. & Dikau, R. (2005) Determination of potential landslide shear plane depth using seismic refraction—a case study in Rheinhessen, Germany. *Bull Eng Geol Environ*, **64**, 151–158. doi:10.1007/s10064-004-0258-1
- Got, J.-L., Mourot, P. & Grangeon, J. (2010) Pre-failure behaviour of an unstable limestone cliff from displacement and seismic data. *Natural Hazards and Earth System Sciences*, **10**, 819–829, Copernicus GmbH. doi:<https://doi.org/10.5194/nhess-10-819-2010>
- Grob, M., Maggi, A. & Stutzmann, E. (2011) Observations of the seasonality of the Antarctic microseismic signal, and its association to sea ice variability. *Geophysical Research Letters*, **38**. doi:<https://doi.org/10.1029/2011GL047525>
- Gualtieri, L., Stutzmann, E., Capdeville, Y., Arduuin, F., Schimmel, M., Mangeney, A. & Morelli, A. (2013) Modelling secondary microseismic noise by normal mode summation. *Geophysical Journal International*, **193**, 1732–1745. doi:10.1093/gji/ggt090
- Gualtieri, L., Stutzmann, E., Capdeville, Y., Farra, V., Mangeney, A. & Morelli, A. (2015) On the shaping factors of the secondary microseismic wavefield. *J. Geophys. Res. Solid Earth*, **120**, 6241–6262. doi:10.1002/2015JB012157
- Gualtieri, L., Stutzmann, E., Farra, V., Capdeville, Y., Schimmel, M., Arduuin, F. & Morelli, A. (2014) Modelling the ocean site effect on seismic noise body waves. *Geophysical Journal International*, **197**, 1096–1106. doi:10.1093/gji/ggu042
- Gualtieri, Lucia, Camargo, S.J., Pascale, S., Pons, F. & Ekström, G. (2018) The persistent signature of tropical cyclones in ambient seismic noise, Columbia University. doi:10.7916/D8-KK97-NR44
- Guillemot, A., Helmstetter, A., Larose, E., Baillet, L., Garambois, S., Mayoraz, R., Delaloye, R., 2020. Seismic monitoring in the Gugla rock glacier (Switzerland): ambient noise correlation, microseismicity and modelling. *Geophys J Int* 221, 1719–1735. <https://doi.org/10.1093/gji/ggaa097>
- Hack, R. (2000) Geophysics For Slope Stability. *Surveys in Geophysics*, **21**, 423–448. doi:10.1023/A:1006797126800
- Hasselmann, K. (1963) A statistical analysis of the generation of microseisms. *Rev. Geophys.*, **1**, 177. doi:10.1029/RG001i002p00177

- Havenith, H.-B., Jongmans, D., Faccioli, E., Abdurakhmatov, K. & Bard, P.-Y. (2002) Site Effect Analysis around the Seismically Induced Ananevo Rockslide, Kyrgyzstan. *Bulletin of the Seismological Society of America*, **92**, 3190–3209. doi:10.1785/0120010206
- Hobiger, M., Wegler, U., Shiomi, K., Nakahara, H., 2016. Coseismic and post-seismic velocity changes detected by Passive Image Interferometry: comparison of one great and five strong earthquakes in Japan. *Geophys J Int* 205, 1053–1073. <https://doi.org/10.1093/gji/ggw066>
- Imposa, S., Grassi, S., Fazio, F., Rannisi, G. & Cino, P. (2017) Geophysical surveys to study a landslide body (northeastern Sicily). *Natural Hazards*, **86**, 327–343.
- James, S.R., Knox, H.A., Abbott, R.E., Screamton, E.J., 2017. Improved moving window cross-spectral analysis for resolving large temporal seismic velocity changes in permafrost. *Geophysical Research Letters* 44, 4018–4026. <https://doi.org/10.1002/2016GL072468>.
- Jongmans, D. & Garambois, S. (2007) Geophysical investigation of landslides: A review. *Bulletin de la Societe Geologique de France*, **178**. doi:10.2113/gssgbull.178.2.101
- Kedar, S., Longuet-Higgins, M., Webb, F., Graham, N., Clayton, R. & Jones, C. (2008) The origin of deep ocean microseisms in the North Atlantic Ocean. *Proc. R. Soc. A*, **464**, 777–793. doi:10.1098/rspa.2007.0277
- Kim, J.-T. & Stubbs, N. (2003) CRACK DETECTION IN BEAM-TYPE STRUCTURES USING FREQUENCY DATA. *Journal of Sound and Vibration*, **259**, 145–160. doi:10.1006/jsvi.2002.5132
- Koper, K.D., Seats, K. & Benz, H. (2010) On the composition of earth's short-period seismic noise field. *Bulletin of the Seismological Society of America*. doi:10.1785/0120090120
- Koper, Keith D., Foy, B. de & Benz, H. (2009) Composition and variation of noise recorded at the Yellowknife Seismic Array, 1991–2007. *Journal of Geophysical Research: Solid Earth*, **114**. doi:<https://doi.org/10.1029/2009JB006307>
- Lapenna, V., Lorenzo, P., Perrone, A., Piscitelli, S., Rizzo, E. & Sdao, F. (2005) 2D electrical resistivity imaging of some complex landslides in Lucanian Apennine chain, southern Italy. *GEOPHYSICS*, **70**, B11–B18, Society of Exploration Geophysicists. doi:10.1190/1.1926571
- Larose, E., Margerin, L., Derode, A., Tiggelen, B. van, Campillo, M., Shapiro, N., Paul, A., et al. (2006) Correlation of random wavefields: An interdisciplinary review. *GEOPHYSICS*, **71**, SI11–SI21, Society of Exploration Geophysicists. doi:10.1190/1.2213356
- Lebourg, T., Binet, S., Tric, E., Jomard, H. & Bedouï, S.E. (2005) Geophysical survey to estimate the 3D sliding surface and the 4D evolution of the water pressure on part of a deep seated landslide. *Terra Nova*, **17**, 399–406. doi:<https://doi.org/10.1111/j.1365-3121.2005.00623.x>
- Lecocq, T., Hicks, S.P., Van Noten, K., Wijk, K. van, Koelemeijer, P., De Plaen, R.S.M., Massin, F., et al. (2020) Global quieting of high-frequency seismic noise due to COVID-19 pandemic lockdown measures. *Science*, **369**, 1338–1343. doi:10.1126/science.abd2438
- Lévy, C., Baillet, L., Jongmans, D., Mourot, P. & Hantz, D. (2010) Dynamic response of the Chamrousset rock column (Western Alps, France). *Journal of Geophysical Research*, **115**. doi:10.1029/2009JF001606
- Lobkis, O.I., Weaver, R.L., 2001. On the emergence of the Green's function in the correlations of a diffuse field. *The Journal of the Acoustical Society of America* 110, 3011–3017. <https://doi.org/10.1121/1.1417528>
- Longuet-Higgins, M.S. (1950) A Theory of the Origin of Microseisms. *Philosophical Transactions of the Royal Society of London. Series A, Mathematical and Physical Sciences*, 243, 1–35.
- Mainsant, G., Jongmans, D., Chambon, G., Larose, E., Baillet, L., 2012a. Shear-wave velocity as an indicator for rheological changes in clay materials: Lessons from laboratory experiments. *Geophys. Res. Lett.* 39, L19301 <https://doi.org/10.1029/2012GL053159>.
- Mainsant, G., Larose, E., Brönnimann, C., Jongmans, D., Michoud, C., Jaboyedoff, M., 2012b. Ambient seismic noise monitoring of a clay landslide: Toward failure prediction. *J. Geophys. Res.* 117, F01030 <https://doi.org/10.1029/2011JF002159>
- Mainsant, G., Chambon, G., Jongmans, D., Larose, E., Baillet, L., 2015. Shear-wave-velocity drop prior to clayey mass movement in laboratory flume experiments. *Engineering Geology* 192, 26–32. <https://doi.org/10.1016/j.enggeo.2015.03.019> McCann, D.M. & Forster, A. (1990) Reconnaissance geophysical methods in landslide investigations. *Engineering Geology*, 29, 59–78. doi:10.1016/0013-7952(90)90082-C
- McNamara, D.E., Ringler, A.T., Hutt, C.R. & Gee, L.S. (2011) Seismically observed seiching in the Panama Canal. *Journal of Geophysical Research: Solid Earth*, **116**. doi:<https://doi.org/10.1029/2010JB007930>
- Meric, O., Garambois, S., Jongmans, D., Wathélet, M., Chatelain, J.L. & Vengeon, J.M. (2005) Application of geophysical methods for the investigation of the large gravitational mass movement of Séchilienne, France. *Can. Geotech. J.*, **42**, 1105–1115. doi:10.1139/t05-034

- MICHEL, C., GUEGUEN, P., AREM, S.E., MAZARS, J. & KOTRONIS, P. (n.d.) FULL SCALE DYNAMIC RESPONSE OF A RC BUILDING UNDER WEAK SEISMIC MOTIONS USING EARTHQUAKE RECORDINGS, AMBIENT VIBRATIONS AND MODELLING, 20.
- Moore, J., Gischig, V., Burjanek, J., Loew, S. & Fäh, D. (2011) Site Effects in Unstable Rock Slopes: Dynamic Behavior of the Randa Instability (Switzerland). *The Bulletin of the Seismological Society of America*, **101**, 3110–3116. doi:10.1785/0120110127
- Nakamura, Y. (1989) A METHOD FOR DYNAMIC CHARACTERISTICS ESTIMATION OF SUBSURFACE USING MICROTREMOR ON THE GROUND SURFACE. *Railway Technical Research Institute, Quarterly Reports*, **30**. Retrieved from <https://trid.trb.org/view/294184>
- Nakata, N., Boué, P., Brenguier, F., Roux, P., Ferrazzini, V., Campillo, M., 2016. Body and surface wave reconstruction from seismic noise correlations between arrays at Piton de la Fournaise volcano. *Geophysical Research Letters* **43**, 1047–1054. <https://doi.org/10.1002/2015GL066997>
- Nakata, N., Gualtieri, L. & Fichtner, A. (Eds.). (2019) *Seismic Ambient Noise*, Cambridge: Cambridge University Press. doi:10.1017/9781108264808
- Nishida, K. (2017) Ambient seismic wave field. *Proceedings of the Japan Academy. Ser. B: Physical and Biological Sciences*, **93**, 423–448. doi:10.2183/pjab.93.026
- Obermann, A., Plan`es, T., Larose, E., Campillo, M., 2013a. Imaging preeruptive and coeruptive structural and mechanical changes of a volcano with ambient seismic noise. *Journal of Geophysical Research: Solid Earth* **118**, 6285–6294. <https://doi.org/10.1002/2013JB010399>
- Panzera, F., D'Amico, S., Lotteri, A., Galea, P. & Lombardo, G. (2012) Seismic site response of unstable steep slope using noise measurements: the case study of Xemxija Bay area, Malta. *Natural Hazards and Earth System Sciences*, **12**, 3421–3431, Copernicus GmbH. doi:<https://doi.org/10.5194/nhess-12-3421-2012>
- Pazzi, V., Tanteri, L., Bicocchi, G., D'Ambrosio, M., Caselli, A. & Fanti, R. (2017) H/V measurements as an effective tool for the reliable detection of landslide slip surfaces: Case studies of Castagnola (La Spezia, Italy) and Roccalbegna (Grosseto, Italy). *Physics and Chemistry of the Earth, Parts A/B/C Advance in seismic site response: usual practices and innovative methods*, **98**, 136–153. doi:10.1016/j.pce.2016.10.014
- Peterson, J.R. (1993) Observations and modeling of seismic background noise (USGS Numbered Series No. 93–322). *Observations and modeling of seismic background noise Open-File Report*, Vol. 93–322, U.S. Geological Survey. doi:10.3133/ofr93322
- Poupinet, G., Ellsworth, W.L. & Frechet, J. (1984) Monitoring velocity variations in the crust using earthquake doublets: An application to the Calaveras Fault, California. *J. Geophys. Res.*, **89**, 5719–5731. doi:10.1029/JB089iB07p05719
- Preiswerk, L.E., Walter, F., 2018. High-Frequency (>2 Hz) Ambient Seismic Noise on High-Melt Glaciers: Green's Function Estimation and Source Characterization. *Journal of Geophysical Research: Earth Surface* **123**, 1667–1681. <https://doi.org/10.1029/2017JF004498>
- Pyle, M.L., Koper, K.D., Euler, G.G. & Burlacu, R. (2015) Location of high-frequency P wave microseismic noise in the Pacific Ocean using multiple small aperture arrays. *Geophysical Research Letters*, **42**, 2700–2708. doi:<https://doi.org/10.1002/2015GL063530>
- Rickett, James, and Jon Claerbout. "Passive seismic imaging applied to synthetic data." *Stanford Exploration Project* 92 (1996): 83-90.
- Rivet, D., Campillo, M., Shapiro, N.M., Cruz-Atienza, V., Radiguet, M., Cotte, N., Kostoglodov, V., 2011. Seismic evidence of nonlinear crustal deformation during a large slow slip event in Mexico. *Geophysical Research Letters* **38**. <https://doi.org/10.1029/2011GL047151>.
- Roult, G. & Crawford, W. (2000) Analysis of 'background' free oscillations and how to improve resolution by subtracting the atmospheric pressure signal. *Physics of the Earth and Planetary Interiors*, **121**, 325–338. doi:10.1016/S0031-9201(00)00172-2
- Shapiro, N.M., Campillo, M., 2004. Emergence of broadband Rayleigh waves from correlations of the ambient seismic noise. *Geophysical Research Letters* **31**. <https://doi.org/10.1029/2004GL019491>.
- Sens-Schönfelder, C. & Wegler, U. (2006) Passive image interferometry and seasonal variations of seismic velocities at Merapi Volcano, Indonesia. *Geophysical Research Letters*, **33**. doi:10.1029/2006GL027797
- Sounding Out Earth's Hum. (2019, January 11) *EARTH Magazine*. Retrieved January 21, 2021, from <https://www.earthmagazine.org/article/sounding-out-earths-hum>
- Taira, T., Brenguier, F., 2016. Response of hydrothermal system to stress transients at Lassen Volcanic Center, California, inferred from seismic interferometry with ambient noise. *Earth, Planets and Space* **68**, 162. <https://doi.org/10.1186/s40623-016-0538-6>
- Tanimoto, T., Hadziloannou, C., Igel, H., Wassermann, J., Schreiber, U., Gebauer, A. & Chow, B. (2016) Seasonal variations in the Rayleigh-to-Love wave ratio in the secondary microseism from colocated ring laser and

- seismograph. *Journal of Geophysical Research: Solid Earth*, **121**, 2447–2459.  
doi:<https://doi.org/10.1002/2016JB012885>
- Tanmoto, T. & Um, J. (1999) Cause of continuous oscillations of the Earth. *J. Geophys. Res.*, **104**, 28723–28739.  
doi:10.1029/1999JB900252
- Taruselli, M., Arosio, D., Longoni, L., Papini, M., Corsini, A. & Zanzi, L. (2018) Rock Stability as Detected by Seismic Noise Recordings - Three Case Studies, Presented at the 24th European Meeting of Environmental and Engineering Geophysics, Porto, Portugal. doi:10.3997/2214-4609.201802611
- Telford, W.M., Geldart, L.P. & Sheriff, R.E. (1990) *Applied Geophysics*, 2nd ed., Cambridge: Cambridge University Press. doi:10.1017/CBO9781139167932
- Torgoev, A., Lamair, L., Torgoev, I. & Havenith, H.-B. (2012) A Review of Recent Case Studies of Landslides Investigated in the Tien Shan Using Microseismic and Other Geophysical Methods, pp. 285–294.  
doi:10.1007/978-3-642-32238-9\_29
- Tsai, V.C. & McNamara, D.E. (2011) Quantifying the influence of sea ice on ocean microseism using observations from the Bering Sea, Alaska. *Geophysical Research Letters*, **38**. doi:<https://doi.org/10.1029/2011GL049791>
- Uchiyama, Y. & McWilliams, J.C. (2008) Infragravity waves in the deep ocean: Generation, propagation, and seismic hum excitation. *J. Geophys. Res.*, **113**, C07029. doi:10.1029/2007JC004562
- Valentin, J., Capron, A., Jongmans, D., Baillet, L., Bottelin, P., Donze, F., Larose, E., et al. (2017) The dynamic response of prone-to-fall columns to ambient vibrations: comparison between measurements and numerical modelling. *Geophysical Journal International*, **208**, 1058–1076. doi:10.1093/gji/ggw440
- Voisin, C., Garambois, S., Massey, C. & Brossier, R. (2016) Seismic noise monitoring of the water table in a deep-seated, slow-moving landslide. *Interpretation*, **4**, SJ67–SJ76. doi:10.1190/INT-2016-0010.1
- Walter, F., O'Neil, S., McNamara, D., Pfeffer, W.T., Bassis, J.N. & Fricker, H.A. (2010) Iceberg calving during transition from grounded to floating ice: Columbia Glacier, Alaska: CALVING TRANSITION AT COLUMBIA GLACIER. *Geophys. Res. Lett.*, **37**, n/a-n/a. doi:10.1029/2010GL043201
- Walter, F., Roux, P., Roeoesli, C., Lecointre, A., Kilb, D., Roux, P.-F., 2015. Using glacier seismicity for phase velocity measurements and Green's function retrieval. *Geophys J Int* 201, 1722–1737.  
<https://doi.org/10.1093/gji/ggv069>
- Wapenaar, K., Draganov, D., Snieder, R., Campman, X. & Verdel, A. (2010) Tutorial on seismic interferometry: Part 1 — Basic principles and applications. *GEOPHYSICS*, **75**, 75A195–75A209. doi:10.1190/1.3457445
- Webb, S.C. (2007) The Earth's 'hum' is driven by ocean waves over the continental shelves. *Nature*, **445**, 754–756.  
doi:10.1038/nature05536
- Wegler, U., Sens-Schönfelder, C., 2007. Fault zone monitoring with passive image interferometry. *Geophys J Int* 168, 1029–1033. <https://doi.org/10.1111/j.1365-246X.2006.03284.x>
- Wisén, R., Auken, E. & Dahlin, T. (2005) Combination of 1D laterally constrained inversion and 2D smooth inversion of resistivity data with a priori data from boreholes. *Near Surface Geophysics - NEAR SURF GEOPHYS*, **3**. doi:10.3997/1873-0604.2005002
- Withers, M.M., Aster, R.C., Young, C.J. & Chael, E.P. (1996) High-Frequency Analysis of Seismic Background Noise as a Function of Wind Speed and Shallow Depth, 9.

# CHAPTER 2

## Ambient seismic noise processing methods

### 1. Introduction

This section of the manuscript describes all methodologies that have been used within this work to provide reliable information about the monitored sites from recordings that most of us would think of as noise. It, therefore, aims to explain how it is possible to turn ambient seismic noise into useful data for geo-hazard applications. The chapter is subdivided into three sub-sections depending on the analysis type. It firstly shows which are the spectral analysis techniques used for the estimation of the ambient vibration spectral content. Further, it describes the different existing techniques to study the polarization of the seismic noise wavefield. Finally, deep insight into the ambient seismic noise cross-correlation method is provided.

To facilitate and speed up the ambient seismic noise analysis, a Matlab Graphical User Interface (GUI) App, called PassiveBarinda, has been developed. The software can be divided into two main sections: basic and advanced processing. The former regards the pre-processing that is generally performed when dealing with ambient seismic noise, that is: cut, resampling, merge, filter, alignment of signals, and the instrument response removal. The latter includes the methodologies that will be treated within this chapter. It, therefore, contains functions that allow performing the spectral and polarization analysis, the HV Spectral Ratio and the passive interferometry. The PassiveBarinda App would not be treated within this chapter; however, the Appendix section of the manuscript provides a Manual that documents how to use all the up-to-date available tools in PassiveBarinda for ambient seismic noise processing.

### 2. Spectral analysis

Within this paragraph, a description of the techniques used for the spectral analysis of the ambient seismic noise is provided. Robust estimation of the spectral content is fundamental when studying the vibrational modes of the unstable rock blocks. This is particularly true when the purpose of the study is the monitoring over time of the unstable compartment's fundamental frequencies. Indeed, since the vibrational modes of the investigated structure are identified by peaks in the amplitude spectrum of the recordings, it is extremely important to be able to discern oscillations occurring at closely spaced frequencies. Moreover, when tracking the evolution in time of rock block stability by means of modal analysis, the spectral estimation must also guarantee the ability to identify tiny movements of the spectral peaks towards close frequencies. The reason for this is that frequency changes of the spectral peaks may reveal a variation of the unstable rocks' stability.

The goal of spectral density estimation (SDE) is to accurately describe a time series into the frequency domain providing the best possible power spectrum estimate (Appendix A). The SDE techniques are based on the spectral analysis which decomposes a waveform signal into its underlying oscillations. The result of the analysis is the power spectrum that is a function that shows the power of the oscillations at each frequency. The theoretical basis of the spectral density estimation is the Fourier transform (FT) which is a mathematical method for decomposing a time-domain signal into its frequency components. The FT assumes that signals are repeated periodically for an infinite period of time and that they can be decomposed into pure sinusoids. This condition guarantees that using the Fourier analysis it is possible to measure an ideal spectrum, which will show perfect peaks at each of the frequencies contained in the time series. However, this theoretical assumption breaks down when considering ambient seismic noise which is a finite, discrete, aperiodic and time-varying signal. Therefore, spectral analysis of real data can produce results that largely differ from the ideal spectrum, hence potentially leading to inaccurate outcomes.

Given the importance of providing a robust measure of the unstable compartments' vibrational modes, in this work, we made use of two different spectral density estimation techniques: the Welch's periodogram and the Multitaper Spectral Analysis.

#### 2.1. Welch's Periodogram

Among the spectral density estimation techniques, the most straightforward approach for computing the power spectrum is the periodogram that consists of computing the squared magnitude of the signal Fourier transform as an estimate of the spectral content (Schuster 1898).

$$\widehat{S_p}(f) = \Delta t \left| \sum_{k=0}^{N-1} x_k e^{2\pi k f \Delta t} \right|^2$$

Unfortunately, this simple method does not provide satisfying results since it suffers from two possible problems. First, the periodogram has high variance because the power spectral density is computed upon a single realization of the random process. In addition, the spectral estimate is biased meaning that the obtained power spectrum is different from the ideal one. An intuitive way to explain the latter problem is to think of a finite time series as the product of an infinite signal and a rectangular window equal to 1 for the duration of the selected data and equal to 0 elsewhere (Prerau *et al.* 2017). The result is the convolution of the ideal data spectrum with the spectrum of the rectangular window, which is a multipeaked function characterised by the main lobe and side lobes. The latter produce noise at a given frequency that “leak” into the estimate at other frequencies generating a distortion of the true spectral content of the data. This spectral leakage, as it is called, reduces the accuracy of the estimate, and makes it difficult to clearly distinguish peaks in the ambient noise recordings. The side and main lobes contribute to the periodogram bias in different ways. The side lobes generate a broadband bias that brings power to frequencies where it should not exist. This bias can be particularly problematic when computing the modal analysis of unstable rock blocks from ambient vibration. Indeed, these recordings are noisy and may show multiple closely spaced frequency peaks. In such cases, the side lobes redistribute power from noise or multiple oscillations to unrelated frequencies (Prerau *et al.* 2017). On the other side, the main lobe introduces a narrowband bias because it blurs all the frequencies that are within the small range of its bandwidth. In other words, if there are oscillations that are separated by a frequency less than the width of the main lobe, they will be erroneously blended in a single oscillation. The consequence of both these two biases is that peaks within the spectrum can appear less distinct and blurred across frequencies.

To mitigate the disadvantages of the basic periodogram, many improvements for spectral estimation have been proposed in the years. In 1948 Bartlett provided a way to reduce the variance of the periodogram in exchange for a reduction of the resolution compared to Schuster’s method (Bartlett 1948). He provided a spectrum estimate by averaging the periodograms derived from non-overlapping windows of the original time series. Even though this improvement led to a better estimate of the power spectrum, the turning point was provided by Welch in 1967 (Welch 1967). He introduced two upgrades to the Barlett periodogram providing the so-called “modified periodogram”. First, since the windowing procedure introduces substantial endpoint discontinuities that bias the spectral estimate, Welch proposed to smooth out these transitions by multiplying each window of the time series by a taper function (e.g. Hamming, Hann, ...) that gradually goes to zero at the corners. While this trick reduces the bias, the windowing procedure affords a higher contribution of the central part of the window than to data at the edges. To overcome this problem, thus, to mitigate the loss of information caused by the tapering, Welch suggested splitting up the signal into overlapping windows. We can thus sum up that the modified periodogram consists of the computation of periodogram for each overlapping tapered sub-window that are then averaged together to produce the final estimate of the power spectral density of the signal (Appendix B). A scheme of the periodogram improvements is shown in Figure 1 Illustration of different periodogram methods.

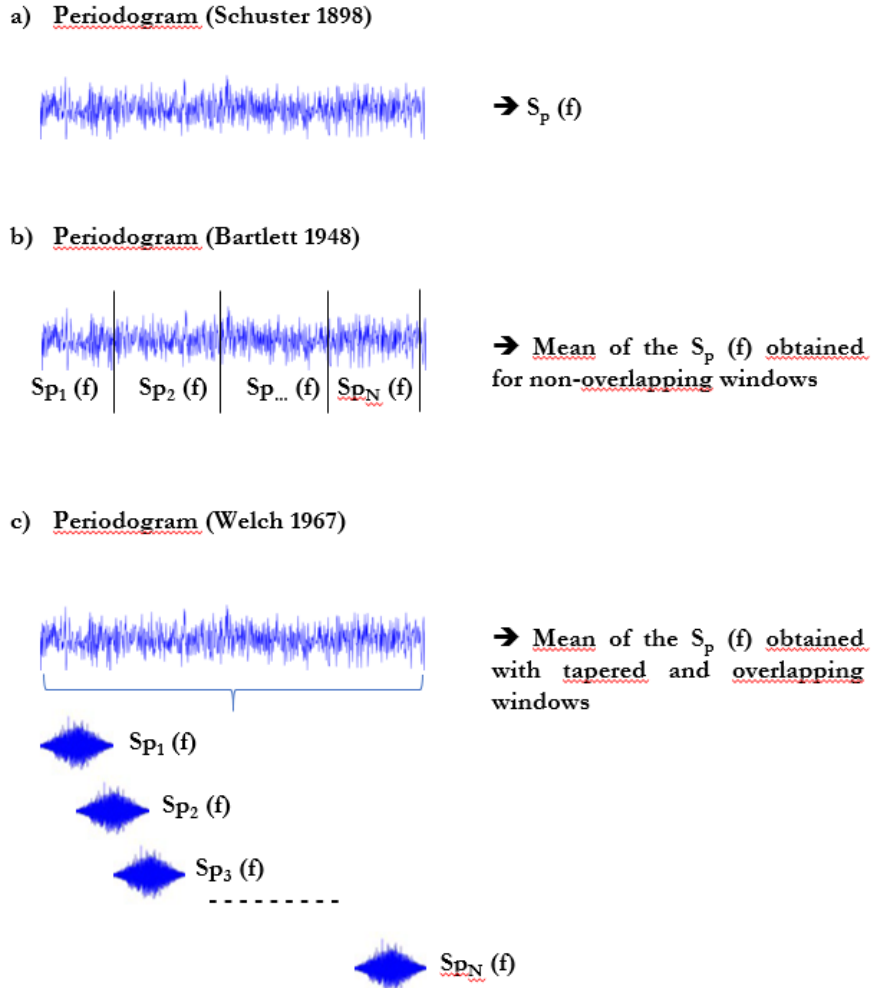


Figure 1 Illustration of different periodogram methods.

## 2.2. Multitaper spectral estimation

Currently, when dealing with long data series, the Welch periodogram is likely the most used technique for spectral estimation. However, in this work, we propose the use of a far less popular methodology that has been developed by Thomson in 1982: the multitaper method (Thomson 1982). The latter evolved from the need to reduce both local and broadband biases as well as the variance of the spectral estimate. The innovation of this approach is that it does not use a single-taper function to compute the spectrum, but rather it makes use of multiple taper functions that lead to a unique set of spectra that are averaged together. The tapers functions are called discrete prolate spheroidal sequences (DPSS), also known as Slepian sequences, and, in addition, to reduce the bias, they own the property of being orthogonal to each other. This feature makes it possible to extract independent spectral estimates from the same dataset. Since the obtained spectrums are independent of each other, they can be average together producing a spectral estimate with reduced variance. The power spectrum estimate of a time series by means of multitaper can be simply summarized as the average of several independent-taper spectra.

In practice, the steps for estimating the spectrum of a dataset by means of the multitaper method are (Figure 2):

- 1) Generation the Slepian tapers (DPSS)
- 2) For each DPSS estimate the corresponding spectrum
- 3) Computation of the average among the obtained spectrum to form the multitaper spectral estimate

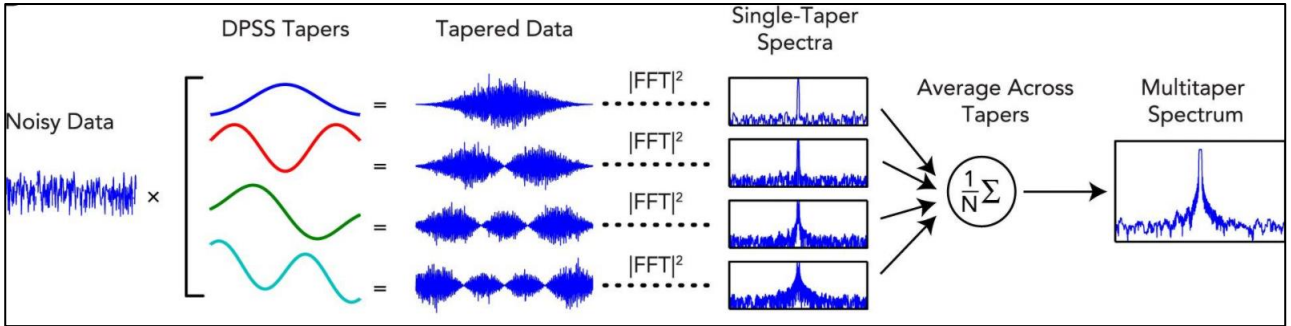


Figure 2 Framework of multitaper spectral estimation (Prerau *et al.* 2017).

The number of Slepian tapers and their own properties are defined by several parameters:

- $N$  represent the size of the data segment [s]
- $TW$  is the time-half-bandwidth product [-]
- $L$  is the number of tapers

For the correct selection of these parameters, it is important to know the time period where the data are thought to be stationary and the desired spectral resolution ( $\Delta f$ ). The former is represented by the  $N$  parameter, whereas the latter is the bandwidth [Hz] of the main lobe and it controls the distance of the minimum peak that can be resolved. Given these two parameters, the  $TW$  can be obtained as the product of the window duration ( $N$ ) with half the bandwidth of the main lobe ( $\frac{\Delta f}{2}$ ).

$$TW = \frac{N\Delta f}{2}$$

Where  $TW \geq 1$ .

Finally, the number of tapers used to have an efficient spectral estimate (Babadi & Brown 2014) is defined by:

$$L = [2TW] - 1$$

The choice of the number of tapers is based on the fact that the benefit of increasing  $L$  drops when the number of tapers reaches the so-called Shannon number, which is equal to  $2TW$  (Percival *et al.* 1993). Thus, using the above-mentioned equation to compute  $L$ , it is possible to produce an efficient spectral estimate that uses the minimum required number of significant tapers. It can be demonstrated that the multitaper approach reduces the variance by a factor  $L$  compared with the single-taper estimate.

In conclusion, given a number  $L$  of Slepian tapers  $\{w^1, w^2, \dots, w^L\}$ , the multitaper spectral estimate at frequency  $f$  can be defined as:

$$\widehat{S_{mt}}(f) = \frac{1}{L} \sum_{l=1}^L \left| \sum_{k=0}^{N-1} w_k^l x_k e^{2\pi k f \Delta t} \right|^2$$

### 2.3. Spectrogram

While discussing the SDE, we must not forget that this analysis also includes the study of the spectrum time-variation by means of a spectrogram that plots the signal power as a function of time and frequency. This methodology is therefore well suited to track the temporal evolution of unstable compartments modal frequencies. Indeed, if the intention is to characterize how the dynamic, hence the stability, of unstable rock blocks change in time, the estimate of a single power spectrum for the entire dataset is useless. To this purpose, the construction of the spectrogram is therefore necessary. The spectrogram is simply made of power spectrum estimates computed for the consecutive moving window of the data. In this perspective, both the spectral density estimation techniques mentioned in the previous paragraph can be used for the computation of the power spectrum of each sub-window and thus we do not enter in detail this methodology because it would be a repetition of the previous concepts. We

just want to draw attention to the time-resolution, thus the size of the data window, that must be chosen such that the selected dataset is approximately stationary for the entire window.

### 3. HVSR Analysis

In the last years, another technique that has been largely implemented for the frequency domain analysis of the ambient seismic noise is the Horizontal-to-Vertical Spectral Ratio (HVSR). Nakamura's method (HVSR) has gained widespread popularity in many applications (Nakamura 1989). It was initially adopted in seismic microzonation investigations to estimate the seismic site effects. Thanks to its low cost both in terms of survey and analysis, the HVSR has been then used for many other purposes. Among these, in this work, we focus on the application of the Horizontal-to-Vertical Spectral Ratio technique for monitoring landslides. Indeed, a very common approach to monitoring rock cliffs is to deploy three-component seismic sensors and compute the HVSR of the collected ambient noise to estimate the vibrational modes of the unstable compartments (Bottelin *et al.* 2017, Valentin *et al.* 2017). The method simply consists of estimating the ratio between the Fourier amplitude spectra of the horizontal (H) and vertical (V) components of the ambient noise vibrations recorded at one single station. In more details, the computation of the H/V ratio of the ambient seismic noise follows different steps. First, the three-component recordings are bandpass filtered to remove both low-frequency trends and high-frequency noise. They are then divided into sub-windows and those nonstationary in time are rejected to avoid transient noise. The retained sub-signals are generally overlapped and tapered to improve the HVSR estimation. Then the amplitude spectra are computed for each window, thus for each component, and a frequency-dependent smoothing is applied (e.g. Konno & Ohmachi ). The horizontal components (North and East) are merged together and the HVSR is computed. Finally, the HVSRs obtained for each window are averaged using a quadratic mean. The latter is chosen since it is most sensitive to low values and thus it produces a more robust HVSR estimate. The presence of well-defined peaks in the HVSR curve indicates the presence of preferential vibration modes of the monitored structure. The workflow for the HVSR computation is shown in Figure 3.

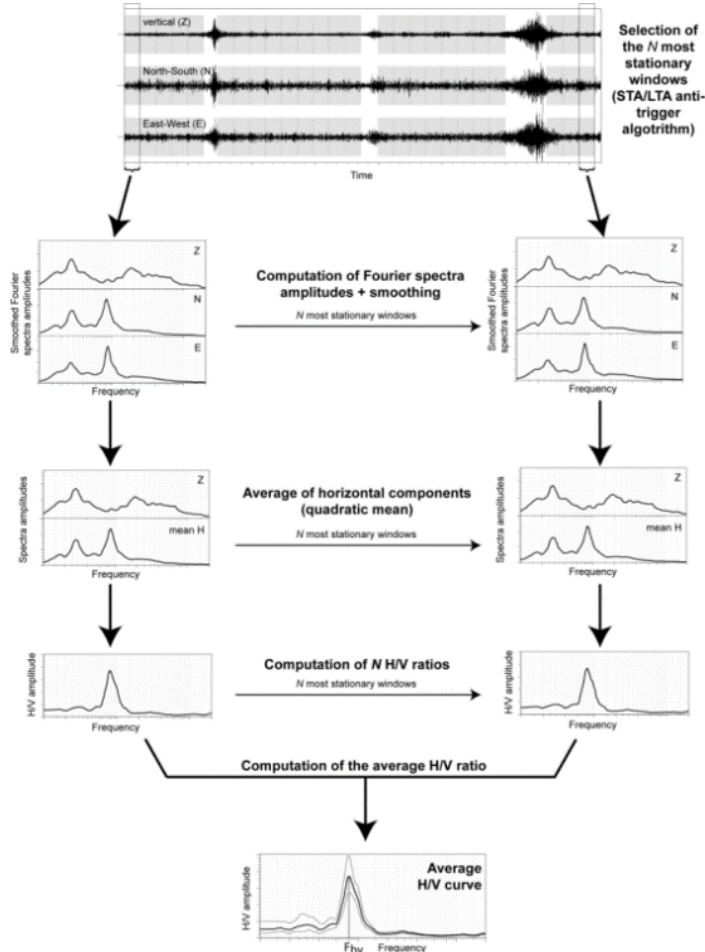


Figure 3 HVSR workflow ('Tutorial H/V')

#### 4. Polarization analysis

To increase the amount of information regarding the monitoring of slopes stability over time, it is important to extract the polarization features of the recorded ambient seismic noise (Arosio *et al.* 2019). Indeed, the ground particles displacement, affected by elastic waves, shows a preferential direction of polarization which depends on the physical properties of the investigated medium. To this concern, in this chapter, we present different approaches that have been used to estimate the polarization characteristics of the ambient vibrations collected on both unstable rock blocks as well as on unstable slopes. In this paragraph, we do not use the beamforming approach because is viable where the ambient noise is recorded using an array of seismometers. For our purpose, we rather prefer the single-station techniques because they are more suitable to study the ambient noise wavefield in those areas where the objective is to monitor the response of specific zones of the site. This is particularly true for landslide investigations where the dynamic response may differ between close areas, e.g., between stable and unstable compartments.

The 3C single-station polarization analysis provides the amplitude and phase relationships of the ambient seismic recordings along with the three orthogonal components (N, E and Z). By means of this analysis is possible to observe linear, circular, and elliptical polarization of the wavefield. However, when random particle displacement occurs, it is difficult to infer a clear polarization of the collected dataset. Among the single-station polarization techniques, we present in this work the hodogram, the Horizontal-to-Vertical Spectral Ratio as a function of azimuth and the principal component analysis performed both in time and frequency domain.

##### 4.1. Hodogram

The easiest way to evaluate the polarization of a three-component seismic ambient noise trace is to visually examine the triaxial hodograms. The latter shows the particle motion of the ambient vibration as a function of time in the three orthogonal planes (X-Y, X-Z, and Y-Z). In other words, the hodograms show the phase relationships among the 3-components (Figure 4). This simple method is useful to obtain an illustration of the polarization direction as well as the degree of rectilinearity of the particle displacement. However, the particle motion of ambient seismic noise data is generally a superposition of different type of waves which results in 3D complex hodograms. To avoid this problem one solution is to filter the data before hodograms are computed. However, without a priori knowledge of the seismic sources as well as of the site characteristics, it is generally difficult to know which bandwidth must be used to perform the data filtering.

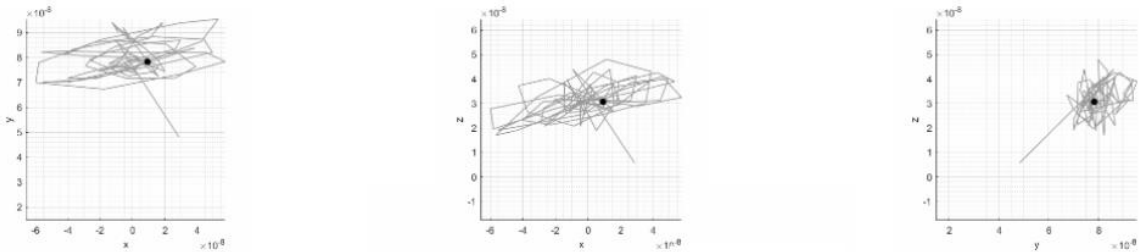


Figure 4 Examples of hodograms computed for different component pairs.

##### 4.2. HVSR-Rotate

The polarization of seismic wavefield measured simply by tracing the projection of the motion as a function of time is useful to illustrate the particle motion of simple arrivals. Nevertheless, this practice is only qualitative and resulted to be pointless when used to process complicated signals such as the ambient seismic noise. For this reason, the researchers moved their attention to the Horizontal-to-Vertical Spectral Ratio as a function of azimuth (HVSRA or HVSR-Rotate). The latter technique is often used for studying unstable rock compartments due to its simple and fast computation. The HVSRA is obtained by projecting the horizontal components along with different azimuthal directions before taking the ratio with the vertical component (Bottelin *et al.* 2013). The standard processing flow implies that first each of the 3-component recordings is divided into sub-windows that will be overlapped and tapered for spectral estimation purposes. Then, after a rejection of the non-stationary time windows, the amplitude spectra are computed for each window applying a frequency-dependent smoothing. Finally, the HVSRA are computed and averaged generally using a quadratic mean to produce a more robust

HVSRA estimate. Obviously, the outcome of this methodology is limited to the azimuthal plane and thus it does not provide any information of the oscillations occurring along the vertical direction.

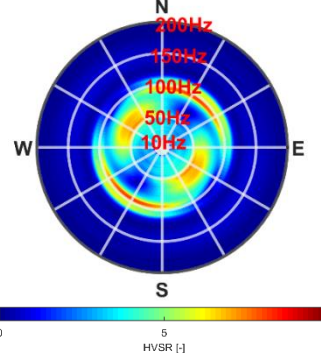


Figure 5 Example of an HVSRA result

#### 4.3. Principal Component Analysis (PCA)

The most complete approach for studying the polarization of seismic wavefield is the estimation of the particle motion throughout the principal component analysis. This method is generally used to determine the wave types and source location of seismic signals. However, in the context of the manuscript, the methodology is applied to investigate the dynamic response of the unstable compartments.

The technique is based on the work of Samson (1983) and a flow chart is shown in Figure 6. Essentially, the eigendecomposition of the covariance matrix, or of the spectral density matrix, is applied to retrieve various polarization features as a function of time or frequency, respectively (Samson 1983, Vidale 1986, Park *et al.* 1987, Koper & Hawley 2010).

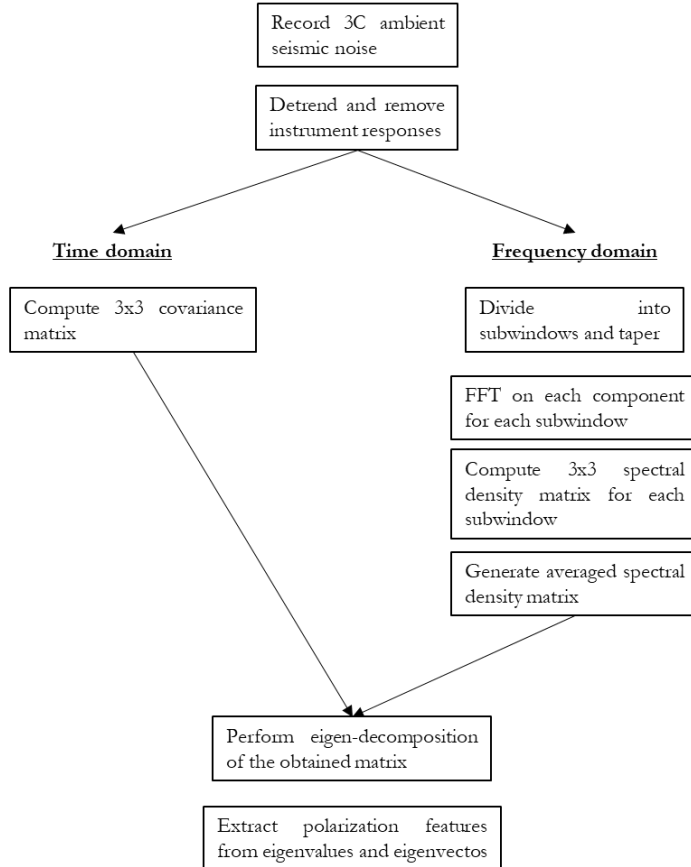


Figure 6 Flow chart for the principal component analysis computation

Considering the time domain, the processing begins by computing the covariance matrix. For a three-component seismic ambient noise dataset  $u(t) = [x(t), y(t), z(t)]$ , the covariance matrix is a positive semidefinite  $3 \times 3$  matrix defined as follow:

$$C(t) = \frac{1}{N} \sum_{t=1}^N u(t)u^T(t) = \frac{1}{N} \sum_{t=1}^N \begin{bmatrix} x^2 & xy & xz \\ yx & y^2 & yz \\ zx & zy & z^2 \end{bmatrix}$$

Where  $T$  is the transpose operator and  $N$  is the number of samples of each signal.

The elements along the diagonal are the variances of each component, whereas the off-diagonal elements represent a measure of the correlation between the two respective components. In the case that the analysis is performed in the frequency domain, the  $T$  operator is replaced by the Hermitian one  $H$  and the covariance matrix is called spectral density matrix (SPM). The latter contains the power spectra of each component along the diagonal and the cross-spectral among the three components on the off-diagonal elements:

$$S(f) = \begin{bmatrix} S_{XX}(f) & S_{XY}(f) & S_{XZ}(f) \\ S_{YX}(f) & S_{YY}(f) & S_{YZ}(f) \\ S_{ZX}(f) & S_{ZY}(f) & S_{ZZ}(f) \end{bmatrix}$$

Moreover, if the study is performed in the frequency domain, to increase the reliability of the estimate it is necessary to split the investigated dataset into sub-windows and calculated the spectral density matrix as the average of all the SDMs of the sub-traces. This step is not required when performing the analysis in the time domain. In fact, whether the covariance matrix is obtained by splitting the signals into sub-windows or by direct use of the entire dataset would not change the result of the estimate.

To obtain the polarization characteristics of the ambient seismic noise, the eigendecomposition is then performed on the covariance matrix (spectral density matrix) using the principal component analysis (PCA). In this work, we investigate the eigenstructure of  $\mathbf{C}$  performing the singular value decomposition (SVD):  $M = UDV^T$  where:

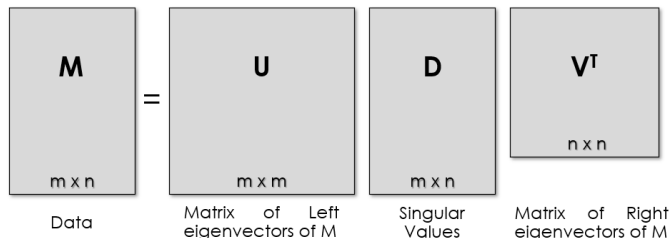


Figure 7 Matrix notation of the singular value decomposition method.

Note, if the polarization of the signal is linear,  $\mathbf{C}$  has just one non-zero eigenvalue  $\lambda_1$ , with the others  $\lambda_2$  and  $\lambda_3$  equal to 0. The first eigenvector defines the direction of the dominant particle motion. Whereas, if there are two non-zero eigenvalues, the polarization is elliptic (e.g., as for Rayleigh waves). For real data, zero eigenvalues will rarely occur. Instead, linear polarization is usually indicated by  $\lambda_1$  being considerably larger than  $\lambda_2$  and  $\lambda_3$ .

Once the eigendecomposition is performed, the obtained principal eigenvalues and eigenvectors are used to infer the polarization features of the collected ambient noise recordings:  $\beta^2$ ,  $\Theta_H$ ,  $\Theta_V$ ,  $\phi_{HH}$ ,  $\phi_{VH}$ .

$\beta^2$  represents the degree of polarization for the three-component dataset and it is computed using the equation defined by Samson (1983):

$$\beta^2 = \frac{3\text{tr}(\mathbf{D}^2) - [\text{tr}(\mathbf{D})]^2}{2[\text{tr}(\mathbf{D})]^2}$$

where  $\text{tr}$  is the trace. The degree of polarization can range from 0 to 1. When  $\beta^2$  is equal to 0, the wavefield is unpolarized. On the contrary, when it is equal to 1 the seismic signals have a well-defined polarization. Note, that high values of  $\beta^2$  do not necessarily imply a linear polarization. Indeed, both circular and elliptical particle motion can provide high values as well.

The eigenvalues describe the contribution of the principal axes (eigenvectors) of the estimated particle motion (Samson 1983, Park *et al.* 1987), thus they represent the power along the principal axes. Park et al. (1987) proposed to extract frequency-dependent angular quantities by projecting along with the three components the complex right eigenvector associated with the dominant singular value. Hence, to infer the polarization features of the wavefield, the computation of various ratios of eigenvalues  $\lambda$  or eigenvectors ( $\mathbf{u} = [\psi_E, \psi_N, \psi_Z]$ ) of the covariance matrix (spectral density matrix) is carried out. In more detail, the direction of polarization  $\Theta_H$  is estimated from the horizontal components of the dominant polarization direction by means of the eigenvector:

$$\Theta_H = \arctan(\psi_E / \psi_N)$$

Thus,  $\Theta_H$  is the azimuth of the main polarization axis measured counterclockwise from East. The dip of the direction of polarization measured from the horizontal is computed as follow:

$$\Theta_V = \arctan\left(\frac{\psi_Z}{\sqrt{\psi_N^2 + \psi_E^2}}\right)$$

Graphic visualization of both  $\Theta_H$  and  $\Theta_V$  is represented in **Figure 8**:

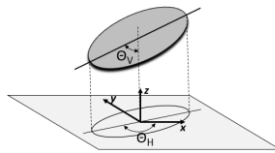


Figure 8 Representation of  $\Theta_H$  and  $\Theta_V$

Throughout this polarization analysis, it is also possible to estimate the  $\phi_{HH}$  and  $\phi_{VH}$  parameters that quantify the phase relationships between the two orthogonal horizontal components and between the vertical and the principal horizontal components, respectively.

The principal component analysis in the time or frequency domain follows the same logic. The main difference in computing the PCA using the covariance matrix or the spectral density matrix is that in the latter case the resulting eigenvectors are complex and thus the above equations must be applied to the real part of the eigenvectors. Of course, polarization analysis performed on the spectral density matrix also provide a frequency characterization of the wavefield that is precious information when the objective is to characterise the vibrational modes of unstable rock blocks.

## 5. Passive Seismic interferometry

All applications of ambient seismic noise, whether to study the source of the noise or the medium properties, share the same challenge of searching coherent signals hidden in the randomness of the ambient vibration. The technique of extracting the deterministic signals from noise measurements is known by different names that include Green's function retrieval, passive seismic interferometry, passive imaging through ambient noise correlation, and others (Larose *et al.* 2015). Whatever the chosen name, this technique is the foundation for many applications ranging from seismic tomography to time-lapse monitoring. The general term *interferometry* refers to the technique used to study the interference phenomena between pairs of signals to obtain information from their differences (Curtis *et al.* 2006). Noise interferometry simply refers to the case in which the ambient seismic noise is used as input signals. Although this technique requires only two seismic stations, it is only from the past decade that interferometry based on ambient noise cross-correlations has become a popular and widely used tool. The fundamental principle of ambient noise interferometry was conjectured by Claerbout in 1996. He stated that by cross-correlating noise traces recorded at two locations on the surface, it is possible to reconstruct the wavefield that would be recorded at one station if there was a source at the other (Rickett & Claerbout 1996). Thus, the passive seismic interferometry results are based on Green's function retrieval which is assumed to be approximated by the cross-correlation of ambient vibration collected at two stations. By treating the correlation-based Green's function approximations as signals generated by conventional active sources, traditional geophysical methods can be applied to estimate the subsurface properties of the medium between the two stations.

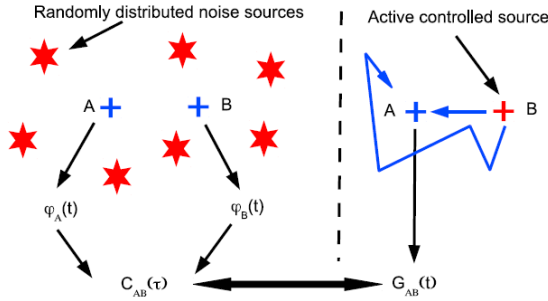


Figure 9 Equivalence between passive and active surveys (Larose et al. 2015).

In general, it is assumed that the cross-correlation converges to the Green's function when the ambient noise wavefield is equipartitioned and the sources are uncorrelated in time and randomly distributed all around the receivers. Even though these conditions are hardly met in nature, they are indirectly satisfied with multiple scattering. Indeed, the latter compensates for the lack of equipartition in modes and propagation directions (Lobkis & Weaver 2001, Larose *et al.* 2005).

Hereafter, a general workflow to obtain the daily relative velocity changes ( $dV/V$ ) using passive interferometry is provided. In its current state, the procedure can be divided into three main stages: (1) single-station data pre-processing, (2) cross-correlation computation and (3) estimation of the relative velocity changes ( $dV/V$ ). These steps are schematically represented in Figure 10.

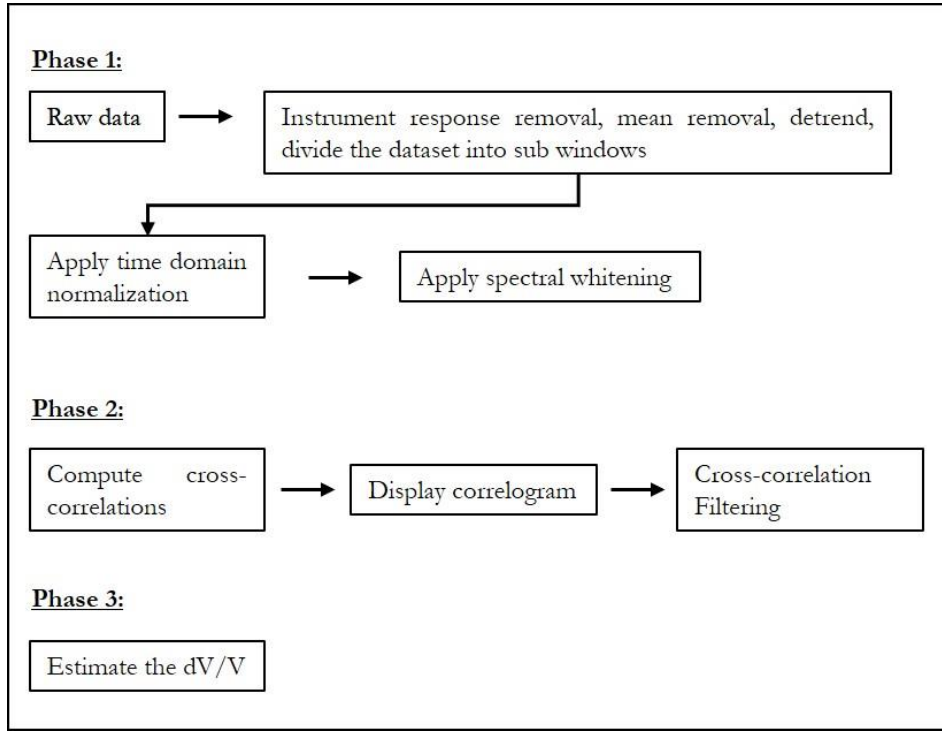


Figure 10 Workflow for passive interferometry computation

### 5.1. Single-station data pre-processing

The first phase consists of individually prepare the data collected at every single station. The purpose of this stage is to avoid that energetic signals (e.g., earthquakes) or instrumental irregularities may obscure the ambient seismic noise. Phase 1 begins with simple data processing where it is necessary to remove the instrument response, the mean and the trend and to perform a bandpass filtering of the recordings. The latter step can be either performed within this stage or in stage 2. However, it is suggested to filter the cross-correlation and not the signals itself because is less time-consuming. Besides this routine signal processing, which is basic steps generally performed in

almost all seismic applications, the most important pre-processing of seismic noise data includes the time-domain or temporal equalization and the frequency-domain equalization (whitening).

The time-domain normalization is a procedure used to reduce the effect of earthquakes, instrumental noise and non-stationary noise sources that can be activated near the stations (Bensen *et al.* 2007). Within this paragraph, we present five different methods to remove contaminants from ambient seismic noise data. The first one is called running absolute mean time-domain weighting and it is defined as follows:

$$W(t_n) = \frac{1}{N+1} \sum_{j=n-N/2}^{n+N/2} |u(t_j)|,$$

where time is presented on a discrete grid. Thus, at time grid point  $t_j$ , the weight is defined as the absolute mean of the seismic trace in a time window of length  $N$  spanning the time point. For this method,  $N$  should be chosen to be at least the length of the maximum period, ensuring that the longer periods are not filtered out. One drawback of the method is that it does not remove data spikes but spreads them out in time. When  $N$  is set up equal to 0, we move to the second methodology called one-bit normalization, in which signal amplitudes become  $\pm 1$  (the positive amplitudes of the raw signal are replaced with 1 and all negative amplitudes with a -1). Contrary to the first method, in this case, the data spikes are removed from the dataset. This method showed to increase the signal-to-noise ratio (SNR) in acoustic experiments performed in the laboratory (Larose *et al.* 2004) and it has been used in many studies of coda waves and ambient noise (Campillo & Paul 2003, Shapiro & Campillo 2004). The third method involves the application of a clipping threshold equal to the RMS amplitude of the signal for the selected time window (Sabra 2005). The fourth method of the list involved automatic event detection and removal. In this perspective, the waveform is set to zero if the amplitude of the waveform itself is above a critical arbitrary threshold. Finally, Bensen et al. proposed the so-called “water-level” normalization method in which amplitudes higher than a specified multiple of the daily RMS amplitude are down-weighted (Bensen *et al.* 2007). The procedure is repeated until the entire waveform is below the “water level”. Within this work, we have been using the running-absolute-mean normalization method since it has greater flexibility and adaptability to the data compared to the others (Bensen *et al.* 2007).

The ambient seismic noise is not spectrally white, thus its spectrum is not flat. It is, therefore, necessary to also apply a spectral normalization (whitening) to flatten the frequency content. The reasons that brought researchers to perform the frequency-domain whitening are mainly two. First, it allows broadening the bandwidth of the estimated Green's functions. Secondly, it is used to reduces the impact of band-limited spatially localized sources such as the primary or secondary microseisms and the Earth ‘hum’ (Shapiro *et al.* 2006). As well as for time-domain normalization, it is applied to seismic records before the cross-correlation computation. The most used methodologies for performing the spectral normalization are two. The first one consists of dividing the observed spectrum by its modulus in some finite bands ( $N(\omega) = |u(\omega)|$  in that specific band). This results in a flat spectrum. The alternative is to perform normalization using a smoothed version of the amplitude spectrum itself, that is  $N(\omega) = S(\omega) * |u(\omega)|$ . Where  $S(\omega)$  is the smoothing filter and  $u(\omega)$  is the spectrum.

After the data have been pre-processed it is necessary to cut them into sub-signals of duration  $T$ . The choice of the data length depends on the distance between the two stations, thus on the seismic wavefield velocity, and on the variation rate of the phenomenon that we want to study. One advantage in using short time windows for computing cross-correlations is that if a signal irregularity is identified it will affect only a few cross-correlations without the need to sacrifice a longer signal to eliminate such effect. However, one must keep in mind that these effects are generally attenuated when computing the time domain and the spectral normalization.

Once the entire signals collected at two locations have been pre-processed and subdivided into sub-signals, we finally move to the second phase.

## 5.2. Computation of the cross-correlations

Cross-correlation is a mathematical operation that measures the similarities of two signals by identifying the time lag ( $\tau$ ) at which they are most similar. In other words,  $\tau$  represents how much a signal is shifted relative to the other. Let  $u_i(t)$  and  $u_j(t)$  be the vertical ground motion recorded on a finite time interval  $t \in [0, T]$  at station  $i$  and  $j$ , respectively. The cross-correlation between these two recordings,  $C_{ij}(\tau)$ , is a function of time lag and is commonly defined as:

$$C_{ij}(\tau) = \int u_i(t) * u_j(t-\tau) dt$$

$C_{ij}(\tau)$  is maximum when the sum of the product  $u_i(t)*u_j(t-\tau)$  is at maximum. Thus, the two signals will be most similar when  $u_j$  is shifted by that amount relative to  $u_i$ . An auto-correlation, a cross-correlation of a signal with itself, has its own maximum at zero lag. The role of cross-correlation in seismic noise interferometry is to highlight the travel times of seismic ambient waves. A wavefield that has travelled between two stations will generate a similar signal at each sensor but shifted in time. The cross-correlation function (CCF) of the two records will therefore exhibit a peak at a specific time lag corresponding to the travel time that the wavefield takes to go from station  $i$  to station  $j$  (Figure 11).

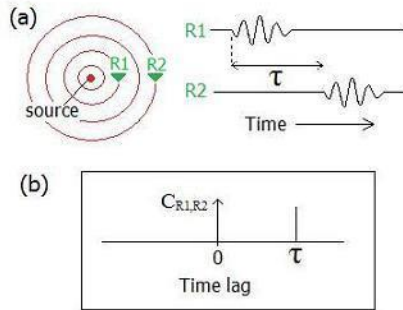


Figure 11 (a) A source of seismic energy (left) is recorded at receivers 1 and 2, causing identical signals separated by a time  $\tau$  (right), corresponding to the travel time of the wavefield between the receivers. (b) the cross-correlation function of the two records, on which the travel time is highlighted as a peak (IASPEI/LAVCEI Joint Commission on Volcano Seismology - Tutorial 6 - Seismic noise interferometry').

We have seen that the ambient seismic noise is supposed to be randomly distributed in space and time and thus it arrives at the seismometers from all directions. The noise records will contain waves that have travelled in both directions along the interstation path. Therefore, the approximated Green's function that emerges from noise cross-correlation functions, will contain energy for both positive ("causal") and negative ("acausal") time lags. The causal part represents energy travelling from station  $i$  to station  $j$ ; the acausal part is the wavefield that arrive at station  $i$  from station  $j$  (Figure 12).

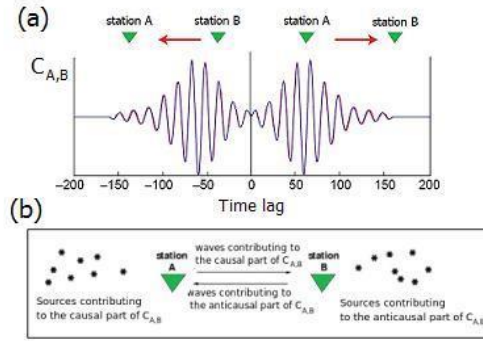


Figure 12 Causal and anticausal parts of an CCF. (a) Idealised CCF for the cross-correlation order station A to station B. The arrows indicate the energy path which is represented by the positive and negative parts of the cross-correlation function. (b) Representation of the noise sources which (theoretically) contribute to the causal and anticausal part of the station A - station B CCF (IASPEI/LAVCEI Joint Commission on Volcano Seismology - Tutorial 6 - Seismic noise interferometry').

Based on the assumptions for the converge of cross-correlations toward Green's function, the two sides of the CCF should represent the same information but reverse in time. In reality, the cross-correlation functions will be perfectly symmetrical at zero-time lag only if ambient noise wavefield arrives from both sides of the

interstation path with an energy content as similar as possible. This condition is usually difficult to obtain due to the anisotropy of the ambient seismic noise (Figure 13). Nevertheless, Hadzioannou et al. showed that even though this condition is not satisfied, the convergence of cross-correlations to the GFs is still guaranteed if the noise sources are stable over time (Hadzioannou et al. 2011).

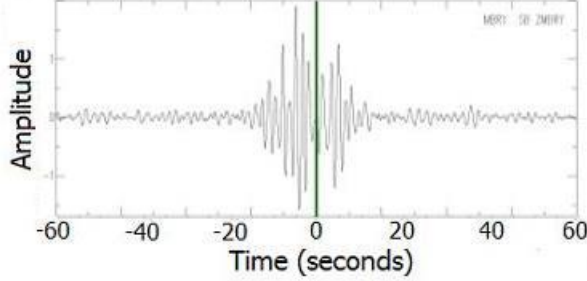


Figure 13 Daily noise cross-correlation example. Note the asymmetry due to source anisotropy. In the upper part, it is possible to see more energy propagate in one direction with respect to the other (left side).

After the cross-correlations are computed for each sub-signal, they are subjected to a frequency band filtering. The latter is performed based on the assumption that the vertical component of the ambient seismic noise is mainly composed of surface waves (Rayleigh waves) and thus, by considering particular frequency bandwidths it is possible to investigate different depths and thus locate dV/V changes associated with the different phenomenon that occur in the subsurface (e.g., water table variations, sliding material, ...). Phase 2 ends by putting in sequence the filtered cross-correlations into the so-called correlogram where the x-axis represents the time lag and y-axis the amplitude of the CCFs (Figure 14).

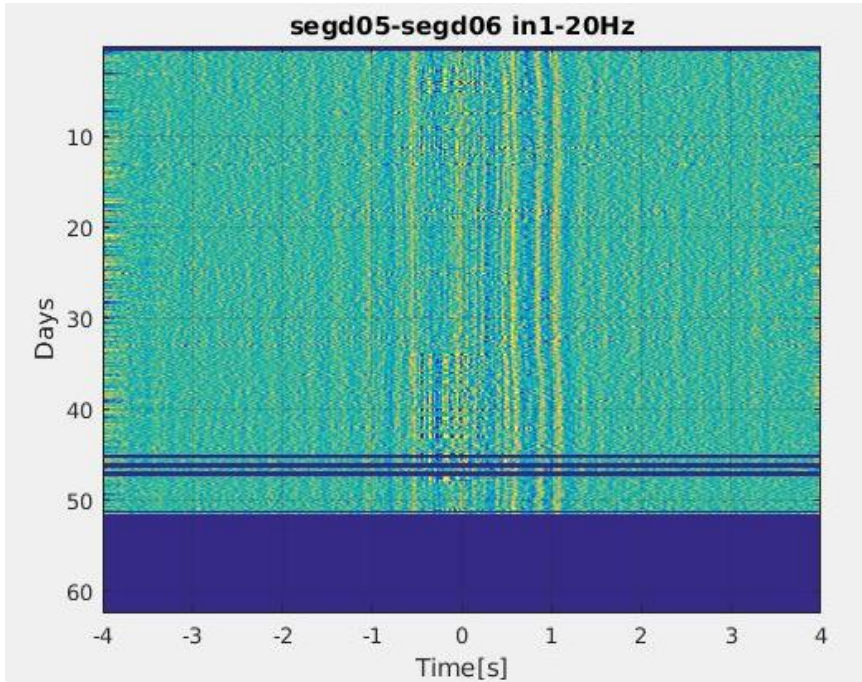


Figure 14 Broadband correlogram resulting from the cross-correlation of the vertical components of two different stations. The light blue horizontal bands are missing data. It is possible to see the stability of arrivals confirming the temporal stability of the noise sources.

### 5.3. Estimation of the relative velocity changes (dV/V)

Once the recorded data have been cross-correlated and displayed in the correlogram, the seismic velocity variation ( $dV/V$ ) can be estimated. In this perspective, it is first necessary to define a reference cross-correlation function ( $f_{ref}(t)$ ) that is obtained by averaging all the CCFs. The seismic velocity changes can be then estimated by comparing the time delay between the  $f_{ref}(t)$  and  $f_{cur}(t)$  that is the considered cross-correlation function relative to a specific

time. If the time shift is produced by a spatially homogeneous relative velocity change  $dV/V$ , the relative time lag is independent of the lapse time at which it is measured (Poupinet *et al.* 1984, Snieder *et al.* 2002, Sens-Schönfelder & Wegler 2006), thus:

$$\frac{dv}{v} = \frac{dt}{t}$$

In the context of seismic velocity changes estimation four strategies are presented in the literature: the Moving-window cross-correlation technique, the Moving-window cross-spectrum technique, the Stretching technique (ST) and the Moving-window stretching technique (MWST) (Liu *et al.* 2010). Among them, it has been decided to use the Stretching technique for the purpose of this work. This choice has been made based on the advantages of this methodology compared to the other ones. Indeed, Sens-Schönfelder *et al.* stated that using his method there is no need to have small  $dt/t$  and that the  $dt$  itself does not have to respect any relation with the dominant wavelength of the cross-correlations. In this sense, it is possible to use different time windows length without losing information in the  $dV/V$  estimation (Sens-Schönfelder & Wegler 2006). Moreover, the Sens-Schönfelder *et al.* approach gives a direct estimation of the relative velocity changes (Larose *et al.* 2015).

Basically, with the Stretching technique the relative delay time, and thus the seismic velocity changes, are determined as the factor by which the time axis of the  $f_{cur}$  trace must be stretched or compressed to obtain the best correlation with the reference one ( $f_{ref}$ ).

First of all, a specific time window of the obtained cross-correlation functions is selected with the help of the correlogram. In fact, the stretching technique will not be applied for the entire Green's function time lag, but only for a specific time interval. The reason behind this procedure is that the GFs are formed of both ballistic (P, S and surface waves) and coda waves (wavefield composed of reflected and diffracted events) which arrive at different time-lags within the correlogram (Garambois *et al.* 2019). Therefore, considering different time windows of the correlogram it is possible to select part of the GFs dominated by specific types of waves. Thus, for different time-lag of the GFs, it is possible to obtain diverse  $dV/V$  curves since seismic waves have different sensitivities to the medium properties. Of course, the selection of time window in the correlogram depends on the seismic velocity wavefield of the site and on the inter distance between the stations' pair.

Once the time-lag interval is identified, the “limited”  $f_{cur}$  are ready to undergo the stretching technique. In this perspective, each of the  $f_{cur}$  time axes is stretched/compressed as follow:

$$f_{cur(\varepsilon)}(t) = f_{cur}[t(1 + \varepsilon)]$$

Where  $\varepsilon = -\frac{dt}{t}$  and it is the stretching coefficient.

Different values of  $\varepsilon$  are tested and the one that provides the maximum cross-correlation coefficient (CC) between the  $f_{ref}$  and the  $f_{cur}$  is considered.

$$CC(\varepsilon) = \frac{\int f_{cur(\varepsilon)}(t)f_{ref}(t)dt}{\sqrt{\int f_{cur(\varepsilon)}^2(t)dt \int f_{ref}^2(t)dt}}$$

The tested stretching factors  $\varepsilon$  could be either positive (i.e., the seismic phases arrive later than their reference time) or negative (i.e., the seismic phases arrive before their reference time) (Voisin *et al.* 2016). Finally, the relative seismic velocity changes curve ( $dV/V$ ) is defined by all the stretching coefficient that has been obtained by comparing the  $f_{ref}$  with all the  $f_{cur}$ .

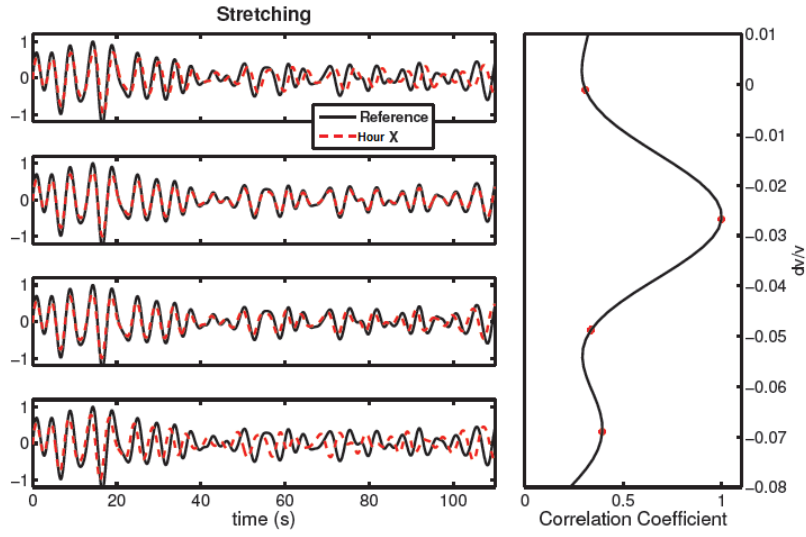


Figure 15. Stretching method: physical understanding. Left: The signal is stretched for different  $e$  values. Right: Coefficient correlation between the signal (red) and the reference (black) is calculated for every test daily signals.

## 6. Conclusion

This chapter illustrated the methodologies that have been used within this work for the analysis of the ambient seismic noise. For each presented method, an extensive description is provided to assist the reader in reproducing and extending the application of these methodologies for other case studies related to geohazard monitoring or to completely different applications. Since the setup of the methodologies' parameters depends on the specific analysed case study, they were not treated within this chapter. They will be provided when discussing the monitored sites in the next sections of the manuscript. Therefore, the core of the following work will be the investigation of the potential use of these methodologies for the monitoring of site with high hydrogeological risk throughout the ambient seismic noise.

## 7. Bibliography

- Arosio, D., Taruselli, M., Longoni, L., Papini, M. & Zanzi, L. (2019) Seismic Noise Polarization Analysis for Unstable Rock Monitoring, Vol. 2019, pp. 1–5, Presented at the 25th European Meeting of Environmental and Engineering Geophysics, European Association of Geoscientists & Engineers. doi:10.3997/2214-4609.201902451
- Babadi, B. & Brown, E.N. (2014) A review of multitaper spectral analysis. *IEEE Trans Biomed Eng*, 61, 1555–1564. doi:10.1109/TBME.2014.2311996
- Bartlett, M.S. (1948) Smoothing Periodograms from Time-Series with Continuous Spectra. *Nature*, 161, 686–687, Nature Publishing Group. doi:10.1038/161686a0
- Bensen, G.D., Ritzwoller, M.H., Barmin, M.P., Levshin, A.L., Lin, F., Moschetti, M.P., Shapiro, N.M., et al. (2007) Processing seismic ambient noise data to obtain reliable broad-band surface wave dispersion measurements. *Geophysical Journal International*, 169, 1239–1260. doi:10.1111/j.1365-246X.2007.03374.x
- Bottelin, P., Baillet, L., Larose, E., Jongmans, D., Hantz, D., Brenguier, O., Cadet, H., et al. (2017) Monitoring rock reinforcement works with ambient vibrations: La Bourne case study (Vercors, France). *Engineering Geology*, 226, 136–145. doi:10.1016/j.enggeo.2017.06.002
- Bottelin, P., Jongmans, D., Baillet, L., Lebourg, T., Hantz, D., Levy, C., Le Roux, O., et al. (2013) Spectral Analysis of Prone-to-fall Rock Compartments using Ambient Vibrations. *Journal of Environmental & Engineering Geophysics*, 18, 205–217. doi:10.2113/JEEG18.4.205
- Campillo, M. & Paul, A. (2003) Long-Range Correlations in the Diffuse Seismic Coda. *Science* (New York, N.Y.), 299, 547–9. doi:10.1126/science.1078551
- Curtis, A., Gerstoft, P., Sato, H., Snieder, R. & Wapenaar, K. (2006) Seismic interferometry—turning noise into signal. *The Leading Edge*, 25, 1082–1092. doi:10.1190/1.2349814

- Garambois, S., Voisin, C., Romero Guzman, M.A., Brito, D., Guillier, B. & Réfloch, A. (2019) Analysis of ballistic waves in seismic noise monitoring of water table variations in a water field site: added value from numerical modelling to data understanding. *Geophysical Journal International*, 219, 1636–1647. doi:10.1093/gji/ggz391
- Hadzioannou, C., Larose, E., Baig, A., Roux, P. & Campillo, M. (2011) Improving temporal resolution in ambient noise monitoring of seismic wave speed. *Journal of Geophysical Research: Solid Earth*, 116. Retrieved from <http://onlinelibrary.wiley.com/doi/10.1029/2011JB008200/full>
- IASPEI/IAVCEI Joint Commission on Volcano Seismology - Tutorial 6 - Seismic noise interferometry. (n.d.) . Retrieved July 5, 2017, from [http://volc\\_seis\\_commission.leeds.ac.uk/index3d3a.html?option=com\\_content&task=view&id=75&Itemid=44](http://volc_seis_commission.leeds.ac.uk/index3d3a.html?option=com_content&task=view&id=75&Itemid=44).
- Konno, K. & Ohmachi, T. (n.d.) Ground-Motion Characteristics Estimated from Spectral Ratio between Horizontal and Vertical Components of Microtremor, 14.
- Koper, K.D. & Hawley, V.L. (2010) Frequency dependent polarization analysis of ambient seismic noise recorded at a broadband seismometer in the central United States. *Earthq Sci*, 23, 439–447. doi:10.1007/s11589-010-0743-5
- Larose, E., Carrière, S., Voisin, C., Bottelin, P., Baillet, L., Guéguen, P., Walter, F., et al. (2015) Environmental seismology: What can we learn on earth surface processes with ambient noise? *Journal of Applied Geophysics*, 116, 62–74. doi:10.1016/j.jappgeo.2015.02.001
- Larose, E., Derode, A., Campillo, M. & Fink, M. (2004) Imaging from one-bit correlations of wideband diffuse wave fields. *Journal of Applied Physics*, 95, 8393–8399. doi:10.1063/1.1739529
- Larose, E., Derode, A., Clorennec, D., Margerin, L. & Campillo, M. (2005) Passive retrieval of Rayleigh waves in disordered elastic media. *Phys Rev E Stat Nonlin Soft Matter Phys*, 72, 046607. doi:10.1103/PhysRevE.72.046607
- Liu, Z., Huang, J. & Li, J. (2010) Comparison of four techniques for estimating temporal change of seismic velocity with passive image interferometry. *Earthq Sci*, 23, 511–518. doi:10.1007/s11589-010-0749-z
- Lobkis, O.I. & Weaver, R.L. (2001) On the emergence of the Green's function in the correlations of a diffuse field. *J. Acoust. Soc. Am.*, 110, 7.
- Nakamura, Y. (1989) A METHOD FOR DYNAMIC CHARACTERISTICS ESTIMATION OF SUBSURFACE USING MICROTREMOR ON THE GROUND SURFACE. Railway Technical Research Institute, Quarterly Reports, 30. Retrieved from <https://trid.trb.org/view/294184>
- Park, J., Lindberg, C. & Vernon, F. (1987) Multitaper spectral analysis of high-frequency seismograms. *Journal of Geophysical Research*, 921, 12675–12684. doi:10.1029/JB092iB12p12675
- Percival, D.B., Walden, A.T., B, P.D. & T, W.A. (1993) *Spectral Analysis for Physical Applications*, Cambridge University Press.
- Poupinet, G., Ellsworth, W.L. & Frechet, J. (1984) Monitoring velocity variations in the crust using earthquake doublets: An application to the Calaveras Fault, California. *J. Geophys. Res.*, 89, 5719–5731. doi:10.1029/JB089iB07p05719
- Prerau, M.J., Brown, R.E., Bianchi, M.T., Ellenbogen, J.M. & Purdon, P.L. (2017) Sleep Neurophysiological Dynamics Through the Lens of Multitaper Spectral Analysis. *Physiology*, 32, 60–92. doi:10.1152/physiol.00062.2015
- Rickett, J. & Claerbout, J. (1996) Passive seismic imaging applied to synthetic dataa, 8.
- Sabra, K.G. (2005) Extracting time-domain Green's function estimates from ambient seismic noise. *Geophysical Research Letters*, 32. doi:10.1029/2004GL021862
- Samson, J.C. (1983) Pure states, polarized waves, and principal components in the spectra of multiple, geophysical time-series. *Geophysical Journal International*, 72, 647–664. doi:10.1111/j.1365-246X.1983.tb02825.x
- Schuster, A. (1898) On the investigation of hidden periodicities with application to a supposed 26 day period of meteorological phenomena. doi:10.1029/tm003i001p00013
- Sens-Schönfelder, C. & Wegler, U. (2006) Passive image interferometry and seasonal variations of seismic velocities at Merapi Volcano, Indonesia. *Geophys. Res. Lett.*, 33, L21302. doi:10.1029/2006GL027797
- Shapiro, N.M. & Campillo, M. (2004) Emergence of broadband Rayleigh waves from correlations of the ambient seismic noise: CORRELATIONS OF THE SEISMIC NOISE. *Geophysical Research Letters*, 31, n/a-n/a. doi:10.1029/2004GL019491
- Shapiro, N.M., Ritzwoller, M.H. & Bensen, G.D. (2006) Source location of the 26 sec microseism from cross-correlations of ambient seismic noise. *Geophysical Research Letters*, 33. doi:<https://doi.org/10.1029/2006GL027010>

- Snieder, R., Grêt, A., Douma, H. & Scales, J. (2002) Coda wave interferometry for estimating nonlinear behavior in seismic velocity. *Science*, 295, 2253–2255. doi:10.1126/science.1070015
- Thomson, D.J. (1982) Spectrum estimation and harmonic analysis. *Proceedings of the IEEE*, 70, 1055–1096, Presented at the Proceedings of the IEEE. doi:10.1109/PROC.1982.12433
- Tutorial H/V. (n.d.) . Retrieved March 9, 2021, from <http://www.geopsy.org/documentation/geopsy/hv.html>
- Valentin, J., Capron, A., Jongmans, D., Baillet, L., Bottelin, P., Donze, F., Larose, E., et al. (2017) The dynamic response of prone-to-fall columns to ambient vibrations: comparison between measurements and numerical modelling. *Geophysical Journal International*, 208, 1058–1076. doi:10.1093/gji/ggw440
- Vidale, J.E. (1986) Complex polarization analysis of particle motion. *Bulletin of the Seismological Society of America*, 76, 1393–1405, GeoScienceWorld.
- Voisin, C., Garambois, S., Massey, C. & Brossier, R. (2016) Seismic noise monitoring of the water table in a deep-seated, slow-moving landslide. *Interpretation*, 4, SJ67–SJ76. doi:10.1190/INT-2016-0010.1
- Welch, P. (1967) The use of fast Fourier transform for the estimation of power spectra: A method based on time averaging over short, modified periodograms. *IEEE Trans. Audio Electroacoust.*, 15, 70–73. doi:10.1109/TAU.1967.1161901

## Appendix A

### Introduction to the power spectral density (PSD)

Before going into detail about the methodologies used within this thesis for estimating the spectral content of the seismic signals, we provide the definition of the power spectral density.

Considering a time series  $x(t)$  we can define its energy as

$$E \triangleq \int_{-\infty}^{\infty} |x(t)|^2 dt.$$

For the Parseval's theorem, we can express it in the frequency domain

$$\int_{-\infty}^{\infty} |x(t)|^2 dt = \int_{-\infty}^{\infty} |X(f)|^2 df$$

Where  $X(f)$  is the Fourier transform of  $x(t)$ :

$$X(f) \triangleq \int_{-\infty}^{\infty} e^{-i2\pi ft} x(t) dt$$

Since the integral on the right-hand side is the energy of the signal, the integral  $|X(f)|^2$  can be interpreted as a density function describing the energy contained in the signal at the frequency  $f$ . Thus, the energy spectral density of  $x(t)$  is defined as:

$$E(f) \triangleq |X(f)|^2$$

However, this definition is suitable for transients (pulse-like signals) whose energy is concentrated around a single time window; then the Fourier transforms of the signals generally exists. For continuous signals, it is appropriate to define the power spectral density (PSD) which exists for stationary processes. The PSD describes how the power of a time series is distributed over frequency.

The average power  $P$  of a signal  $x(t)$  is given by the following equation:

$$P = \lim_{T \rightarrow \infty} \frac{E(f)}{T} = \lim_{T \rightarrow \infty} \int_{-\infty}^{\infty} \frac{|X(f)|^2}{T} df$$

Then the power spectral density (PSD) is simply defined as:

$$PSD(f) = \lim_{T \rightarrow \infty} \frac{|X(f)|^2}{T}$$

## Appendix B

### Computation of the Welch's Periodogram

The computation of the Periodogram based on the Welch method can be summarized into 4 phases:

- 1) Signal partition into K segments.

Data sequence:

$$x[0], x[1], x[2], \dots, x[N - 1]$$

Segment 1:  $x[0], x[1], \dots, x[M - 1]$

Segment 2:  $x[S], x[S + 1], \dots, x[M + S - 1]$

.

.

Segment K:  $x[N - M], x[N - M + 1], \dots, x[N - 1]$

Where: M = Number of points in each segment or batch size

S = Number of points to shift between segments

K = Number of segments

- 2) Computation of the windowed discrete Fourier transform (DFT) for each segment.

$$X_k(f) = \sum_m x[m]w[m] \exp(-j2\pi fm)$$

Where:

$$m = (k - 1)S, \dots, M + (k - 1)S - 1$$

$w[m]$  = window function

- 3) From the DFT calculate the modified periodogram value,  $P_k(f)$ , for each segment.

$$P_k(f) = \frac{1}{W} |X_k(f)|^2$$

Where:

$$W = \sum_{m=0}^M w^2[m]$$

- 4) Average the obtained periodograms value to obtain Welch's estimate of the PSD:

$$S_x(f) = \frac{1}{K} \sum_{k=1}^K P_k(f)$$



# CHAPTER 3

## Raspberry Shake sensor laboratory and field tests for shallow passive seismic applications.

### 1. Introduction

In the last decades, passive seismic techniques have become more and more appealing because they do not require active sources and, a great amount of information can be extracted by the so-called “seismic noise” considering both single-station and array recordings. The initial studies have been mainly focused on the analysis of seismic noise measurements for both assessment and monitoring purposes in civil and mining engineering (e.g., Burjánek et al. 2010). In recent years, passive techniques have become increasingly popular in many other applications and, with the global growth of climate-related disasters, they have also been used to monitor unstable slopes (Larose et al., 2015). To this regard, research activities have demonstrated that by cross-correlating the ambient noise recorded at two different locations, it is possible to continuously monitor the seismic velocity changes occurring within a slope and correlate them with both the displacements and the water table variations (Mainsant et al., 2012; Voisin et al., 2016). In addition to this technique, the seismometers have also been installed directly on unstable rock compartments to study the evolution over time of their fundamental frequency by processing the recordings with the horizontal-to-vertical spectral ratio technique (HVSР) (Burjánek et al., 2012; Taruselli et al., 2019). The success of these passive methodologies in different application fields lies in the fact that the ambient seismic noise can be recorded at any time and in any location since it does not require any specific active source. Nevertheless, the logistic and cost advantage of passive surveys may be nullified if expensive low-frequency broadband seismic sensors are required, especially in the case of spatially dense surveys where many recording stations are required to produce a detailed subsurface 2D/3D image (Gimbert et al. 2020). In this perspective, researchers are now extremely interested in newly-developed low-cost seismometers. These solutions may be convenient in terms of both economic savings and limited installation and maintenance efforts (Manconi et al., 2018). Moreover, they can be more suitable for long-term monitoring than classical seismological sensors, since they can be set up to transmit real-time data with affordable costs (Anthony et al., 2019). However, many inexpensive sensors do not generally guarantee ground motion measurements in a broad frequency band. This issue may prevent their use in some application fields, including monitoring of unstable rock blocks, in which the detection of low frequencies is extremely important. A candidate sensor for these scenarios may be the recently-developed all-in-one OSOP RaspberryShake 3D. This sensor provides an interesting cheap plug-and-play solution that combines both the three-component geophone and the digitizer in a single waterproof enclosure, ideal for outdoor studies. However, their application for ambient seismic noise monitoring in areas with a high hydrogeological risk is still unexplored. To this perspective, in this work, we evaluate the performance of the Raspberry Shake 3D (RS-3D) seismometers by performing both laboratory and field tests. Concerning the former analysis, we characterized the RS-3D frequency response function (FRF) using a vibrating table. Whereas with regard to the field case studies, we collected data with both RaspberryShake and the Nanometrics Trillium seismometers. We then compared the recordings performing the HVSР method to study the vibrational properties of unstable rock blocks as well as the component-wise spectral ratios for each analysed couple of sensors (RS & Trillium) deployed at different sites. In the following sections, we provide the sensors’ technical specifications, a description of the performed analyses, and the results regarding the RaspberryShake performances.

### 2. Method

#### 2.1. Sensors description

The instrumentation used within this work consists of two 3-component seismometers (Figure ).

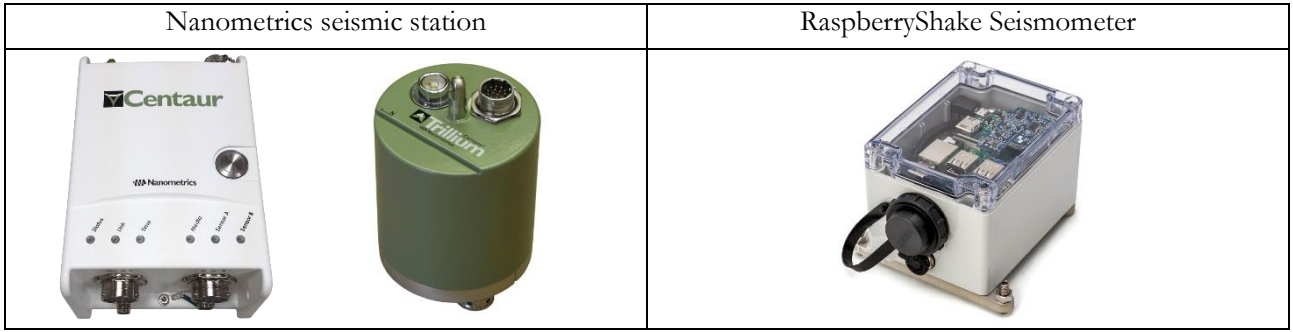


Figure 1 Left column: Nanometrics Digitizer and seismometer; Right column: RaspberryShake seismic station.

The Raspberry Shake is an all-in-one seismometer developed by OSOP company. The 3D version provides a plug-and-go solution that integrates three-component geophones, the digitizers, the hyper dampers and the computer into a single enclosure (IP10 or IP67). Other options are available, i.e., the vertical velocimeter (1D) and the 4D version which is basically a 1D model coupled with a 2G orthogonal MEMS accelerometer. Within this test, we analyse only the three-component seismometers which are the most complete devices for passive-seismic applications. The unit comes with 8Gb storage that allows recording miniSEED data for approximately 110 days. However, the internal memory can be furthermore increased with the micro-SD card. The onboard computer is a Wi-Fi-enabled device, and it is designed to send data to a remote computer. The clock synchronization of the seismometer is based on the Network Time Protocol (NTP) providing 1 sample of accuracy (+/- 10ms at 100 Hz). However, when the internet connection is not available, e.g., during field surveys, it is possible to get the timing through the GPS module connected by USB port. The power supply voltage of the unit is 5V (2.5A). This makes easy the on-field powering using an external battery. The seismometer is mounted with three orthogonally placed 4.5 Hz Sunfull PS-4.5B electromagnetic geophones with the corner frequency electronically extended down to 2 seconds. More in detail, OSOP's specifications declare a -3dB frequency bandwidth from 0.7 to 39 Hz (Figure 2-left). The sampling rate of the Raspberry Shake is fixed to 100Hz. For other technical details, the reader can refer to the web page <https://raspberryshake.org/>. The RS-3D has been compared with a Nanometrics sensor since the latter is considered the standard in broad-band seismological surveys. This device does not come within a single-enclosure solution. Indeed, the seismometer (Trillium 20s) and the digitizer (Centaur) are arranged within two different cases. The Trillium Compact 20s (IP67) incorporates a symmetric triaxial force feedback sensor design with a response flat to velocity from 20s to 100Hz (Figure 2-right). The recorded ground motion is then digitalized within Centaur Digital Recorder (IP68) with a sampling frequency spanning from 1 up to 5000 Hz. The data can be recorded either on a removable SD card or on the internal memory, each up to 64 Gb. The time synchronization of the device is based on the Precision Time Protocol (PTP), but, as well as for the RS-3D, it is also possible to use the GPS antenna. More functionalities are available with this sensor, but these are not useful for the scope of this study.

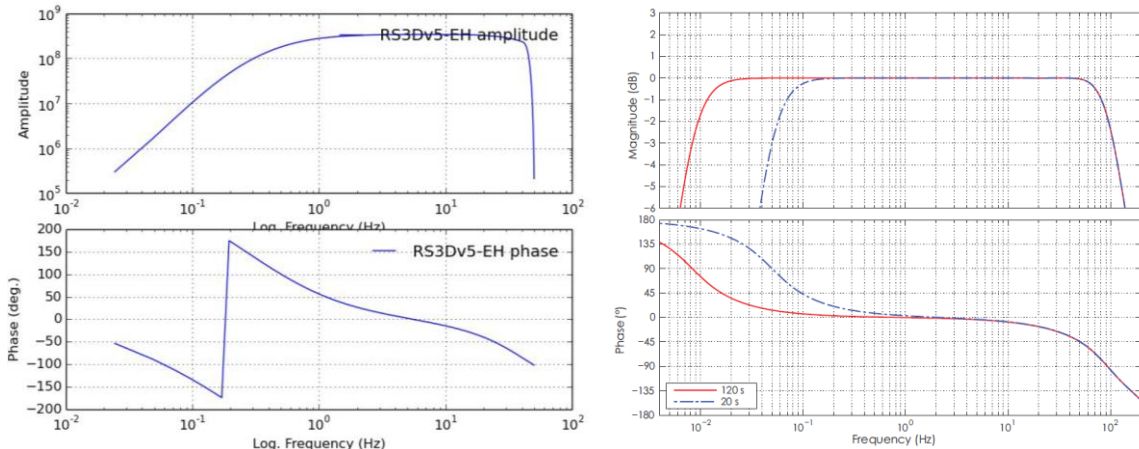


Figure 2 Instrumental response of Raspberry Shake (left) and Trillium sensors (right: dashed blue curve).

## 2.2. Laboratory tests

Dynamic characterization of the Raspberry Shake 3D performances has been carried out using a vibrating table considering four different seismometers: two Trillium Compact 20s and two RShakes. The testing facility

comprised a shaker (TIRA Vib shaker) operated in an open-loop by means of an Agilent signal generator and a laser Doppler vibrometer (Polytech OFV 505) used as a reference for the velocity measurement of the vibrating table interface (Figure 3).

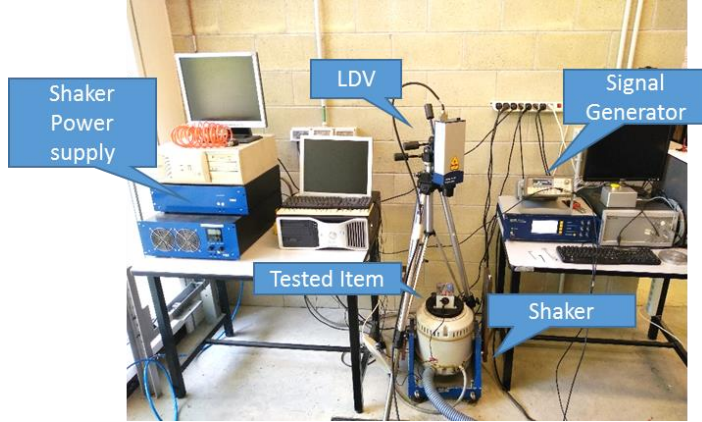


Figure 3 Setup of the laboratory test

The testing procedure provided sweep sine excitation between 0.5 and 40 Hz to investigate the entire nominal measurement bandwidth of the RShakes. The excitation amplitude of the sweep sine was varied at three different levels (i.e. 10, 20 and 30 mV) and for each test, at least three subsequent sweeps were acquired. Usage of different amplitudes for the sweep sine excitation was deemed necessary to investigate the linearity of the tested items, especially for the RShakes. The RaspberryShake seismometers were additionally tested with twelve monochromatic sinusoidal signals (step sine tests at different frequency, i.e. 0.6, 0.7, 0.8, 1, 2, 10, 20, 30, 35, 37, 39, 40 Hz) with a duration of 90 s. This was done as an additional characterization of the dynamic behaviour of the RShakes, especially at frequencies close to the corner values.

Figure 4 (left) shows an example of the measured excitation during the sweep sine testing whereas sinusoidal excitation measured in the step sine testing is provided in Figure 4 (right).

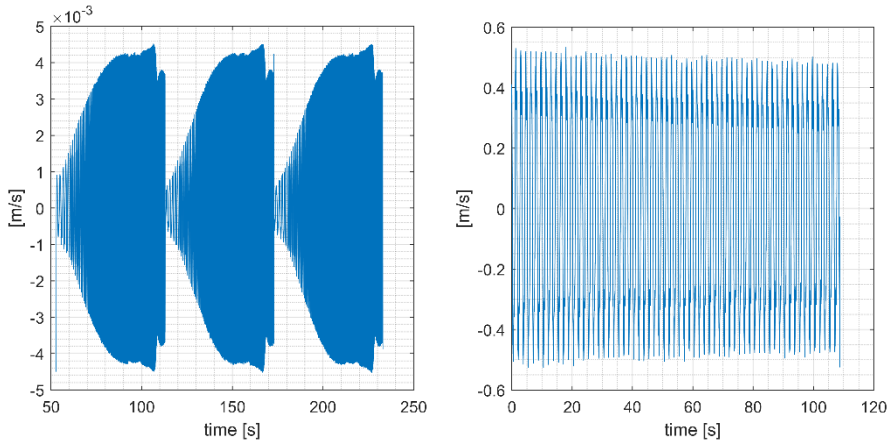


Figure 4 Left: Sweep sine test with 10 mV amplitude from the generator. Right: 10mV monochromatic sinusoidal signal at 0.6Hz

The entire collected time histories were firstly high pass filtered (Butterworth 3<sup>rd</sup> order, 0.05 Hz) and resampled to obtain a common sampling frequency between the seismometers and the vibrometer. Considering the sweep sine testing, the three obtained sweeps (an example in Figure 4-left) have been divided into three independent signals. Then, the amplitude of the Frequency Response Function (FRF) was obtained averaging the spectra estimated for each of the sub-sweeps and computing the ratio among the measured output (RaspberryShake) and input spectra (vibrometer). The procedure has been performed for the three tested amplitudes 10, 20 and 30mV.

Results of the step sine testing were divided into nine buffers, each one lasting 10s and the obtained spectra were filtered with Hanning window. Thus, for each tested frequency we derived the amplitude of the FRF as the ratio

between the amplitude of the RaspberryShake and vibrometer spectra. As well as for the logarithmic input signal, we did perform the analysis for the three considered amplitudes (10, 20 and 30mV).

### 2.3. Field application

The comparison of 2 RS and Trillium sensors for field applications have been carried out at different sites, mainly consisting of potentially unstable rock blocks and pillars (i.e., Torrioni di Rialba (LC, Italy), Il Qarraba (Malta) and, Il Prajet (Malta)). In addition, sensors have also been occasionally installed at sites where groundwater pumping tests were ongoing (i.e., Ventasso (RE, Italy) test site) or across slopes showing both significant and negligible displacements (Ca' Lita earth flow (RE, Italy)). Deployed sensors have always been equipped with a GPS receiver so that a common accurate time reference is available. Based on the outcomes of the previously described laboratory tests, we will evaluate the performance of the RS sensors by performing the HVSR technique as well as amplitude spectral ratios considering the data collected by the Trillium sensors as a reference. To minimize the coupling error, we installed the sensors using the same spikes provided for the Trillium seismometer. In these scenarios, we recorded the ambient seismic noise installing the RaspberryShake and the reference Nanometric sensors one next to the other (**Figure 5**).



*Figure 5 Nanometrics and RaspberryShake seismometers during the field test.*

The obtained time-series firstly underwent the following pre-processing sequence. The first 15min the collected data have been discarded in order to consider sensor stabilization after field deployment (especially for the Trillium seismometer). Likewise, the last part of the recording was eliminated to get rid of the close-range high-amplitude signals generated by the field technicians when switching off the sensor. The dataset has been resampled to a common sampling frequency. In our case, taking into account that the RS and Trillium sampling frequencies were set to 100Hz and 200Hz, respectively (actually the RTS sampling frequency is fixed and cannot be modified), we resampled the raw time series by means of interpolation to 1000Hz. Accordingly, we are able to find a common initial time independently of when the two sensors actually started recording. After resampling, the signals of the two sensors could be perfectly aligned and cut over a common time interval. Decimating signals to a lower sampling frequency (e.g., 200Hz) was not considered because it was not found to vary the computational cost significantly. High-amplitude signals with very low frequency were then rejected by means of a high-pass zero-phase IIR filter with a corner frequency of 0.05Hz and time series were converted from counts to physical units assuming, at this stage, a flat broad-band transfer function for the two sensors and the nominal sensitivity reported in the technical specifications (i.e., 3.4000e8 counts/(m/s) for RS and 3.0052e8 counts/(m/s) for Trillium).

The obtained pre-processed data were firstly analysed by computing the ratio between the estimated Fourier amplitude spectra of the horizontal and vertical components recordings (HVSR) considering only the signals that

were recorded on the unstable rock compartments. Peaks in the obtained HVSR curve can reveal the resonance properties of the investigated site (Nakamura 1989). For the application of this technique, the ambient recordings have been divided into 60 s signal segments tapered with a Hamming window and KonnoOhmachi spectral smoothing has been applied before computing the horizontal to vertical spectral ratio (Konno & Ohmachi 1998). With these settings, the lowest resolvable frequency is roughly 0.17 Hz (McNamara & Buland 2004). We additionally estimated the Welch PSD in terms of acceleration to check whether the RS geophone's self-noise levels (proposed by Anthony et al. 2019) could impact the characterization of HV peaks. For this analysis, the signals firstly underwent the instrument response removal. This procedure introduces some low-frequency amplifications that have been attenuated by applying a zero-phase high-pass filter with a 0.4Hz cut-off frequency. We then derive the velocity by multiplying the raw by  $j2\pi f$  and, through the inverse fast Fourier transform, we retrieved the acceleration signals. The latter has been finally used to estimate the PSD which has been smoothed using the moving average method.

The second analysis has been performed comparing the amplitude spectra. In this perspective, we resorted to a non-parametric spectral estimation technique, namely the multitaper method (Thomson, 1982), that makes use of orthogonal data tapers to reduce bias and variability in the final estimate. In more detail, we set the parameters of the computation so as to obtain amplitude spectra with 0.05Hz frequency resolution and this resulted in the use of 19 orthogonal tapers, two of which were eventually discarded to retain only the ones with optimal frequency concentration in the specified resolution bandwidth. For statistical robustness of the comparison, the collected time series were divided into 200s-long time windows and spectral estimation was applied to each of them. The length of the selected time window should guarantee accurate spectral estimation down to a frequency of 0.05Hz, obtained with the relationship  $10/T_w$  (McNamara and Buland, 2004). We then computed component-wise spectral ratios for each analysed couple of sensors deployed at different sites, after the estimated spectra were smoothed with the frequency-dependent averaging function proposed by Konno and Ohmachi (1998).

### 3. Results And Discussions

#### 3.1. Laboratory test

**Figure 6** and **Figure 7** show the measured moduli of the FRFs obtained from the laboratory test. The results of the dynamic characterization confirm that the FRFs of RaspberryShake vertical geophones are within the OSOP-specifications. Indeed, the computed FRFs show a -3dB frequency bandwidth from 0.7 to 39 Hz for both tests with the sweep sine and step sine testing (**Figure 7**). In the same way, the Trillium Compacts reveal a flat FRF in the tested bandwidth in accordance with the nominal amplitude response which is -3dB from 0.05 to 100Hz (**Figure 6**). From this analysis, two remarkable points arise while observing the RaspberryShake FRFs. First, the frequency responses of the two low-cost seismometers slightly differ from each other in terms of amplitude with the same velocity input. This variability could be linked to small intrinsic differences among the two sensors, thus as a consequence of the manufacturing of the RaspberryShake sensors both in terms of mechanics and electronics. However, we deem that these differences are negligible in the perspective of monitoring ambient seismic noise. Secondly, the variation of the velocity RMS for the sweep sine testing clearly highlighted the nonlinear behaviour of the RaspberryShakes (**Figure 7**). It can be observed that a low RMS input velocity, results in a "higher" FRF compared to the one obtained increasing the input velocity. Considering the average FRF among the tested cases it can be said that variability is about 0.7 dB among the – 3 dB bandwidth. On the contrary, the reference Trillium sensor provides coherent FRFs for all three amplitudes. This was explained by the fact that the RaspberryShake is a non-force-feedback sensor, leading to non-linear behaviour related to the mechanical response of the geophone mass suspension when the system is excited at different velocity amplitudes. In fact, the Trillium sensors, which are force feedback sensors, provided constant FRFs for all the tested cases, showing a maximum discrepancy of 0.15 dB.

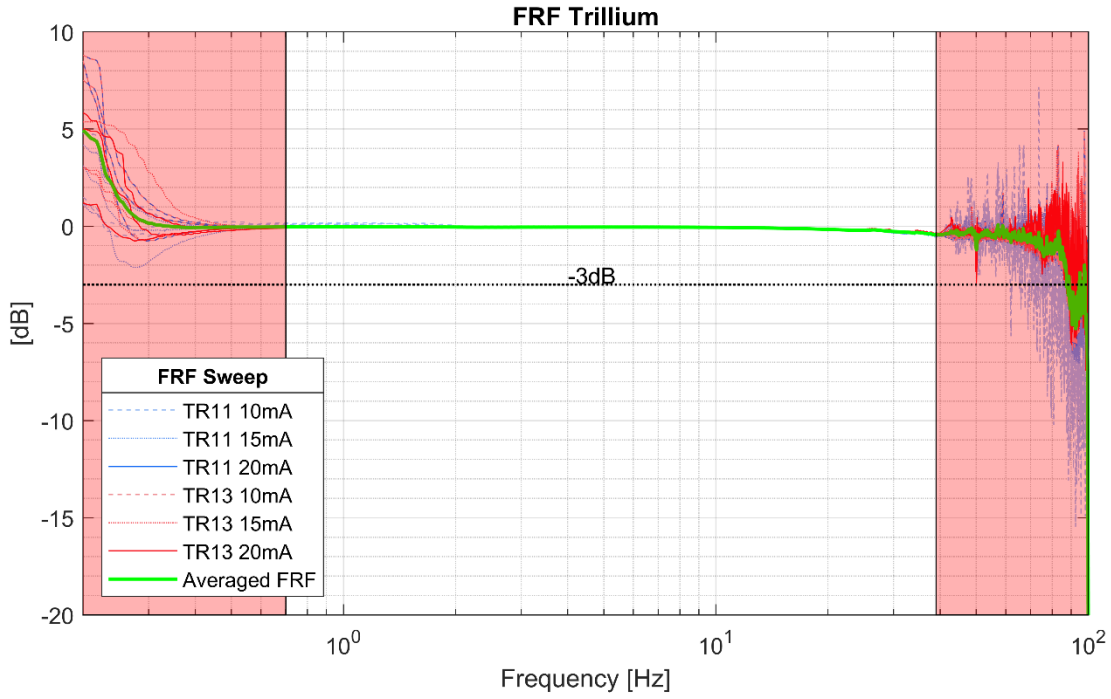


Figure 6 FRF Nanometrics station (Centaur digitizer + Trillium seismometer).

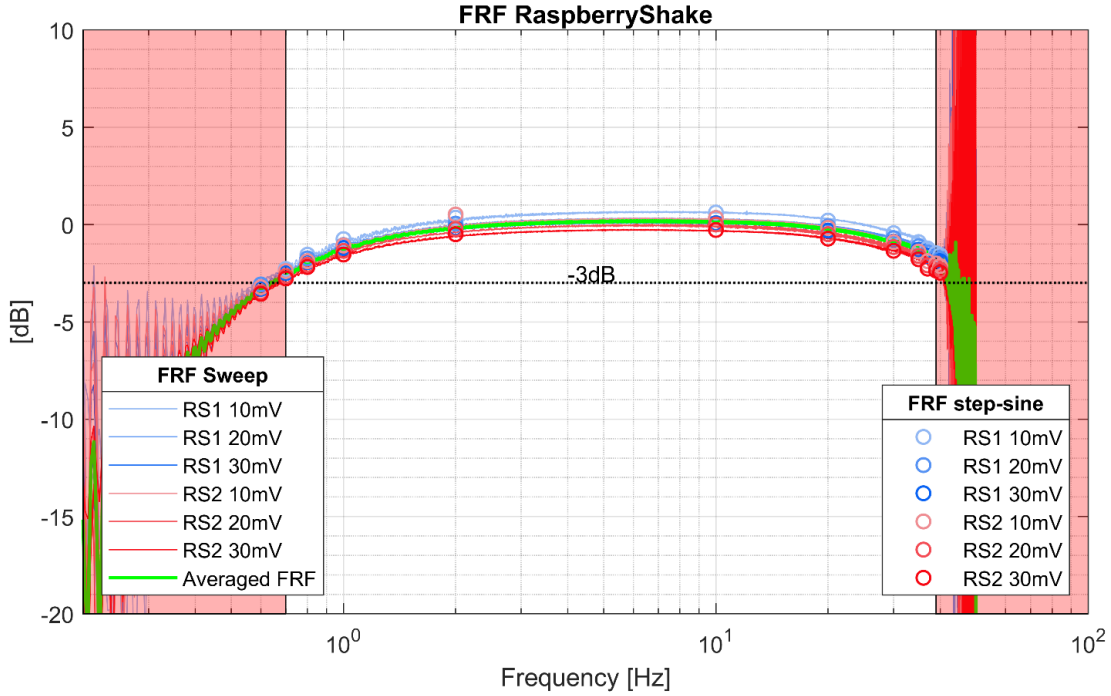


Figure 7 FRF RaspberryShake.

### 3.2. Field application

In the laboratory test, we observed that the FRF of the RS vertical component line up with the datasheet specifications. We performed the Horizontal to Vertical Spectral Ratio with the assumption that the response of the horizontal geophones has negligible differences compared to the tested vertical one. The results of the field seismic surveys reveal a good agreement of the HVSR curves computed with the RaspberryShake and Trillium sensors (Figure 8-top shows three examples). The overall trend is similar for both sensors even though some differences arise in terms of amplitude (Figure 8). This is particularly true at the corners of the sensor response. To highlight this tendency, we compute for each case study the difference between the Trillium and RaspberryShake HVSRs (Figure 8-bottom). The analysis shows that the standard deviation (green shaded area) is approximately close to zero between 2-10Hz, whereas it increases outside this frequency range. We exclude that

these discrepancies occurring at the corner frequencies are related to different FRFs between the vertical (tested) and horizontal geophones (not tested). Indeed, we observed that the power spectral densities of Trillium and RaspberryShake sensors differ from each other both along with vertical and horizontals directions. Moreover, for some case studies, the PSDs are very similar for both seismometers, whereas, for others, the RS signal's power content is sometimes higher and sometimes lower than the Trillium one.

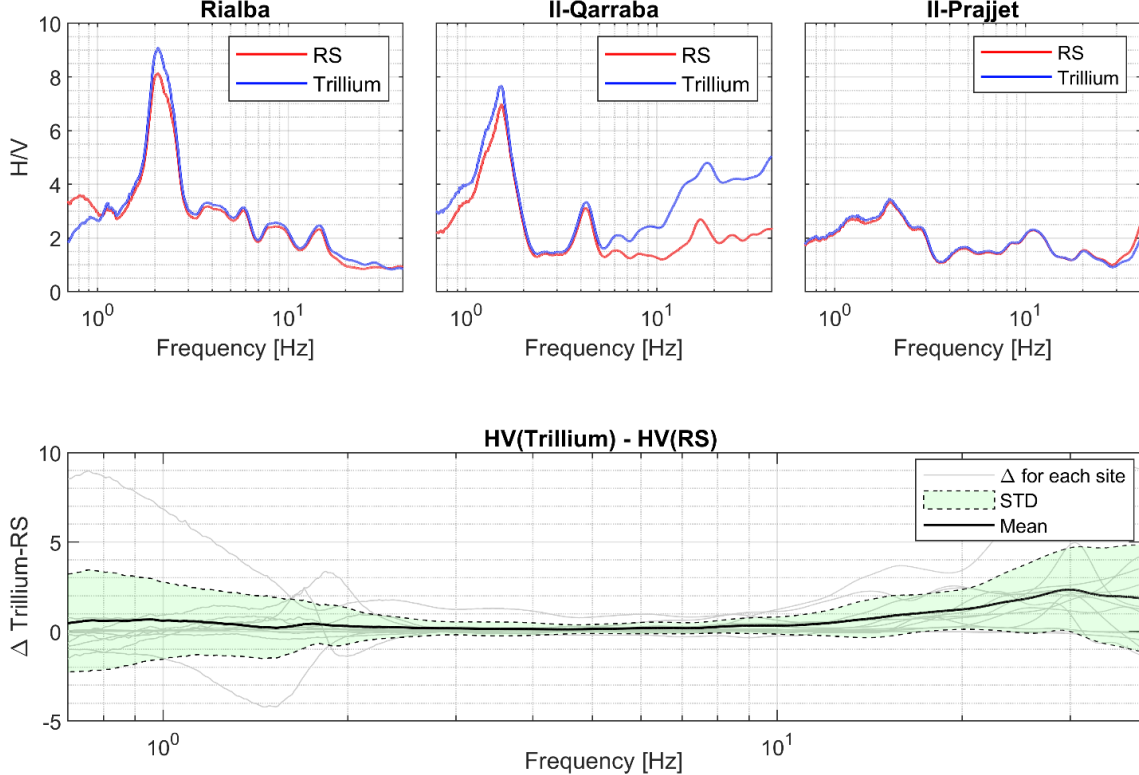


Figure 8 Top: Examples of HVRS curves computed considering three different sites. Bottom: Difference between the Trillium and RaspberryShake HVSRs.

We, therefore, checked whether the differences between the two devices were linked to the RaspberryShakes self-noise that interferes with the recorded ambient seismic vibration. In this perspective, we considered the self-noise estimated by Anthony for the RS-4D vertical-component geophone which is lower than -160dB (Anthony et al. 2019). We observed that the energetic content of the ambient ground motion recorded on the unstable rock blocks is higher than the sensors self-noise (Figure 9). We, therefore, came to the hypothesis that the differences arising between the two seismometers are mainly linked to the ground-sensor coupling. In fact, there is not a general rule governing the discrepancies observed between the RaspberryShake and the Trillium velocimeters. In detail, it is not possible to observe a tendency that occurs for all the case studies or a specific component or in a certain frequency band. Sometimes differences come out for the vertical component, sometimes for the horizontal ones, sometimes at high- and not at low-frequencies and vice-versa. Unfortunately, it is not possible neither to infer how much the ground-sensor coupling influences the HVSR and neither to distinguish whether this problem affects more the low-cost sensor rather than the expensive one.

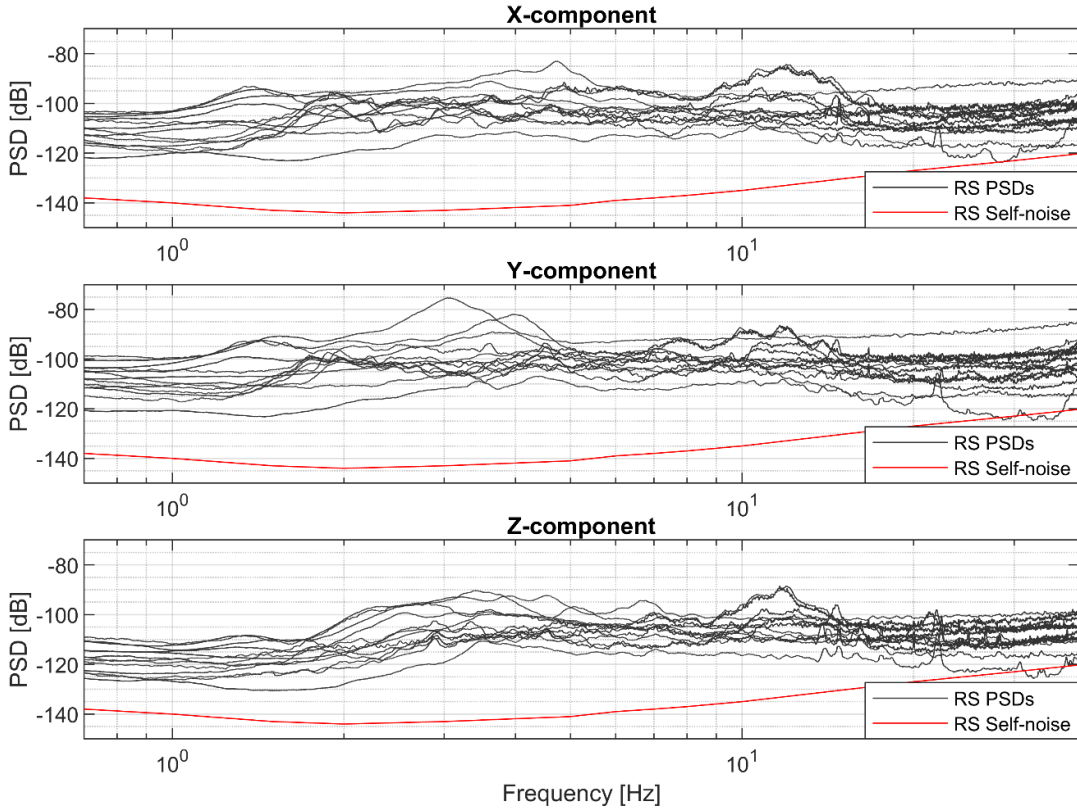


Figure 9 PSDs computed for each sensor component vs RaspberryShake self-noise provided by Anthony et al. 2018.

With regards to the last analysis, Figure 10 illustrates the results obtained for the two tested RS sensors, hereafter named RS1 and RS2, in the 0.1Hz-45Hz band. Overall, we considered approximately 37 hours and 20 hours of recording for the two sensors, respectively. Ratios are expressed in decibel and presented in terms of relative probability, that is, for each frequency, the values of the estimated amplitude spectra are partitioned into bins and the value of each bin is the ratio of the number of elements in the bin to the total number of elements (i.e. the sum of all the bin values gives unity). The images also show the median spectral ratio, together with the 25th and the 75th percentiles ratios. In addition, red lines limit the -3dB bandwidth of the RS sensors, that according to the technical specifications of the V5 release, should span across the 0.7-39Hz frequency range. It can be noted that the best matching between RS and Trillium is observed in a limited band, approximately ranging from 1.4Hz to 18Hz, although the spectral values of the low-cost sensor are always larger than the Trillium ones (ratios always greater than 0dB). Actually, if we consider the median curves, the nominal -3dB band of the RS seems to be underestimated, and according to the field results this could be extended down to 0.3Hz and up to about 45Hz (although in the case of RS2 x-component, the -3dB high-frequency limit was below 39Hz; Figure 10b). The vertical component seems to show a lower variance of the estimated spectral ratios across the considered frequency range, although we noticed in nearly all the components of the tested sensors overshooting close to the limits of the nominal -3dB band. In Figure 11 we show images similar to those reported in Figure 10, but without considering data collected at the Malta test site, in order to verify if the sub-optimal sensor coupling achieved with long screws instead of proper spikes could have compromised the performance of the RS sensors. In this case, we considered approximately 32 hours and 16 hours of recording for the RS1 and RS2 sensors, respectively. It can be noted that difference between spectral ratios reported in Figure 10 and Figure 11 are negligible.

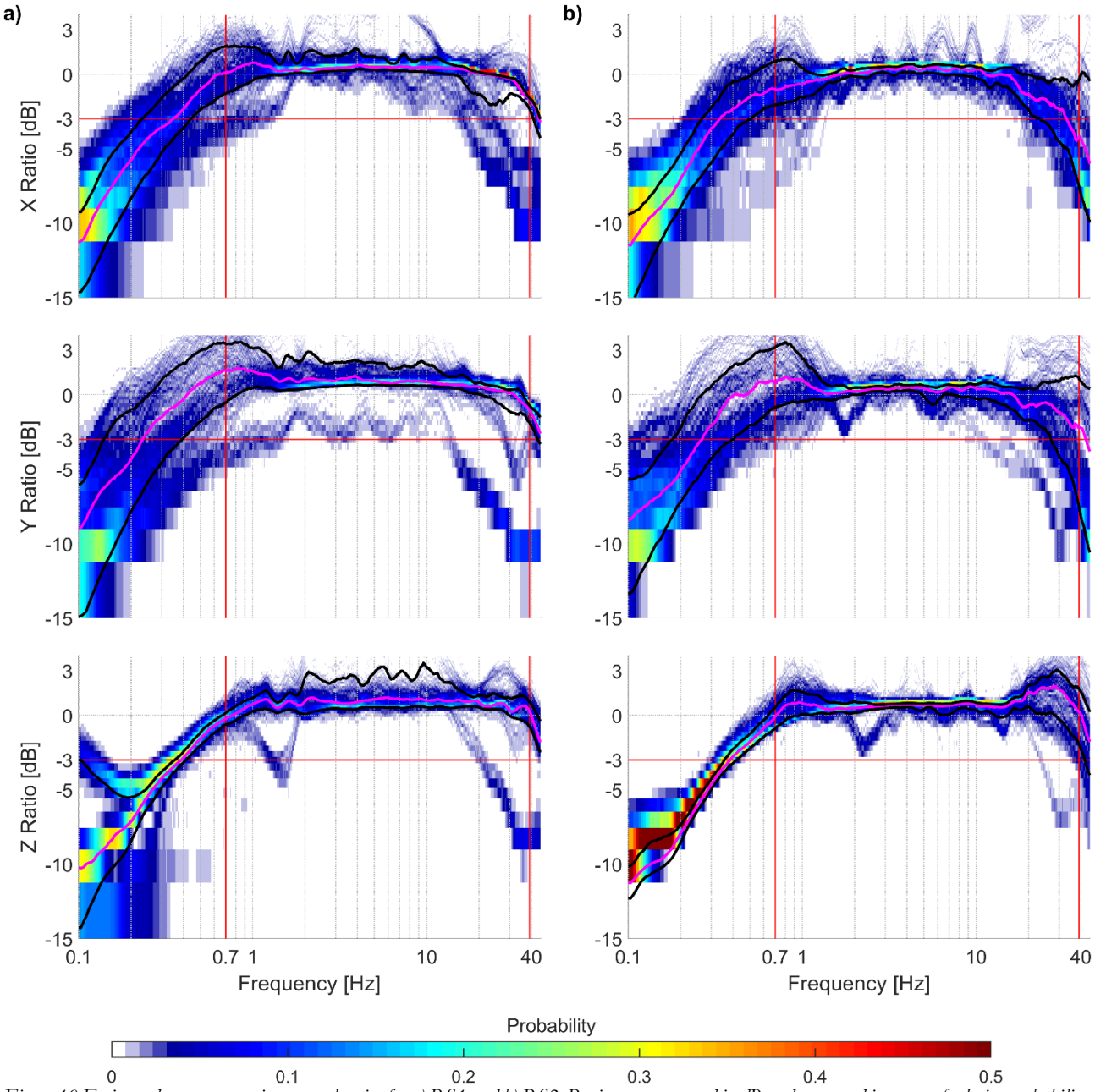


Figure 10 Estimated component-wise spectral ratios for a) RS1 and b) RS2. Ratios are expressed in dB and presented in terms of relative probability. Magenta curve is the median spectral ratio (i.e., 50th percentile), while upper and lower black curves are 75th and 25th percentile, respectively.

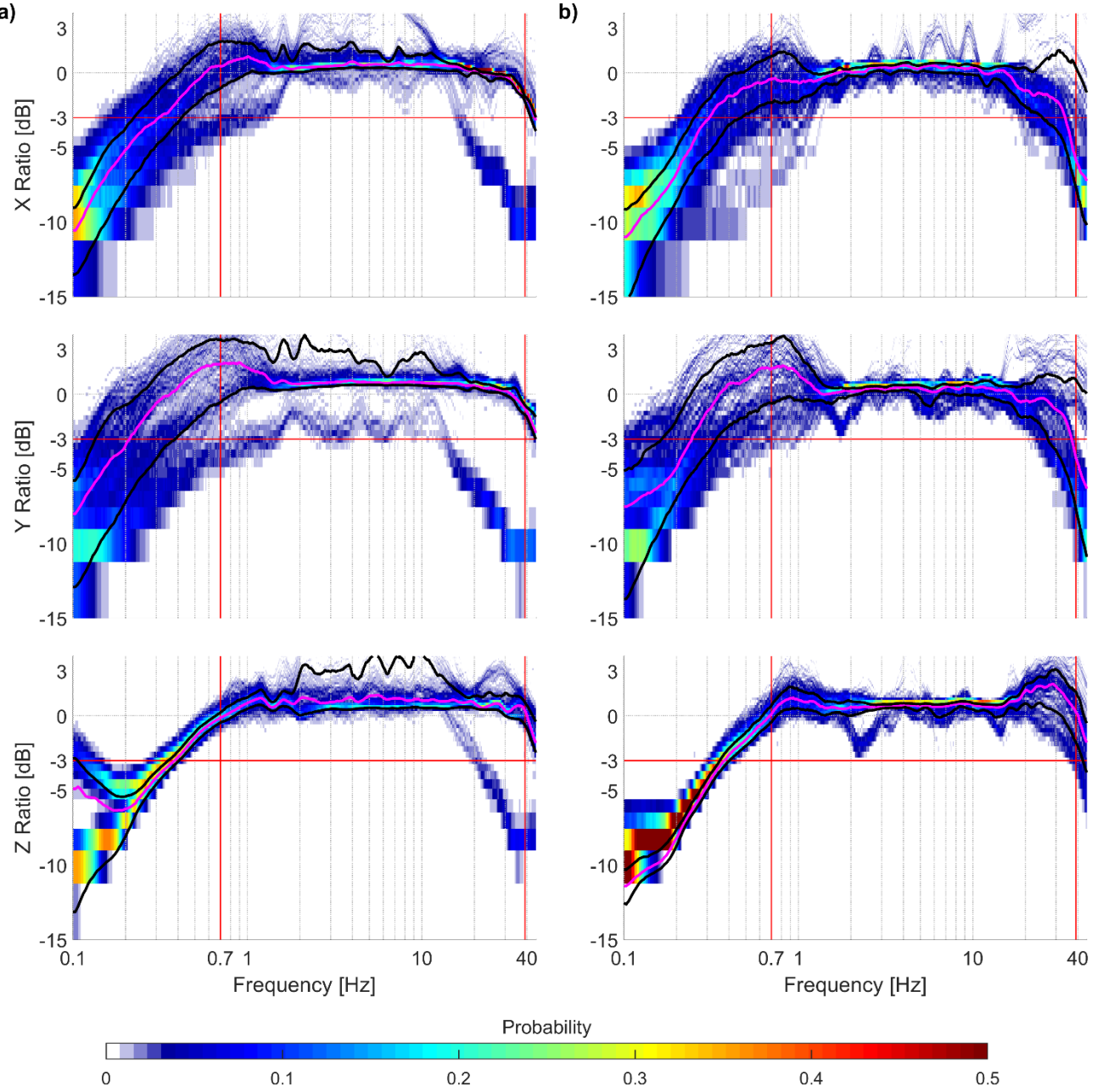


Figure 11 As in Figure 1, but without considering the datasets collected at Malta test sites, where sub-optimal sensor coupling could have compromised RS performance.

#### 4. Conclusions

In this work, we evaluated the Raspberry Shake 3D performances to assess whether this low-cost seismometer can be used for ambient seismic noise applications with a strong focus on the characterization of the unstable rock pillars dynamic response. Both laboratory and field experimental tests showed that the low-cost velocimeters perform within the OSOP specifications with a -3dB frequency bandwidth from 0.7 to 39Hz. In the laboratory tests, we did observe an amplitude nonlinearity and slightly different FRFs for the two analysed sensors. Nevertheless, we deem that these two flaws lead to negligible differences in the ambient seismic noise recordings. The field surveys showed that the RaspberryShake HVSР peaks are comparable with those obtained by the reference Trillium sensors with slight amplitude discrepancies occurring at the corners of the RS frequency response. However, these differences could be linked to the ground-sensor coupling and thus they may also interest the reference sensor (Trillium). Within this work, we did not evaluate the phase response of the RaspberryShake seismometers because of the impossibility to connect them and the laser vibrometer to a single acquisition board, featuring a common reference clock and sampling frequency. In this perspective, experimental tests are underway

with the objective to evaluate whether these sensors could be also used for the passive interferometry technique. Indeed, for the application of this methodology, it is fundamental that the recorded ambient seismic noise signals do not undergo a phase distortion which would make it impossible to evaluate the lag-time between seismic sensors.

This work demonstrates that the RaspberryShake-3D seismometers could be a valuable alternative to the high-cost broadband sensors in the evaluation of unstable rock dynamic response, provided the vibrational frequencies are within the RS flat frequency response. Moreover, their low cost combined with the limited installation and maintenance efforts as well as the possibility to send real-time data to a remote computer, make them an ideal candidate for rock-fall monitoring purposes. Furthermore, considering the Raspberry Shake is about eight times cheaper than the Nanometrics seismometer station, the deployment of more sensors on the same unstable rock block may be practicable, and could be helpful to investigate the shape of the block vibration modes.

## 5. Bibliography

- Anthony, R.E., Ringler, A.T., Wilson, D.C. and Wolin, E. [2019] Do Low-Cost Seismographs Perform Well Enough for Your Network? An Overview of Laboratory Tests and Field Observations of the OSOP Raspberry Shake 4D. *Seismol. Res. Lett.* 90, 219–228.
- Burjánek, J., Gassner-Stamm, G., Poggi, V., Moore, J.R. and Fäh, D. [2010] Ambient vibration analysis of an unstable mountain slope. *Geophys. J. Int.* 180, 820–828.
- Burjánek, J., Moore, J.R., Yugsi Molina, F.X. and Fäh, D. [2012] Instrumental evidence of normal mode rock slope vibration: Evidence of normal mode rock slope vibration. *Geophys. J. Int.* 188, 559–569.
- Gimbert, F., Nanni, U., Roux, P., Helmstetter, A., Garambois, S., Lecointre, A., Walpersdorf, A., et al. (2020) The RESOLVE project: a multi-physics experiment with a temporary dense seismic array on the Argenti\`ere Glacier, French Alps. arXiv:2009.06321 [physics]. Retrieved from <http://arxiv.org/abs/2009.06321>
- Konno, K. & Ohmachi, T., 1998. Ground-motion characteristics estimated from spectral ratio between horizontal and vertical components of microtremor, *Bull Seismol Soc Am*, 88(1):228–241.
- Larose, E., Carrière, S., Voisin, C., Bottelin, P., Baillet, L., Guéguen, P., Walter, F., Jongmans, D., Guillier, B., Garambois, S., et al. [2015] Environmental seismology: What can we learn on earth surface processes with ambient noise? *J. Appl. Geophys.* 116, 62–74.
- Mainsant, G., Larose, E., Brönnimann, C., Jongmans, D., Michoud, C. and Jaboyedoff, M. [2012] Ambient seismic noise monitoring of a clay landslide: Toward failure prediction. *J. Geophys. Res.* 117, F01030
- Manconi, A., Covello, V., Galletti, M. and Seifert, R. [2018] Short Communication: Monitoring rockfalls with the Raspberry Shake. *Earth Surf. Dyn.* 6, 1219–1227.
- McNamara, D.E. & Buland, R.P. (2004) Ambient noise levels in the continental United States. *Bulletin of the Seismological Society of America*. doi:10.1785/012003001
- Nakamura, Y.A. [1989] Method for dynamic characteristics estimation of subsurface using microtremors on the ground surface. *Q Rep Railway Tech Res Inst* 30:25–30
- Taruselli, M., Arosio, D., Longoni, L., Papini, M., Corsini, A. and Zanzi, L. [2019] Rock stability as detected by seismic noise recordings—three case studies. *Proceedings of the 24th European Meeting of Environmental and Engineering Geophysics*, Code 143674, doi: 10.3997/2214-4609.201802611
- Voisin, C., Garambois, S., Massey, C. and Brossier, R. [2016] Seismic noise monitoring of the water table in a deep-seated, slow-moving landslide. *Interpretation* 4, SJ67–SJ76.



# CHAPTER 4

## Seismic noise monitoring of unstable rock blocks

### 1. Introduction

In recent years, the dramatic increase in climate-related events, such as floods and landslides, has fostered the development of research activities and investigations able to cope with such phenomena. Nevertheless, reliable forecasting systems for natural disasters are still to be achieved, and this is particularly true for rock slope failures because of the lack of precursory patterns prior to collapse. With the aim of preventing, or at least reducing, damages and fatalities caused by rockfalls, integrated assessment and monitoring strategies have been designed by combining multidisciplinary approaches (D. Arosio *et al.* 2009, Longoni *et al.* 2012). In this perspective, passive seismic techniques have been largely used to monitor prone-to-fall sites by means of two different approaches. The classical one, borrowed from historical applications in underground mines, is to deploy a network of seismic sensors (either 1C or 3C) in order to detect, classify and localize microseismic signals that can give information on the evolution of the kinematic and dynamic conditions of the investigated slope (e.g. Diego Arosio *et al.* 2018). However, classical microseismic monitoring relies on the capability of the network to record an event according to a triggering methodology whose effectiveness is dependent upon several parameters (e.g., triggering algorithm, sensor sensitivity, source-sensor distance, slope geomechanical parameters, etc.). On the other hand, the second approach aims to analyse the ambient vibrations to extract dynamic features of unstable rock blocks and link them to the stability of the structure itself. The main idea is that whenever excited, a structure can vibrate at its peculiar resonance frequencies associated with its different vibration modes. Thus, since resonance frequencies are dependent upon the constraints of the studied structure, monitoring their dynamic response variations may provide knowledge of the stability conditions. In the perspective of the second approach, the initial studies were related to civil engineering applications (Clinton 2006). In this field, the ambient vibrations analysis proved to be an effective solution for health-structure monitoring (Potenza *et al.* 2015, Saisi *et al.* 2015, Lorenzoni *et al.* 2018). Indeed, stiffness changes showed to affect the modal frequencies of the buildings leading to a modification of their dynamic responses. These changes may be related to reversible phenomena, thus linked to temporal variations of the structural properties and of its boundary conditions (examples are the variations induced by temperature fluctuations). Conversely, in the worst situations, the dynamic response of the structure changes due to irreversible causes such as variations of the soil-structure interaction or of the material physical properties. Similarly, it has been observed that this permanent worsening can appear as a result of stiffness decrease due to earthquake damages (Clinton 2006). Given the success of the ambient noise in engineering applications, it has been then applied to infer the dynamic response of both landslides and potentially unstable rock blocks. The employment of the noise-related techniques to different geological contexts as well as to different unstable volume sizes showed that ambient noise recordings can be effectively used to investigate reversible and irreversible changes of the unstable compartment's modal response (Pierre Bottelin *et al.* 2013, P. Bottelin *et al.* 2017, Valentin *et al.* 2017). In more detail, frequency peaks and preferential directions of motion corresponding to vibration modes are sought for by considering periodograms and spectrograms, and different processing algorithms are applied in both time and frequency domains to estimate polarization in the 3D space (Diego Arosio *et al.* 2019). Since several authors have investigated column-like rock structures partially detached from the rock mass, a standard analysis consists of estimating the horizontal to the vertical spectral ratio (HVSR) and the HVSR as a function of azimuth (HVSRA). The basic principle behind the use of modal analysis as a monitoring tool is the analogy between the dynamic response of unstable compartments and the simple oscillator. If we consider the first vibrational mode ( $f_0$ , also known as resonance frequency, fundamental or natural frequency of the system) of the simple oscillator, we can define it as follow:

$$f_0 = \sqrt{\frac{k}{m}}$$

Where  $k$  and  $m$  are the spring stiffness and the mass, respectively.

It is clear that if we assume the mass does not change over time, the resonance frequency of the monitored structure changes when a variation of the stiffness occurs. Clear evidence of this phenomenon has been observed in several past studies. The latter demonstrated that spectral peaks in ambient noise recordings collected on prone-to-fall compartments are associated with their resonance frequencies (Lévy *et al.* 2010, Burjánek *et al.* 2012, Pierre Bottelin

*et al.* 2013). This discovery is supported by the fact that spectral peaks do not appear when considering seismic signals recorded on stable mass. Moreover, researchers observed that when a block decouples from the rock mass, thus when the rock bridges undergo a rupture, the resonance frequencies drop down to lower values. In his doctoral thesis, Bottelin (2014) analysed four unstable rock compartments by means of seismic ambient noise recordings (Bottelin *et al.* 2014). The prone-to-fall blocks were characterized by diverse geological properties (limestone, argillite, and shale-sandstone) and involved volumes, and by different failure mechanisms. Nevertheless, the spectral analysis performed on all the unstable rocks' dataset revealed clear spectrum energy peaks that were interpreted as the resonance frequency of the unstable compartments. Unfortunately, within this study, it has not been possible to observe fundamental frequency changes resulting from damage processes of the rock bridges. On the contrary, this phenomenon was clearly observed in the France Alps, where seismic ambient noise was recorded for six months on the Chamousset unstable column (in the Vercors massif) (Lévy *et al.*, 2010). In this contest, two weeks before the column collapse, the first resonance frequency clearly moved from 3.4 Hz to 2.6 Hz highlighting the strong relationship between vibrational modes and the rupture of rock bridges. All these literature results demonstrated that damaging processes occurring on natural structures lead to changes in resonance frequencies of the monitored unstable rock blocks. However, other studies performed on buildings as well as on unstable slope revealed that vibrational modes of structures may also exhibit reversible variations that are controlled by weather conditions (e.g. temperature, freeze-thaw cycle). In 2010, Xia *et al* performed a laboratory test on a reinforced concrete slab that showed a 3% variation of its fundamental frequency as a consequence of 20°C temperature variation (Xia *et al.* (2010)). In real conditions, Nayery *et al.* (2008) observed a 1 % variation of the fundamental mode due to natural temperature fluctuations. Whereas, in the study performed on the Chamousset rock column, Lévy *et al* (2010) measured 20°C temperature variation that generates a reversible change of about 5% in the first resonance frequency. Additionally, he observed that the ice formation within the crack leads to a temporarily increase of contact stiffness between the stable and unstable compartments, hence, to raise the first vibrational mode (Lévy *et al.* 2010). Even the prone-to-fall compartments analysed by Bottelin (2013) showed reversible changes of the identified spectral peaks, but he additionally noticed that the variations were site-dependent. Indeed, over a six-month monitoring period, he observed a frequency change of 0.5% at La Praz site, and of 9% at Les Arches. Moreover, the reversible fluctuations of the resonance frequencies did occur both at long (weeks) and short-time period (daily cycles). This leads to the conclusion that the reversible variations in modal vibrations are mainly linked to the thermal effects. The effect of temperature on the dynamic properties of investigated structures was linked to the thermal expansion of rock that result in a closure of the rear fracture. Even though the latter hypothesis worked for almost all case studies showed in the literature, for the La Praz site, the resonance frequency variation was found to be anti-correlated and out-of-phase with respect to air temperature. This particular case seems to be related to the absence of a deep open fracture making the unstable compartment less sensitive to temperature fluctuations. The presented literature makes clear that resonance frequencies variations induced by reversible thermal effects can be confused with the structural ones, hence link to the stability of the investigated structure. The discrimination between reversible and irreversible variation is therefore necessary in the perspective of building monitoring systems. Nevertheless, even though several attempts to tackle this problem have been proposed in civil engineering applications, there is not a validated method that guarantee the discrimination between the two effects (Yuean and Kuok 2010; Lin *et al.* 2011). While analysing the ambient seismic recordings, many authors observed that spectral peaks own specific directionalities (Burjánek *et al.* 2012, Pierre Bottelin *et al.* 2013, Vincenzo Del Gaudio *et al.* 2014). In detail, rock slopes with simple fracture settings shows that the fundamental frequency is often polarized perpendicularly to the main open fracture that separate the unstable part from the stable rock mass. In the Alpine context, Burjánek *et al.* (2010) and Moore *et al.* 2011 recorded ambient seismic noise on an unstable rock slope above the village of Randa in the southern Swiss Alps. Polarization analysis revealed vibration occurring at 5 Hz was oriented parallel to the slope, hence in agreement with the displacement directions measured by means of geodetic tools. Another survey was performed 6 Km far from Randa on the Walkersmaat unstable slope. In this case the fundamental frequency retrieved from the ambient noise recording exhibited a peak at 1.6 Hz that was oriented perpendicular to surface cracks (Burjánek *et al.*, 2012). While considering more complex situations (e.g. soft rocks or loose sediments on a stable bedrock), the directionality is influenced by both topographic and geological factors that contribute to polarize a large amount of energy towards specific azimuths, mainly centred on directions related to local topography. The polarization features of seismic recordings collected on landslides have been inferred in several

studies. In south Italy, seismic measurements were performed on three different landslides. The analysed dataset showed a polarization of the recordings along the direction of the slope movements (Gallipoli and Mucciarelli, 2007). Del Gaudio and Wasowski (2007) and Del Gaudio et al. (2008, 2013, 2014) explored a seismically active area of the Apennine chain (central Italy) by analysing energy content of low/moderate magnitude earthquakes recorded within weakly-cemented sedimentary rocks which underwent slope failure in the past (Gaudio & Wasowski 2007, V. Del Gaudio *et al.* 2008, Vincenzo Del Gaudio & Wasowski 2011, Vincenzo Del Gaudio *et al.* 2014). For some sites, the shaking maxima resulted to be oriented in according to the locally topographic features (i.e. maximum slope or steep scarp rim). However, a more detailed analysis revealed that these phenomena are caused not only by topographic effect, but also by the anisotropies of the slope material properties. This led to the conclusion that the polarization of seismic wavefield is governed by either topographic, geological and structural factors. In order to provide a more complete modal analysis of the investigated structures, 3D numerical modelling may represent a valuable approach for the validation and interpretation of ambient noise spectral analysis. Several applications in civil field evinced the success of this methodology (Yuen & Kuok 2010). However, its extension for unstable compartments is more difficult due to their complexity both in term of geometry and mechanical properties estimate. In this perspective only few modelling attempts are reported in the literature. In 2010, Lévy et al. performed a 3d modelling of the Chamousset rock column by deriving its geometrical features by means of LIDAR survey. He set up clamped boundary conditions where fresh rock ruptures surfaces were observed after the collapse. The result of the modal analysis was in agreement with the first three resonance frequencies extracted from the ambient seismic noise analysis. The advantage of the modelling is that it showed the modal shape associated with each of the retrieved vibrational modes. In particular, the fundamental frequency was found to be associated to the flexion of the column which result in a displacement of the structure itself perpendicular to the rear fracture. Whereas the second and third modal shapes were linked to the torsion and flexion of the unstable compartment, respectively. Three years later, a similar study was presented by Bottelin et al. (2013) who investigated the resonance properties of Les Arched rock column. The obtained results are similar to the Lévy's ones. Indeed, Bottelin has been able to reconstruct the first three vibrational modes as well showing that the fundamental frequency was associated to the bending of the prone-to-fall column. The latter vibrational mode was again associated to a bending perpendicular to the rear fracture. A more complex numerical modelling was provided by Moore et al. in 2016. The authors performed a three-dimensional numerical modal analysis of the Rainbow Bridge (Utah). In spite of the structure complexity, the numerical analysis of the photogrammetric model of the bridge succeeded in reproducing the vibrational characteristics retrieved from the ambient noise recordings (Jeffrey R. Moore *et al.* 2016). Within this section of the thesis, we focus our attention on the use of ambient seismic noise for monitoring prone-to-fall rock compartments. Due to the lack of monitored collapsed structures in the literature, we firstly perform a controlled collapse test on a small limestone block that was progressively detached from the stable cliff by mechanically widening a fracture in four steps, until it collapsed. This experiment aims to validate the hypothesis according to which the collapse of a structure is preceded by a drastic decrease of its resonance frequencies. Thus, the test is extremely useful to check the effectiveness of the ambient seismic noise spectral analysis for monitoring prone-to-fall compartments. In addition to this main goal, we further want to implement different techniques of spectral and polarization analysis to infer which of the available ones provide the most accurate and reliable results. In this perspective, we also collected ambient seismic noise recordings on bigger prone-to-fall compartments to guarantee the feasibility of the tested methodologies also for the application on rock columns that are nowadays monitored due to their unstable conditions. The chapter is subdivided into four subsections that respectively treats the following case studies: small rock block collapse test, Torrioni di Rialba, Pietra di Bismantova and the Malta cliff.

## 2. Small rock block collapse test

In this paragraph, we analyse seismic noise data collected during a field test in which a rock block was forced to collapse. Though relatively small, the investigated block has an irregular geometry defined by one rear and one side fracture and it is different from the column-like geometry of rock structures usually investigated in the scientific literature. We consider both spectral and polarization analyses, the support of numerical modelling, with the final

aim of identifying particular features of the collected seismic noise that might be used for rock failure forecasting purposes.

## 2.1. Field test

The controlled collapse test was performed in January 2018 on an unstable rock block located in the lower section of a 200 m-high cliff diving into Como Lake, in the Italian Prealps (Fig. 1a). The slope consists entirely of Perledo-Varennia limestone having sub-horizontal bedding ( $S_0$ , 8/16) with thickness ranging from 0.1 to 1 m. In addition, the geological and photogrammetric surveys identified two main joint families approximately perpendicular to each other, namely K1 (245/85) and K2 (155/86), that may promote both plane and wedge failures. The unstable rock compartment selected for the experiment had an approximately trapezoidal prism shape of  $0.7 \times 0.7 \times 0.3$  m LxHxW, resulting in a total volume of about 0.15 m<sup>3</sup> (Fig. 1b). From a structural point of view, the rock block was partially detached from the rock mass by two main fractures, namely F1 and F2 belonging to K1 and K2 joint sets respectively, and it was delimited at the top and at the bottom by the bedding discontinuities (Fig. 1b). Actually, the block was divided into two parts, with a top bigger one laying onto a smaller one (Fig. 1b), that fell together when the ultimate collapse occurred at the end of the test and split apart after the impact onto the ground (Fig. 1d). To record ambient noise, we installed a Nanometrics Trillium Compact 20s seismometer on top of the unstable block with the Z and Y components oriented along the vertical and the North-South directions, respectively (Fig. 1b).

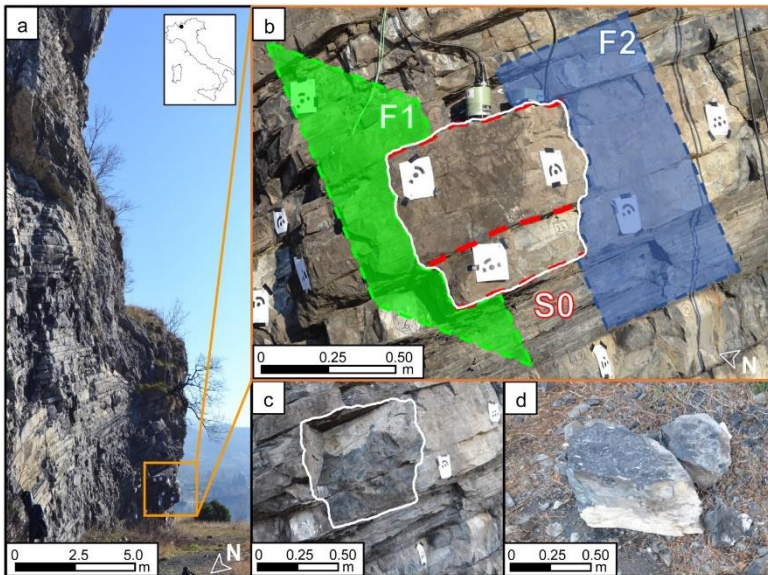


*Figure 1 Pictures taken at the site where the test was performed. a) Rock cliff. b) The rock block that was forced to collapse (white contour) with the two main fractures F1 and F2 together with the bedding  $S_0$  (targets for the photogrammetric survey are also visible); Nanometrics Trillium Compact sensor is placed on top of the block. c) Pictures of the rock surface after the failure and d) of the collapsed blocks.*

The sensor was coupled to a Nanometrics Centaur data logger and we set a sampling frequency of 1000 Hz. The sampling frequency has been defined by performing eigenfrequency analysis tests with COMSOL Multiphysics software on cubic-shaped blocks modelled with the same volume and geo-mechanical properties of the studied rock block. We performed the modal analysis testing different areas for the rock bridges to have an insight of the resonant frequencies of the real case study and found out that a sampling frequency of 1000 Hz was sufficient to record roughly the first six vibration modes of the unstable rock block. Though generally recommended, we could not deploy any reference station on the rock mass to effectively isolate the response of the monitored rock block mainly because of the impossibility to safely reach the top of the 200m-high cliff and to find a position on the cliff face whose vibrations could be confidently interpreted as representative of the whole rock mass behaviour. During the test, fracture F2 was mechanically widened with an iron lever approximately every thirty minutes and four stages were performed before ultimate collapse. Fracture F2 was chosen because of its higher initial persistence and aperture with respect to F1. Ambient vibrations have been continuously recorded and, at the beginning of each stage, sensor levelling was checked and fixed whenever necessary to be sure noise was constantly collected along the same directions, and the fracture aperture was measured in four distinct control points along F2 using a digital calliper (Fig. 2). Collected ambient vibrations have been divided into five sub-signals according to the different stages of the test, with stages 0 and 4 corresponding to the initial undisturbed condition and to the condition immediately before ultimate failure, respectively. Before performing spectral and polarization analyses, the time series recorded during each stage has been time-cut to discard the first 10 minutes in order to remove

transients caused by fracture widening and to take into account sensor stabilization after re-leveelling. Subsequently, time series have been deconvolved to remove the instrument response (Templeton 2017) and filtered with a zero-phase 0.5 Hz high-pass filter to attenuate low-frequency components greatly amplified by the deconvolution process.

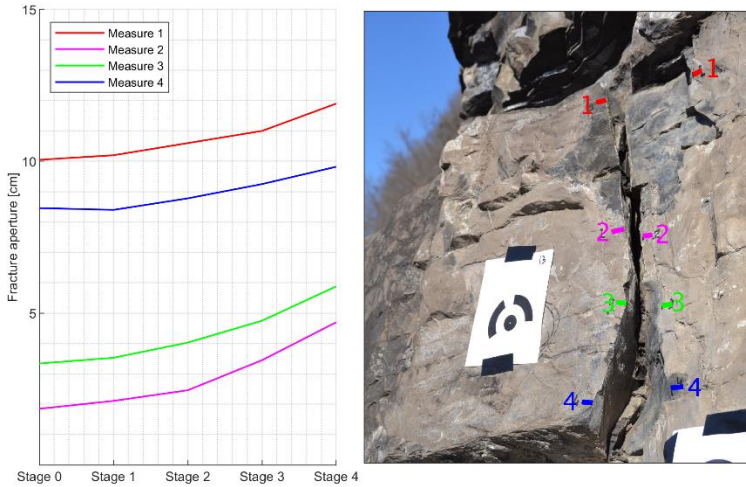


Figure 2 Control points used to monitor the aperture of fracture F2 during the collapse test. Fracture aperture was measured with a digital calliper.

In order to study variations of rock block vibration in response to climatic parameters, we took into account data collected by meteorological stations located close to the lake shore approximately 4 and 5.5 km south of the test site (Fig. 3).

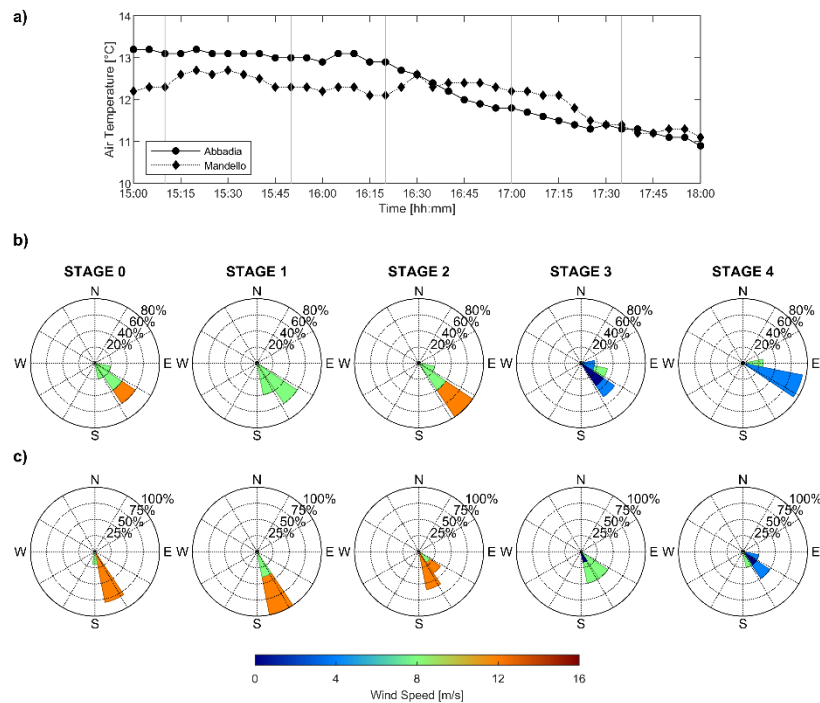


Figure 3 Meteorological data collected by the climatic stations installed close to the Como Lake in Abbadia Lariana and in Mandello del Lario, roughly 5.5 km and 4 km south of the test site, respectively. a) Air temperature (vertical grey lines mark the beginning of each stage of the test). Polar plot of wind speed measured in b) Abbadia Lariana and in c) Mandello del Lario.

## 2.2. Methods

### 2.2.1. Spectral analysis

We studied the spectral content of the collected seismic noise by estimating the power spectral density (PSD) by means of two non-parametric spectral estimation methods, namely the modified periodogram according to Welch's overlapped segment averaging (WOSA; Welch 1967), and the multitaper method (MT) first proposed by Thomson (1982). In addition, we computed the spectrogram using the short-time Fourier transform (5 s signal sub-windows, Hamming taper, 50 per cent overlap) and the HVSR. Except for the multitaper estimate, time series have been divided into 5 s signal segments, tapered with a Hamming window and with 50 per cent overlapping. As a result, we obtain the lowest resolvable frequency of roughly 2 Hz (McNamara & Buland 2004), which is considerably lower than the expected resonance frequencies of the tested block, a satisfactory spectral resolution of 0.2 Hz computed as the reciprocal of the time window, as well as enough time windows for statistical robustness of the results. Conversely to what is commonly done in seismic site resonance analysis (e.g., Konno & Ohmachi 1998), we did not apply any additional spectral smoothing so as to avoid any merging of close spectral peaks possibly related to different vibration modes of the studied structure (Arosio et al. 2019a). For the MT method, we set a frequency resolution  $W$  of 1 Hz and a number of tapers equal to  $2TW-1$  (Percival & Walden 1993), where  $T$  is the signal duration in seconds, i.e. the duration of each stage in our case. Both the WOSA and the MT methods are spectral estimator aimed to reduce bias and variability of the PSD estimate. Bias is reduced thanks to the use of tapers that, in the case of WOSA are simple windowing functions (e.g., Hamming, Gaussian, etc.), whereas in the case of MT are a set of mutually orthogonal functions that are chosen to have optimal time-frequency concentration properties. Variability is reduced by averaging over approximately uncorrelated PSD estimates, that are obtained through segmenting in the time domain in the WOSA, and through orthogonal tapers in the MT (Percival & Walden 1993).

### 2.2.2. Polarization analysis

We performed a polarization analysis to study preferential oscillation directions associated to the eigenmodes of the rock block during the different stages of the collapse test. We took into account the principal component analysis (PCA) of the time-domain covariance matrix (Flinn 1965), the HVSRA (Bottelin et al. 2013a), as well as the singular value decomposition (SVD) of the Hermitian spectral density matrix (Samson 1983). Considering the general case of elliptical particle motion in the 3D space, the spectral SVD approach can provide the most complete set of polarization features overcoming the drawbacks of the two other methodologies (Arosio et al. 2019b). As a matter of fact, spectral SVD allows to perform the analysis as a function of frequency, in the 3D space and to estimate the phase lags between the components of the polarization vector. To quantify polarization, we compute the degree of polarization parameter  $\beta_2$  from the matrix of the singular values (Samson 1983).  $\beta_2$  can range from 0 to 1, the former corresponding to unpolarized signals and the latter indicating a well-defined polarization; high values of  $\beta_2$  do not necessarily imply linear polarization, as circular or elliptical particle motion can provide high values as well. In addition, we estimate frequency-dependent angular quantities by projecting along the three axes the complex right eigenvector associated to the dominant (if any) singular value (Park et al. 1987). In more detail,  $\Theta H$  is the azimuth of the main polarization axis measured counter clockwise from East,  $\Theta V$  is its dip measured from the horizontal, while  $\phi_{HH}$  and  $\phi_{VH}$  indicate the phase relationships between the two orthogonal horizontal components and between the vertical and the principal horizontal components, respectively.

## 2.3. Numerical modelling

We performed an eigenmode analysis of the studied rock block with the finite element software COMSOL Multiphysics to support the interpretation of the results obtained with the spectral and polarization analyses. Our aim was to investigate the relationship between the observed fundamental frequency drop and the rock-bridges breakage, and to simulate the block eigenmodes to confirm the polarization of seismic noise detected during the experimental test.

The unstable block has been modelled as an undamped system with multiple degrees of freedom. The 3D geometry was built by meshing the point cloud obtained through the photogrammetric survey with tetrahedral finite elements. However, the back and side of the block were approximated with plane surfaces. The rock block has been considered as an isotropic, homogeneous medium with density 2680 Kg/m<sup>3</sup>, Poisson ratio 0.3 and Young's modulus 30E9 N/m<sup>2</sup>. The latter parameter was estimated using an empirical equation relating Young's modulus and Schmidt hammer rebound values recorded in the field (Katz et al. 2000). In addition, the estimated values were crosschecked by using an empirical chart that relates Young's modulus to both density and the point load strength index (Sonmez et al. 2006) obtained by performing the point load test according to the ISRM guidelines (Franklin

1985). We set the constraints of the block model at locations where fresh rock ruptures were thought to be observed after the collapse. In more detail, fracture F2 is characterized by an upper brighter section covered by a calcite layer, which denotes that the block was already partially detached from the cliff, and by a lower darker section that might show evidences of rock bridge breakage due to the collapse test (Fig. 1c). According to this, we tried to detect newly exposed rock areas by identifying groups of pixels with values ranging in a predetermined interval in the RGB matrix of nearly frontal images of fractures F1 and F2. Images were first smoothed with a 2D convolutional filter to limit the scattering of the identified points. The estimated rock bridges were then modelled with the same geo-mechanical properties of the rock mass. In particular, an elastic constraint has been introduced for each identified contact surface imposing an isotropic stiffness of  $3E10$  N/m<sup>3</sup>. The bedding interface between the two parts of the block (Fig. 1b) was modelled as an anisotropic elastic thin layer with normal ( $k_n$ ) and shear ( $k_s$ ) stiffness of  $3E10$  N/m<sup>3</sup> and  $9E9$  N/m<sup>3</sup>, respectively, according to the deformation properties of the rock mass and the intact rock (Kulatilake et al. 2016).

## 2.4. Results

### 2.4.1. Seismic monitoring

The obtained PSD estimates with the abovementioned approaches do not show appreciable differences for all the test stages and reveal several spectral peaks at relatively high frequency, in the range 50-300 Hz, in agreement with the small size of the specimen. Though PSD is regularly used to effectively identify and track the resonance modes of rock structures (e.g., Starr et al. 2015), we found it difficult to evaluate with confidence the frequency peaks across the following stages of the test. We did observe amplitude and shape variations in the block spectral response, but we found it difficult to follow their evolution (Fig.4).

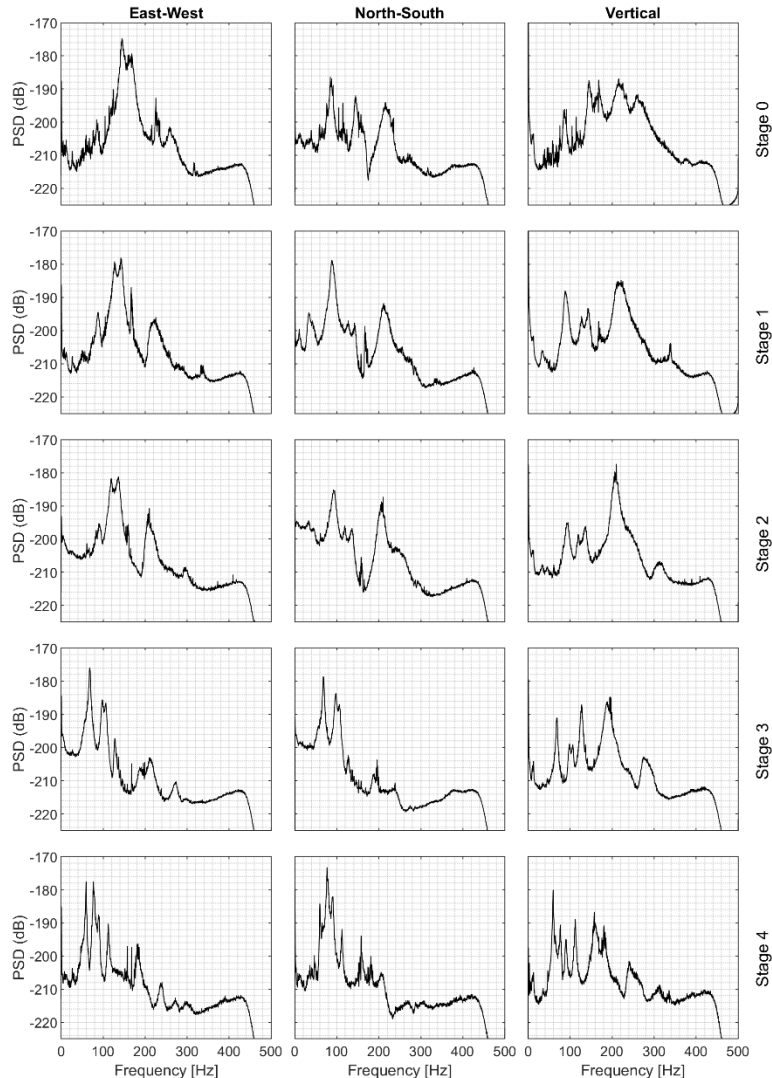


Figure 4 PSDs of the different components estimated with the Welch's periodogram method for each stage of the rock collapse test.

To ease visual interpretation of the evolution of spectral peaks across the following stages of the test, we used the short-time Fourier transform (5 s signal sub-windows, Hamming taper, 50 per cent overlap) to compute the spectrograms that are displayed together with the MT results in Fig. 5. We identified two main decreasing trends over time roughly associated with two different frequency bands. A first high-frequency peak moves from about 220 to 150 Hz and it is more easily interpreted on the vertical component. The second frequency peak is clearly observed along the East-West direction, appears to be the dominant peak (though may not be the fundamental) and shifts from around 150 Hz at the initial condition to 80 Hz prior to collapse. In more detail, the lower frequency peak actually involves several different peaks that split up and approach monochromatic signals towards failure. Finally, during the second and third stages of the test, we observe the occurrence of high-amplitude signals at frequencies below 10 Hz on the horizontal components only. Given the complex geometry of the block (i.e., non-column-like) and of the constraints, the recorded seismic noise has a large vertical component, and peaks and troughs of both horizontal and vertical spectra interfere in a complex manner.

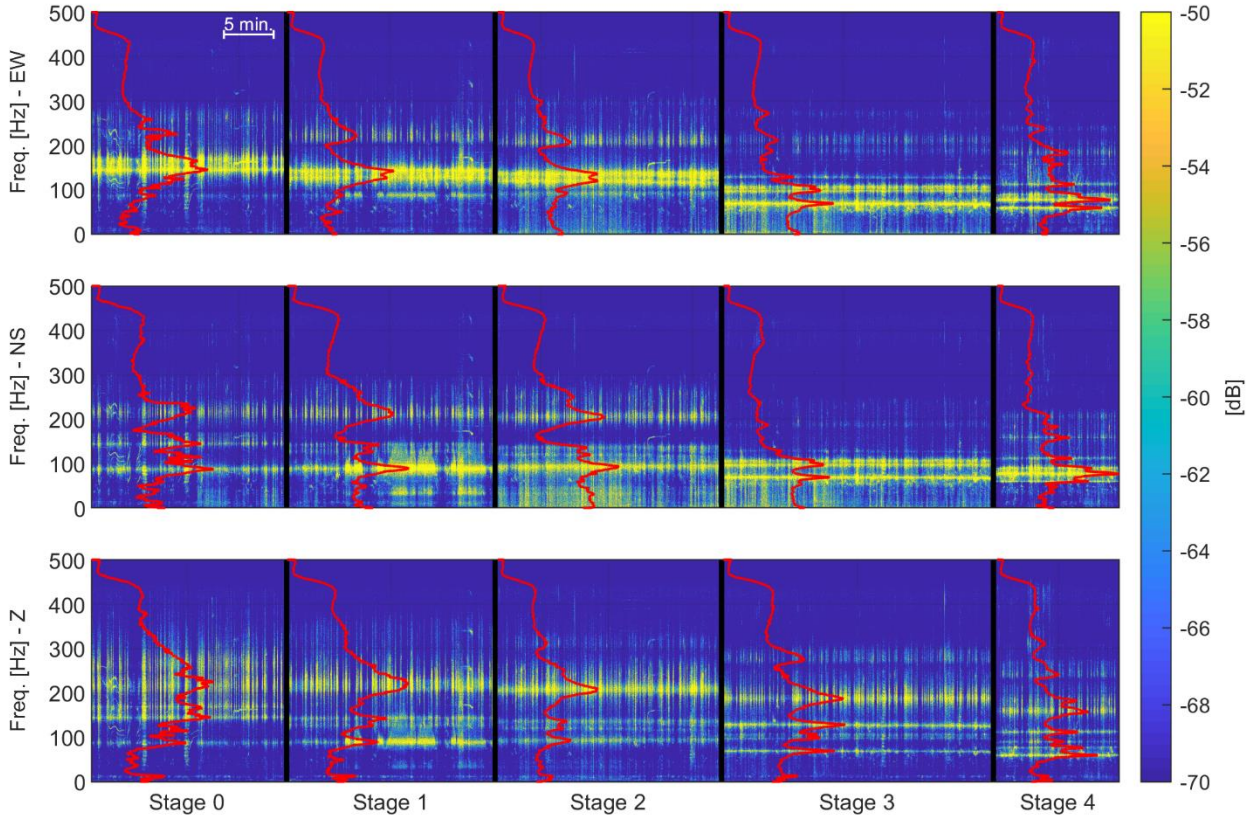


Figure 5 PSD estimates of the ambient noise recorded during the different stages of the test obtained with the multitaper method (red solid lines) over imposed to the spectrograms (colormap). Both the PSDs and the spectrograms are normalized to the absolute maximum of all the stages.

Accordingly, the HVSR technique is able to provide unambiguous evidence of the decreasing trend in the lower frequency band (Fig. 6). On the contrary, the information related to the higher vibration mode is completely lost because of spectral division. In addition, HVSR results show the occurrence of high-amplitude signals at frequencies below 10 Hz during the second and third stages of the test, as can also be inferred by comparing the spectrograms of the horizontal and vertical components related to the same stages (Fig. 5). A simple smoothing test performed on the HVSR curves caused merging of different spectral peaks (Fig. 6), so this processing step was rejected.

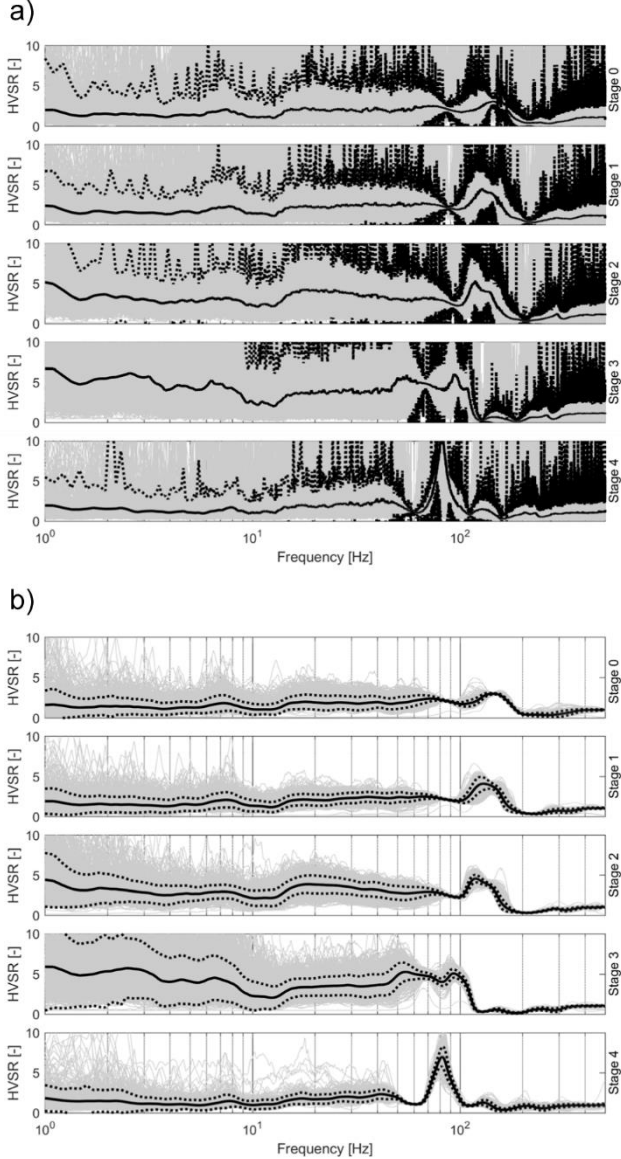


Figure 6 HVSRs computed for each stage of the rock collapse test. a) HVSRs without any smoothing; b) HVSRs with Konno and Ohmachi spectral smoothing (smoothing parameter  $b = 40$ ; Konno and Ohmachi, 1998). The 3C recordings were first lowpass filtered to discard low-frequency trends, then they were divided into 5 s time windows, applying 50% window overlapping and Hamming tapering. Nonstationary time windows were rejected and (smoothed) amplitude spectra were computed for each window. The north and east components were merged into the horizontal component and the HVSR was computed. Finally, all the HVSRs were averaged using a quadratic mean that is most sensitive to low values so as to produce robust HVSR estimates. Grey lines are HVSRs for each time window, black solid lines are mean HVSR values, and black dotted lines are mean HVSR values +/- the standard deviation.

Fig. 7, 8 and 9 illustrate the polarization parameters estimated with the spectra PCA, HVSRA and SVD approaches, respectively. Parameters were computed using 10 s Hamming-tapered time windows with 90 per cent overlap, and 20 spectral density matrixes were averaged in the frequency domain (Koper & Hawley 2010). Regarding the SVD method, results are presented in terms of relative probability, that is, for each frequency, the estimated values of the parameter are partitioned into bins and the value of each bin is the ratio of the number of elements in the bin to the total number of elements (i.e., the sum of all the bin values gives unity).  $\beta_2$  values close to 1 through the different test stages indicate that polarization is significant over several frequency bands between 50 and 300 Hz. The polarization parameters have higher probability values around 130-140 Hz during the first 3 stages, whereas higher probability values are observed around 65-75 Hz for the last two stages. In fact, the most dramatic change is from stage 2 to stage 3 and may correspond to the higher slopes of measured displacements (Fig. 2). Because of the oscillating nature of the vibration modes together with the  $0^\circ$ - $360^\circ$  admissible range,  $\Theta_H$  probability values generally cluster around two intervals that are  $180^\circ$  apart. For the first three stages and around the maximum

probability values, there is just one angular value around  $180^\circ$ , so the estimate seems to be biased towards the West. This result reveals that, actually, there is some minor displacement perpendicular to fracture F1, even at the initial stage, as supported by the non-zero values of  $\phi_{HH}$ , that progressively decreases from  $-20^\circ$  to  $-70^\circ$  until stage 2, indicating that the polarization in the azimuthal plane is elliptical. Higher probability values for  $\Theta_V$  generally cluster close to  $0^\circ$ , hence the dominant vibration mode has negligible vertical motion, although the block does exhibit at least one higher frequency mode with significant vertical displacement, as already observed in the spectrogram and as can also be noted in the PCA and HVSRA plots.  $\phi_{VH}$  probability values are lower than the values of the other parameters because the azimuthal displacement of the dominant mode and the vertical displacement of the higher mode dwarf their respective vertical and horizontal displacements. As a general trend, phase relationships between components become more complex when approaching failure.

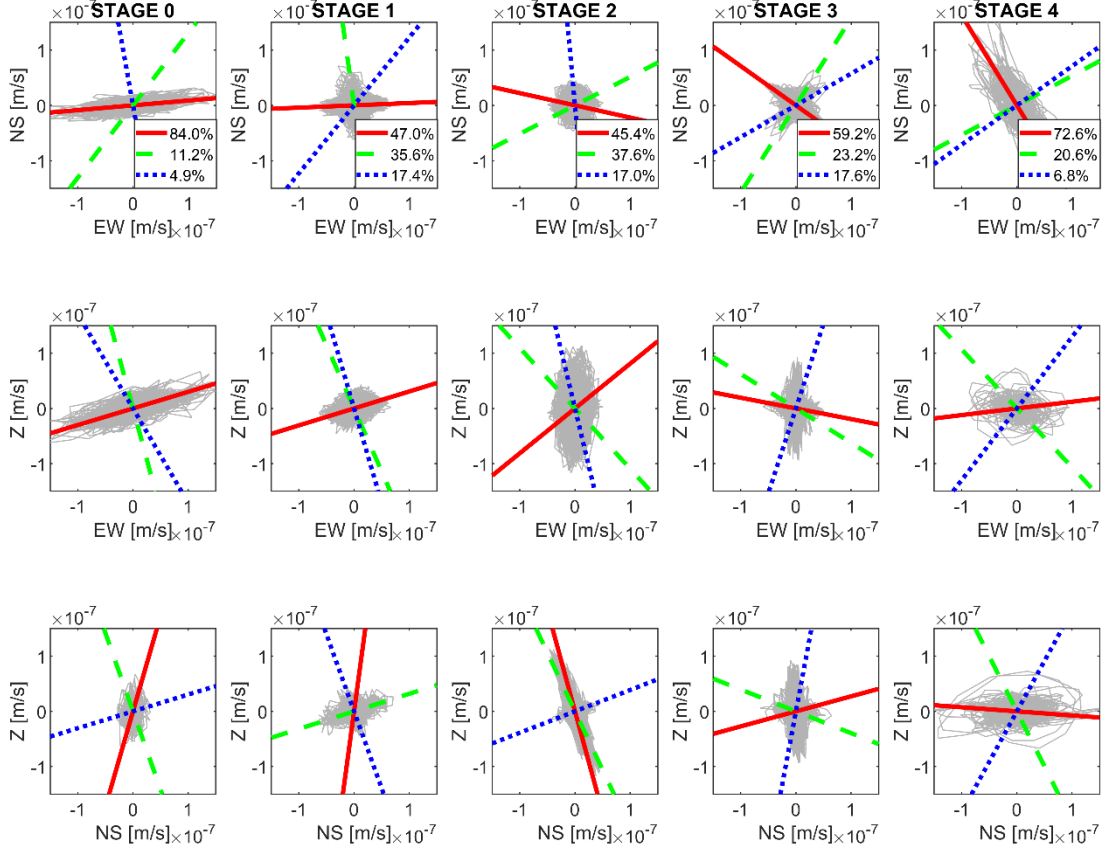


Figure 7 Polarization analysis performed with the PCA of the covariance matrix computed from the 3C seismic noise collected during the stages of the rock collapse test. Each plot shows the projection on the relative plane of both the 3C hodogram (grey line) and the 3 orthogonal eigenvectors found with the PCA. Legends indicate the percentage of hodogram variance explained by each principal component.

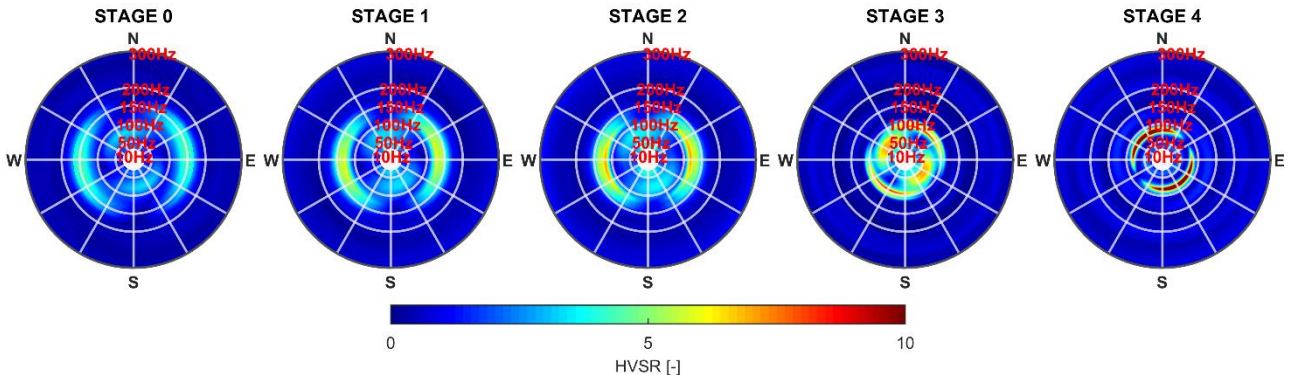


Figure 8 Polarization results obtained with the horizontal-to-vertical spectral ratio as a function of azimuth (HVSRA method) computed from the 3C seismic noise collected during the stages of the rock collapse test.

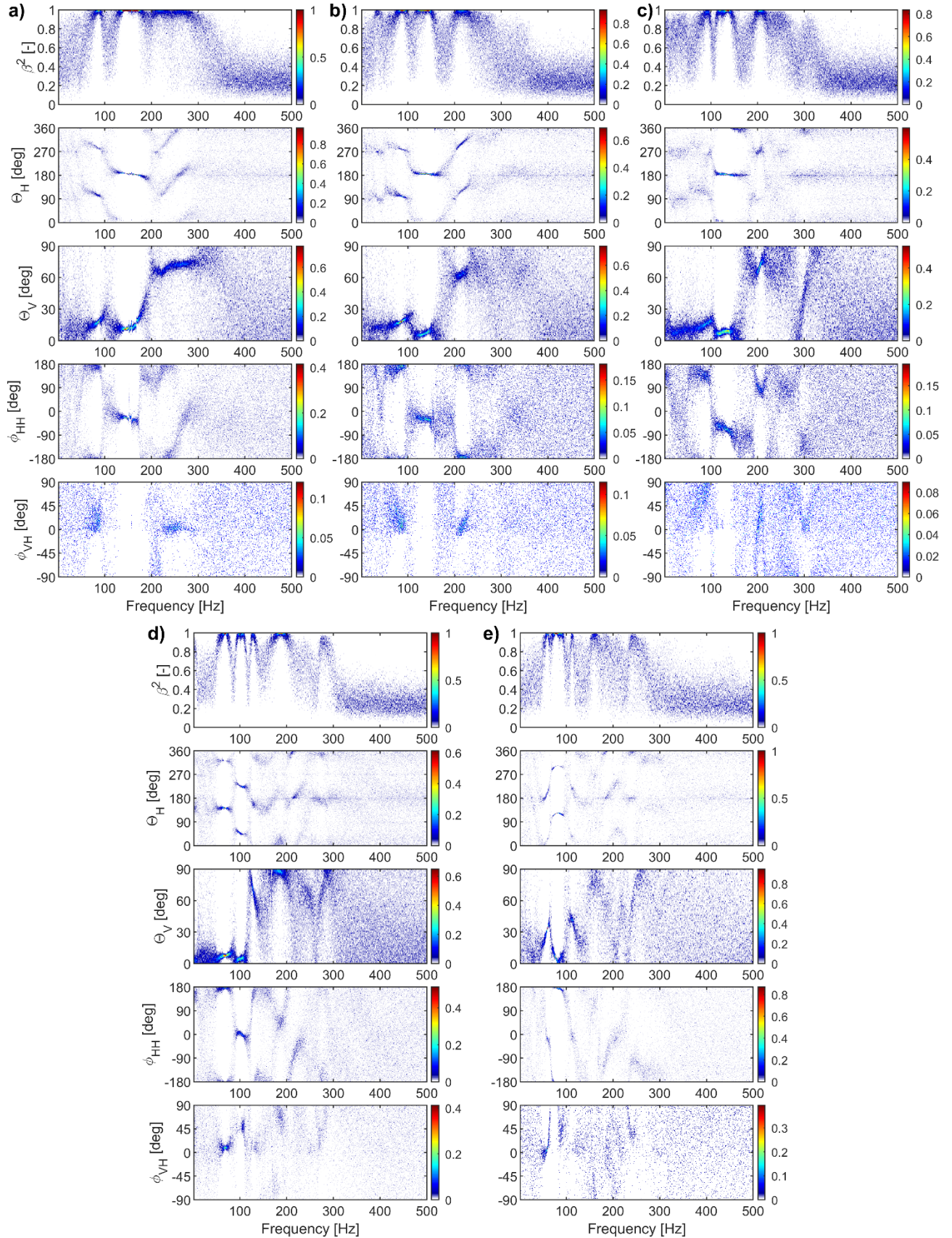


Figure 9 Polarization parameters estimated with the spectral SVD method for stages 0 (a), 1 (b), 2 (c), 3 (d) and 4 (e) of the collapse test. The colormap indicates relative probability of the estimated parameter and limits of each colormap are set to the minimum and maximum values of the related parameter. See text for details.

#### 2.4.2. Numerical modelling

The block behaviour modelled according to its estimated mechanical parameters and to the estimated, mechanical and geometrical features of the rock bridges gave results showing unsatisfactory matching with real data in terms of both resonance frequency and polarization. In fact, we obtained poor outcomes at all the stages of the test, which were modelled by assuming a gradual reduction of rock bridges caused by a progressive opening of the rear fracture F2 (Fig. 1b), starting from where the destabilizing force was applied. We did observe a gradual shift of the eigenmodes towards lower frequencies, but neither the spectral peaks nor the modal shapes matched the measured ones.

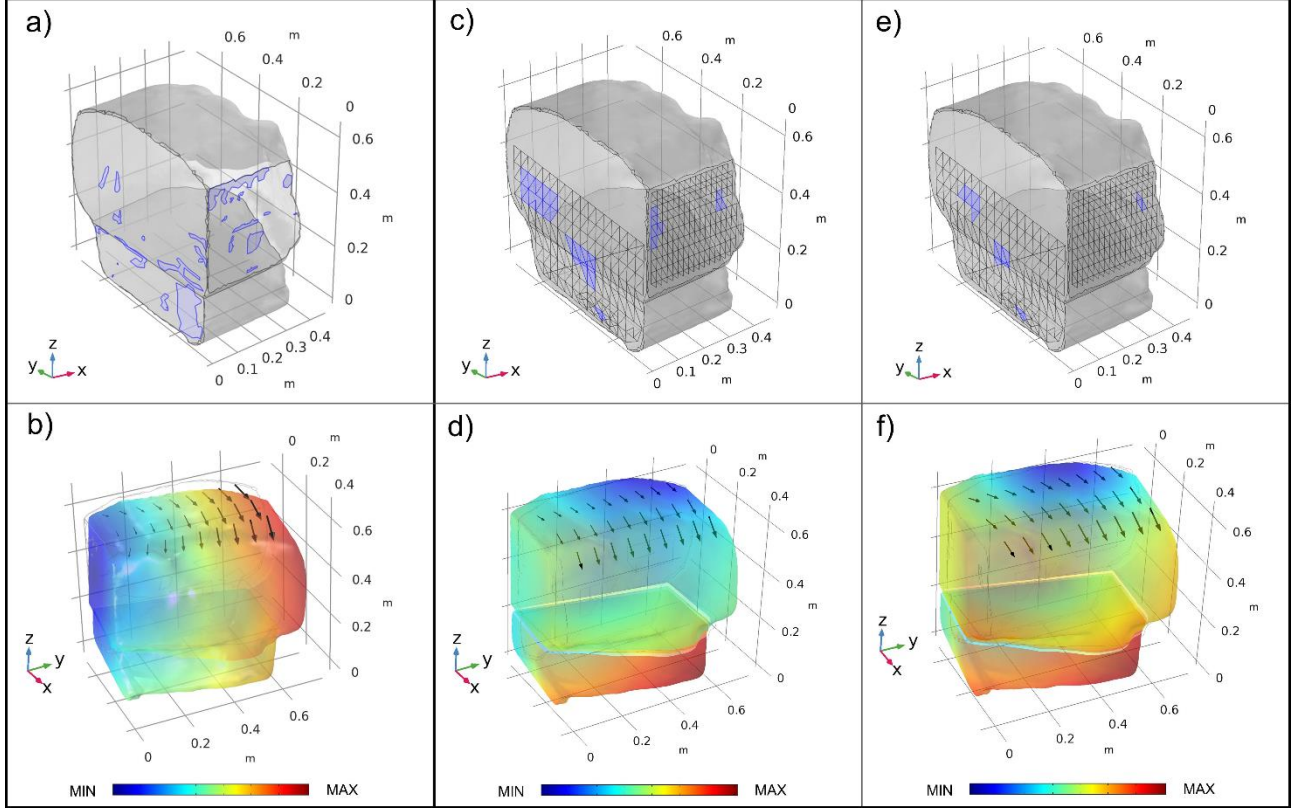


Figure 10 a) Block model with rock bridges (in purple) estimated from the RGB matrix of near frontal images of rear and side fractures and b) modelling results with colormap and arrows indicating displacements. c) Block model used in the modelling exercise having discretized rear and side fractures with rock bridges (in purple) set to match the resonance frequencies observed at stage 0. d) Modelling results for model in c). e) and f): same as c) and d) for stage 4.

Given the poor obtained results, as a modelling exercise, we discretized the side and rear surfaces of the rock block (excluding the calcite area) and ran several simulations tuning the geometrical configurations of the rock bridges and the bedding stiffness values in order to match the first five resonance frequencies observed during stages 0 and 4. Final normal and shear stiffness values for the bedding, respectively  $3\text{E}10 \text{ N/m}^3$  and  $9\text{E}9 \text{ N/m}^3$ , are in good agreement with the ones proposed by Kulatilake et al. (2016) for limestone. Figs. 4c to 4f show the best models with an average mismatch between observed and modelled resonance frequencies lower than 5 per cent (Table 1).

	Stage 0		Stage 4	
	Polarization analysis $\beta^2$ peak [Hz]	Numerical modelling eigenfrequency [Hz]	Polarization analysis $\beta^2$ peaks [Hz]	Numerical modelling eigenfrequency [Hz]
Mode 1	87.2	86.1	59.4	56.4
Mode 2	144.6	141.7	77.1	74.3
Mode 3	168.1	185.8	89.8	97.4
Mode 4	215.1	211.5	112.2	118.5
Mode 5	260.3	265.5	160.0	158.7

Table 1 Resonance frequencies obtained with the SVD analysis and with the numerical modelling exercise.

## 2.5. Discussion

In this study, we processed seismic noise recordings collected with a 3C broadband velocimeter deployed on top of a 0.15 m<sup>3</sup> limestone block that was forced to collapse through four following stages. To fully test the effectiveness of the technique, we decided to select a rock structure with arbitrary geometry, though not too complex, being separated from the rock mass by rear and side fractures and possibly having similar moments of inertia about orthogonal axes. This is different from case studies investigated in the scientific literature, which generally consider bigger isolated rock columns with a single rear fracture and thus could approximate slender beams with preferential oscillation in the azimuthal plane perpendicular to the rear fracture plane (Bottelin et al. 2013a; Valentin et al. 2017).

The spectral analysis we performed confirms that there is a decreasing trend of resonance frequencies towards failure (Levy et al. 2010). It is clear that vibration modes varied dynamically across the test, according to changes that occurred to the constraints between the block and the rock mass. Some frequency peaks are only visible on a single component (Fig. 5), suggesting the polarization of the associated modes. The presence of several closely-spaced and transient frequency peaks prevents a quantitative estimate of the decrease through the stages, but considering the two main vibration modes in the spectrogram having central frequencies around 220 and 150 Hz at the initial condition (Fig. 5), we can observe a decrease roughly as large as 50 per cent before ultimate failure. The spectral plots also show that the low frequency dominant mode has negligible energy along the NS component until the end of stage 2, while at stages 3 and, in particular, 4, most of the seismic energy is equally recorded by the EW and NS components. This is consistent with our expectations, because we assumed oscillation of the block mainly in the azimuthal plane and perpendicular to fracture F2 in the beginning and, as the aperture of F2 is increased and possibly affects the persistence of F1, perpendicular to both side and rear fractures towards the final stage (Fig. 1b). On the other hand, the high frequency mode is always larger on the vertical component and has its maximum at stage 2, where its energy is comparable with the one of the low frequency mode, before decreasing towards failure. Differently from other authors (e.g., Valentin et al. 2017), no significant amplifications in amplitude spectra were observed when approaching failure. In addition, causes of low frequency signals observed during stages 2 and 3, mainly on the NS component (Fig. 5), remain unclear.

Polarization features qualitatively observed in the spectrograms are confirmed by the results obtained with the spectral SVD approach. Two general aspects can be noted by observing the plots of the polarization parameters as a function of frequency and through the following stages (Fig. 9). First, a global trend towards lower frequency can be observed, although it is very difficult to track the temporal evolution of different vibration modes because each mode presents changing energy depending upon the boundary conditions of the rock block. Second, there are broader polarization frequency bands in the beginning, that become narrower when approaching failure. We believe that the first aspect could be due to the increased size and mass of the vibrating rock block caused by the reduction of rock bridges between the rock mass and the block itself. As far as probability of the estimated parameters is concerned, we observed relatively high values at the initial stage, then a decrease across stages 1 and 2, and, finally, an increase to highest values at stage 4. This nonlinear trend of the probability values may indicate the different emergence of the vibration modes that the block experiences through the stages. The different delineation of the vibration modes is confirmed by observing the amplitude peaks in the HVSRA polar plots and

by noting the percentages of the total variance explained by each principal component in the PCA plots (Figs. 7 and 8). The analysis of data collected by two meteorological stations in Mandello del Lario and Abbadia Lariana shows that air temperature and wind speed experienced minor variations during the test (Fig. 3), surely not sufficient to cause the observed spectral and polarization changes (Levy et al. 2010; Starr et al. 2015; Bottelin et al. 2017; Colombero et al. 2017).

Although the limited size of the investigated structure allowed for high resolution 3D modelling, the obtained results were unsatisfactory in terms of matching with observed data. We believe that the most critical point is to model correctly the spatial and mechanical features of the constraints. In addition, the fact that the collapse test involved two blocks separated by the bedding discontinuity may have increased uncertainty in the modelling procedure. As a consequence, we cannot infer any relationship between variations of resonance frequency versus changes in the area of rock bridges. Given the poor obtained results, as a modelling exercise, we discretized the side and rear surfaces of the rock block (excluding the calcite area) and ran several simulations with different geometrical configurations of the rock bridges in order to match the resonance frequencies observed during stages 0 and 4. Fig. 10 shows the best models with an average mismatch between observed and modelled resonance frequencies lower than 5 per cent. The obtained results indicate that the frequency drop between the first and the last stage could be obtained by reducing the rock bridge area from 7.5 per cent to 2.7 per cent of the total side and rear fracture areas. This finding is in agreement with post-failure observations of fresh rupture areas performed on limestone cliffs in south-east France (Frayssines & Hantz 2006). Unfortunately, modelling was not able to reproduce modal shapes of the block in stages 0 and 4, as we observed differences nearly as large as 90° between the modelled vibration directions in the azimuthal plane and the values of  $\Theta H$  estimated with the spectral SVD method.

## 2.6. Conclusions

Failures of rock structures are sudden phenomena that pose serious threats to human settlements and infrastructures because of their difficulty to be predicted. The deployment of a microseismic monitoring network across the investigated area can provide a predictive capability based on changes of the collected waveforms, generated where the slope is mechanically unstable (Spillmann et al. 2007). However, several factors could reduce the performance of the sensors in detecting microseismic signals and, as a result, the effectiveness of the network as an early warning tool. Seismic noise monitoring needs no specific events to be generated since it is based on continuous recording of ambient vibrations that excite the studied rock structure and, therefore, could overcome the drawbacks of classical microseismic monitoring.

The controlled collapse test we performed confirms previous findings according to which the collapse of an unstable rock is preceded by the drop of resonance frequencies as a consequence of the breakage of rock bridges. We deem that spectrograms obtained from seismic noise recordings provided evidence of the frequency decreasing trend in a way clearer than the PSD estimates do. Nevertheless, we noticed that the vibration modes of the studied structure varied dynamically through the test, with some spectral peaks emerging and vanishing according to the evolving constraints of the rock block. The abrupt changes in the block vibration modes may have prevented the observation of spectral amplification phenomena. Spectral analysis of rock structures by means of HVSR should be considered carefully because spectral division between the horizontal and vertical components may delete some frequency peaks associated to vibration modes whose vertical component dwarfs the horizontal ones. This is particularly true for rocks with arbitrary geometry and uncertain boundary conditions that, for instance, cannot be considered as a simple cantilever beam. Non-parametric spectral estimation techniques, such as WOSA and MT, could be used to generate spectrograms with reduced bias and variability. Polarization analysis performed by means of the spectral SVD approach proved to be very useful in tracking over time the frequency bands of polarized oscillations together with their angular parameters in the 3D space. Again, we were able to observe a shift towards lower frequencies before ultimate failure, as well as the narrowing of the polarized bands.

Generally, spectral smoothing should be applied carefully and different smoothing filters and their parameters should be tested because they may merge peaks associated to different vibration modes. Also, choice between linear and logarithmic sampling of the frequency axis should be tuned according to the bands of interest of the considered case study.

Over all, the results of our collapse test indicate that both spectral and polarization analyses could be useful monitoring tools to track the behaviour of unstable rock compartments with arbitrary geometry over time. In fact, the spectral SVD approach alone could provide comprehensive knowledge needed for forecasting purposes. A sound monitoring approach should take into account diverse pieces of information, such as the shift, emerging and vanishing of resonance frequencies, the bandwidth of vibration modes and the changes in their polarization. Surely, the boundary conditions of the block we forced to collapse have undergone dramatic changes in a very

short period of time. This can make interpretation of the evolution of the polarization trend with frequency very complex. We believe that, in real case studies, the evolution of the dynamic conditions of a rock are not as fast, and this may allow a better tracking of the vibration modes over time. On the other hand, sudden variations of the monitored parameters may provide useful indications for early warning systems. Given the short duration of our test, we could not investigate the influence of meteorological factors on the vibration modes of the rock block. Dealing with long-term monitoring systems, one should not forget that the dynamic characteristics of the investigated structures may vary for instance as a consequence of freeze-thaw cycles or because of rock dilation/contraction linked to temperature fluctuations (e.g., Levy et al. 2010). Since predictive capability depends on the ability to observe subtle changes over time, the accuracy and reliability of the estimated spectral and polarization features are of fundamental importance. According to this, development of uncertainty analysis of the estimated parameters is encouraged.

Our work shows that realistic numerical modelling of the dynamic behaviour of rock structures is still a challenging task, even when considering small specimen, especially in terms of the accurate definition of the spatial and mechanical features of the constraints. Therefore, the support of modelling to guide processing and interpretation of seismic noise data still needs to be improved. However, non-destructive electromagnetic techniques, both radar and infrared, could be employed to characterize rock fractures and rock bridges in a non-destructive manner (Arosio 2016; Guerin et al. 2019).

Improvements concerning seismic noise studies on unstable rock structures could be borrowed to monitor: i) drops in natural frequency of buildings as a result of stiffness decrease due to earthquake damages (Clinton et al. 2006); ii) the effectiveness of rock bolting works (Bottelin et al. 2017); iii) preferential polarization on sliding rock slopes and its relationship with measured displacements (Burjánek et al. 2012).

### 3. Torrioni di Rialba

Given the promising results of the controlled collapse test in using ambient seismic noise for monitoring rockfall, we then moved our attention to unstable rock blocks that are nowadays considered natural hazards for citizens. Therefore, this thesis' section aims to check whether the previously applied techniques are valuable and reliable in the perspective of building monitoring systems for real applications. In this regard, in the next paragraphs, we present the results obtained from Torrioni di Rialba's measurement campaign.

#### 3.1. Case study

The Rialba's towers are four rock towers located 5 km northeast of Lecco city, Northern Italy (Figure 1). This high rock cliff has sub-vertical walls up to 100 m high and it is interrupted by evident fractures that suggest the probability of future collapse occurrence. The stability of these rock pillars represents a serious threat to the surrounding areas, as the possible collapse of the towers would crash into a corridor full of infrastructures. Indeed, the Rialba's towers are located approximately 200m upslope to national road and railway, gas pipeline and electric power lines that run parallel to each other and connect the northern part of the region to the Po Plain. Besides, a small ENEL hydroelectric power plant is located on the lakeshore and collects water from a pipe running downslope on the east side of the towers. Due to this high-risk environment, monitoring activities have been carried out in 2004 and 2005 using 16 extensometers deployed among the main fractures separating the towers from each other. Moreover, 7 prism reflectors have been bolted on the south face of the southernmost tower to survey the stability using the total station. Over the monitoring period, no significant displacements were detected and, due to the lack of financial support, the surveying has been stopped. Nevertheless, in the last decade numerous small rock collapses ( $< 0.5 \text{ m}^3$ ) have been observed (Arosio *et al.* 2019a) and, considering the geological and geomorphological settings of the site, a brittle failure of one or more of the rock pillars could occur with no premonitory signals. A potential catastrophe of the slope failure is that the compartments would fall into Como lake with a consequence generation of a tsunami which would propagate reaching the neighbouring towns. In this perspective, there is some evidence that proves that the hypothesis of a collapse is not so remote. Indeed, scuba divers retrieved enormous blocks inside the Lake, which are constituted of the same material of the Torrioni, suggesting that a massive collapse of one tower occurred in the past.

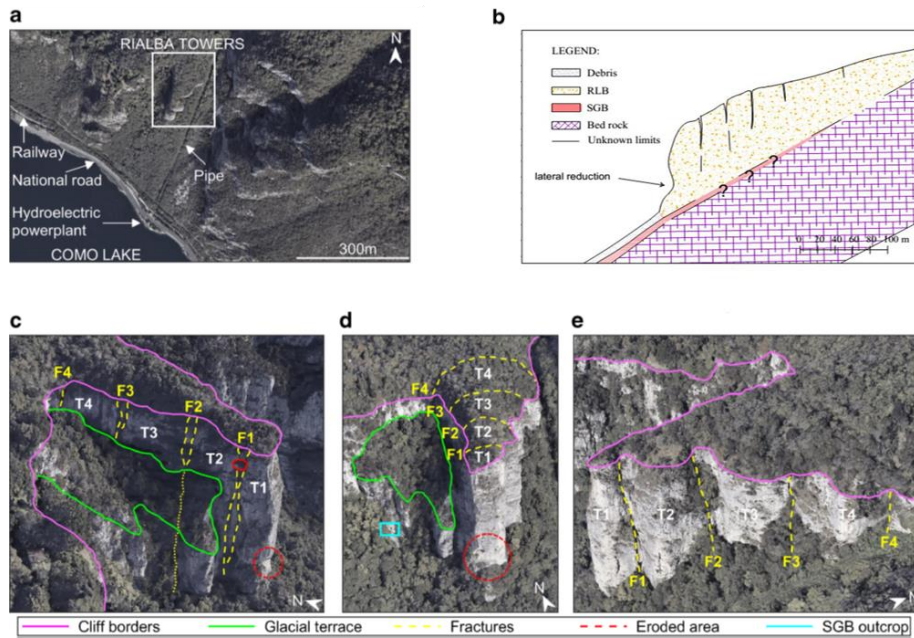


Figure 1 a) View of the Rialba Towers area. b) Geological section with a lateral view: RLB Rialba conglomerate, SGB San Giovanni Bianco shale. c,d,e) Northwest, south, and southeast view of the Rialba Towers, respectively. Figure c also highlights the presence of a rock block with an estimated volume of about  $150 \text{ m}^3$ , stuck in the upper section of the fracture (red circle).

In this regard, we collected ambient seismic noise to investigate the vibration modes of the towers and, possibly, their change with time associated with the variations of the stability conditions (Bottelin *et al.* 2013, 2017, Kleinbrod *et al.* 2017, Taruselli *et al.* 2018). We performed three seismic noise field campaigns in January 2017, March 2018

and March 2019. During the first measurement session, we deployed 20-s Nanometrics Trillium 3C geophones at the top of each tower plus one on the top stable rock mass to be used as a reference (Figure 2a). In the second session, we surveyed the previous points, and we also deployed four sensors at the base of the towers, two on the western side and two on the eastern one (Figure 2a) to investigate possible amplification phenomena of the ambient vibration wave-field soliciting the rock towers. The most recent survey was performed to infer whether different locations of the most exposed towers (1 and 2) provide the same dynamic responses. In this perspective, we installed three sensors on tower 1, and four sensors at each cardinal side of tower 2 (Figure 2).

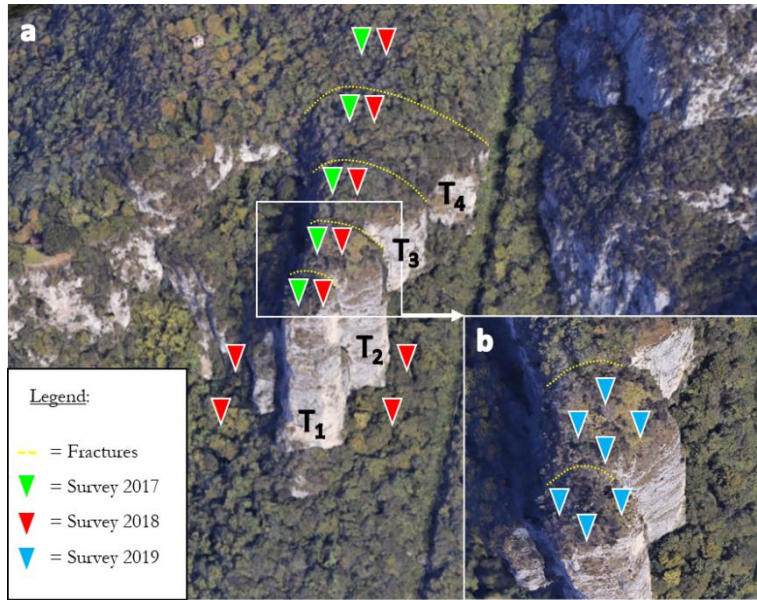


Figure 2 a) Seismometers position during the surveys performed in 2017 and 2018. b) Sensors location for survey 2019.

### 3.1.1. Geological investigations

The Torrioni di Rialba are made of Rialba conglomerate (RLB), which is a carbonate surface deposit composed of limestone clasts with an angular shape. Field investigations revealed widespread rock weathering, promoted by karst erosion, that results in the presence of several cavities and voids. The effects of this erosion are particularly visible at the foot of the southern face of tower 1 where there is a large-eroded cavity (Figure 3b) that could lead to stability problems in presence of triggering factors (i.e. earthquakes). In particular, the reduction of the base area could represent a preferential zone from which the toppling of the first rock column can occur.

Rialba conglomerate is bounded both to the east and the west by Esino limestone, a formation resulting from a carbonate platform and consisting of massive layers of limestone, grey dolomitic limestone and dolomite, whose thicknesses range from 250 to 800 m. The upper limit of the Rialba conglomerate is at the top of the towers and consists of an erosional plane over which glacial deposits can be found. The existence of a glacier in a former epoch is supported by the presence of glacial erratics completely different from the site lithology on the erosional plane. Furthermore, a glacial terrace northwest of the towers (Figure c,d) confirms erosion, transport and sedimentation activities promoted by the glacier during the Quaternary epoch.

The geological survey shows that the Rialba's towers are separated by four mainly parallel fractures (Figure c,d and e). They have dip direction ranging from 205° to 215° and dip close to 85°. The fractures (named F1 to F4 south to north; Figure e) have metric aperture with linear persistence of about 90%. Into detail, fracture F1 runs straight from the top to the bottom of the cliff (about 100 m) on the south-eastern face. The base is 4 m large and it is filled with weakly cemented conglomerate blocks. This is the only fracture that can be observed completely also on the north-western face. However, on this side of the cliff, the aperture is more complex since it is divided into two unparallel sub-fractures a few meters apart (Figure c). Fracture F2 is about 2m wide and, on the top plane of the cliff, is completely open and thus it is possible to observe its characteristics. It is persistent for about 80 m and, in the upper part, it splints into two segments that isolate an overhanging section (Arosio *et al.* 2019b). Fracture F3 and F4 are 70 m and 60 m long, respectively. Provided this information the size and volumes of the four pillars have been estimated are sum-up in Table 2.

Tower	Size (L x W x H) [m]	Volume [m <sup>3</sup> ]
1	48 x 30 x 100	144,00
2	66 x 36 x 80	190,08
3	82 x 38 x 75	233,70
4	100 x 45 x 65	292,50

Table 2 Estimated dimensions of each rock column.

Another problem that may affect the stability of the monitored site, is the San Giovanni Bianco (SGB) claystone at the base of the towers. The tectonic contact between the RLB and SGB led to erosional processes that make it difficult to estimate the thickness and extension of the SGB under the Torrioni di Rialba. This information is crucial to determine the stability of the rock columns since the widespread presence of a thick plastic claystone stratum under the high rock cliff made of conglomeratic rigid rocks can lead to the lateral spreading phenomenon. In fact, lateral expansion of the plastic layer below the towers can occur in presence of the just described conditions, bringing to the consequent fracture formation within the rock towers. This could lead to rock instability with consequent rock topple due to the verticality of the cliff.

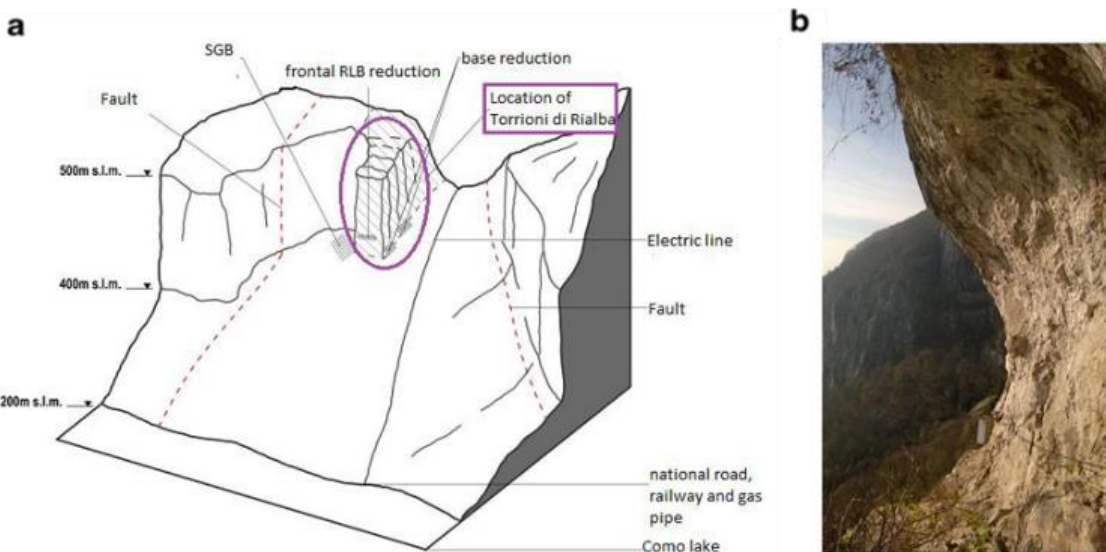


Figure 3 a) 3D representation of the Rialba site. b) Picture of the frontal eroded cavity of the first tower.

### 3.1.2. Geoelectrical investigations

Given the importance of this phenomena, geoelectrical surveys have been carried out to deeply characterize the extension of the SGB which can be considered the predisposing factor for the occurrence of a massive collapse of one or more towers (Arosio *et al.* 2019b). Electrical resistivity tomography (ERT) is an imaging technique now widely applied to the investigation of landslides in various lithological contexts (from fine-grained soils to compact and cemented rocks). Fundamentals about the technique can be found in reference books (e.g. Reynolds 2011) and specifics about landslide investigation are exposed in more or less recent review articles (Jongmans & Garambois 2007, Perrone *et al.* 2014).

In this work, four ERT profiles at different elevations and with various orientations along the slope have been carried out. The profiles conducted in this work are represented with black lines in Figure 4. Measurements were collected with a SYSCAL-Pro resistivimeter working with 48 electrodes and the spread had a constant electrode spacing of 1 m (E1 and E2), 2 m (E3) and 3 m (E4), respectively. Profile E2 was the only one collected according to the roll-along mode, with a single shift of 24 electrodes. Electrodes were georeferenced in the field using GNNS receivers, and accurate elevations were further extracted from a digital elevation model (DEM) with a grid size of 2 m. To achieve both good vertical and lateral resolution along with high signal-to-noise (SNR) ratio, measurements were carried out using both the Wenner and Schlumberger configurations. For the former configuration, the spacing between the electrodes was varied between 1 and 15 single-electrode spacing, whilst for the latter, the spacing between potential electrodes was kept to 1 electrode spacing, and the spacing between current electrodes varied between 1 and 15.

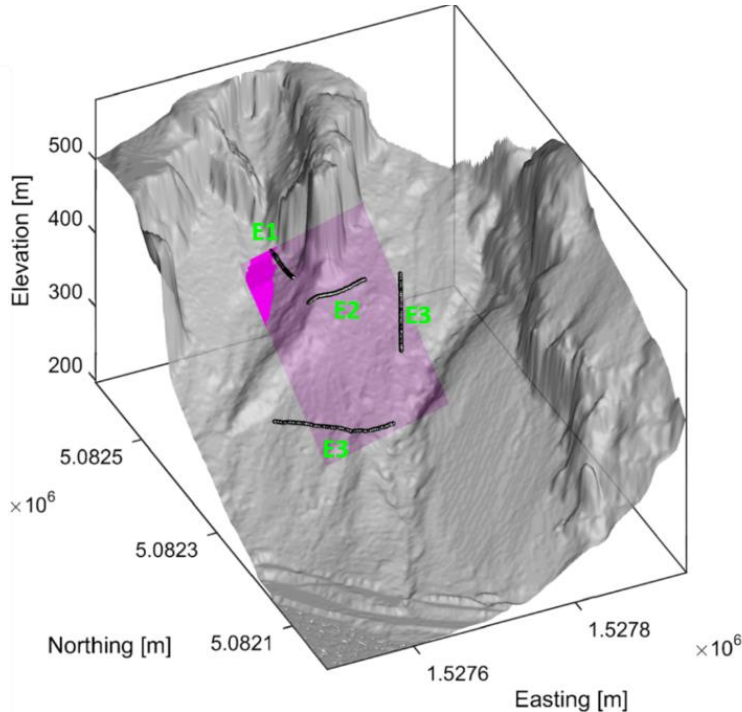


Figure 4 The  $2 \times 2\text{-m}$  DTM of the investigated area with the best-fit plane (magenta surface) representing the top of the shale layer obtained by interpreting the results of the ERT surveys (black lines).

Experimental data were filtered by removing strong outliers and also measurements with very low potential values. They were then inverted using the Boundless Electrical Resistivity Tomography (BERT) software package developed by Günther et al. (2006) that uses finite element computations with irregularly shaped triangles (Rücker et al. 2006). For profiles E1 to E3, resistance values were used to force the algorithm to compute ad hoc 2D geometric factors. Considering that profile E4 is not entirely linear (Figure 4), we decided to compute the 3D geometric factor of each measurement using the methodology proposed by Bièvre et al. (2018). Accordingly, we used the measured resistance values and the geometric factors computed *a posteriori* to correct the apparent resistivity data for 3D topographic effects and we obtained variations in inverted resistivities up to 30% and down to  $-20\%$  concerning the 2D approach. As far as the inversion procedure is concerned, we set homogenous starting models with resistivity equal to the mean apparent resistivity of each pseudo-section. The investigation depth was computed automatically. In the iterative process, we used the L1 norm to enhance the contrasts between adjacent lithological units. The discrepancy between experimental and theoretical data was evaluated with a chi<sub>2</sub> test (Günther et al. 2006). This test normalises the residuals by a measurement error of several per cent (voltage error and geometrical error). For the four profiles, chi<sub>2</sub> values close to 1 were obtained after a few iterations by manually tuning the regularisation strength, indicating that the data were fitted within an error of 3% (default value). All relative root mean square (RRMS) errors were below 10%. Inverted resistivity sections are presented in Figure 5 with a common colour scale ranging from 25 to 2500  $\Omega\text{m}$ . The degree of transparency on the images corresponds to the sensitivity matrix: the higher the transparency is, the lower the sensitivity is. In all sections, it is generally possible to identify two main units: one with resistivity from 25 to around 100  $\Omega\text{m}$  and a second with resistivity ranging between 100 and 2500  $\Omega\text{m}$ . The low-resistivity unit could be associated with the shale layer, because spread E1 was partly deployed on the outcrop of San Giovanni Bianco formation found adjacent to the base of the first tower. We deem that high resistivity values may be associated with Rialba conglomerate and slope debris coming mainly from the Rialba Towers and partly from the neighbouring Esino limestone rock cliffs. One may speculate that an additional unit with a resistivity between 200 and 400  $\Omega\text{m}$  (greenish colour in Figure 5) is placed between the (shallow) high and (deeper) low-resistivity formations. This unit could be associated with Rialba conglomerate more compact than the surface one or with a conglomerate that was partially mixed with the underlying shale during the sliding process described above. Organic soil was found at a few places along spreads E2 and E3 where lower resistivity values are observed at the surface. It is interesting to note that shallow higher resistivity values at the beginning of profile E3 (Figure 5 c) correspond to an outcrop of the Rialba conglomerate that we mapped on-site. Besides, the sharp resistivity variation at about 35 m along profile E4 (Figure 5 d) may be due to the continuation of the fault between Rialba conglomerate and Esino limestone formations that can be observed upslope. No evidence of shale was found at the end of spread E4, so that very low resistivity values at the surface may be due to wet organic soil (Figure 5 d). Finally, we computed the plane that best fits points belonging to the

top of the shale layers in each section as the least square of the distance to the plane (Figure 4). The computed plane is approximately 10 m below the surface, parallel to the slope (attitude  $205^\circ/31^\circ$ ), and outcrops close to spread E1 where shale outcrops were observed on the field. The resistivity section of spread E1 suggests that the San Giovanni Bianco layer could be very thin (i.e. around 20–25 m), although the investigation depth of the ERT surveys prevents any accurate assessment. This analysis confirmed the presence of a plastic shale layer underneath the rock cliff that may promote lateral spreading involving both slow and faster displacements. Unfortunately, it is difficult to investigate the extension of the layer below the towers and thus to determine whether the SGB could affect the stability of one or more columns.

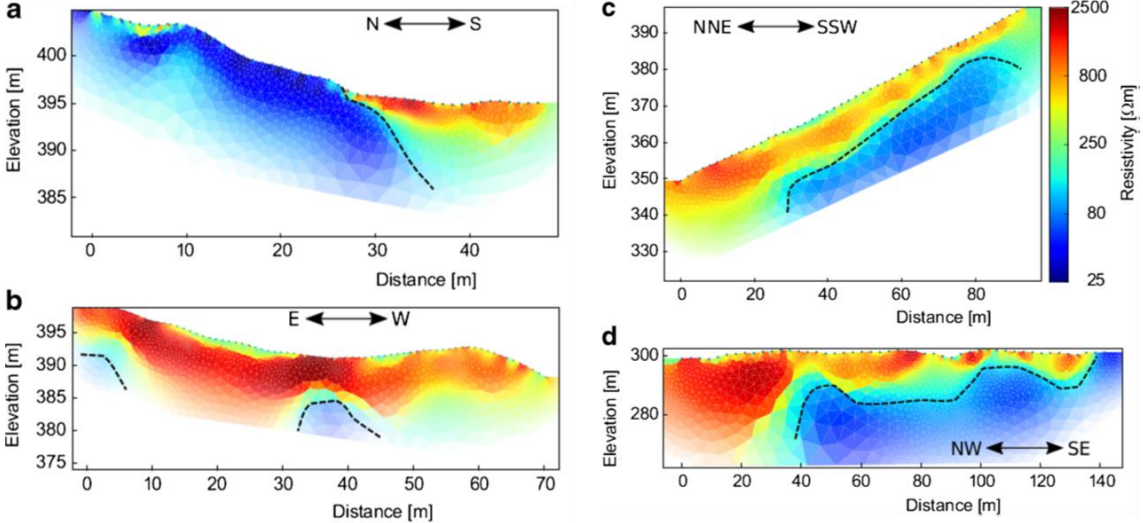


Figure 5 Electrical resistivity tomography results for profiles a E1, b E2, c E3 and d E4. The resistivity sections are represented with a common colour scale. The black dashed lines correspond to isocontours of  $90 \Omega\text{m}$ .

### 3.2. Methods

The analysis of the collected data has been performed using both spectral and polarization analysis. To study the spectral content of the collected seismic noise we did use the Horizontal-to-Vertical Spectral Ratio technique and we estimated the power spectral density (PSD) with Welch's periodogram. We did exclude from the analysis the Multitaper method because by performing a comparison with the modified periodogram (Welch) we observed that the latter provides a PSD estimation equal to the one obtained with the MT technique in a much shorter time (the computation time depends on the time-length of the analysed signals). A result of the comparison between the two methodologies is presented in the **appendix**. For the periodogram computation, the time series have been divided into 60 s signal segments, tapered with a Hamming window and with 50 per cent overlapping. As a result, we obtain a spectral resolution of 0.02 Hz (computed as the reciprocal of the time window) and enough time windows for statistical robustness of the results. Considering the HVSR technique, the recordings have been divided into 60s sub-signals and tapered with Hamming window as well. Additionally, the Konno-Ohmachi spectral smoothing has been applied before computing the horizontal to vertical spectral ratio. With regards to the polarization analysis, thus to study the preferential oscillation directions associated with the resonance frequencies of the towers, we took into account both the HVSR as a function of azimuth, as well as the singular value decomposition (SVD) of the spectral density matrix techniques. We decided to not apply the hodogram and the principal component analysis of the time-domain covariance matrix since their results are implicitly provided by the SVD method.

### 3.3. Results and discussions

Considering the 2017 and 2018 surveys, the spectral analysis reveals that the amplitude of the vertical component collected on the rock pillars is generally smaller than the horizontal one (Figure 6). This fact suggests that the vibrational modal shapes of the towers may be associated with displacements that occur mainly in the azimuth plane and not in the zenithal one. In general, we can observe a slight to moderate amplification of signals recorded on the towers compared to the signals recorded on the stable rock mass and at the base of the towers (Figure 6 & **Appendix**). In terms of rock columns' vibrational modes, the PSDs show the presence of well-defined spectral peaks at 1.9 and 2.8 Hz for tower 1 and 2, that are emphasized on the East-West component. The peaks become less and less distinguishable as we move from tower 3 to the stable compartment (Figure 6). Ambient vibrations

at the same locations across the two monitoring sessions show a dual behaviour. First, if we limited our analysis to the 0–20Hz bandwidth, we notice that the surveys carried out in the two different epochs are roughly unchanged. The only difference arises at 4.7 Hz where a visible peak appears in 2017's PSD and not in the more recent one. We exclude that this peak is associated with a different ground-sensor coupling because it appears for tower 1, 2 and 3 and all the three components. We found it difficult to assess whether the peak is associated with a specific vibrational mode of the towers or if it generated by a particular ambient source that accentuates that specific frequency. On the contrary, considering the PSDs in the bandwidth above 20 Hz we notice that the curves do not appear to have constant features across the two monitoring sessions (**Appendix**). We hypothesize that the discrepancies at high frequencies (>20Hz) are not related to stability variations between 2017 and 2018's surveys, but rather to two possible factors. The first one regards a change in the seismic ambient noise wavefield composition. Indeed, the higher frequencies are linked to sources generated by human activities and it is, therefore, safe to suppose that during the two measurement campaigns there was a different configuration of the seismic passive sources that brought to differences in the higher part of the spectrum. The second factor that can introduce spectral changes is different ground-sensor couplings. Our hypotheses are supported by the fact that the discrepancies between the two surveys appear for all monitored locations and, especially for the stable compartment that should not exhibit any variation in time. This fact brings to light the issue of monitoring rock block vibrational modes by performing surveys on different days and not continuous in time. Indeed, in such a case, it is difficult to assess whether spectrum differences are linked to the stability of the monitored structures or external causes, such as changes in the ambient seismic noise wavefield and ground-sensor coupling.

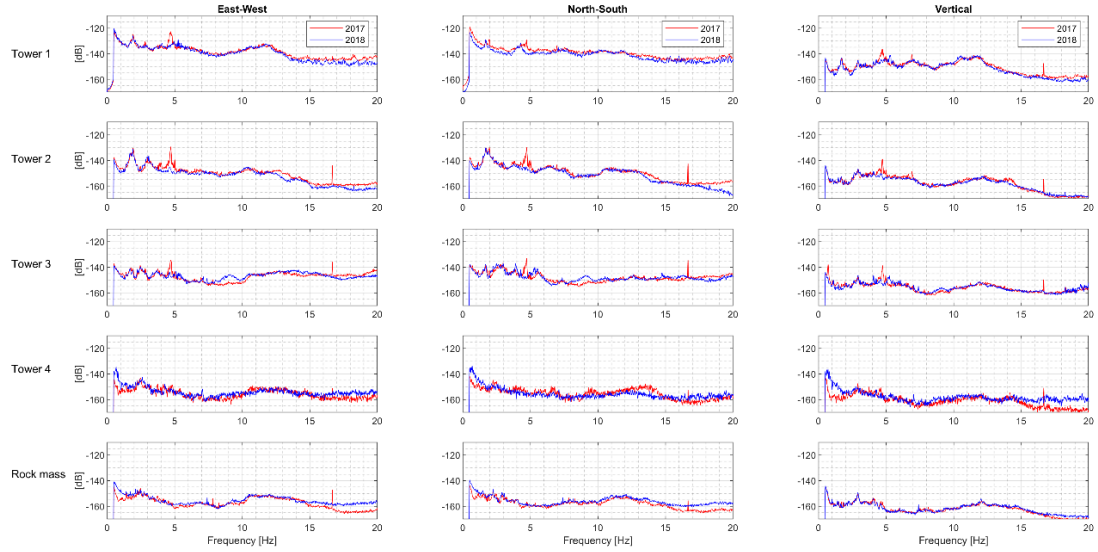


Figure 6 PSDs of the three components estimated with the Welch's periodogram method for the two epochs (2017–2018).

With regards to the HVSR analysis, the results obtained at each location offer a clearer picture than the PSD method. Figure 7 shows that HV curves are stable in the two monitoring sessions for the entire bandwidth and that strong peaks are only discernible for towers 1 and 2. In more detail, tower 2 displays a sharp high-amplitude peak at about 1.90 Hz, as observed in the estimated spectrum, with the remaining HVSR curve close to 1 and with a low standard deviation. On the contrary, tower 1 seems to show a complex behaviour, especially in the 0.02–1.50 Hz frequency range where high HVSR values and large standard deviation could be related to several over-imposed vibration modes due to the complex geometry of the tower, including the erosion cave in the lower part (Figure 3) and the complex trend of the fracture F1 on the north-western side (Figure ). The other locations do not show any significant HVSR peaks, at least at frequencies that could be usually associated with the vibration mode of the investigated structures and feature low standard deviations.

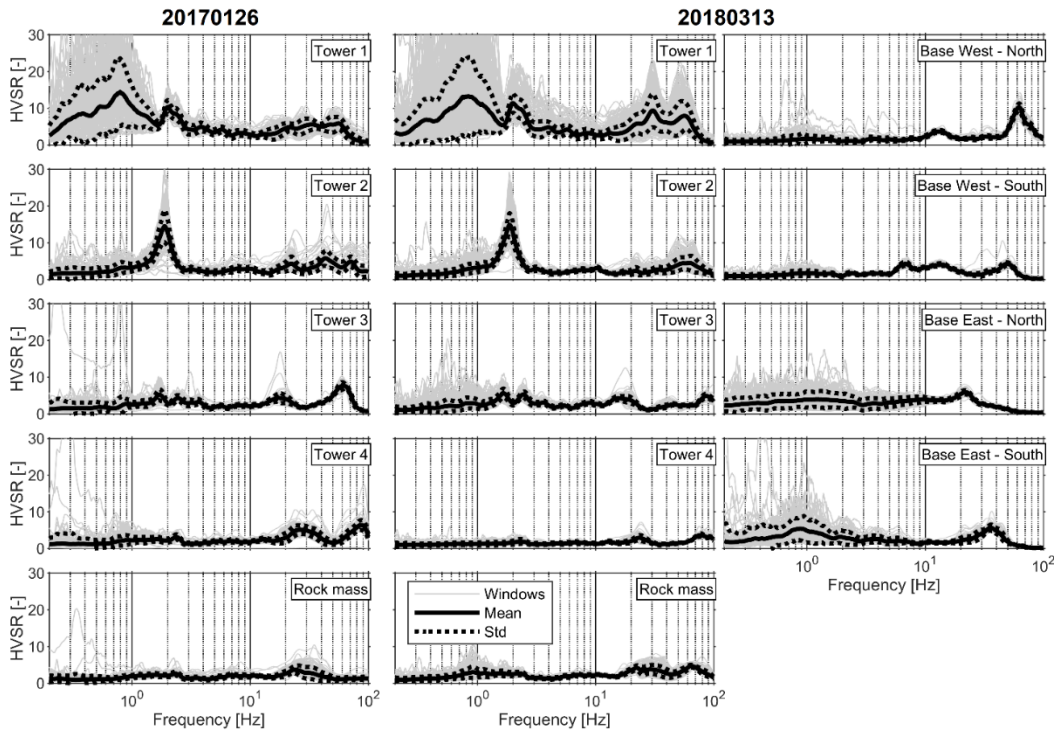


Figure 7 HVS estimates obtained from the seismic noise collected in the two recording session 2017 and 2018.

To obtain indications about the order of magnitude of the theoretical vibration frequencies of the rock towers, we can consider the natural vibration frequency of a cantilever beam with uniform mass per unit length  $m$  (kg/m). Taking into account only the deflection associated with bending stress in the beam and neglecting the effect of rotational inertia and shear deformation, the  $n^{\text{th}}$  resonance frequency can be expressed as (Chopra 2012):

$$f_n = \frac{K_n}{2\pi} \sqrt{\frac{EI}{mH^4}}$$

where  $E$  is Young's modulus (Pa),  $I$  is the area moment of inertia ( $\text{m}^4$ ),  $H$  is the length of the beam (m) and  $K_n$  is a dimensionless coefficient that varies according to the vibration mode (e.g. 3.516 for the first mode). For each tower, we computed the mean value and the standard deviation of the first four vibration mode frequencies (Table 3) by considering the accuracy of  $\pm 5\%$  in the geometrical parameters reported in Table 2; Young's modulus ( $E$ ) for Rialba conglomerate between 15.3/29.4 Gpa; density spanning from 2500 to 3000 kg/m<sup>3</sup>; and the area moment of inertia was computed by considering two orthogonal rotation axes parallel to the sides of the (approximated) rectangular base of each tower. Although the resonance frequencies obtained are to be considered estimates, they provide indications of the expected values. In particular, it is interesting to note that the first vibration mode for tower 2, when considering the barycentric axis parallel to the longer side of the rectangular base ( $L$ ), has a frequency very close to that estimated with the HVS method. In addition, this vibration direction is in accordance with the one associated with the lower resonance frequency identified in the plot of the HVS as a function of azimuth (Figure 9). Moreover, the frequency computed for the first vibration mode of tower 1 (Table 3) appears to be close to the results provided by the HVS analysis, although a comparison between the analytical and experimental vibration directions is more difficult to make in this case.

$I = LW^3/12$				
Tower	First mode [Hz]	Second mode [Hz]	Third mode [Hz]	Fourth mode [Hz]
<b>T1</b>	$1.1 \pm 0.3$	$7.1 \pm 1.7$	$19.8 \pm 4.9$	$38.9 \pm 9.6$
<b>T2</b>	$2.1 \pm 0.5$	$13.3 \pm 3.3$	$37.2 \pm 9.2$	$72.9 \pm 18.0$
<b>T3</b>	$2.5 \pm 0.6$	$15.9 \pm 3.9$	$44.7 \pm 11.0$	$87.6 \pm 21.6$

<b>T4</b>	$4.0 \pm 1.0$	$25.1 \pm 6.2$	$70.4 \pm 17.3$	$138.0 \pm 34.0$
$I = WL^3/12$				
<b>T1</b>	$2.4 \pm 0.4$	$15.0 \pm 2.3$	$42.1 \pm 6.4$	$82.4 \pm 12.6$
<b>T2</b>	$5.1 \pm 0.8$	$32.3 \pm 4.5$	$90.4 \pm 13.8$	$177.0 \pm 27.0$
<b>T3</b>	$7.3 \pm 1.1$	$45.6 \pm 7.0$	$127.7 \pm 19.5$	$250.3 \pm 38.2$
<b>T4</b>	$11.8 \pm 1.8$	$74.0 \pm 11.3$	$207.4 \pm 31.7$	$406.4 \pm 62.0$

Table 3 First four vibration mode frequencies of the rock towers considering area moments of inertia for the barycentric axis parallel (top) and perpendicular (bottom) to the longer side of the rectangular base, respectively.

Turning to the polarization analysis, the two applied techniques provided interesting results. Considering the SVD method, we confirmed the assumption made with the PSD analysis that the pillars' oscillation occurs in the azimuthal plane (Figure 8). Indeed, the  $\Theta_V$  plot clearly shows that for the entire bandwidth the polarization of the ambient noise in the zenith plane is close to zero ( $< 15^\circ$ ). This condition does not change across the different monitored periods. As well as the results obtained in the spectral analysis, also the polarization investigation reveal that frequencies in the 20-100 Hz bandwidth have features that change across the two monitoring sessions, whereas the wavefield with a frequency content lower than 20 Hz does not show substantial changes one year after the first survey (Figure 8). Nevertheless, in the latter bandwidth, it is very difficult to distinguish the polarization characteristics of the recordings and thus infer the vibrational modes of the towers.

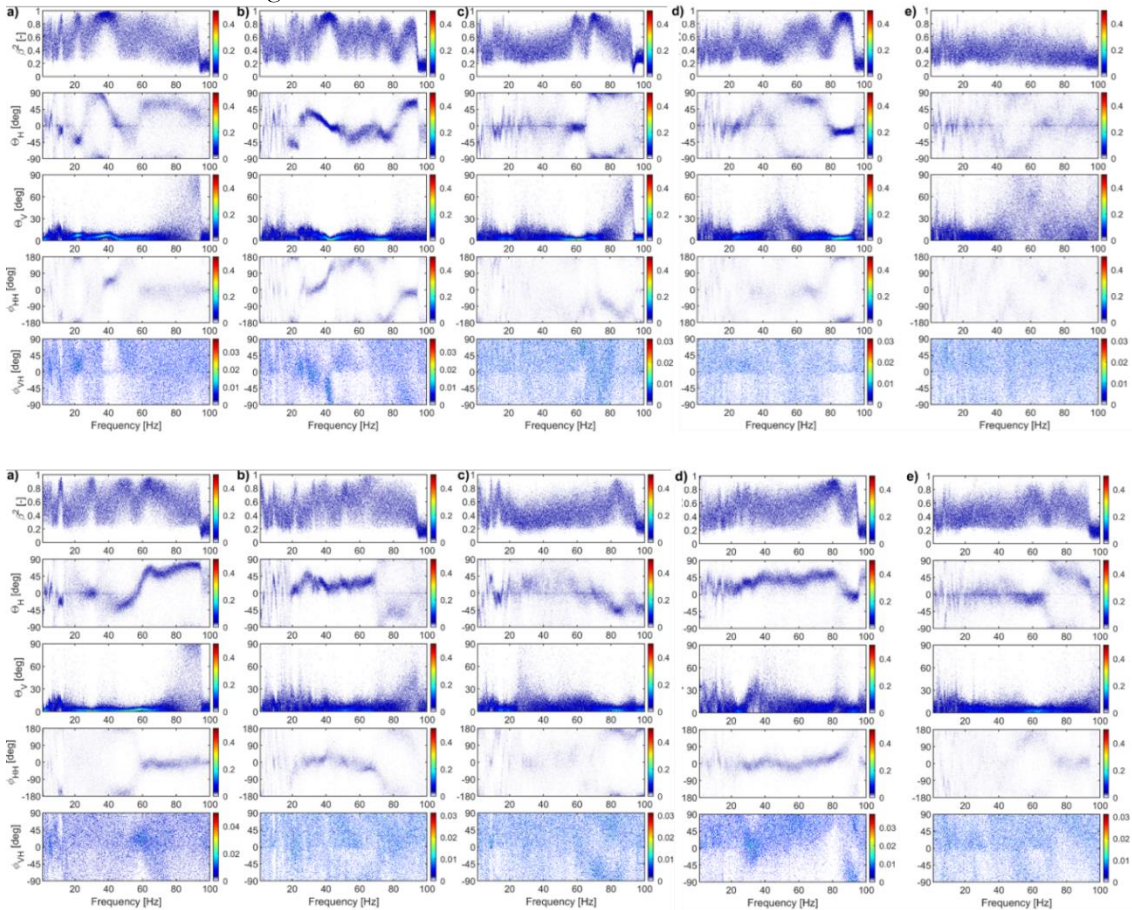


Figure 8 Polarization parameters estimated with the spectral SVD method for tower 1 (a), 2 (b), 3 (c), 4 (d) and stable mass (e). The colormap indicates relative probability of the estimated parameter. Top: 2017 survey. Bottom: 2018 survey.

The polarization analysis gets easier if we consider the HVSR as a function of azimuth computed in the frequency band where clear peaks have been observed with the spectral analysis, that is 0-4 Hz. Indeed, the HVSR plots reveal that tower 2 seems to display two different, though close, resonance frequencies: the one with the highest energy at about 1.90 Hz along the  $45^\circ$ - $225^\circ$  direction and a lower energy one at 1.80 Hz and oscillation along the  $125^\circ$ - $305^\circ$  direction. Tower 1 has again a more complex situation with low-frequency spectral features changing across the two measurements, but a constant peak at 1.90 Hz along the  $15^\circ$ - $195^\circ$  direction that can be identified also in the HVSR plots (Figure 7). When computing the HVSRs as a function of azimuth, it is important to note that spectral smoothing should be applied carefully because it may merge vibration modes with different directions

but similar frequencies. By comparing the plots in Figure 9 with the datasets collected at the meteorological station about 1.8 km from the site, we suggest that the oscillation in the direction  $125^\circ$ – $305^\circ$  may be caused by the wind. Actually, the wind was present in both measurement sessions (Figure 9 b) and during the day with the strongest wind (i.e. 26 January 2017) we observed a higher amplitude peak of the vibration mode. The temperature may also affect the vibration mode of the rock structures, although previous studies (e.g. Colombero *et al.* 2017) seem to suggest that the temperature difference across the two measurements (Figure 9 c) is not enough to generate an appreciable variation of the frequencies.

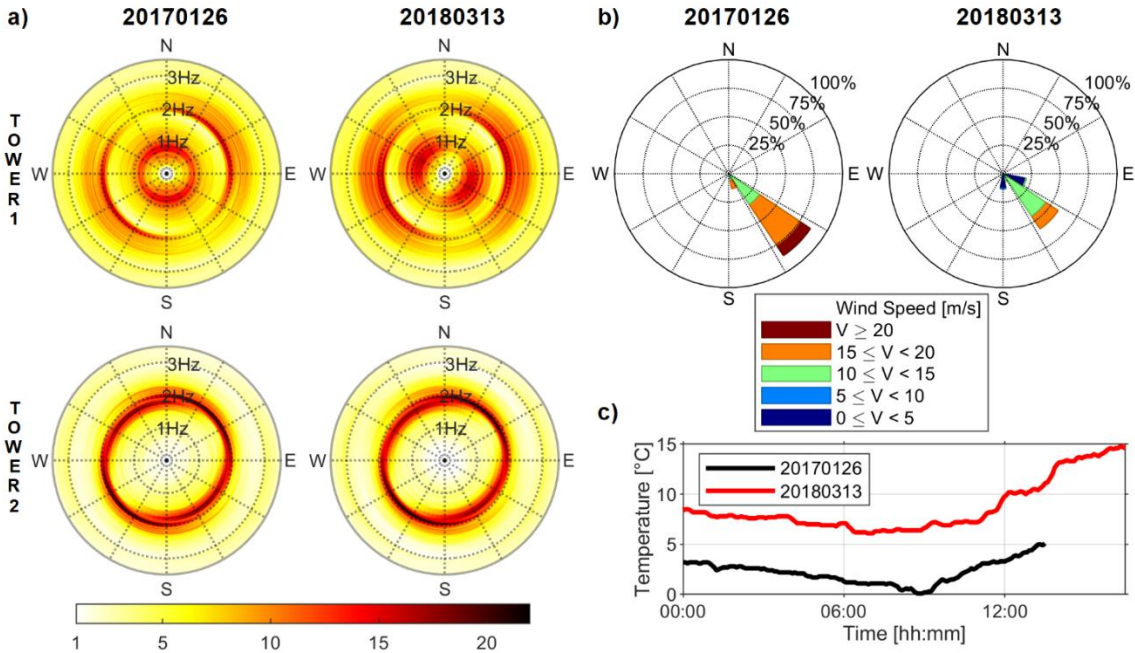


Figure 9 a) HVSRs computed as a function of azimuth. b) Wind rose plot and c) temperatures collected during the two recording sessions.

The analysis of the 2017 and 2018's surveys clearly showed that for column-like rock structures, the firsts vibrational modes can be related to displacements that occur mainly in the azimuthal plane (i.e. bending and torsional deformations). For these case studies, we have just seen that the Horizontal-to-Vertical Spectral Ratio technique is particularly suitable to provide useful results. For this reason, the analysis of the data collected during the 2019 measurement campaign has been performed through HVSR and the HVSR as a function of azimuth techniques. Considering the tower at the southernmost point of the site, we observed that the HVSR curves obtained for the north, west and east locations on top of the tower share a very similar trend (Figure 10 -left). In detail, the survey confirms the presence of a well-defined peak at almost 2 Hz that preserve the same amplitude at the three positions. Moreover, the HVSRa analysis reveals that this vibrational mode also shares the same polarization. Indeed, Figure 11 shows that the peak at 2 Hz is polarized along the  $30$ - $210^\circ$  direction whatever sensor is considered. This preferential direction of vibration turns out to be perpendicular to the rear fracture that separate tower 1 from tower 2. Considering the second investigated tower, slight differences have been observed. First of all, only the data collected on the East-side of the tower present a well-defined peak at 1.90 Hz (Figure 10 - right). On the contrary, the HVSRs obtained at the other three locations (North, South and West) show peaks that have lower amplitude than the one measured at the Eastside. One hypothesis that could explain the presence of a spectral peak with twice amplitude on the East side compared to the other three cardinal points, is the internal fracture state that may lead to different amplification of the ambient seismic noise components recorded at different locations on the tower. The discrepancies get even worse if we consider the frequency band above 10 Hz. Indeed, the obtained HVSRs curves are completely different at each of the four monitored spots. Other possible causes that bring a different result in the higher part of the spectrum may be the already mentioned ones or the presence of trees that may cause signals' disturbances.

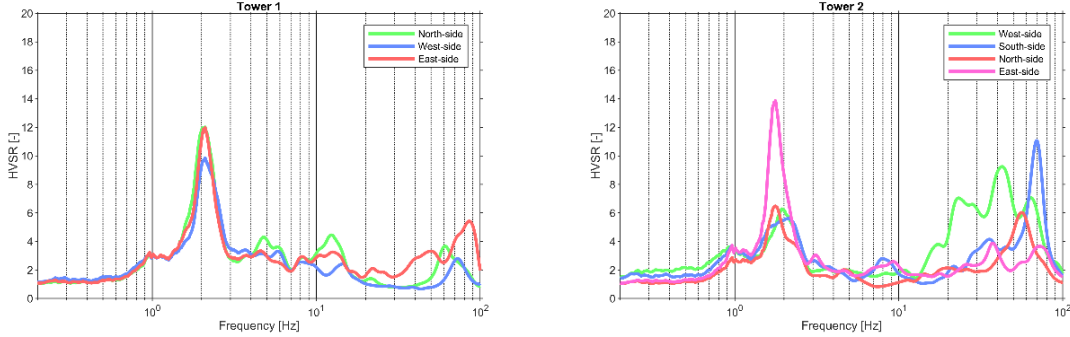


Figure 10 HVSR curves obtained by recordings collected in different locations on tower 1 and 2.

More details about the characteristics of the peak at 2 Hz for tower 2 are provided by the HVSR as a function of azimuth analysis (Figure 11). First of all, we can notice that each HVSRA plot in Figure 11 shows a spectral peak at 1.9 Hz that is polarized, for each monitored spot, approximately along 135-315°. Additionally, except for the North-side, we notice a very close second peak at 2 Hz oriented along 45-225°. In terms of modal analysis, it is difficult to explain the presence of two adjacent peaks that show perpendicular polarization with each other. We suppose that the different polarizations are associated with a change of source that activates the vibrational modes occurring almost at 2 Hz. In fact, even though these analyses are generally performed under the assumption that ambient seismic noise is stable over time, it is very difficult to guarantee that the polarization features of the wavefield in the monitoring period remain constants. The HVSRA analysis also confirmed that the sensor installed at the East-side shows an HV peak that has a much higher amplitude than the other locations.

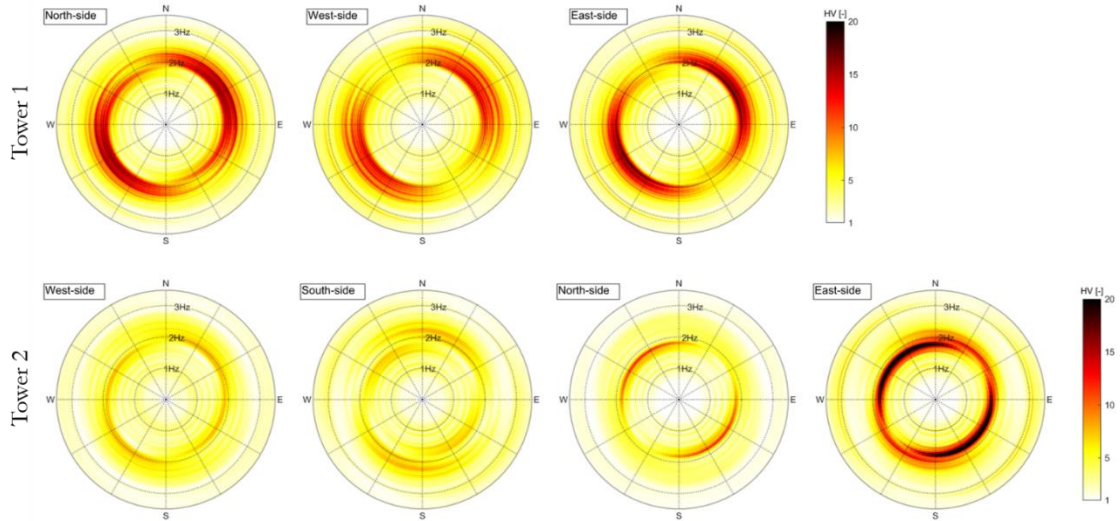


Figure 11 HVSRs computed as a function of azimuth for tower 1 (top) and 2 (bottom).

### 3.4. Conclusions

In this work, we presented the analysis of the ambient seismic noise collected at the Rialba site. The goal of this study was to check whether the techniques presented in the controlled collapse test chapter can be also applied to real unstable columns with different geometries and dimensions. For this purpose, three different measurement campaigns were carried out over three years. The first two surveys (2017 and 2018) aim to assess whether the vibrational modes of the towers exhibit changes across the two monitored epochs. The most recent survey was instead carried out with the objective of evaluating if the two towers with the most persistent fractures showed different frequency responses depending on the position in which the seismometers are installed.

The results of the 2017 and 2018 surveys revealed that is not always possible to clearly identify the resonance frequencies of the monitored structures by means of power spectral density estimation. In fact, when dealing with complex compartments that present a not well-defined geometry and that potentially have internal fractures, the

vibrational modes are not easily discernible. Nevertheless, in the context of unstable rocks monitoring systems development, the PSD estimates gain more value if they are used to obtain the spectrograms. Indeed, in this case, it would be graphically easier to infer the frequency peaks, and, above all, it is possible to track their variations across time. The latter condition is extremely important if we consider the goal of assessing the stability of the unstable rock blocks. Although the PSDs did not provide useful results in terms of vibrational modes identification, it revealed that the horizontal components are more energetic than the vertical one, suggesting that the oscillation of the towers mainly occur in the azimuthal plane. This presumption has been confirmed by the  $\Theta_V$  parameter retrieved computing the polarization analysis. Indeed, the dip of the polarization direction measured from the horizontal plane was practically nil for any frequency and at all the monitored locations. Given the azimuthal displacement of the investigated structures, the HVSR technique resulted to be the most useful tool to clearly identify the fundamental frequency of the most vulnerable Rialba's towers. In fact, this technique returned clear frequency peaks for tower 1 and 2, showing that they did not undergo significant variations across the two surveys. In addition, also the HVSR as a function of azimuth proved to be very useful in understanding preferential vibration directions with respect to the SVD. Comparing the two different measurement campaigns, we noticed that at low frequencies (<20 Hz) the results obtained with each method are very similar between 2017 and 2018. On the contrary, a lot of differences arise if we consider a higher frequency band. We suppose that such changes are probably linked to a different composition of the ambient seismic noise wavefield or to a different ground-sensor coupling that took place in the two epochs. For this reason, we deem that monitoring rock stability performing surveys at different periods may introduce "false" variation that makes it difficult to infer whether they are associated with changes in the vibrational modes or to external causes. With regards to the 2019 campaign of measure, we observed that the fundamental modes of the most critical towers (1 and 2) are visible in the recordings of all the sensors that have been installed. This result suggests that one seismometer is sufficient to monitor the dynamic response of the unstable rock columns. Seismic noise tests have provided preliminary outcomes since a rigorous investigation should involve continuous monitoring for an extended time length and through different climatic conditions, especially where unstable slopes lack clear indications of collapse. Nevertheless, the results of this study suggest that spectral and polarization analyses may help to design suitable monitoring strategies. For instance, a ground-based interferometric microwave radar could be coupled to continuous monitoring with seismic noise sensors since they have the capability to monitor displacements in terms of accuracy and frequency.

#### 4. Bismantova Rock Cliff

In the previous paragraphs, we saw how the methods used in the collapse test performed in Lierna were successfully extended to monitor the dynamic response of the Rialba towers. Nevertheless, we noticed that the signals recorded in 2017 and 2018 showed spectral dissimilarities that were not negligible. In this regard, we hypothesized that these differences, which mainly occurred at high frequencies, were not linked directly to a variation in the stability of the monitored structures, but rather to either a change in the configuration of the ambient passive seismic sources or to a slightly different ground-sensor coupling performed in the two measurement campaigns. To this concern, in the following paragraphs, we will propose the analysis of the ambient noise dataset collected on the Sirotti tower (Bismantova rock cliff) that underwent a different installation setup. Indeed, given the presence of the soil layer above the Rialba's towers, we have been forced to couple the seismometers with the ground using the spikes. On the contrary, the Sirotti column is completely made of rock and we thus installed the sensors using the provided supports. This different seismic stations setup can provide insight into the spectrum discordance that occurs at the high-frequency band. This case study will thus allow us to test the ambient seismic noise methods on another unstable rock block and, additionally, to deduce whether using a different ground-sensor coupling system it is possible to remove such important variations in the spectral estimates of the collected seismic recordings.

##### 4.1. Case study

Pietra di Bismantova is a site located in the Northern Apennines (**Figure 1**) and consists of a plateau of calcareous sandstone (PAT5 formation in Figure 2) overlaying marls and clay shales (CGT, RAN3, AVV formations in Figure 2). The rock formation covers an area of approximately 400'000 m<sup>2</sup> and it is distinctively bordered by steep walls up to 100 m high. Due to its peculiar geomorphic feature, it is one of the most important natural heritage of the Tuscan-Emilian Apennine National Park. The past tectonic stresses, as well as the effect of lateral spreading phenomena, generated numerous joint sets that determine a high rockfall risk (Conti and Tosatti 1994). Such phenomena have been a significant geomorphic process in the area (GSUEG 1976). This is evidenced by the widespread rockfall deposits at the base of the cliffs, including rock blocks as large as more than one thousand cubic meters. Rockfalls are considered the main factor of natural risk for tourist that visits the Bismantova rock cliff every year (at least 30,000 tourists, hikers, climbers per year). Additionally, a collapse of the rock compartments can destroy the small church, so-called "Eremo", and restaurant located right at the feet of the south-eastern cliff. In this regard, analysis and modelling of the possible rockfall trajectories were proposed by many authors who concluded that the involvement of such assets is possible in case of rocks failure (Migliazza and Giani 2005; Borgatti and Tosatti 2010). The structural setting of the site has been investigated by Roveri (1968) and, later, by Conti and Tosatti (1994) who defined 6 main joint sets. Recently, by means of terrestrial laser scanner surveys, Corsini et al. (2016) identified 10 joint sets (Corsini et al. 2016b). These discontinuity sets produce many rock blocks and pillars that are nowadays considered unstable. For such reason, a monitoring system made of continuous crack meters has been deployed in 2014 on twenty of these unstable rock blocks. The analysis of the dataset shown clear variations of the fractures aperture which means that there is a high risk of rock blocks failure (Corsini et al. 2016a). One of the crack meters was able to detect the rockfall failure (200 m<sup>3</sup>) that occurred in 2015 and that threatened the church at the base of the cliff. Among the unstable rocks of the site, seismic noise surveys were carried out on Torrione Sirotti, a 30 m-high rock pillar (Figure 3a), which is believed of some criticality concerning possible toppling failure (Arosio et al. 2017).



Figure 1 Picture of the Pietra di Bismantova (summit altitude 1047 m a.s.l.). Mean geographical coordinates of the study area: 44° 25' 16" latitude N; 10° 24' 43" longitude E.

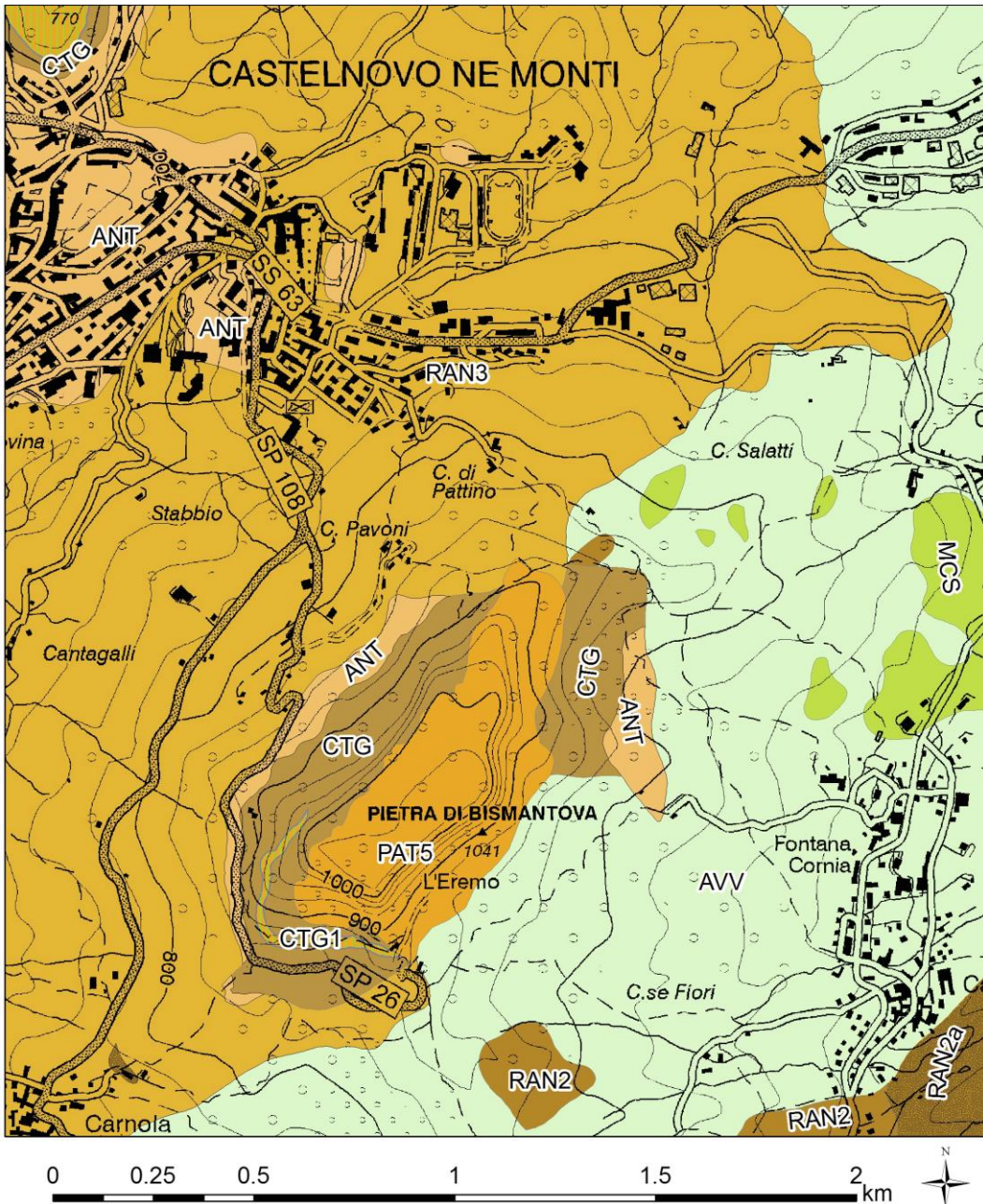


Figure 2 Geological map of the study area: (AVV) Argille varicolori Formation (Upper Cretaceous-Lower Eocene); (RAN2, RAN2a, RAN3) Ranzano Formation (Upper Eocene-Lower Oligocene); (ANT) Antognola Formation (Upper Oligocene); (PAT5) Pantano Formation-Pietra di Bismantova Member (Mid-lower Miocene); (CTG) Contignaco Formation (Lower Miocene); (MCS) Monte Cassio Formation (Late Cretaceous)

#### 4.2. Methods

At the Pietra di Bismantova site, a seismic noise survey was carried out on the Sirotti rock pillar (Figure 3a). Ambient seismic vibrations were collected using a 3-component broadband seismometer, featuring a  $-3$  dB frequency response spanning from 0.05 to 100 Hz, connected to 24-bit digital recorders (Figure 3b). We recorded ambient seismic noise for at least 40 minutes with a 200 Hz sampling frequency. Time synchronization and sensor position were obtained thanks to a GPS antenna connected to the logger. The 3-C seismometer was deployed for each measurement campaign so that the X, Y and Z components were oriented along the East-West, North-South and vertical direction, respectively. Noise datasets were processed applying both spectral and polarization analysis. For the former, Welch's periodogram as well as the HVSR technique were used. In this regard, signals firstly underwent high-pass filtering (0.5 Hz) to reject constant offset and unwanted noise link to the corner frequency. The PSD has been estimated using 60s signal segments, tapered with Hamming window and with 50% overlap.

For the HVSR we compute the amplitude spectra with 60 s-long-time tapered windows that were successively smoothed with the method proposed by Konno and Ohmachi (1998). According to the guidelines, the selected time window duration allows for obtaining reliable spectral peaks for frequencies higher than 0.02 Hz. With regards to the polarization analysis, thus, to retrieve the polarization of the wave field that may indicate the preferential vibration direction of the rock mass, we did use both the HVSR as a function of azimuth and the singular value decomposition (SVD) of the spectral density matrix techniques. In this perspective, for the former, we used the same setup that has been used in the HVSR computation, whereas for the SVD we used 5s-long series, tapered with Hamming window and with an overlapping of 90%.

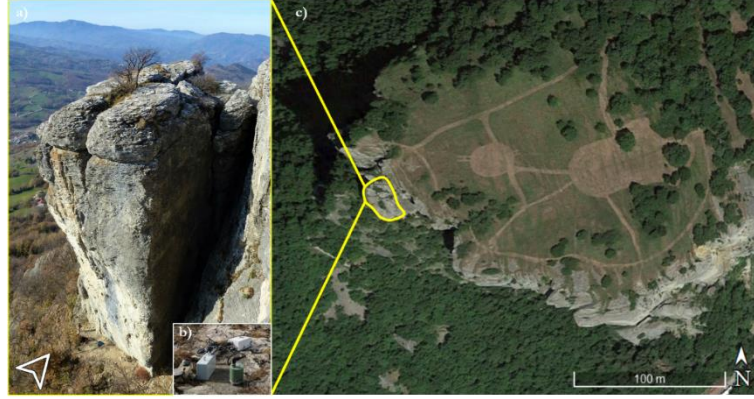


Figure 3 a) Sirotti tower; b) Seismic station. c) Location of the Sirotti tower.

#### 4.3. Results and discussions

The PSDs obtained applying the Welch periodogram method to the data collected on the Sirotti tower still show slight discrepancies when comparing the 2016 survey with the most recent one (Figure 4). The trends of the PSDs (grey and black line in figure 4) are very similar to each other, nevertheless, light differences are present between the two curves especially in terms of amplitude. The 2016's spectrum shows, for all three components, a slightly higher energy content than the one obtained analysing the 2017's recordings. We deem that such amplitude differences could be linked to a different configuration of the seismic noise sources during the two-measurement campaigns rather than to the ground-sensor coupling.

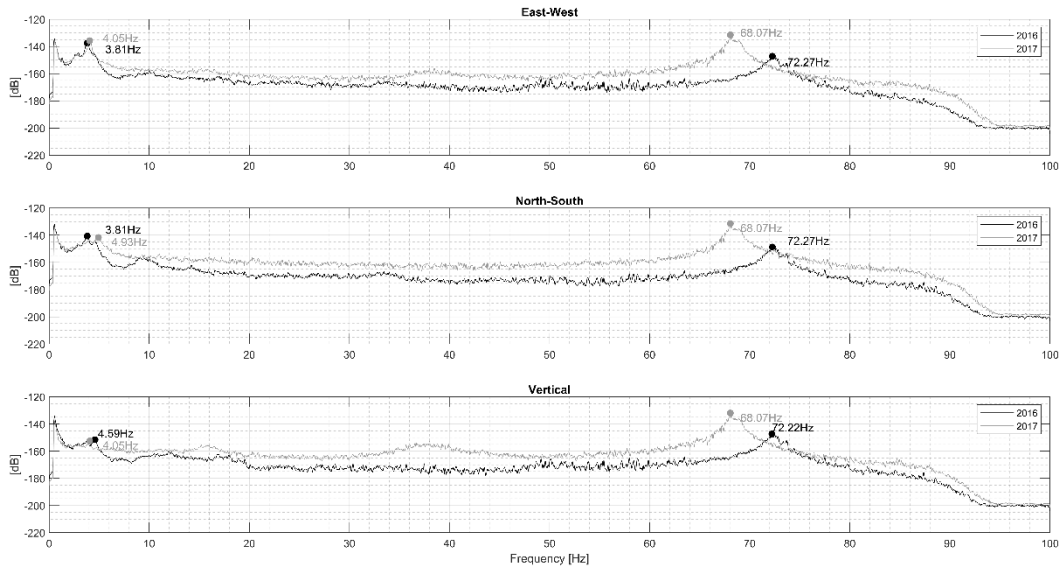


Figure 4 Power Spectral Density curves obtained for the 2016 and 2017 surveys and for all the three components.

The obtained spectral estimates show the presence of two evident peaks for all three components (Figure 4). The first occurs at low frequency, around 4 Hz, while the second appears close to 70 Hz. More in detail, we can see that the high-frequency peak shifts from 72 Hz (2016) to 68 Hz in 2017, showing a drop of 5% (Figure 4). Additionally, it can be observed that the measured signals underwent an important amplitude amplification in the

most recent survey which can be correlated to an increase in structure displacement. These variations between the two measurements campaigns suggest a change in the stability of the Sirotti tower. However, it is difficult to confirm this hypothesis for two main reasons: first, we do not have any information about the rear fracture aperture because no crack meter data are available; secondly, without continuous recordings is not possible to infer whether the observed frequency peak reduction is linked to a temporary or permanent phenomenon. In addition, it is also complicated to assess whether the peak is related to a vibration mode of the entire tower or if it concerns only a portion of it. In fact, as can be seen in figure 3a, the Sirotti tower is affected by a high degree of fracture state which results in a tower fragmentation. Our hypothesis is that this frequency peak is linked to a vibration mode of a portion of the tower itself because, at this frequency, the energy content is almost identical along with all three components. In fact, for column-like structures, one would expect modal shapes that affect more the horizontal components than the vertical ones since their shape eases oscillations that occur along the azimuthal plane. However, deeper investigations are necessary to demonstrate this hypothesis. As far as the low-frequency peak is concerned, we have different behaviour with respect to the previous vibrational mode. Figure 4 shows that the peak shifts to a higher frequency if we consider the horizontal components (East component: from 3.81 Hz (2016) to 4.05 Hz (2017); North component: from 3.81Hz (2016) to 4.93 Hz (2017)), while the estimated PSD computed for the vertical component shows that the peak shifts to a lower frequency in the 2017 survey (from 4.59 Hz to 4.05 Hz). This non-unique frequency response along the three components is difficult to be interpreted. However, the fact that the peak along the horizontal components shifts to higher frequencies leads to suppose that the observed variations between the two measurement sessions are not in this case associated with a permanent worsening of the tower stability conditions but rather to a temporary variation of the vibrational mode (i.e. temperature). It is also noticeable that conversely to the peak frequency at 70 Hz, in this case, the North and East components are amplified with respect to the vertical one (figure 4). Moreover, the East component has a slightly bigger amplitude because the rock pillar is a rectangular-base prism, with the longer side along the  $150^\circ$ – $330^\circ$  direction. In keeping with this, ambient vibrations should cause maximum displacement orthogonally to this direction. The higher amplitude of the horizontal components than the vertical one leads to the generation of a well-defined peak close to 4 Hz in the HVSR curves (Figure 5). Elsewhere, the HV ratio remains close to 1 demonstrating that for the rest of the frequency band the horizontal and vertical components are energetically similar. The analysis makes it possible to emphasize the first vibrational mode of the Sirotti tower in a more evident way than the periodograms. It furthermore highlights an HV peak shift from 2.86 Hz to a higher frequency (4.55 Hz) referring to the 2016 and 2017 surveys, respectively. The analysis shows that the HVSR curve obtained for the most recent survey it is characterized by a greater variance and by a narrower peak than the older survey.

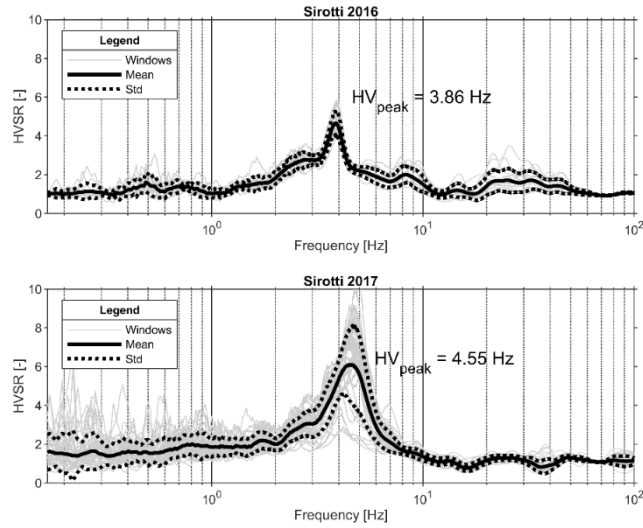


Figure 5 Horizontal-to-Vertical Spectral Ratio obtained for 2016 (top) and 2017 (bottom) recordings.

To examine in depth the modal shapes associated with the two identified frequency peaks, we analysed the collected ambient seismic noise through the SVD method. The results show that the frequency peak close to 70 Hz shows a maximum degree of polarization ( $\beta^2$ ) and a vertical motion ( $\Theta_V$ ) around  $30^\circ$  for both measurement campaigns (Figure 6). With regards to the  $\Theta_H$  parameter, it can be observed that in the azimuth plane the recordings of 2016 and 2017 show an oscillation in different directions. In fact, in 2016 there is polarization at  $45^\circ$  while, in 2017, the preferential direction of oscillation becomes perpendicular to the previous one ( $-45^\circ$ ). Despite this variation, we note that the polarization is linear in both surveys.

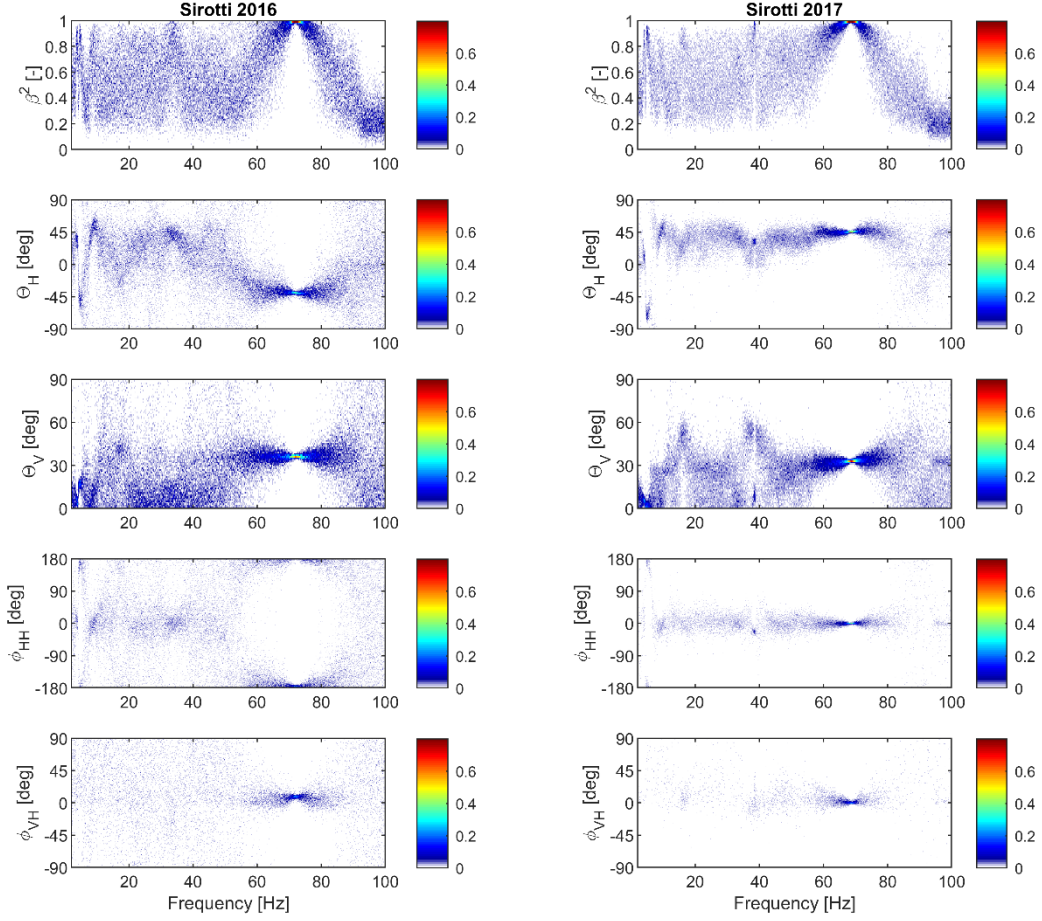


Figure 6 Polarization parameters estimated with the spectral SVD method.

Concerning the vibrational mode at low frequency, the  $\beta^2$  parameter shows the presence of two very close peaks with a strong degree of polarization but with different preferential oscillations in the azimuthal plane. For the 2016 survey,  $\Theta_H$  shows oscillation at  $45^\circ$  and at  $-45^\circ$  for the first and second peak, respectively. Comparing these polarization directions with the results of the HVRS as a function of the azimuth method, we can notice that with the latter analysis we lose the information about the  $-45^\circ$  polarization (Figure 7). As far as the most recent survey is concerned, the two peaks are oriented in the azimuthal plane at about  $20^\circ$  and  $-70^\circ$ , respectively. In this case, both polarizations are present also in the HVSRA plots (Figure 7). In terms of  $\Theta_V$ , we can say that the dominant vibration modes have negligible vertical motion. Given the shape of the tower, we earlier stated that its preferential oscillation should occur perpendicular to its long side, therefore in a direction of about  $60-240^\circ$ . If we took into consideration the results obtained through the HVSRA analysis, we note that the peak close to  $4\text{Hz}$  is roughly in accordance with this statement. We can therefore say that the identified low-frequency vibrational mode has a preferential oscillation perpendicular to the rear fracture that separates the tower from the Bismantova cliff.

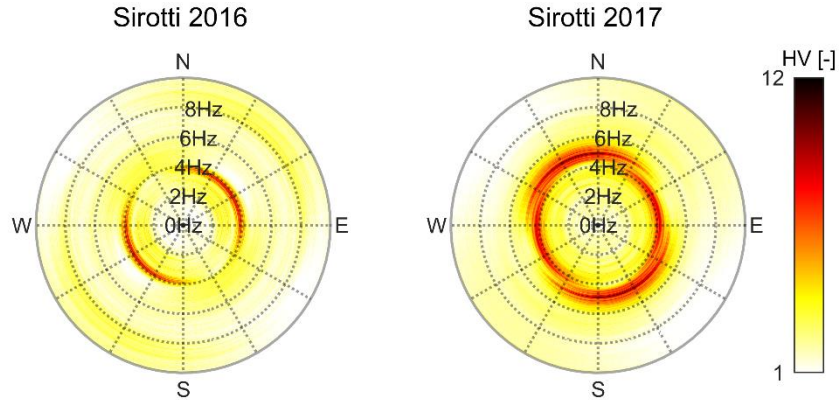


Figure 7 Polarization analysis computed with the HVSR as a function of azimuth.

#### **4.4. Conclusions**

Within this work, we presented the analysis of ambient seismic noise collected at Pietra di Bismantova. The objective of this study was to analyse the dynamic response of the monitored Sirotti tower as well as to infer if a different ground-sensor coupling, with respect to the one used for the Rialba towers, could improve the quality of the ambient seismic noise recordings. On these grounds, we compared the seismic data collected in two different measurement campaigns (2016 and 2017). The computed PSDs displayed an overall similar trend between the two surveys. Nevertheless, a slight difference, especially in term of amplitude, is still present. This made us believe that the differences occurring in the spectral estimates are mostly linked to a change in the ambient seismic noise sources configuration between the two measurement sessions rather than connected to the ground-sensor coupling. The obtained results reveal the presence of significant frequency peaks, indicating vibrational modes of the rock pillar. In detail, two peaks have been observed in the frequency band between 0 and 100 Hz. The first vibrational mode occurs close to 4 Hz and is associated with a bending moment of the tower. Indeed, both the applied polarization techniques highlight a preferential oscillation in the azimuthal plane. On the contrary, the second identified vibrational mode close to 70 Hz, makes it difficult to recognise which is the modal shape that describes the displacement/deformation of the tower. The results furthermore highlight that both peaks experience a frequency variation between the two surveys. However, with the available data, it is difficult to infer whether these variations are related to a change in the stability condition of the tower or to a temporary change due to different climatic conditions. For this reason, it is important to investigate in details the causes of the peaks variations and to perform additional survey campaigns with extended recording duration and other techniques (recording of weather parameters, crack meters, etc) with the final aim of evaluating the stability of rock block.

## 5. Unstable rocks blocks at Malta

In this study, we surveyed the Maltese coasts characterized by coastal slope instability caused by the lateral spreading phenomenon. In this regard, one seismic noise measurement campaign has been performed to evaluate whether the collected signals could provide spectral and polarization features of the analysed unstable compartments even in environmental conditions that are partially different compared to the previously treated case studies. Indeed, dealing with unstable rock blocks along the coasts of the Island of Malta the local passive seismic sources are mainly linked to the sea waves that break against the coast.

### 5.1. Case study

The Maltese archipelago is located between Italy and Africa, in the Sicily Channel. It comprises three main islands: Gozo, Comino and Malta, the latter being the biggest with an area of approximately 246 km<sup>2</sup> (Figure 1). The islands are composed of four Oligo-Miocene geological formations. In order of decreasing age, the layers are the Lower Coralline Limestone (shallow-water carbonates), the Globigerina Limestone (marly-carbonate), the Blue Clay formation (marly-clayey units) and the Upper Coralline Limestone (shallow-water carbonates) (H. M. Pedley *et al.* 1978, M. Pedley 2002, Baldassini & Di Stefano 2017). The presence of the Upper Coralline Limestone formation generates vertical cliffs along the coastline. The superposition of this fragile rock mass over the softer underlying Blue Clay layer fosters the development of the lateral spreading phenomenon. The deformation of the clay lithological unit causes tensile stresses in the limestone plateau resulting in the formation of large surface fractures that produce partially, or totally, isolated blocks having a volume of thousands of cubic meters (Pasuto & Soldati 2013). This condition promotes rock falls and toppling of the rock compartments that slide down to the coast creating large accumulations on the seaside (Figure 1).

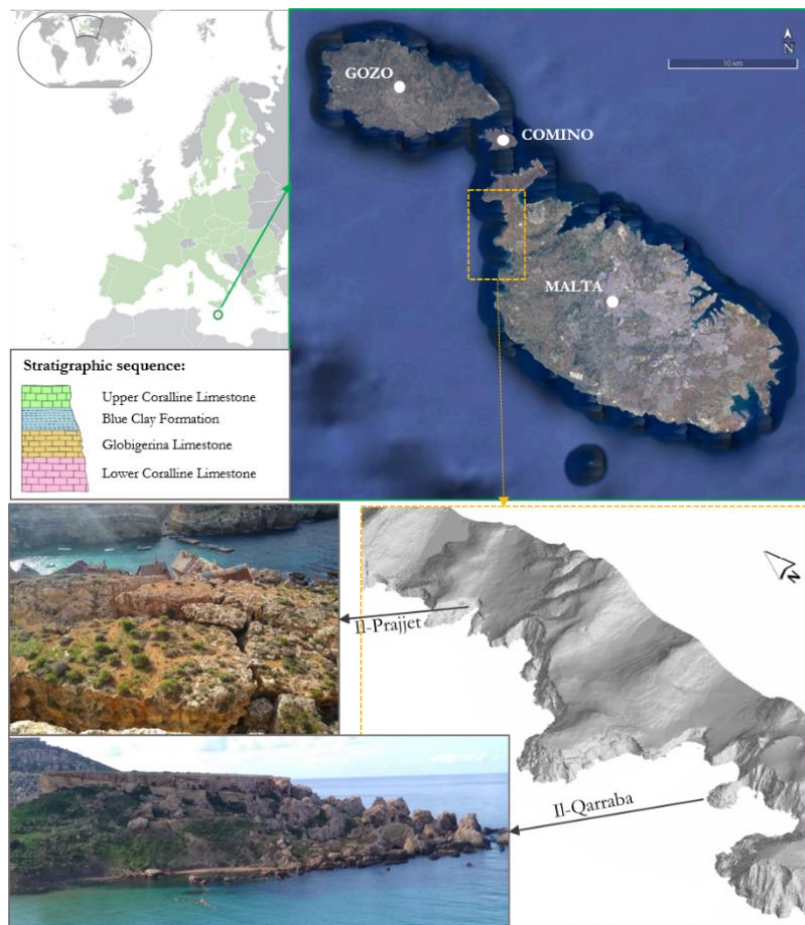


Figure 1 Location of the Maltese archipelago. Stratigraphic sequence of the lithological units. The monitored area is limited with an orange square and two pictures of both Il-Prajjet and Il-Qarraba sites are provided.

Such landslides are also facilitated by coastal erosion. Given the high risk induced by this situation, an ongoing long-term monitoring programme has been carried out at two sites located along the north-western coast of the Malta island with outstanding examples of unstable rock compartments: the Il-Qarraba (Għajnej Tuffieha Bay) and the Il-Prajjet (Anchor Bay) (Figure 1). The project has started in 2005 with the main goal of assessing whether the lateral spreading phenomena and the block slides were active and thus investigating the rate of their movements. In this perspective, two GPS monitoring networks have been deployed on rock plateaus together with extensometers. The former consists of 2 reference stations with 17 benchmarks positioned all over the unstable areas. Additionally, a Satellite Persistent Scatterer Interferometry analysis was carried out for the entire north-western coast of Malta to study the deformation trends and perform a landslide susceptibility assessment of the area (Piacentini *et al.* 2015, Mantovani *et al.* 2016). The first results of the collected data revealed that the movement of the unstable compartments is “extremely slow”, according to the velocity classification provided by Cruden and Varnes (1996). In detail, at Anchor Bay, GPS measurements show a vertical displacement in the area affected by lateral spreading between 5.8 and 10.2 cm in 10 years. Whereas the surveyed isolated blocks revealed an overall planar displacement of 5 cm. Considering the Il-Qarraba site over a 10-year monitoring period, the vertical movements were mostly lower than 1 cm, while the horizontal displacement ranged between a few mm to 2.7 cm. Such results were confirmed by the interferometry analysis both in terms of displacements and velocities (Devoto *et al.* 2013, Mantovani *et al.* 2013). Given the already existing monitoring systems, as well as geological condition similar to Rialba towers, we decided to perform ambient seismic noise measurements both at Anchor Bay and Il-Qarraba sites. Nevertheless, we did perform only one measurement campaign that, even though not sufficient to evaluate changes in unstable compartments stability, provides insight into the feasibility of the ambient noise-based techniques in studying the dynamic response of the unstable rocks.

## 5.2. Method

At each site, four blocks with different dimensions have been selected for ambient noise characterization as shown in Figure 2. Additionally, a seismometer has been also installed on the plateau that was considered stable. At these locations, seismic stations have been deployed to record the ambient noise vibrations for at least 40 minutes. Each station consists of a Nanometric Trillium seismometer and Centaur digitizer. The seismometer features a frequency response function at -3dB spanning between 0.05 and 100 Hz. For the surveys, we set up a sampling frequency at 200 Hz and we deployed the seismic station with the Y-axis oriented towards the North-South direction (thus X-axis was oriented to the East-West direction and the Z-axis tracked the vertical velocity). A GPS antenna has been connected to the digitizer allowing the time-synchronization of the station.

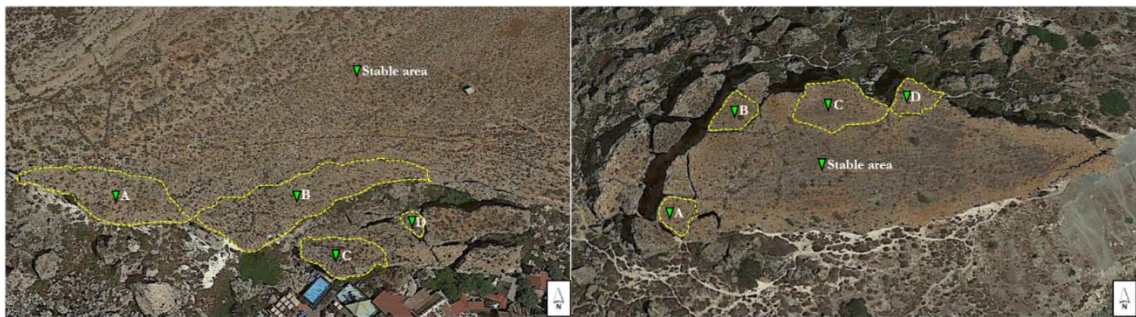


Figure 2 Left: rock compartments analysed at Il-Prajjet (Anchor Bay) site; right: block compartments analysed at Il-Qarraba (Għajnej Tuffieha Bay).

As well as for the previous analysed case studies we did process ambient seismic vibration in the perspective of retrieving both spectral and polarization features of the monitored unstable rock compartments. To this goal, the recordings have been firstly high pass filtered at 0.05 Hz to reject constant offset and unwanted noise link to the corner frequency. We then estimated the spectral features employing Welch’s periodogram as well as the HVSR technique. For this purpose, signals have been divided into 60s length sub-segments tapered with Hamming window. Additionally, for the periodogram computation the spectrum has been estimated with 50% overlap among the obtained windows; whereas for the HVSR curve the windows underwent a spectral smoothing based on the Konno and Oh machi methodology (Konno & Ohmachi n.d.). Concerning the polarization analysis, we did use

both the HVSR as a function of azimuth and the singular value decomposition of the spectral density matrix technique (SVD). In this perspective, for the former, we used the same setup that has been used in the HVSR computation, whereas for the SVD we used 5s-long series, tapered with Hamming window and with an overlapping of 90%.

### 5.3. Results and discussions

The analysis of the ambient seismic noise collected along the Malta coasts did provide different results compared to the ones obtained for the other case studies (Lierna, Rialba and Sirotti unstable blocks). In detail, considering the spectral estimates obtained throughout Welch's periodogram, it can be noticed an amplification occurring at 0.5 Hz. Such a peak exists along with the three components for all the stations installed at the Il-Prajjet site (Figure 3). Whereas, considering the Il-Qarraba cliff, the peak at 0.5 Hz is visible only along with the vertical component (Figure 4). Given the presence of this peak at all studied locations we think that this spectral amplification is connected to a site-effect and not to a vibrational mode of the unstable compartments. Considering the unstable blocks investigated at the Il-Qarraba place, another spectral peak occurs at 1.5 Hz along with the horizontal components. It is curious to notice that at the same frequency, the vertical component spectrum shows an amplitude drop. Even in this case, as a matter of fact, that such behaviour is visible for all the Il-Qarraba compartments despite their different dimensions, we believe that the peak at 1.5Hz is not related to a vibrational mode of the unstable blocks. In figure 3 it is furthermore noticeable the presence of very narrow spectral peaks along with the three components whose occurrence involved almost all stations installed at the Il-Prajjet site and the frequency band up to 60 Hz (the figures are limited to 20 Hz to highlight the occurrence of peaks at low frequencies). We relate these amplifications of the spectrum to the wind for three main reasons. First, their occurrence approximately interests the same frequencies for all the monitored blocks. Second, such peaks are also visible for the seismometer installed on the stable compartment. Finally, the Il-Prajjet survey was performed one day before the Il-Qarraba one and wind was present only during the first measurement session.

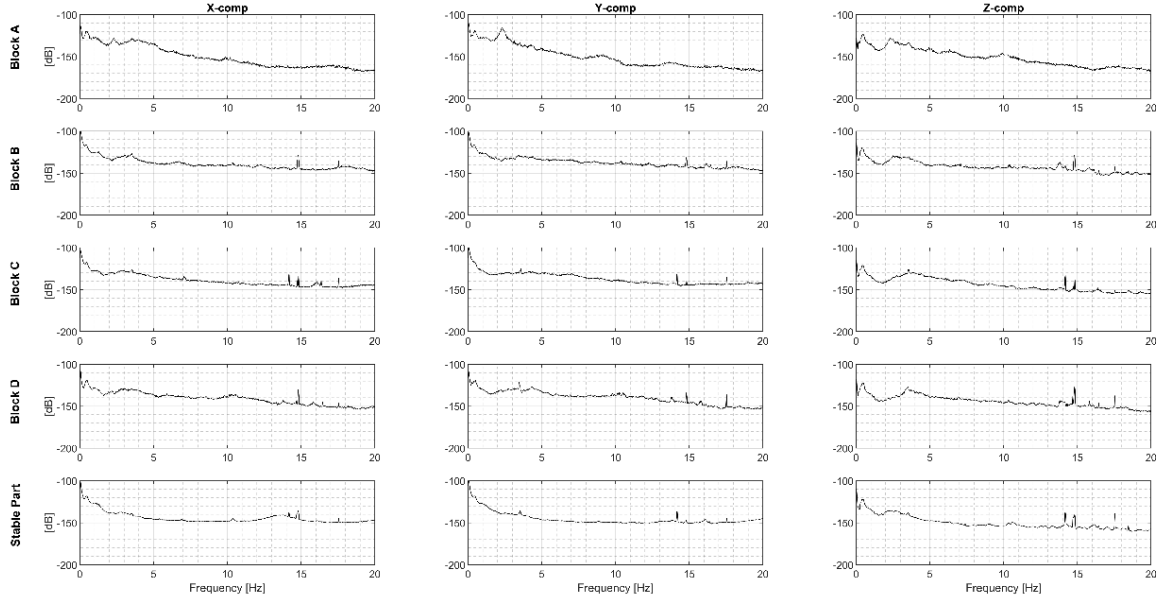


Figure 3 Welch periodograms limited in the 0.05-20 Hz frequency band computed for the ambient seismic noise collected at the Il-Prajjet site.

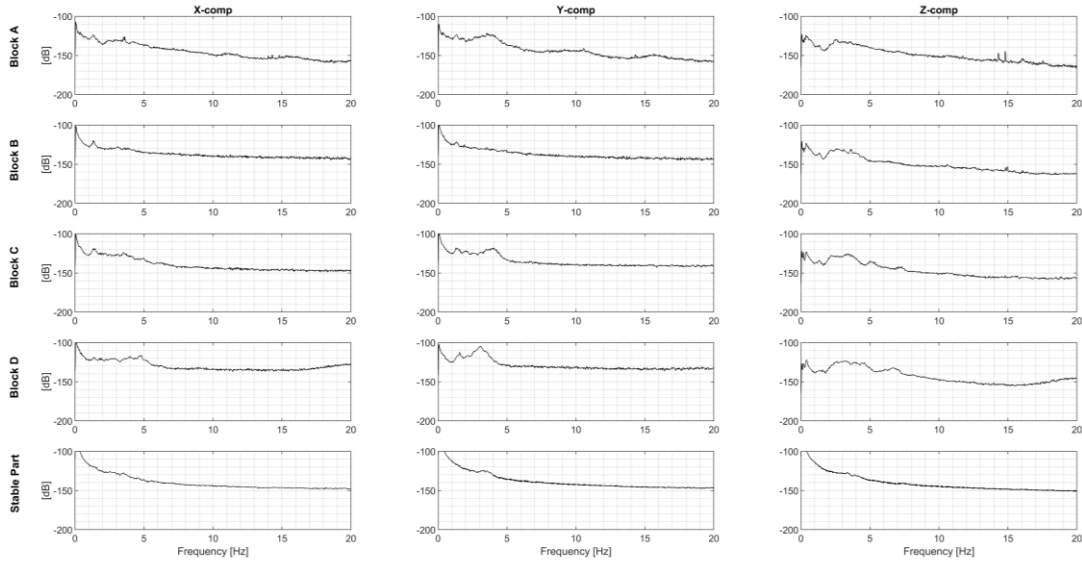


Figure 4 Welch periodograms limited in the 0.05-20 Hz frequency band computed for the ambient seismic noise collected at the Il-Qarraba site.

As far as concerns the HVSR analysis, the results show the presence of a predominant peak at 1.5 Hz for all the monitored sites except for the Il-Qarraba stable area. This outcome is not surprising because previous seismic noise studies highlight the presence of such resonance frequency all around Malta island (Panzera *et al.* 2012, 2013; Vella *et al.* 2013). Such a phenomenon may be related to the interface between the Blue Clay and the Globigerina Limestone formations. Indeed, the lower shear wave velocity of the GL layer, with respect to the UCL formation, gives rise to a velocity inversion (Panzera *et al.* 2012). Such hypothesis was confirmed by Panzera *et al.* (2012) who performed 1-D modelling computing synthetic HVSR curves. The presence of such resonance peak could conceal the vibrational modes of the monitored unstable blocks that occur at similar frequencies. This is particularly true for the Il-Prajjet site where block A, C and D exhibit another peak at 2 Hz which fuse together with the one at 1.5 Hz. Since this secondary peak does not exist in the HVSR curves of the other compartments, neither considering the Il-Qarraba ones, one may suppose that it refers to a vibrational mode of the monitored unstable blocks. Nevertheless, Panzera *et al.* 2012 already observed such HVSRs bimodal dominant peaks in the range of 1-3 Hz and he associated this phenomenon with the interface between the rock-fall, the detritus unit, and the Blue Clay formation, as well as the contact between the latter and the Globigerina Limestone layer. He furthermore noticed that the thickness of the rockfall and the detritus deposits plays an important role in the appearance of the bimodal peaks. Indeed, it seems that the latter phenomenon occurs when the thickness is of the order of tens meters, whereas the fundamental frequency at 1.5 Hz associated with the contact between the BC and the GL occurs for lower thicknesses (Panzera *et al.* 2012). Others amplifications of the HV ratio are visible at 4 Hz for block A of the Il-Prajjet site, at 4.2 and 3 Hz for block C and D of the Il-Qarraba site, respectively. Nevertheless, given the influence of site-effects for this particular case study, it is difficult to infer whether these spectral peaks are associated with vibrational modes of the investigated structures.

With regards to the directional effects of the site response, we observed a very complex polarization pattern both with the HVSR rotate and with the singular value decomposition of the spectral covariance matrix. Figure 6 shows the results of the Horizontal-to-Vertical Spectral Ratio as a function of azimuth for both sites. Considering the Il-Prajjet site, we can observe a prevailing oscillation of the peak around 1.5 Hz along the South-East direction for all four monitored rock blocks (Figure 6-top). Whereas the peak at 2 Hz, which is visible only for the A, C and D structures, is mainly oriented along the North/North-East direction. Due to the fact that the analysis provides quite similar polarization for all the structures of the Il-Prajjet site, we believe, in accordance with the hypothesis stated above, that such spectral peaks polarizations are not linked to the vibrational modes of the structures themselves but rather to are related to the amplification of seismic waves due to the geological setting. Concerning the Il-Qarraba site, more complex polarization features have been observed. Indeed, figure 5 (bottom) shows that the peak at 1.5 Hz has not an obvious polarization in all monitored unstable structures. Regarding the D-block there is clear evidence that the HV peak at 3 Hz is polarized along the North-South direction. Nevertheless, it is

very difficult to identify if such behaviour is related to the dynamic response of the block rather than linked to a site effect.

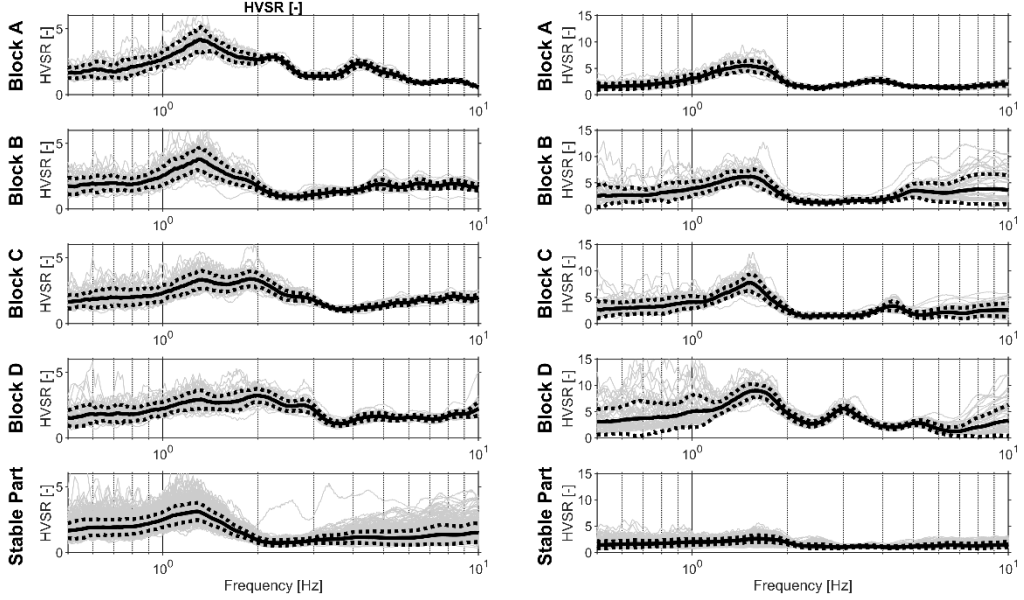


Figure 5 Left: HVSR curve for the Il-Prajet site. Right: HVSR curve for the Il-Qarraba site.

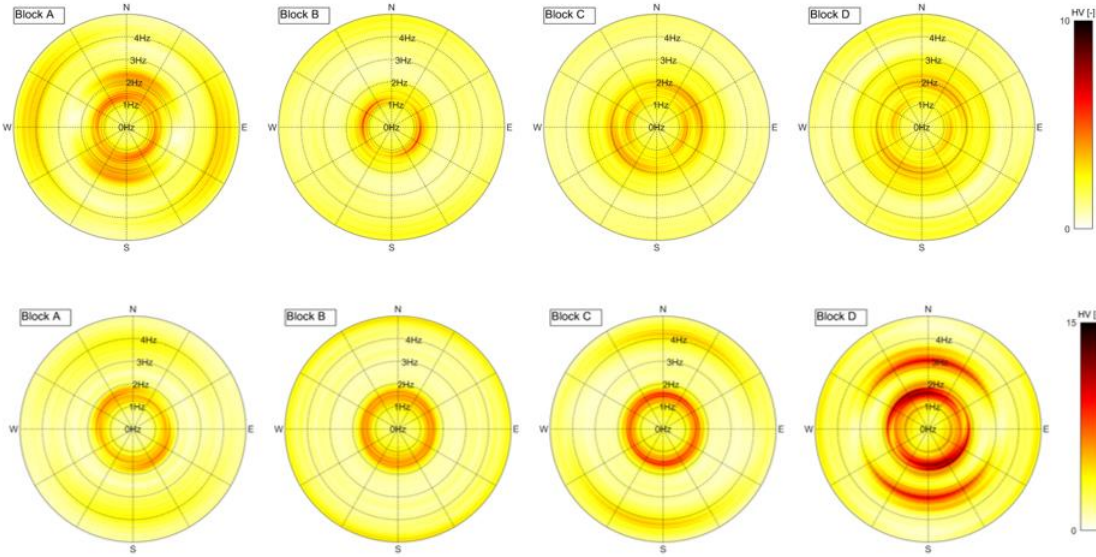


Figure 6 Horizontal-to-Vertical Spectral Ratios as a function of azimuth computed for the Il-Prajet (top) and Il-Qarraba sites. The plots have been limited in the frequency band where HV peaks have been observed.

The observed polarization wavefield complexity in the HVSRA has been highlighted also with the SVD method. The degree of polarization ( $\beta^2$ ) rarely shows unitary values and thus it is difficult to identify polarized frequencies. Nevertheless, for the B-block of the Il-Prajet site the  $\beta^2$  parameter converges towards a unitary value for 32 Hz and 60 Hz. As observed by Burjanek et al. (2010), the presence of high-frequency ground motion can be controlled by the vibration of smaller blocks that imply both different resonant frequencies and directions with respect to the main compartment. Similar behaviour is observed for the Il-Qarraba measurement campaign. For this case, blocks A, B and C show a degree of polarization close to 1 in the range of 20-60 Hz. Such polarization of the wavefield occurring at high frequency at both sites are characterized by a zero value of the  $\Theta_V$  parameter meaning that the oscillation takes place in the azimuthal plane. With regards to the corresponding  $\Theta_H$  values, it can be noticed that

each block exhibits different polarization directions. This may confirm the fact that such oscillations are associated to vibrational modes of smaller blocks and not to site effects or weather conditions (i.e., wind) because, in such a case, we would expect a common polarization response for all the monitored blocks.

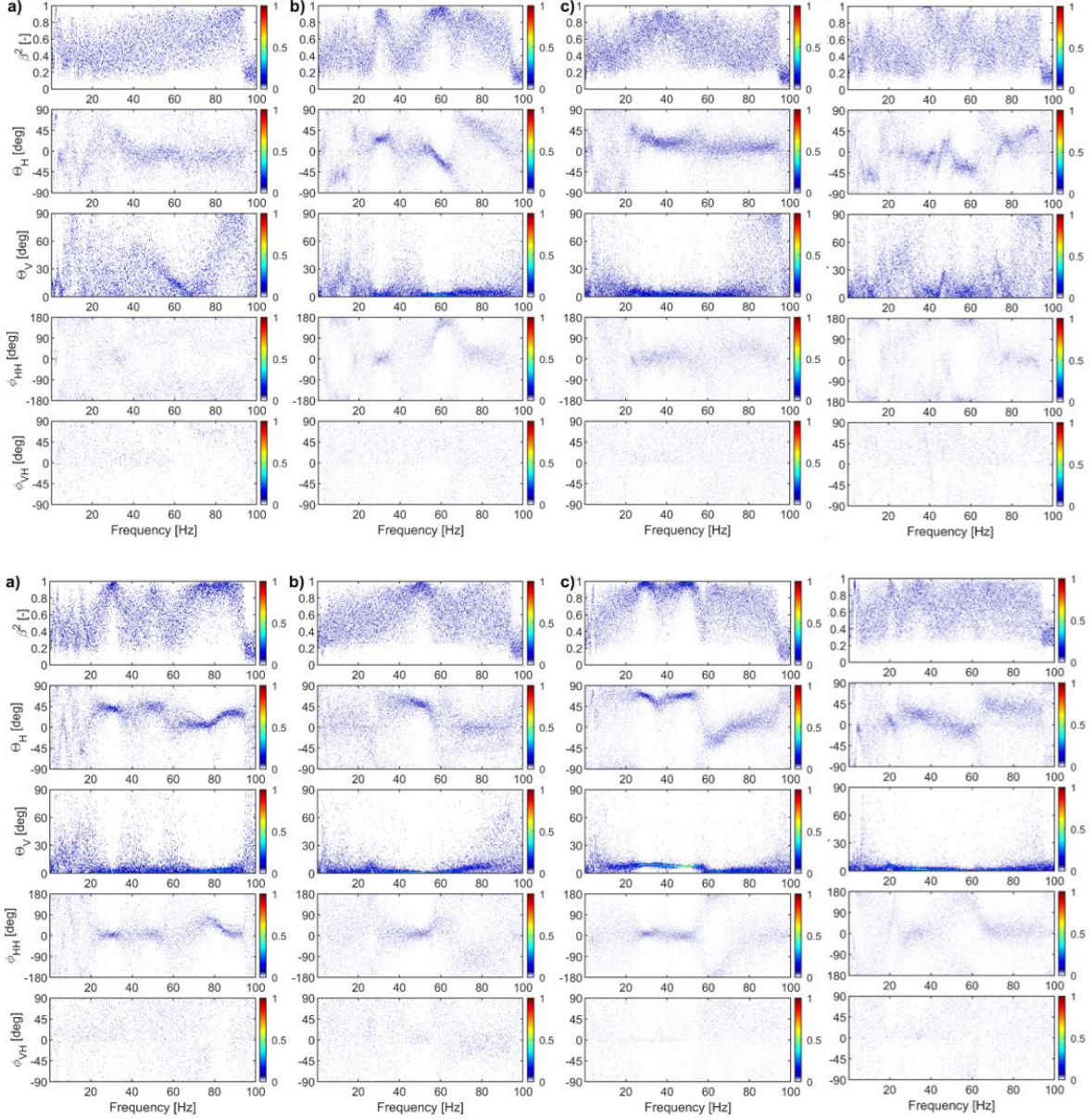


Figure 7 Polarization parameters estimated with the spectral SVD method for all blocks of the Il-Prajet (top) and Il-Qarraba sites. The colormap indicates the relative probability of the estimated parameter.

#### 5.4. Conclusions

This section of the manuscript presents the analysis of the ambient seismic noise collected on unstable compartments of Malta island. The area is interested by collapse mechanisms, such as rockfalls, toppling and sliding of rock structures, that are most likely induced by lateral spreading phenomena due to the different stiffness of the clay and the overlying limestone. In this perspective, both spectral and polarization analyses have been performed to infer the dynamic response of the investigated unstable rock blocks. The obtained results indicate that the dynamic response of the potentially unstable compartments is very complex. Such complexity seems to be related to the amplification of seismic ground motion related to a lithologic factor rather than directly connected to the

vibrational modes of the blocks themselves. The application of the horizontal-to-vertical spectral ratio technique points out the existence of single and bimodal dominant peaks at about 1.5 and 2 Hz that we deem to be linked to the presence of the Blue Clay in the shallow lithologic sequence. This condition raises difficulties in assessing the vibrational modes of the unstable structures. In fact, in such environments, amplifications occurring in the HVSR curves due to site effects may hide the existence of structures vibrational modes making it difficult to investigate changes in the rocks' stability employing modal analysis. Moreover, we also observed that the presence of wind may generate spectral amplification in the power spectral density plots which can lead to erroneous evaluations of the vibrational modes. Nevertheless, such problems can be elided through continuous recordings because such peaks should disappear in the dataset where the wind is absent. Finally, the polarization analysis revealed complex directivity phenomena of the collected recordings. Even in this case, it is hard to assess how much the polarization features are influenced by the geological factors rather than the vibrational modes of the unstable compartments. To conclude, the results of this study highlighted a potential problem when monitoring the unstable rock block stability using the above-mentioned techniques. In fact, we have observed that in particular geological conditions it is challenging to distinguish the vibrational modes from the spectral amplifications linked to site effects. In this case, it is, therefore, necessary to pay close attention and preliminary geological and geophysical investigations are necessary to infer whether spectral peaks are effectively connected to the dynamic response of unstable blocks.

## 6. General conclusions

In this first macro-section of the manuscript, we investigated the effectiveness of the ambient seismic noise recordings in monitoring rock structures stability. In this perspective, we started our analysis by performing a controlled collapse test with a dual aim. First, we wanted to confirm the literature findings according to which the collapse of unstable rocks is preceded by a drop of its resonance frequencies as a consequence of the rock bridges breakage. Second, we did analyse the ambient seismic noise recordings using different spectral and polarization techniques to infer which of them is more suitable to retrieve dynamic features of the unstable rock blocks. We finally extended the application of the techniques that have been found to be the most effective ones, to rock structures that represent a serious threat to the surrounding areas.

With this work, we confirmed that both spectral and polarization features of seismic noise recordings are strictly linked to the evolving constraints of the unstable rock blocks thus, with their stability. In detail, we observed that rock bridges breakage may lead to a drop of resonance frequencies but also to a new dynamic response if the monitored rock undergoes an abrupt change of its initial stability condition. In the perspective of spectral analysis, we deem that the most easily understandable results are provided by the spectrograms. The latter's bias and variability can be reduced using Welch's periodogram or Multitaper techniques which can lead to similar results if proper input parameters are chosen. However, spectrogram results must be coupled to spectral estimates to precisely identify the frequency occurrence of the spectral peaks. With regards to the Horizontal-to-Vertical Spectra Ratio, we think that it is a useful technique to highlight resonance frequencies associated with deformations occurring in the azimuthal plane, that is the case of column-like structures. Nevertheless, it should be carefully considered because the spectral division between the horizontal and vertical components may delete some frequency peaks associated with vibration modes whose vertical component dwarfs the horizontal ones. This is for instance the case of rocks with arbitrary geometry and uncertain boundary conditions. Additionally, we also observed that in certain circumstances such a method may lead to misleading results. In fact, HVSR peaks may be linked to site effects and not to the vibrational modes of the unstable structures. We, therefore, suggest performing preliminary geological and geophysical investigations to infer whether spectral peaks are effectively associated with unstable blocks dynamic response. Polarization analysis performed using the spectral SVD approach proved to be the most complete method to study 3D motion characteristics of rock structures, to understand their vibration modes and to track their variation over time. This analysis provides more knowledge on the kinematic and dynamic conditions of unstable slopes with respect to the hodograms, the time-domain covariance matrix method and the HVSRA approach. Our work also shows that realistic numerical modelling of the dynamic behaviour of rock structures is still a challenging task especially in terms of the accurate definition of the spatial and mechanical features of the constraints. Therefore, the support of modelling to guide the processing and interpretation of seismic noise data still needs to be improved. However, non-destructive geophysical techniques (i.e. radar) could be employed to characterize rock fractures and rock bridges in a non-destructive manner (Arosio 2016; Guerin et al. 2019).

This study leads us to state that a proper monitoring approach should take into account both spectral and polarization features of the collected ambient seismic noise since both of them provide precious information regarding the dynamic response of the monitored structures. We must say that the analysed case studies have provided preliminary outcomes since a rigorous investigation should involve continuous monitoring to distinguish between changes linked to the variation of the stability condition by those linked to temporary changes of the rocks' dynamic response (i.e. climatic conditions). Indeed, dealing with long-term monitoring systems, one should not forget that the dynamic characteristics of the investigated structures may vary for instance as a consequence of the rock dilatation due to temperature increase and the ice formation in the fractures (e.g., Levy et al. 2010). Freeze-thaw cycles can also contribute to the irreversible fissure growth that may eventually cause the collapse of the rock structure. Moreover, we have observed that performing seismic noise measurement campaigns in different epochs can introduce changes in both spectral and polarization features as a result of a different configuration of the seismic noise sources among the measurement campaigns. We thus suggest avoiding the measure of unstable compartments dynamics properties at different survey sessions if it is not possible to characterize the influence of the seismic background noise. The results of this study suggest that the evolution of fundamental frequency could be a reliable precursor of rock falls, provided that reversible and irreversible effects are correctly identified. This leads to the conclusion that seismic noise monitoring may be a reliable tool whose integration with standard geological/geotechnical techniques could improve our capabilities for rock failure forecasting.

## 7. Bibliography

- Arosio, D., Longoni, L., Papini, M., Scaioni, M., Zanzi, L. & Alba, M. (2009) Towards rockfall forecasting through observing deformations and listening to microseismic emissions. *Natural Hazards and Earth System Science*, 9, 1119–1131. doi:10.5194/nhess-9-1119-2009
- Arosio, D., 2016. Rock fracture characterization with GPR by means of deterministic deconvolution, *Journal of Applied Geophysics*, 126, 27–34.
- Arosio, D., Corsini, A., Giusti, R., & Zanzi, L. (2017). Seismic Noise Measurements on Unstable Rock Blocks: The Case of Bismantova Rock Cliff. In M. Mikoš, Ž. Arbanas, Y. Yin, & K. Sassa (Eds.), *Advancing Culture of Living with Landslides* (pp. 325–332). Springer International Publishing. [https://doi.org/10.1007/978-3-319-53487-9\\_37](https://doi.org/10.1007/978-3-319-53487-9_37)
- Arosio, Diego, Longoni, L., Papini, M., Boccolari, M. & Zanzi, L. (2018) Analysis of microseismic signals collected on an unstable rock face in the Italian Prealps. *Geophysical Journal International*, 213, 475–488. doi:10.1093/gji/ggy010
- Arosio, D., Longoni, L., Papini, M., Bièvre, G. & Zanzi, L., 2019a. Geological and geophysical investigations to analyse a lateral spreading phenomenon: the case study of Torrioni di Rialba, northern Italy, *Landslides*, 16(7), 1257–1271.
- Arosio, D., Taruselli, M., Longoni, L., Papini, M. & Zanzi, L. 2019b. Seismic Noise Polarization Analysis for Unstable Rock Monitoring, in *Proceedings of the 25th European Meeting of Environmental and Engineering Geophysics*, The Hague, The Netherlands, pp. 1-5, Vol. 2019, doi:10.3997/2214-4609.201902451.
- Baldassini, N. & Di Stefano, A. (2017) Stratigraphic features of the Maltese Archipelago: a synthesis. *Nat Hazards*, 86, 203–231. doi:10.1007/s11069-016-2334-9
- Bièvre G, Oxarango L, Günther T, Goutaland G, Massardi M (2018) Improvement of 2D ERT measurements conducted along a small earth-filled dyke using 3D topographic data and 3D computation of geometric factors. *J Appl Geophys* 153:100–112
- Borgatti L, Tosatti G (2010) Slope instability processes affecting the Pietra di Bismantova geosite (Northern Apennines, Italy). *Geoheritage* 2:155–168
- Bottelin, P., Baillet, L., Larose, E., Jongmans, D., Hantz, D., Brenguier, O., Cadet, H. & Helmstetter, A., 2017. Monitoring rock reinforcement works with ambient vibrations: La Bourne case study (Vercors, France), *Engineering Geology*, 226, 136–145.
- Bottelin, P., Jongmans, D., Baillet, L., Lebourg, T., Hantz, D., Lévy, C., Le Roux, O., Cadet, H., Lorier, L., Rouiller, J.D., Turpin J. & Darras, L., 2013a. Spectral analysis of prone-to-fall rock compartments using ambient vibrations, *Journal of Environmental and Engineering Geophysics*, 18, 205–217.
- Bottelin, P., Levy, C., Baillet, L., Jongmans, D. & Gueguen, P., 2013b. Modal and thermal analysis of Les Arches unstable rock column (Vercors Massif, French Alps), *Geophysical Journal International*, 194, 849–858.
- Bottelin, P., Jongmans, D., Daudon, D., Mathy, A., Helmstetter, A., Bonilla-Sierra, V., Cadet, H., et al. (2014) Seismic and mechanical studies of the artificially triggered rockfall at Mount Néron (French Alps, December 2011). *Natural Hazards and Earth System Sciences*, 14, 3175–3193. doi:10.5194/nhess-14-3175-2014
- Burjánek, J., Gassner-Stamm, G., Poggi, V., Moore, J. R., and Fäh, D.: Ambient vibration analysis of an unstable mountain slope, *Geophys. J. Int.*, 180, 820–828, doi:10.1111/j.1365-246X.2009.04451.x, 2010.
- Burjánek, J., Gischig, V., Moore, J.R. & Fäh, D., 2018. Ambient vibration characterization and monitoring of a rock slope close to collapse, *Geophysical Journal International*, 212, 297–310.
- Burjánek, J., Kleinbrod, U. & Fäh, D., 2019. Modelling the seismic response of unstable rock mass with deep compliant fractures, *Journal of Geophysical Research: Solid Earth*, 124, 13039–13059.
- Burjánek, J., Moore, J.R., Yugsi Molina, F.X. & Fäh, D., 2012. Instrumental evidence of normal mode rock slope vibration, *Geophysical Journal International*, 188, 559–569.
- Clinton, J.F., Case Bradford, S., Heaton, T.H. & Favela, J., 2006. The observed wander of the natural frequencies in a structure, *Bull Seismol Soc Am*, 96(1), 237–257.
- Colombero, C., Baillet, L., Comina, C., Jongmans, D. & Vinciguerra, S., 2017. Characterization of the 3-D fracture setting of an unstable rock mass: from surface and seismic investigations to numerical modelling, *J Geophys Res Solid Earth*, 122, 6346–6366.
- Conti S, Tosatti G (1994) Caratteristiche geologico-strutturali della Pietra di Bismantova e fenomeni franosi connessi (Appennino reggiano). *Quad Geol Appl* 1:25–43
- Corsini A, Bonacini F, Deiana M, Giusti R, Russo M, Ronchetti F, Cantini C, Truffelli G, Iasio C, Generali M, Ascari L, Chiesi L, Venturi L (2016a) A wireless crackmeters network for the analysis of rock falls at the

- Pietra di Bismantova natural heritage site (Northern Apennines, Italy). In: Aversa S, Cascini L, Picarelli L, Scavia C (eds) Landslides and engineered slopes. Experience, theory and practice. CRC Press, London, pp 685–690
- Corsini A, Ronchetti F, Giusti R, Deiana M (2016b) Definition of the geological-technical framework regarding the conditions of instability of the Petra di Bismantova (Castelnovo ne' Monti—RE) aimed at preliminary assessment of mitigation actions. University of Modena and Reggio Emilia Open File Report. <http://www.geoapp.unimore.it/>. (in Italian)
- Cruden DM, Varnes DJ (1996) Landslides investigation and mitigation, transportation research board. In: Turner AK, e (eds) Landslide types and process, vol 247. National Research Council, National Academy Press, Washington, pp 36–75 Special Report
- Del Gaudio, V. & Wasowski, J., 2007. Directivity of slope dynamic response to seismic shaking, *Geophys Res Lett*, 34, L12301.
- Del Gaudio, V., Coccia, S., Wasowski, J., Gallipoli, M.R. & Mucciarelli, M. (2008) Detection of directivity in seismic site response from microtremor spectral analysis. *Natural Hazards and Earth System Science*, 8, 751–762. doi:10.5194/nhess-8-751-2008
- Del Gaudio, Vincenzo, Muscillo, S. & Wasowski, J. (2014) What we can learn about slope response to earthquakes from ambient noise analysis: An overview. *Engineering Geology*, 182. doi:10.1016/j.enggeo.2014.05.010
- Del Gaudio, Vincenzo & Wasowski, J. (2011) Advances and problems in understanding the seismic response of potentially unstable slopes. *Engineering Geology*, 122, 73–83. doi:10.1016/j.enggeo.2010.09.007
- Devoto, S., Biolchi, S., Bruschi, V.M., Díez, A.G., Mantovani, M., Pasuto, A., Piacentini, D., et al. (2013) Landslides Along the North-West Coast of the Island of Malta. in *Landslide Science and Practice* eds. Margottini, C., Canuti, P. & Sassa, K., pp. 57–63, Berlin, Heidelberg: Springer Berlin Heidelberg. doi:10.1007/978-3-642-31325-7\_7
- Franklin, J.A., 1985. Suggested method for determining point load strength, *International Journal of Rock Mechanics and Mining Sciences & Geomechanics Abstracts*, 22(2), 51-60.
- Frayssines, M. & Hantz, D., 2006. Failure mechanisms and triggering factors in calcareous cliffs of the Subalpine Ranges (French Alps), *Engineering Geology*, 86(4), 256–270.
- Gallipoli, M. R. and Mucciarelli, M.: Effetti direzionali in registrazioni sismometriche in aree in frana e bordi di bacino, Extended Abstracts of XXVI G. N. G. T. S. Conference, Rome, 13–15 November 2007, last accessed February 2008 as <http://www2.ogs.trieste.it/gngts/gngts/convegniprecedenti/2007/riassunti/tema-2/2-sess-2/22-gall.pdf>, 2007.
- Gaudio, V.D. & Wasowski, J. (2007) Directivity of slope dynamic response to seismic shaking. *Geophysical Research Letters*, 34. doi:<https://doi.org/10.1029/2007GL029842>
- GSUEG—Gruppo di Studio Università Emiliane per la Geomorfologia (1976) Geomorphological conditions of the Pietra di Bismantova area (Reggio Emilia Apennines). *Boll Serv Geol Ital* 97. Roma (in Italian)
- Guerin, A., Jaboyedoff, M., Collins, B.D., Derron, M.H., Stock, G.M., Matasci, B., Boesiger, M., Lefevre, C. & Podladchikov, Y.Y., 2019. Detection of rock bridges by infrared thermal imaging and modelling, *Scientific Reports*, 9(1), 13138.
- Günther T, Rücke C, Spitzer K (2006) Three-dimensional modelling and inversion of DC resistivity data incorporating topography—II. Inversion. *Geophys J Int* 166:506–517
- Jongmans, D. & Garambois, S. (2007) Geophysical investigation of landslides: A review. *Bulletin de la Societe Geologique de France*, 178. doi:10.2113/gssgbull.178.2.101
- Katz, O., Reches, Z. & Roegiers, J.C., 2000. Evaluation of mechanical rock properties using a Schmidt hammer, *Int J Rock Mech Min Sci*, 37, 723–728.
- Kleinbrod, U., Burjánek, J. & Fäh, D. (2017) On the seismic response of instable rock slopes based on ambient vibration recordings. *Earth, Planets and Space*, 69. doi:10.1186/s40623-017-0712-5
- Konno, K. & Ohmachi, T., 1998. Ground-motion characteristics estimated from spectral ratio between horizontal and vertical components of microtremor, *Bull Seismol Soc Am*, 88(1):228-241.
- Koper, K.D. & Hawley, V.L., 2010. Frequency dependent polarization analysis of ambient seismic noise recorded at a broadband seismometer in the central United States, *Earthq Sci*, 23(5), 439-447.
- Kulatilake, P.H.S.W., Shreedharan, S., Sherizadeh, T., Shu, B., Xing, Y. & He, P., 2016. Laboratory Estimation of Rock Joint Stiffness and Frictional Parameters, *Geotech Geol Eng*, 34(6), 1723–1735.
- Lévy, C., Baillet, L., Jongmans, D., Mourot, P. & Hantz, D. (2010) Dynamic response of the Chamouset rock column (Western Alps, France). *Journal of Geophysical Research*, 115. doi:10.1029/2009JF001606
- Longoni, L., Arosio, D., Scaioni, M., Papini, M., Zanzi, L., Roncella, R. & Brambilla, D. (2012) Surface and subsurface non-invasive investigations to improve the characterization of a fractured rock mass. *Journal of Geophysics and Engineering*, 9, 461–472. doi:10.1088/1742-2132/9/5/461

- Lorenzoni, F., Caldron, M., Porto, F. da, Modena, C. & Aoki, T. (2018) Post-earthquake controls and damage detection through structural health monitoring: applications in l'Aquila. *J Civil Struct Health Monit*, 8, 217–236. doi:10.1007/s13349-018-0270-y
- Mantovani, M., Devoto, S., Forte, E., Mocnik, A., Pasuto, A., Piacentini, D. & Soldati, M. (2013) A multidisciplinary approach for rock spreading and block sliding investigation in the north-western coast of Malta. *Landslides*, 10, 611–622. doi:10.1007/s10346-012-0347-3
- Mantovani, M., Devoto, S., Piacentini, D., Prampolini, M., Soldati, M. & Pasuto, A. (2016) Advanced SAR Interferometric Analysis to Support Geomorphological Interpretation of Slow-Moving Coastal Landslides (Malta, Mediterranean Sea). *Remote Sensing*, 8, 443. doi:10.3390/rs8060443
- Migliazza M, Giani GP (2005) Analisi dei fenomeni di crollo nella Pietra di Bismantova (RE). GEAM 116:41–50 (in Italian)
- Moore, J. R., Gischig, V., Burjanek, J., Loew, S. & Fah, D. (2011) Site Effects in Unstable Rock Slopes: Dynamic Behavior of the Randa Instability (Switzerland). *Bulletin of the Seismological Society of America*, 101, 3110–3116. doi:10.1785/0120110127
- Moore, Jeffrey R., Thorne, M.S., Koper, K.D., Wood, J.R., Goddard, K., Burlacu, R., Doyle, S., et al. (2016) Anthropogenic sources stimulate resonance of a natural rock bridge: Resonance of a Natural Bridge. *Geophysical Research Letters*, 43, 9669–9676. doi:10.1002/2016GL070088
- Panzera, F., D'Amico, S., Lotteri, A., Galea, P. & Lombardo, G. (2012) Seismic site response of unstable steep slope using noise measurements: the case study of Xemxija Bay area, Malta. *Natural Hazards and Earth System Sciences*, 12, 3421–3431, Copernicus GmbH. doi:<https://doi.org/10.5194/nhess-12-3421-2012>
- Panzera, F., D'Amico, S., Galea, P., Lombardo, G., Gallipoli, M.R. & Pace, S., 2013. Geophysical measurements for site response investigation: preliminary results on the island of Malta, *Bollettino di Geofisica Teorica ed Applicata*, 54(2), 111–128.
- Park, J., Vernon, F.L. & Lindberg, C.R., 1987. Frequency dependent polarization analysis of high-frequency seismograms, *J Geophys Res Solid Earth*, 92(B12), 12664–12674.
- Pasuto A, Soldati M (2013) Lateral spreading. In: Shroder JF, Marston RA, Stoffel M (eds) Treatise on Geomorphology, Mountain and Hillslope Geomorphology, vol 7. Academic Press, San Diego, pp 239–248. doi:10.1016/B978-0-12-374739-6.00173-1
- Pedley, H.M., House, M.R. & Waugh, B. (1978) The geology of the Pelagian Block : the Maltese Islands. Retrieved from <https://www.um.edu.mt/library/oar/handle/123456789/4307>
- Pedley, M. (2002) Limestone isles in a crystal sea: the geology of the Maltese Islands, San Gwann, Malta: Publishers Enterprises Group.
- Percival, D.B. & Walden, A.T., 1993. Spectral Analysis for Physical Applications: Multitaper and Conventional Univariate Techniques, Cambridge University Press, Cambridge.
- Perrone, A., Lapenna, V. & Piscitelli, S. (2014) Electrical resistivity tomography technique for landslide investigation: A review. *Earth-Science Reviews*, 135, 65–82. doi:10.1016/j.earscirev.2014.04.002
- Piacentini, D., Devoto, S., Mantovani, M., Pasuto, A., Prampolini, M. & Soldati, M. (2015) Landslide susceptibility modeling assisted by Persistent Scatterers Interferometry (PSI): an example from the northwestern coast of Malta. *Nat Hazards*, 78, 681–697. doi:10.1007/s11069-015-1740-8
- Potenza, F., Federici, F., Lepidi, M., Gattulli, V., Graziosi, F. & Colarieti, A. (2015) Long-term structural monitoring of the damaged Basilica S. Maria di Collemaggio through a low-cost wireless sensor network. *J Civil Struct Health Monit*, 5, 655–676. doi:10.1007/s13349-015-0146-3
- Reynolds JM (2011) An introduction to applied and environmental geophysics, 2nd Edition. Wiley-Blackwell
- Roveri E (1968) The Pietra di Bismantova (Reggio Emilia): geomorphological and stability conditions. *L'Ateneo Parmense*, vol 4, fasc. 1. 15 p. (in Italian)
- Rücker C, Günther T, Spitzer K (2006) Three-dimensional modelling and inversion of DC resistivity data incorporating topography—I. Modelling. *Geophys J Int* 166:495–505
- Saisi, A., Gentile, C. & Guidobaldi, M. (2015) Post-earthquake continuous dynamic monitoring of the Gabbia Tower in Mantua, Italy. *Construction and Building Materials*, 81, 101–112. doi:10.1016/j.conbuildmat.2015.02.010
- Samson, J.C., 1983. Pure states, polarized waves, and principal components in the spectra of multiple, geophysical time-series, *Geophys J R Astron Soc*, 72, 647-664.
- Spillmann, T., Maurer, H., Green, A.G., Heincke, B., Willenberg, H. & Husen, S., 2007. Microseismic investigation of an unstable mountain slope in the Swiss Alps, *J Geophys Res Solid Earth*, 112, B07301.
- Sonmez, H., Gokceoglu, C., Nefeslioglu, H.A. & Kayabasi, A., 2006. Estimation of rock modulus: For intact rocks with an artificial neural network and for rock masses with a new empirical equation, *International Journal of Rock Mechanics & Mining Sciences*, 43(2), 224–235.

- Starr, A.M., Moore, J.R. & Thorne, M.S., 2015. Ambient resonance of Mesa Arch, Canyonlands National Park, Utah, *Geophys Res Lett*, 42, 6696–6702.
- Taruselli, M., Arosio, D., Longoni, L., Papini, M., Corsini, A. & Zanzi, L. (2018) Rock Stability as Detected by Seismic Noise Recordings - Three Case Studies, Presented at the 24th European Meeting of Environmental and Engineering Geophysics, Porto, Portugal. doi:10.3997/2214-4609.201802611
- Templeton, M.E., 2017. IRIS Library of Nominal Response for Seismic Instruments. Incorporated Research Institutions for Seismology. Dataset. <https://doi.org/10.17611/S7159Q>
- Thomson, D.J., 1982. Spectrum estimation and harmonic analysis, *Proc IEEE*, 70, 1055–1096.
- Valentin, J., Capron, A., Jongmans, D., Baillet, L., Bottelin, P., Donze, F., Larose, E., et al. (2017) The dynamic response of prone-to-fall columns to ambient vibrations: comparison between measurements and numerical modelling. *Geophysical Journal International*, 208, 1058–1076. doi:10.1093/gji/ggw440
- Vella, A., Galea, P. & D'Amico, S., 2013. Site frequency response characterisation of the Maltese islands based on ambient noise H/V ratios, *Eng. Geol.*, 163, 89–100.
- Yuen, K.-V. & Kuok, S.-C. (2010) Modeling of environmental influence in structural health assessment for reinforced concrete buildings. *Earthq. Eng. Eng. Vib.*, 9, 295–306. doi:10.1007/s11803-010-0014-4

## Appendix

In order to estimate the spectral content of the recorded ambient seismic noise, we deem that the two most valuable techniques are Welch's periodogram and the multitaper spectral estimation. However, we observed that with a proper setting of the required parameters, the two methodologies converge to the same result. If we analyse the result shown in Figure A.1, we can see that the spectral estimates perfectly match each other at each frequency. A small difference occurs above 90 Hz but we think that this discrepancy between the two methods can be associated with the border effects introduced by the windowing of Welch's periodogram. Considering the zoomed spectrum in the range between 5 and 20 Hz (Figure A.1 b), we clearly notice that the modified periodogram (Welch) provides a more smoothed spectral estimate than the multitaper method. Nevertheless, this effect does not interfere with the identification of spectral peaks. The most important difference between the two techniques is the increased computation time when the spectral estimate is performed with the multitaper method. Indeed, if we process a 10 s long signal with a frequency resolution of 0.1 Hz, Welch's method is 15 times faster than the multitaper one. For this reason, and given the length of the collected ambient seismic noise (recordings are generally longer than 1 hour), we decided to perform the spectral estimates using only Welch's periodogram since it provides satisfactory results in a very short time.

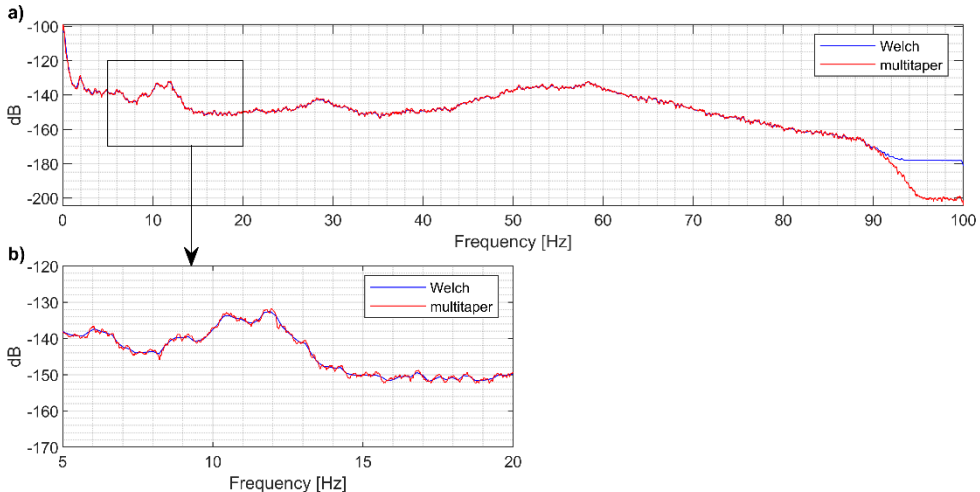


Figura A.1 a) Comparison between Welch's periodogram (blue line) and multitaper method (red line). b) Zoomed spectrum in the range 5-20 Hz.

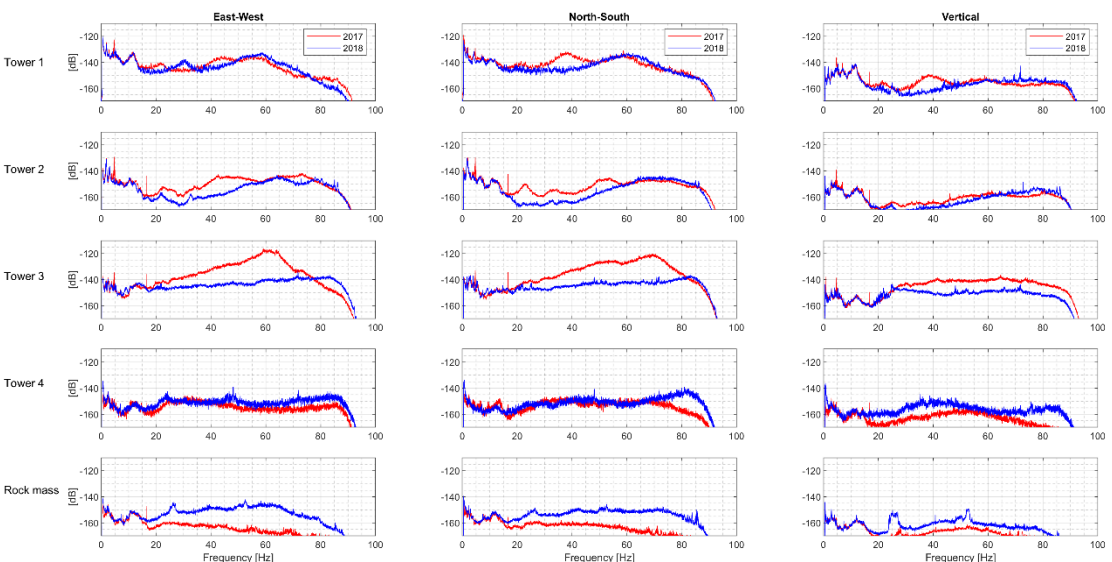


Figura A.2 Welch's periodograms obtained for the dataset collected with the 2017 and 2018 surveys.

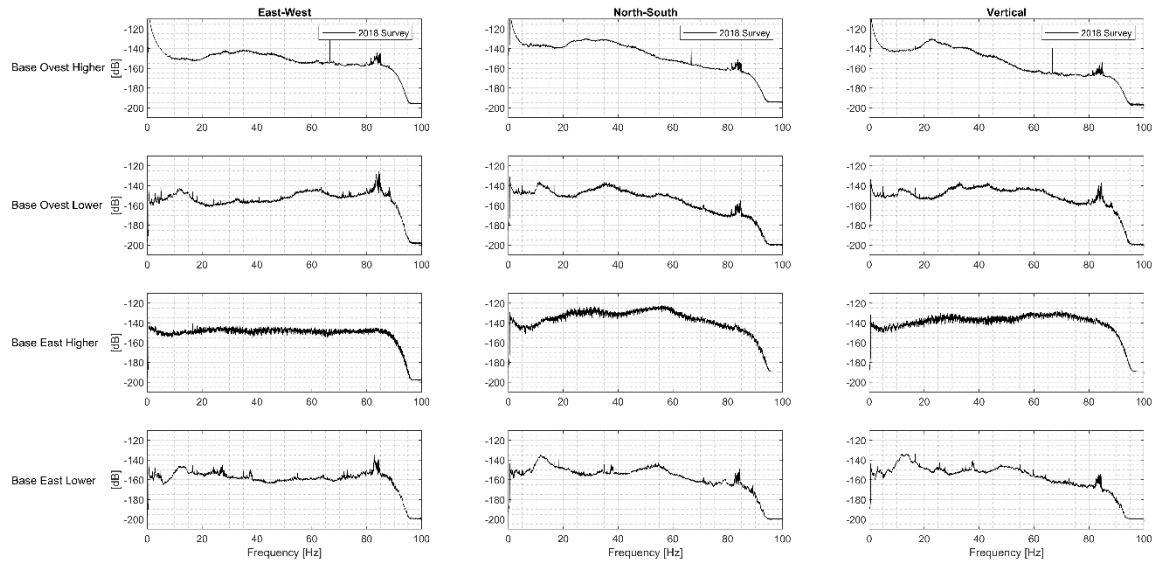


Figura A.3 Welch's periodograms obtained for the ambient seismic noise recorded at the base of the towers 1 and 2.

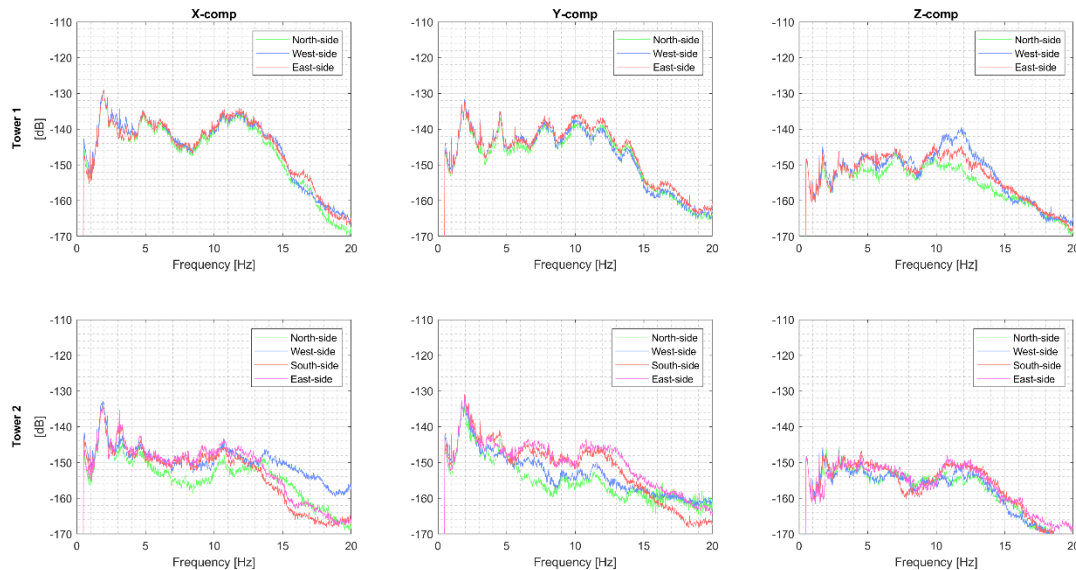


Figura A.47 PSDs obtained from the analysis of the signals recorded in 2019.

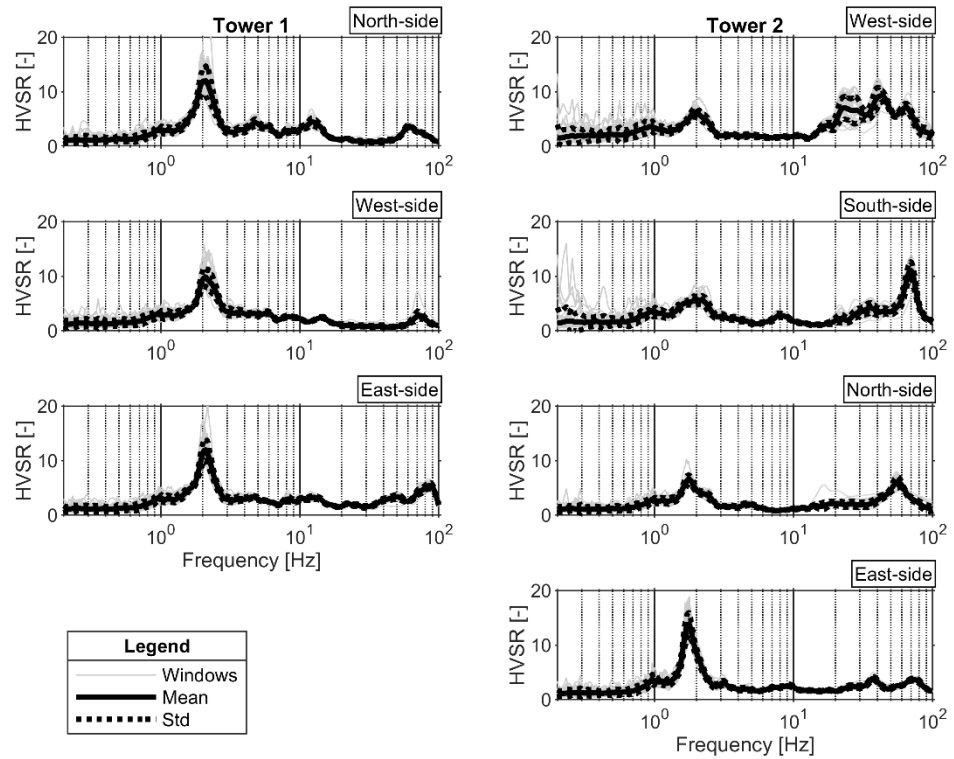


Figura A.58 HVSRs analysis of the dataset collected in 2019.



# CHAPTER 5

## A preliminary test to monitor the Cà Lita landslide using the ambient seismic noise.

### 1. Introduction

Monitoring the kinematic behaviour of unstable slopes represents one of the main aspects related to the management of hydrogeological risks. This objective is now achievable with extensively tested methods, and, in particular, remote sensing tools have proved effective to give an accurate representation of the displacement and the velocity of landslides, though addressing only the surface processes of the phenomenon. For this reason, the geophysical community has been working to give an effective contribution providing non-invasive techniques able to study the inner structure of the unstable slopes. To this perspective, they started investigating the temporal variation of the subsoil seismic velocities, which are strictly connected to the stability of slopes. Commonly, this objective used to be achievable with active methods that proved to be very efficient for many applications, but with the drawback of being economically expensive and poor suitable to monitor processes over a long period. An important breakthrough, that allowed researchers to overcome these weaknesses, have been surely achieved by studying the ambient seismic noise. It has emerged that ambient vibration is far from useless and it is particularly suitable for monitoring purposes since it can be recorded at any time and any location. This feature makes the Earth noise a valuable input data when large time and space scales are involved. Among the techniques available for the analysis of this seismic signal, the one that has found considerable applications in landslide monitoring is surely passive interferometry (Shapiro & Campillo, 2004). This technique allows reconstructing the medium impulse response (Green's function) between two sensors by cross-correlating the acquired ambient noise signals as if an active source had been placed at one of them (Lobkis & Weaver, 2001). Its potential was demonstrated on the *Merapi* volcano where the velocity variations, generated by poroelastic properties changes, were linked to the water table fluctuations (Sens-Schönfelder & Wegler, 2006). The same conclusion has been drawn by Voisin et al. (2017) that applied the technique in a water catchment area where the ground properties, i.e. water content, change quickly as a result of drain and filling procedures of the aquifer. The sensitivity of the seismic velocities to the changes in the medium has led to extend the application of the passive interferometry for monitoring landslides based on the assumption that their occurrence is strictly related to the increase in pore water pressure (Picarelli et al., 2005). Indeed, this has been demonstrated on an active landslide in Switzerland where a drop in the apparent velocity ( $dV/V \%$ ) precede the failure event (Mainsant et al., 2012). While monitoring landslides, polarization features of seismic noise recordings also provided useful insights to track the kinematic behaviour of the mass movement over time (Arosio et al., 2019b). It has been shown that ambient vibrations can show preferential polarization consistent with the direction of slope movement and/or major discontinuities (Del Gaudio & Wasowski, 2007; Burjanek et al., 2012; Arosio et al., 2019a). The polarisation of seismic noise recordings may change following variations in the subsurface, and thus with the landslide-related processes.

In this work, we carried out a preliminary test analysing seismic noise recordings in terms of seismic velocity changes ( $dV/V$ ) and polarization features with the final goal of evaluating whether it is possible to use the ambient vibrations to extract precious information regarding landslide stability. To this perspective, data have been collected on an active landslide at two different epochs: the first one refers to a period in which the landslide was unstable, and the second one to a static situation. We also compare the features extracted from the ambient vibration recordings with the GNSS monitoring data to verify if the results of seismic noise analysis were in agreement with the displacement rate of the landslide.

### 2. Case study

The Ca' Lita landslide is one of the several slope instabilities affecting the Italian northern Apennines (Mulas et al., 2018). It is located in the municipality of Baiso, Reggio Emilia, near the Muraglione village located 30km South-West of Modena. It is approximately 2.5km long and 250m wide with a mean slope angle of 15°. The slope ranges in elevation between 230 and 580 m a.s.l. and mainly consists of two formations belonging to the Ligurian Units. A blocky sandstone formation separated by clay bedding surfaces (Monghidoro flysch) outcrops in the upper part of the slope, while the intermediate and lowermost sections consist of the Val Rossena Melange, a chaotic complex of fine bedded clays and marls together with clay melanges including sandstone and limestone blocks. All the geological units are intensively tectonized and different sets of joints are detectable at any observation scale. The

geological setting controls the kinematics of the landslide, involving a complex roto-translative rockslide with an associated earth slide and flow (Cruden and Varnes, 1996). The rockslide affects the flysch rock mass in the upper part of the slope and is known to have a maximum thickness of around 45 m (Figure ).

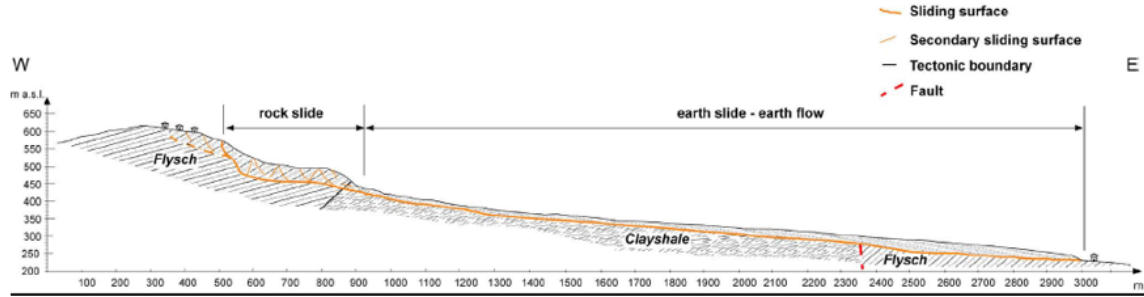


Figure 1 Geological cross-section of the entire landslide. Source: Ronchetti et al. 2009

This work focuses on the earth slide affecting the lower part of the slope (Figure 2) that involves the clay chaotic complex. At the top of the track zone (Figure 2), Borgatti et al. (2006) reported a depth to bedrock of approximately 20 m, but at least five major landslide reactivations have been observed since then. Active seismic surveys performed in November 2020 in the track zone estimated the thickness of the sliding material of about 30 m and a mean S-wave velocity of around 400 m/s.

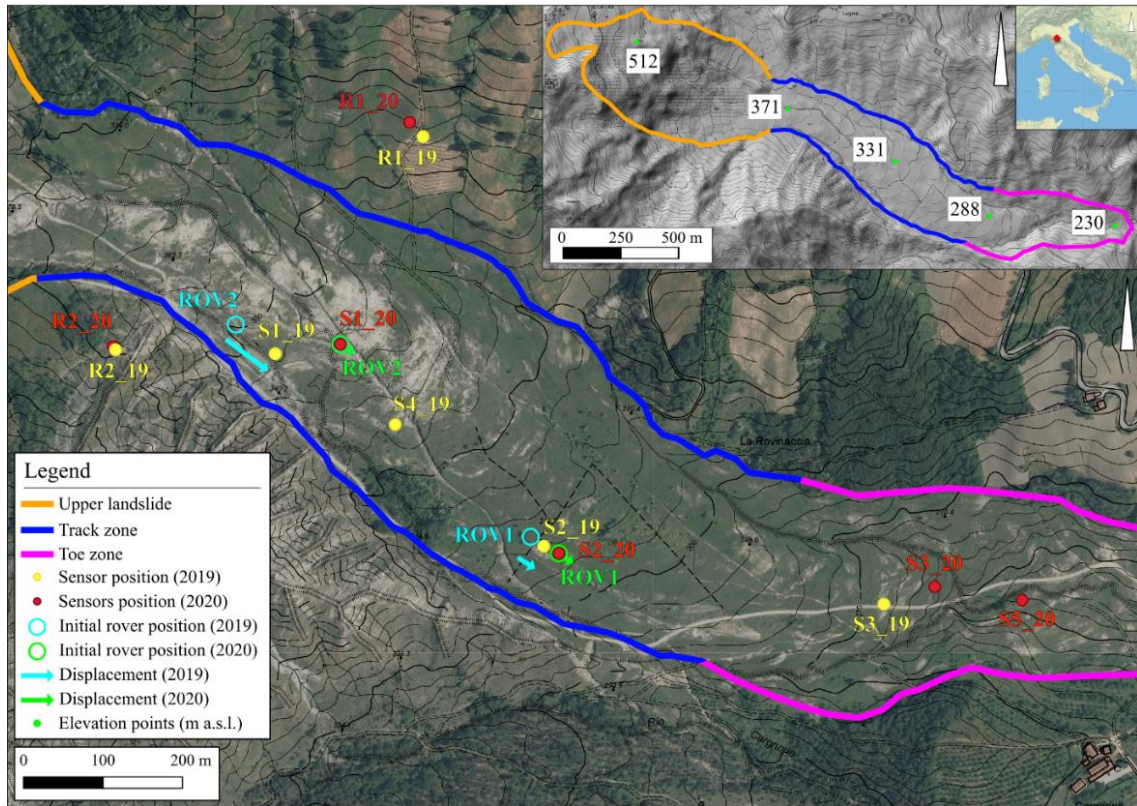


Figure 2 Location and borders of Ca' Lita landslide and positions of the GPS antennas and the seismic sensors.

Data recorded thanks to different monitoring campaigns (using inclinometers, piezometers, time-domain reflectometry and GNSS) suggest that the landslide does not entirely move at the same time, but, on the contrary, is subjected to differential movements depending on the subsurface conditions. This was also confirmed during the most recent significant event that occurred in the late spring of 2019 (Mulas et al., 2020). The interaction between areas of the slope moving with different velocities produces stress zones favouring the formation of joints. In more detail, compressive stress zones cause joints to form along the longitudinal axis of the landslide. On the contrary, in presence of tensile stresses, joints form perpendicular to the slope dip direction. The discontinuities that affect the site induce a high heterogeneity of the hydrogeological properties. In detail, two aquifers are

identified within the study area. The first one, located in the landslide body, is unconfined and thus has a fast response to rainfall events. Whereas the second one is hosted in the fractured flysch below the sliding surface. It is a confined and pressurized unit that is not directly connected to rainfall events.

### 3. Methods

The ambient seismic noise has been recorded at *Ca’ Lita* landslide during two different recording sessions by means of Nanometrics Trillium 20s three-component seismometers. The first survey (hereafter S1) was performed at the beginning of June 2019 by placing two reference sensors approximately 470m apart in stable locations at the sides of the landslide (R1\_19 and R2\_19), and four sensors within the landslide in the track and toe zones (S1\_19, S2\_19, S3\_19 and S4\_19; Figure 2). The second survey (hereafter S2) was performed at the beginning of November 2020 and, apart from one sensor (S5\_20), seismometers were deployed approximately at the same locations of survey S1 (Figure 2). Regarding GNSS monitoring, two GPS antennas were used to accurately monitor displacements in the upper and lower sections of the track zone during the ambient noise surveys (ROV2 and ROV1 respectively; Figure 2). Within this work, both seismic velocity variations ( $dV/V$ ) and polarization features of the collected data have been analysed. The data of the seismic stations installed in the stable area have been processed with the passive interferometry technique. The data have been firstly whitened in order to guarantee that all involved frequencies had a similar contribution. Then, the cross-correlations between the pair of stations have been computed subdividing the recordings into sub-signals of ten-minute length and subsequently stacked into the correlogram. The latter have been subjected to band-pass filtering (1-10Hz) in order to mainly investigate the velocity changes occurring in the sliding material. Finally, the stretching technique has been applied to estimate the velocity changes ( $dV/V$ ). As far as noise polarisation analysis is concerned, for both surveys, we computed the ratio between the horizontal directional spectra of the signals collected by the sensors within the landslide to the ones recorded by the reference sensors. This procedure allows revealing possible directional peaks in the azimuthal plane that could be associated with the sliding direction of the unstable slope (Del Gaudio and Wasowski, 2007) or to the presence of joints creating high contrasts of acoustic impedance within the investigated media (Burjanek et al., 2012), though effects due to topography may still play a role (Del Gaudio and Wasowski, 2007). Finally, we compared the results of the surveys S1 and S2 to find differences between polar plots possibly related to the kinematics of the landslide.

### 4. Results & discussions

From the beginning of May to the beginning of June (i.e., period including survey S1), ROV2 and ROV1 recorded displacements of about 90 m and 30 m, respectively (Figure 3a), with peaks as large as a few meters per day. Considering that the upper section of the track zone slides faster than the lower one, differential movements cause compressive stresses in the area between ROV2 and ROV1 that in turn can generate joints parallel to the longitudinal axis of the landslide. Displacements measured from the beginning of October to the beginning of November (i.e., period including survey S2), though limited to a few centimetres per day (Figure 3b), show that ROV1 moves faster than ROV2 and indicate a different stage of the activity of the landslide with respect to survey S1, in which tensile stress zones may be capable of producing joints or deformations perpendicular to the sliding direction.

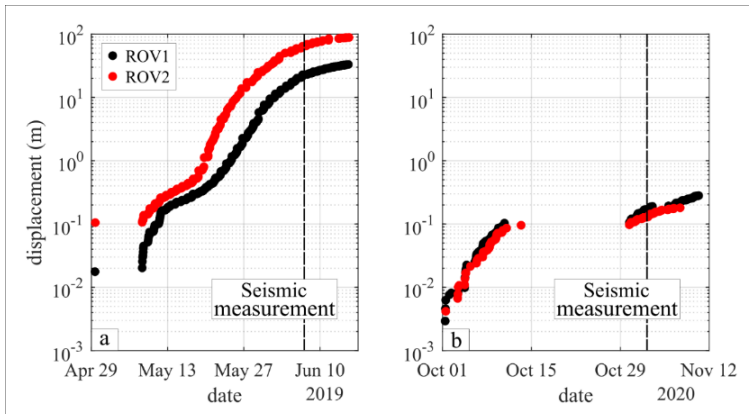


Figure 3 Cumulative displacements measured in 2019 (a) and in 2020 (b) with GNSS receivers. The black dashed line indicates the day in which seismic noise surveys were performed.

The relative velocity changes were analysed within the 0.5 – 5s correlogram time window in order to take into account the coda waves travelling between the considered sensors. The results of the ambient seismic noise cross-correlation analysis reveal that no significant  $dV/V$  changes occurred during the 2020 survey (Figure 4), thus, no variations in the medium have been detected by the seismic waves travelling between the two stations. The latter result is in agreement with GPS data that show almost negligible displacements during the most recent survey. On the other hand, if we consider the survey carried out in 2019 during which the GPS antennas measured displacements in the order of meters per day, the  $dV/V$  curve shows strong fluctuations. We deem that such a trend is the consequence of the subsoil deformation that it turns into a complex and random seismic noise travel path between the considered stations.

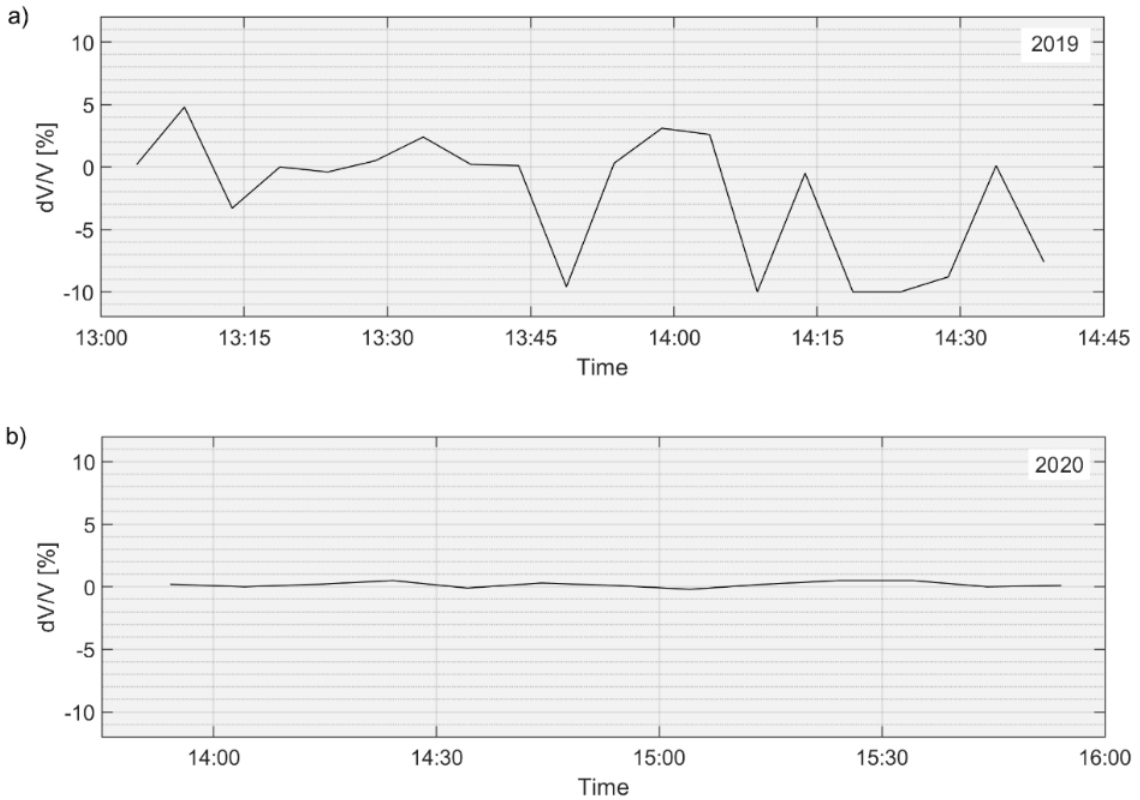


Figure 4 a) Relative seismic velocity changes for 2019 (a) and the 2020 (b) surveys. The  $dV/V$  curves have been obtained considering the data recorded by sensors installed in the stable part.

With regards the second analysis, we firstly checked the polarization features of the stations that have been used as reference. The results of the SVD technique revealed that the signals recorded outside the landslide body, thus on the stable area, have a low degree of polarization ( $\beta_2$ ) within the entire frequency band (0-100Hz). As regards seismometers installed within the active area, Figure 5 illustrates the results of the polarization analysis in the frequency range 1-10 Hz obtained considering sensors R1\_19 and R1\_20 as references for surveys S1 and S2, respectively. All the spectral ratios show a peak around 3 Hz, which, according to the outcomes of active seismic surveys, indicates a high impedance contrast at about 30 m depth. Peaks at higher frequencies may be due to harmonics of the fundamental resonance frequency. During the 2019 survey, all the sensors installed in the track zone of the landslide show preferential polarization perpendicular to the main discontinuities that were observed in the field (i.e., perpendicular to flow direction). For these sensors, polarisation seems to be controlled by fractures that affect the landslide body and it is perpendicular to the surface cracks, thus perpendicular to the slope motion. We hypothesise that this phenomenon is due to the rigidity drop in the direction perpendicular to the surface cracks. Whereas, for the sensor located at the toe of the landslide (S3\_19), where the medium is less affected by the landslide activity, the direction of polarisation is in agreement with the maximum slope direction and the overall direction of the landslide displacement. This trend could be due to the soil particles that more easily vibrate in the direction of freedom created by the direction of the slope. During the most recent survey (S2), apart from sensor S5\_20 that did not show any clear polarization, sensors in the track zone show preferential oscillation along to the longitudinal axis of the landslide. In their research, Pilz et al. (2013) found cases where directionality agrees with the slope direction. However, the DelGaudio et al. (2013) study of different unstable slopes has proved that the

polarization parallel to the slope motion is a recurrent phenomenon though is not a general rule. Indeed, they explain that the directivity of the energy distribution in landslides is complexed and controlled by a mix of geologic and topographic factors. In detail, the anisotropy of the medium and fractures can have an impact on the signal's polarisation. DelGaudio et al. (2013) also found a case where polarisation in an unstable slope is perpendicular to a fault system.

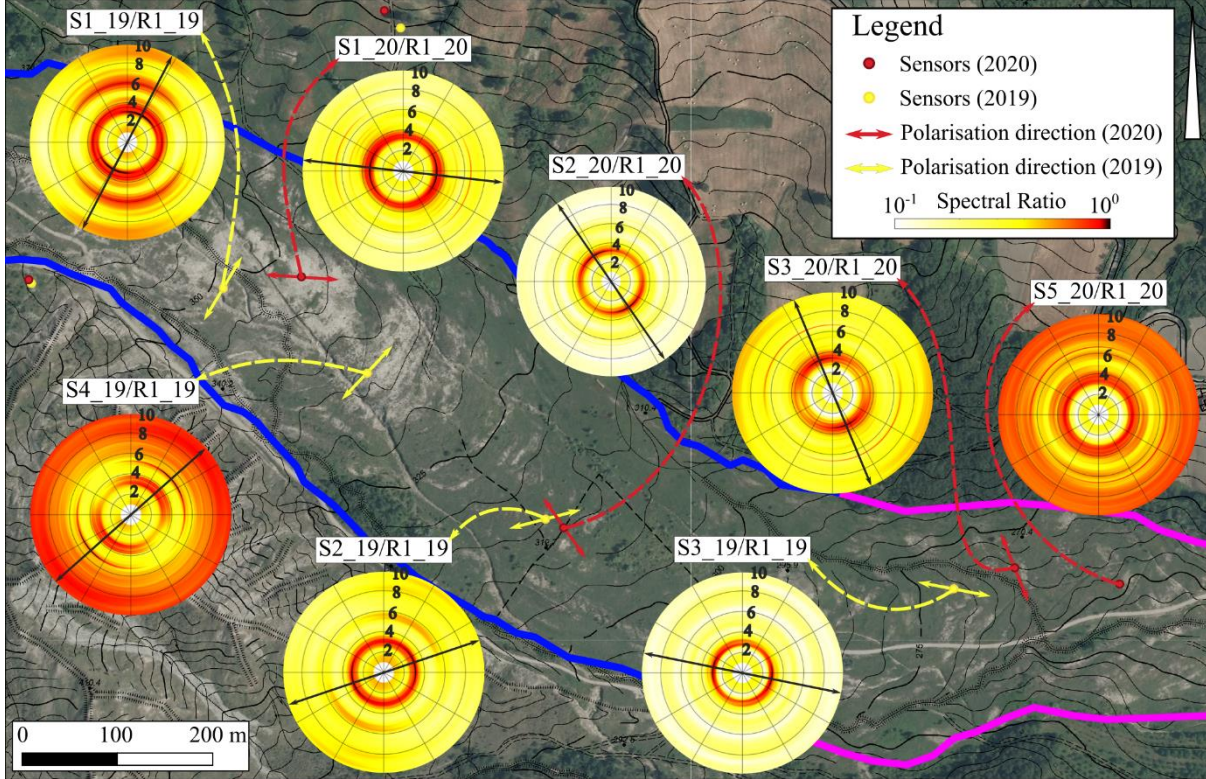


Figure 5 Polar plots of spectral ratios between the horizontal components of the sensors installed within the landslide and the ones of the reference sensors deployed at stable locations. Amplitudes are normalized to the individual maximum of each plot. Arrows indicate directions of preferential polarization estimated as peaks in the polar plots.

## 5. Conclusions

In this work, we carried out a preliminary test to evaluate whether the ambient seismic noise could be effectively used to monitor the evolution over time of the landslides, thus investigating changes in their stability. To this perspective, the ambient vibrations collected on the Ca' Lita landslide were analyzed both in terms of polarization features as well as in terms of seismic velocity variations ( $dV/V$ ). During the most recent and significant sliding event that occurred in 2019, the Ca' Lita landslide was affected by differential displacements causing areas with compressive stresses and producing fractures that were observed to be parallel to the direction of the mass movement. On the contrary, minor slope displacements recorded in 2020 suggest that the sliding body could be subjected to tensile stresses and, accordingly, deformations and joint sets orthogonal to the flow direction may be generated. In this case study, we observed that different stress states and newly formed fractures modify the polarization features of the ambient noise recording (Burjanek et al., 2012). In detail, the azimuthal spectral ratios of seismic noise recorded on the landslide during surveys S1 and S2 revealed a preferential direction of soil vibration perpendicular to the direction of the joints and/or of the deformation areas. The comparison of the azimuthal spectral ratios obtained from the measurement of the seismic noise at stages with small landslide displacements suggests that the polarisation changes in time coherently with the mass stability. Such a hypothesis is also supported by the results of the passive interferometry analysis that highlight a completely different  $dV/V$  curve considering the two measurement campaigns. The results of this study revealed that both methods can provide useful information to characterize the dynamic conditions of the unstable slopes. In particular, different behaviours of the landslide have been observed depending on the analysed epoch (stable and unstable periods). Even though the ambient seismic noise seems able to provide insight into the landslide stability, longer monitoring surveys are needed to better assess the correlation between wavefield changes and landslide events. Nevertheless,

the results of this study suggest that these methods seem promising to improve our capabilities of landslides forecasting.

## 6. Bibliography

- Arosio, D., Longoni, L., Papini, M., Bièvre G., and Zanzi L., [2019a] Geological and geophysical investigations to analyse a lateral spreading phenomenon: the case study of Torrioni di Rialba, northern Italy, *Landslides*, 16.
- Arosio, D., Taruselli, M., Longoni, L., Papini, M. and Zanzi, L. [2019b] Seismic Noise Polarization Analysis for Unstable Rock Monitoring, in Proceedings of the 25th European Meeting of Environmental and Engineering Geophysics, The Hague, The Netherlands, Vol. 2019, 1-5.
- Borgatti, L., Corsini, A., Barbieri, M., Sartini, G., Truffelli, G., Caputo, G., and Puglisi, C. [2006] Large reactivated landslides in weak rock masses: a case study from the Northern Apennines (Italy). *Landslides*, 3(2), 115–124.
- Burjánek, J., Moore, J.R., Yugsí Molina, F.X. and Fäh, D., [2012] Instrumental evidence of normal mode rock slope vibration, *Geophysical Journal International*, 188, 559–569.
- Cruden, D.M. and Varnes, D.J., [1996] Landslide Types and Processes, Special Report , Transportation Research Board, National Academy of Sciences, 247, 36-75
- Del Gaudio, V. and Wasowski, J., [2007] Directivity of slope dynamic response to seismic shaking, *Geophys Res Lett*, 34, L12301.
- Del Gaudio V., Wasowski J., Muscillo S., 2013, New developments in ambient noise analysis to characterise the seismic response of landslide-prone slopes, *Natural Hazards and Earth System Sciences*, 13 (8), p2075-2087.
- Lobkis, O.I. and Weaver, R.L., [2001] On the emergence of the Greens function in the correlations of a diffuse field, *J. acoust. Soc. Am.*, 110, 3011–3017.
- Mainsant, G., E. Larose, C. Broennimann, D. Jongmans, C. Michoud, and M. Jaboyedoff, [2012] Ambient seismic noise monitoring of a clay landslide: Toward failure prediction: *Journal of Geophysical Research: Earth Surface*, 117, F01030.
- Mulas, M., Ciccarese, G., Ronchetti, F., Truffelli, G., and Corsini, A. [2018] Slope dynamics and streambed uplift during the Pergalla landslide reactivation in March 2016 and discussion of concurrent causes (Northern Apennines, Italy). *Landslides*, 15(9), 1881–1887.
- Mulas, M., Ciccarese, G., Truffelli, G. and Corsini, A. [2020] Displacements of an Active Moderately Rapid Landslide—A Dataset Retrieved by Continuous GNSS Arrays. *Data*, 5, 71.
- Picarelli, L., L. Urciuoli, G. Ramondini, and L. Comegna [2005] Main features of mudslides in tectonised highly fissured clay shales, *Landslides*, 2(1), 15–30.
- Pilz M., Parolai S., Bindi D., et al., 2013, Combining Seismic Noise Techniques for Landslide Characterization, *Pure and Applied Geophysics*, 171(8), p1729-1745.
- Ronchetti F., Borgatti L., Cervi F., et al., 2009, Groundwater processes in a complex landslide, northern Apennines, Italy, *Natural Hazards and Earth System Sciences*, 9, p895-904.
- Sens-Schönenfelder C. and Wegler, U., [2006]. Passive image interferometry and seasonal variations of seismic velocities at Merapi Volcano, Indonesia, *Geophys. Res. Lett.*, 33, L21302.
- Shapiro, N. M., and M. Campillo [2004], Emergence of broadband Rayleigh waves from correlations of the ambient seismic noise, *Geophys. Res. Lett.*, 31, L07614.
- Voisin, C., Guzmán, M. A. R., Réfloc'h, A., Taruselli, M., and Garambois, S. [2017]. Groundwater Monitoring with Passive Seismic Interferometry. *Journal of Water Resource and Protection*, 09(12), 1414–1427.



# CHAPTER 6

## Seismic passive interferometry to monitor groundwater level variations.

### 1. Introduction

In recent years, the dramatic increase in climate-related events has fostered the development of research activities and investigations able to cope with such phenomena. This is particularly true for landslide events that cause every year more than 4000 fatalities and tens of billions of euros worth of material damage (Froude and Petley, 2018; Alimohammadi et al., 2013). Such a risk can be reduced by anticipating the slope failures with early-warning systems (Intrieri et al., 2012) which are generally based on the monitoring of ground deformations and groundwater levels. Current tools for water table monitoring primarily consists of piezometers. However, in many unstable slopes, it is impractical to install the monitoring wells since they are difficult to maintain over long periods due to soil displacements. Moreover, such a methodology provides local measurements, and it is therefore expensive to monitor different areas of the landslide body. Recently, the traditional monitoring systems have been coupled with geophysical methods since they can be used for non-destructive evaluation of the internal structure, hydrological and mechanical features of the landslides (Jongmans and Garambois, 2007). In this regards, the passive seismic methods have found considerable applications since their characteristic of making use of passive sources, which can be recorded at any time and any location makes them particularly suitable for the development of the monitoring systems (Shapiro & Campillo 2004). In this perspective, the method that has been largely applied for landslide monitoring is surely the cross-correlation of the ambient seismic noise. This methodology has been used for the long-term investigation of landslides with the main goal of finding precursors of their occurrence through the monitoring of seismic velocity variations ( $dV/V$ ) (Voisin et al., 2016). In this contest, the ambient noise correlation technique has been used to study two phenomena that are considered as the triggering factor of the landslide fluidization: the shear stress and the water content. The mechanisms of fluidization turn landslides to mudflows or debris flows following heavy rainfalls (Van Asch and Malet, 2009). Such a phenomenon can be explained by viscoplastic laws (Huang and García, 1998). In detail, the soil behaves as a viscous fluid when the static shear stress applied is above the yield stress ( $\tau_c$ ). The fluidization can be also triggered by an increase in the water content. Both the latter and the  $\tau_c$  are dependent on each other since also the critical stress decreases when the water content increases (Cousset, 1995). In this regards, seismic wave variations ( $dV/V$ ) are strictly related to such phenomenon through poroelasticity and direct water loading. In the former mechanism, the replacement of air with water in the pore spaces, or vice versa, changes the bulk density of the aquifer material ( $\rho$ ) as well as the material's bulk modulus ( $K$ ) and shear modulus ( $\mu$ ). Compressional and shear seismic velocities,  $V_p$  and  $V_s$  respectively, are directly controlled by these elastic moduli and density ( $\rho$ ):

$$V_p = \sqrt{\frac{K + \frac{4}{3}\mu}{\rho}}, \quad V_s = \sqrt{\frac{\mu}{\rho}}$$

Therefore, changes in saturation due to water table fluctuations implicate changes in the seismic wave velocities. In detail, according to the above equations, an increase of the groundwater would contemporarily increase the P-wave velocity and decrease the S-wave velocity. Such behaviour should result in a decrease of surface wave velocities (Biot, 1962) since they are mostly (90%) sensitive to S-waves velocity (Grèt et al., 2006b). It is clear, that the poroelastic effect affects the layers interested by the water table fluctuations (Meier et al., 2010; Hillers et al., 2014). With regards to the direct water loading mechanism, it may have two different effects. In the area affected by a low-level of drainage, such as in confined layers, the pore pressure generates cracks opening decreasing the area of grains in contact, hence decreasing the seismic velocity (Rivet et al., 2015). Whereas, in deep layers that are under the groundwater table or under other impermeable layers, the water load brings an increase of the stress of the particles resulting in an increase of the seismic velocity (Obermann et al., 2014).

Whether the physical cause of the landslide fluidization, it is clear that water content plays an important role in landslide stability. Moreover, given its influence on seismic waves velocities, the cross-correlation of ambient seismic noise seems a promising method to be implemented in early warning monitoring systems. In this

perspective, Voisin et al. (2016) observed a clear anti-correlation between water table fluctuations and the  $dV/V$  while monitoring the Utiku landslide. In the Pont-Bourquin landslide, the  $dV/V$  was compared to the rainfall revealing that such environmental event has a weak influence on the shallow rigidity variations and either on the seismic velocity changes (Bi`evre et al., 2018). However, the authors stated that to fully understand where the  $dV/V$  are coming from, it is necessary to perform long-term acquisitions and compare the results with the monitored underground water table. Indeed, in other studies, precipitations that resulted in groundwater levels increase were able to decrease the apparent seismic velocity ( $dV/V$ ) (Sens-Schönfelder and Wegler, 2006). Clements and Denolle (2018) observed changes in  $dV/V$  linked to the regionals groundwater levels that underwent a succession of droughts and floods over a 15-year observation period. They did not observe any significant phase lag between the  $dV/V$  response and the groundwater variations, suggesting a pure correlation with the elastic response of the aquifer (Clements and Denolle, 2018). In 2017, Voisin et al. demonstrated the potential of the seismic noise for the monitoring of the water table in an industrial context within a controlled fluid injection experiment. He observed an overall agreement between the  $dV/V$  and groundwater levels within a time frame of hours to days (Voisin et al., 2017).

Even though previous studies demonstrated the effectiveness of passive interferometry in providing precious information regarding the landslide's features, an in-depth investigation of this method is still needed before being effectively integrated into an operational landslide early-warning system. In this perspective, and provided the importance of monitoring groundwater content in rainfall-induced landslides, we did perform two pilot tests to check the reliability of noise interferometry in monitoring water table variations within different hydrogeological contexts. Given the impossibility of installing seismic stations for long-term monitoring, we collected ambient vibrations in Crépieux-Charmy and the Ventasso water catchment fields, located in France and Italy respectively. In both sites, the water level has been artificially modified by activating a pre-existing pumping system. We first estimated the seismic velocity variations using the Stretching technique and then compared the obtained curve with the water table level monitored by the piezometers associated with the pumping systems. In this contest, groundwater lever undergoes fast artificial fluctuations and thus we also investigated the influence of different sub-signals length on the seismic wave velocity variations retrieval. The  $dV/V$  time-resolution is a fundamental parameter to be considered when designing early-warning systems for landslide monitoring purposes. In the following paragraphs, for each case study, we present the description of the site, the setup of the parameters used to estimate the  $dV/V$  using the cross-correlation technique and the results of the seismic monitoring.

## 2. The Crépieux–Charmy water exploitation field test

### 2.1. Site description

The Crépieux-Charmy site is a water catchment area located in the Lyon's agglomeration, in the Auvergne-Rhône-Alpes region (Figure 1). It covers the towns of Villeurbanne, Rillieux-la-Pape and Vaulx-en-Velin and it is crossed by different arms of the Rhone River.

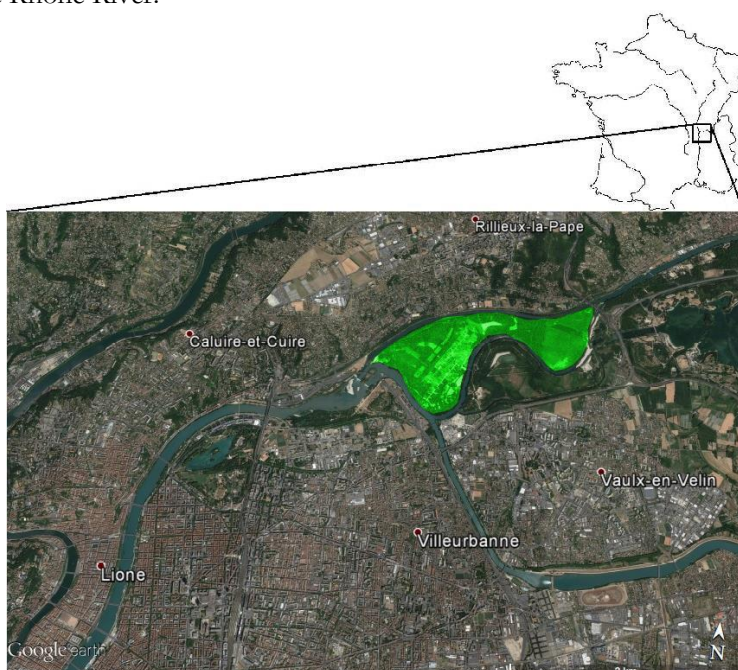


Figure 1 Study area

This zone corresponds to the largest water catchment field in Europe (375 hectares). In this context, Veolia Group has been exploiting the site since 1987 providing more than 95% of drinking water needs ( $150 \div 315 \text{ m}^3/\text{day}$  for 2015) for more than one million inhabitants of Lyon's city. The annual volume of drinking water supply represents 7% of the total water volume collected in this aquifer; however, the greater exploitation of water resource is for agricultural and industrial purposes. In the eastern part of Lyon, the fluvio-glacial deposits allow the infiltration of almost all meteoric waters. The physical boundaries of the water capturing field are the Jonage canal and the Miribel canal that feeds two branches, the Vieux-Rhône and the South canal, before joining the Jonage canal downstream of the site (Figure 32).

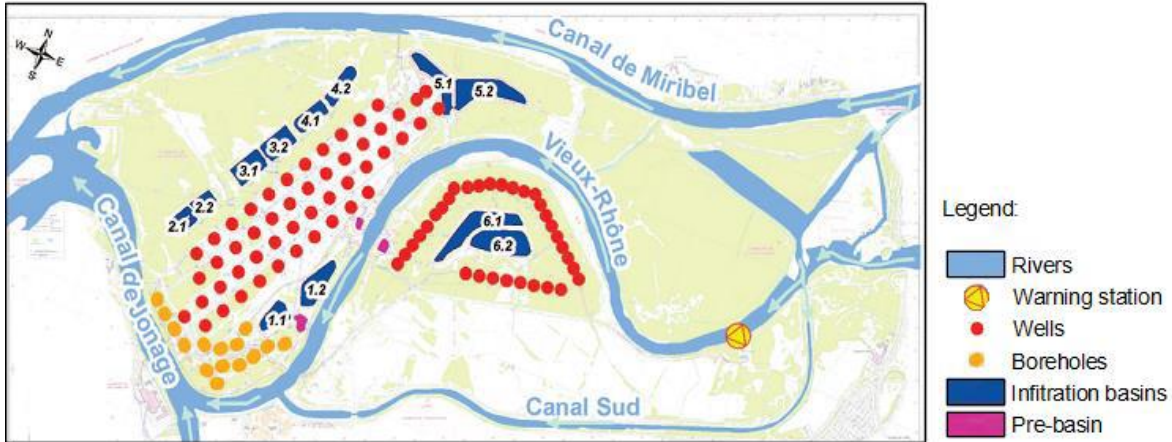


Figure 2 Water catchment area

The capturing field of Crêpieux-Charmy is located between the Bas Dauphiné and the Dombes, in Miocene formations. It extends over an unconfined aquifer characterized by glacial-fluvial Würmien's deposits covered by alluvial deposits of the Rhône river, a sedimentary sequence with a heterogeneous distribution of fine sand, sand-gravel mixtures, and clean gravel-pebbles (Voisin et al., 2017). These materials define the permeability of the aquifer, generally between  $1.10 \div 3 \text{ m/s}$  and  $5.10 \div 2 \text{ m/s}$ . Geological information has been collected during the constructions of the piezometers and pumping wells. This information has been combined with the results of the geophysical surveys (Seismic tomography, GPR and ERT) providing an interpretation of the subsoil within the study area (Figure 3).

Depth [m]	Water level [m]	Lithology	Vp [m/s]	Vs [m/s]	GPR Water content	ERT [ $\Omega \cdot \text{m}$ ]
0		TOPSOIL	300	150		200
1					10%	
2						4000
3						
4						
5						
6		COARSE GRAVEL	800	300		
7						
8						
9						
10						
11		COARSE GRAVEL WITH SAND	1500	250		
12						
13						
14		CLAY	1800	900		
15						
16						

Figure 3 Summary of the geological and geophysical surveys.

The aquifer is characterized by shallow underground water, generally around 5/6 m depth. In the natural process, the recharge of the water table is affected by meteoric waters (rain and snowmelt), by infiltrations of watercourses and by the arrivals of the fluvioglacial corridors. When this is not enough, artificial groundwater recharge can provide a truly effective solution. This method is an anthropogenic process that consists of increasing the amount of water that enters the groundwater reservoir by means of infiltration basins. This artificial recharge is performed by injecting water in the infiltration basins that will then percolate to the water table. When the incoming volumes are greater than the volumes that can be locally evacuated, a rise in the groundwater occurs. In 1989 this approach was applied in Crémieux-Charmy with the construction of 12 infiltration basins with a maximum recharge rate of 389'730 m<sup>3</sup>/day (Figure 2). This decision was taken after a very dry season when the low flow of the Rhône brought the capturing field to the limit of its exploitability. Such basins also prevent potential groundwater pollution by modification of underground fluids flows and recharging the groundwater (Garambois *et al.* 2019). The catchment field counts 114 wells that participate in the pumping of the water resource. These structures have been designed to provide a daily flow of 600'000 m<sup>3</sup>/d. The number of active pumping wells varies in a day, depending on the availability of the structure due to the frequent maintenance.

## 2.2. Methods

During the field test, we recorded the ambient seismic noise using 6 Nanometrics Trillium three-component seismometers (0.05-100 Hz -3dB band) and Centaur data-loggers set with a sampling frequency of 200 Hz and connected to a GPS antenna for the time synchronization. The seismometers have been installed around a pumping station that has been used to produce artificial underground water variation (Figure 4). The recordings firstly underwent a pre-processing phase consisting of mean and trend removal, time-domain normalization and spectral whitening (Bensen *et al.*, 2007). Given the fast changes of the underground water level, the obtained data have been then divided into five-minute-long sub-signals and processed according to the seismic interferometry technique. This methodology consists of cross-correlating the sub-signals of the vertical components recorded at two stations to compose the correlogram. A time window is then selected, generally including the most energetic seismic phases, and the stretching technique is applied to estimate the velocity variations (more details in chapter 2). Additionally, we tested the influence of the sub-signals length on the estimated dV/V curve.

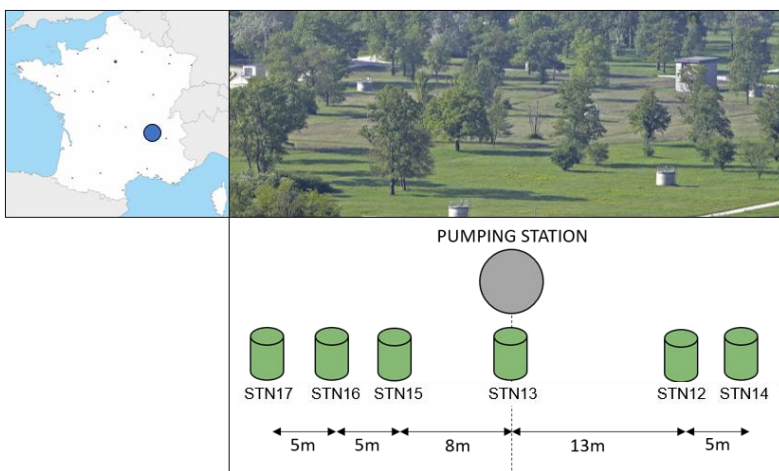


Figure 4 Crémieux-Charmy water catchment field with a scheme of the installed seismic stations. The white structures in the picture represent the pumping stations.

During the acquisition of the ambient vibrations, the pumping system has been activated twice generating two filling-emptying cycles (Figure 5). The evolution of the underground water was monitored using a piezometer located inside the well used to pump the water. The water table ranges almost between 4.5 and 6.5 m in depth. Piezometer data referred to as the seismic noise recording period are presented in Figure 5. The time in which the pump has been activated is represented by the green rectangles.

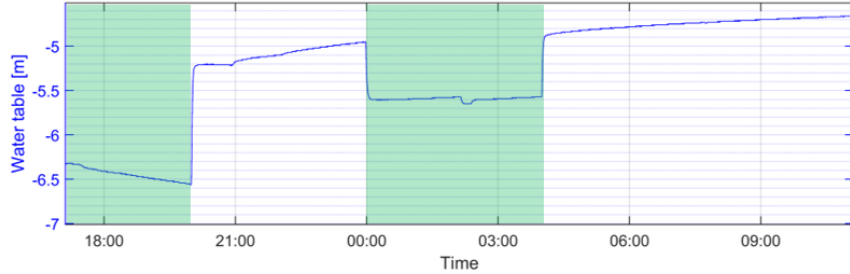


Figure 5 Water level measured at the pumping station. The green rectangles indicate the period in which the pump has been switched on.

### 2.3. Results and discussion

The vertical component of the collected dataset reveals that the amplitude is higher when the pumping system is activated (Figure 6) (Stephane et al 2019). In figure 6 it is in fact possible to clearly distinguish the time windows in which the pump was on from those with the pump off. Comparing all the collected signals we did observe that sensor STN16 exhibits a noisier record compared to the others. We thus decided to exclude it from the computation of the passive interferometry. Considering the time windows where the pumping system was active, it can be noticed that the amplitude of the sensor on the right side of the pump (STN12 and STN14) is higher than those on the left side (STN15 and STN17). Whereas, when the pump is switched off, the amplitude is similar for all the deployed seismometers. We hypothesize that this behaviour is linked to the distribution network of the pumping plant. In more detail, given the different amplitudes of the signal at the sides of the well, it is plausible to think that the pumped water is brought to the distribution plant through pipes that are located below the sensors that show signals with greater amplitude (STN 12 and STN14).

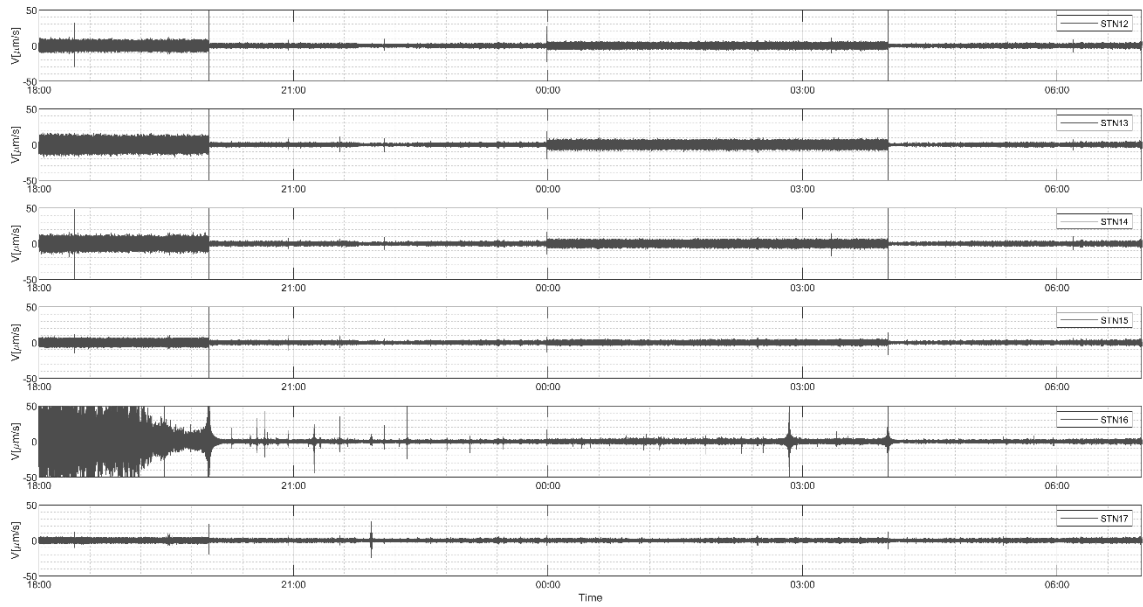


Figure 6 Ambient seismic noise recorded at each seismometer.

The effect of the pump activation gets clearer in the frequency domain. Figure 7 shows the spectrums computed with Welch's method considering signals recorded when the pump has been switched on and off (red and black curves respectively). We can observe that the activation of the pumping system amplifies the ambient seismic noise spectrum content. Such behaviour has a low impact in the frequency range below 20 Hz, whereas, considering the higher frequencies, the amplification gets more evident and, additionally, the spectrum undergoes a shape modification. Into detail, it can be observed that the pump activation leads to the generation of wide spectral peaks that merge the narrower and independent peaks visible in the spectrum obtained considering the signal in the pump-off time-interval (i.e. peaks at 86 Hz in the black curve are merged in a unique peak in the red plot).

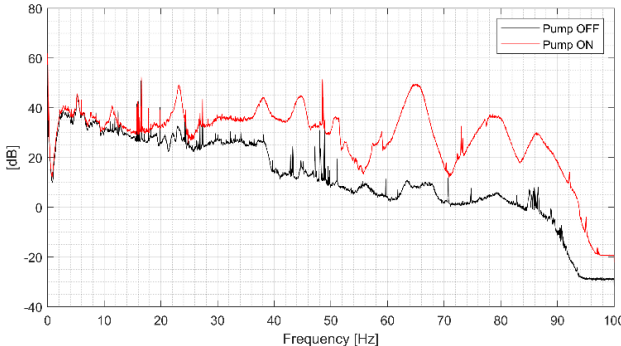


Figure 7 Comparison between the spectrum computed for both the pump-off and pump-on time-interval for station STN12.

With regards to the passive interferometry technique, Figure 8 shows the results obtained for the station pairs STN13-STN14. In the two bottom panels, the blue curve represents the relative piezometric changes measured at the closest piezometer and the dashed and solid grey curves represent the raw and the smoothed seismic velocity variation ( $dV/V$ ) respectively. Considering the broadband correlogram computed in the 1-30Hz frequency range (Figure 8 – top), it can be observed that the most energetic seismic phases arrive at early lags (almost close to 0s). This behaviour occurs for all the available station's pairs and is likely due to their small inter distance. The bottom part of Figure 8 shows the  $dV/V$  curves obtained for two different time windows selected within the causal side of the correlogram. For the 0-0.3s interval, it can be noticed that the  $dV/V$  curve satisfactorily fits the groundwater level measured in the well (Figure 8 – bottom left). This suggests that the P waves dominate the wavefield in the analysed time window. Indeed, an increase in saturation results in an increase in velocity. On the contrary, the  $dV/V$  computed for the 0.5-1.1s time window shows a trend anti-correlated to the water level that can be explained by the decrease of the S-wave velocity due to the density effect (Figure 8 – bottom right). Such a result is in agreement with a previous study where it has been shown that both Rayleigh and P-waves may dominate in different time windows along the correlogram (Garambois et al., 2019). The estimated  $dV/V$  curves undergo a different rate of change considering the two selected correlogram windows. In detail, the velocity variations are in the order of almost 7% when  $dV/V$  and water table curves are correlated, whereas, when the anticorrelated trend is observed, the  $dV/V$  shows 0.8% variation. We hypothesis that such behaviour is due to the different sensitivity of waves to the water saturation. Indeed, even though the short distance between seismic stations may induce a significant wavefield mixing, the P-waves are strongly influenced by water content: an increase of the ground saturation leads to a significant increase of P-waves velocity. Therefore, considering early times in the correlogram, we deem that the wavefield is dominated by primary waves which contribution may guide the  $dV/V$  variations and hide the impact of Rayleigh waves resulting in significant  $dV/V$  changes. On the contrary, Rayleigh waves are slightly sensitive to changes in the saturation rate and provide an inverse response with respect to changes in water table level. This is in agreement with the result obtained considering the late arrivals in the correlogram (in the 0.5-1.1 time window) where the  $dV/V$  undergoes a small variability, between -0.4% to 0.4%, with an inverse trend with respect to the water table fluctuations. In such a case, we, therefore, believe that the wavefield in the 0.5-1.1s correlogram time window is dominated by surface waves (i.e. Rayleigh waves).

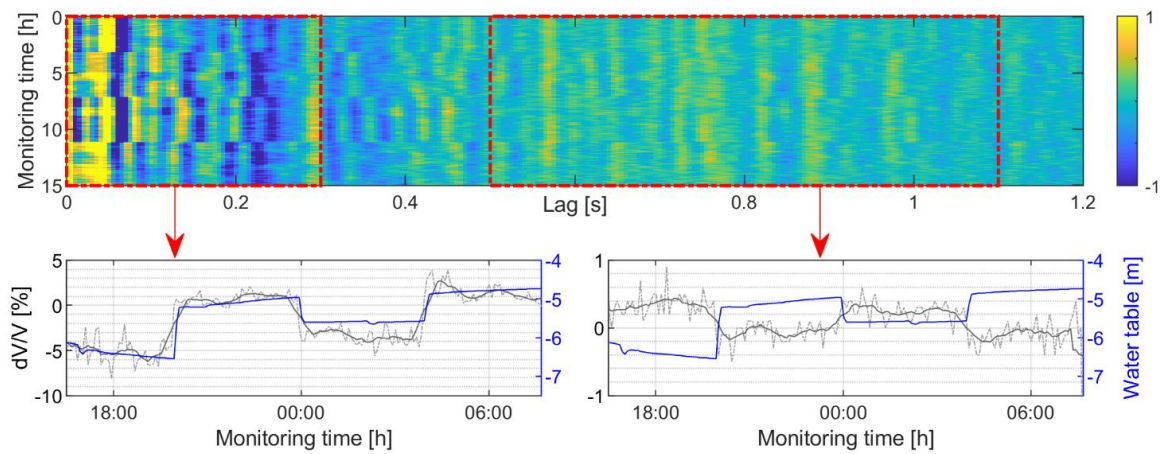


Figure 8 Results of the passive interferometry technique obtained for the station pair STN13-STN14. At of the correlogram; at the bottom the computed  $dV/V$  for the selected red-framed time window. The dashed and solid grey curves represent the raw and the smoothed seismic velocity variation ( $dV/V$ ) respectively. The blue curve is the water level measured in the well during the test.

Figure 9 summarizes the results obtained for four other stations pairs (STN14-STN17, STN13-STN15, STN12-STN13, and STN12-STN14). The  $dV/V$  curves have been computed considering the 0-0.3s correlogram window. In compliance with the above-mentioned result, the obtained seismic velocity variations exhibit fluctuations in agreement with the changes in the water table level. We, therefore, state that in this particular experimental test, and provided the inter distance of the installed seismometers, the early times in the correlogram are dominated by direct and refracted P-waves. Indeed, such a result was also obtained by Garambois et al. (2019) who highlighted the possibility to infer the different type of waves by the selection of different time windows within the correlogram. On the contrary, we found it difficult to identify for each station pair a correlogram window that returns a  $dV/V$  curve anticorrelated with respect to the underground water variation, thus a time window dominated by S-waves, and consequently by Rayleigh waves. We additionally noticed that these windows are not the same for each station pair. In detail, the windows that return anticorrelated results can be either in the casual or a-causal part of the correlogram. We believe that this random behaviour may be linked to the small inter-station distances, thus to the scattering that occurs within the medium, or to the nonstationary noise source distribution (Voisin et al. 2017).

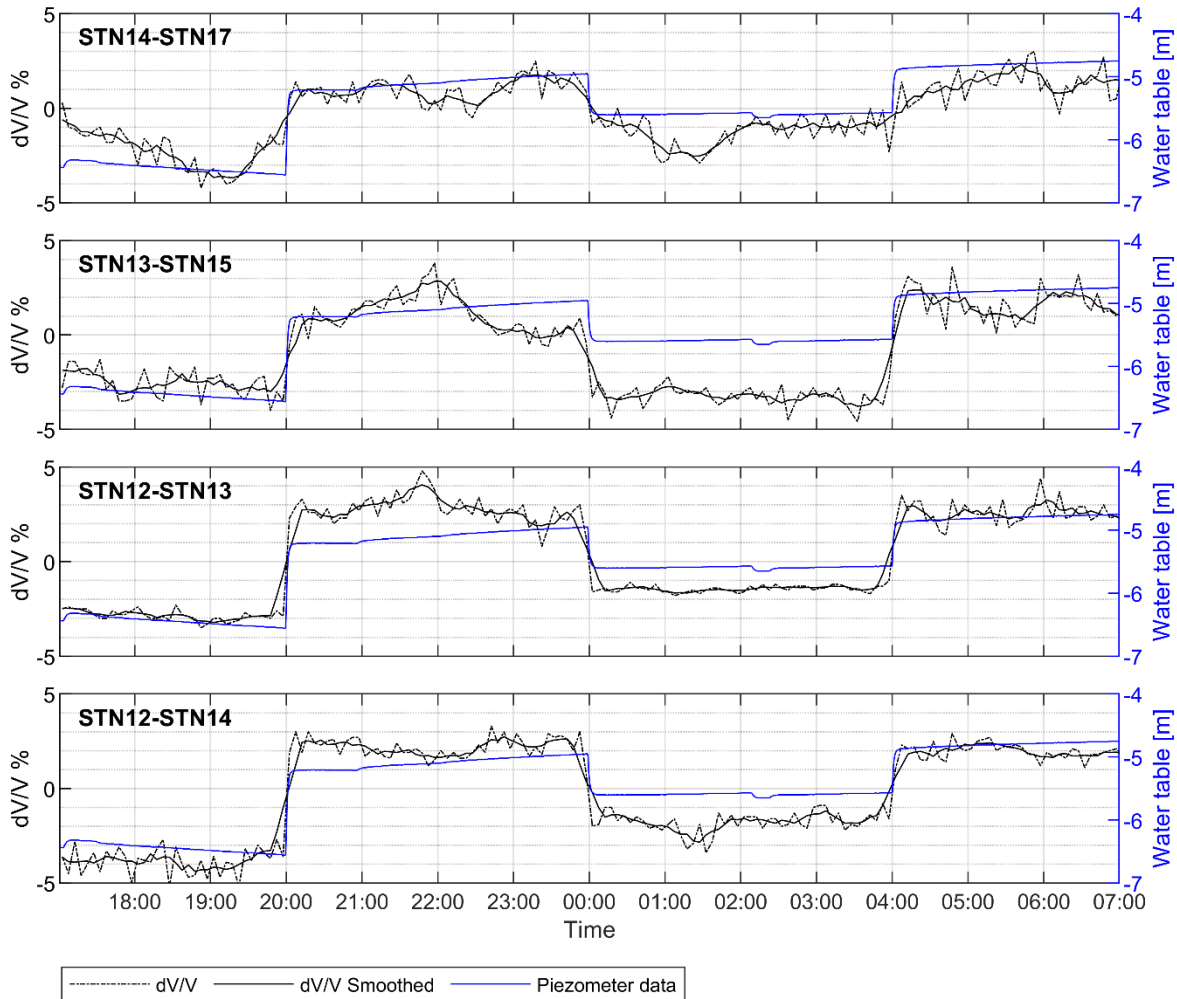


Figure 9  $dV/V$  curves estimated for different stations pairs.

When performing passive interferometry, the traces are generally split into one-hour sub-records to guarantee a robust and stable  $dV/V$  estimate. However, this time resolution is not sufficient when studying fast changes occurring within the investigate medium. This is particularly true for this experimental test where the underground water level underwent sudden changes. For this reason, in the perspective of implementing this technique in early-warning monitoring systems we did estimate the  $dV/V$  curve using 60, 30-, 10-, 5- and 1-minutes sub-signals lengths. Figure 10 shows the results obtained considering the 1-30Hz frequency range and the 0-0.3s correlogram window for the station pair STN13-STN14. The estimated  $dV/V$  curves did not undergo any smoothing. The obtained results reveal that all the tested sub-signals lengths lead to an acceptable reconstruction of the water table.

The seismic velocity variation obtained considering one-hour segments provide the most stable curve. Nevertheless, it is clear that this time resolution is not sufficient to track the fast variations of the underground water. Indeed, the water table changes occurring at 8:00 pm, 00:00 am and, 04:00 am are smoothed, making it impossible to precisely estimate the instant where the water level starts to change. The same behaviour is observed considering the  $dV/V$  curve estimated using 30 minutes sub-signals length. We can notice that for this experimental test, sub-signals 10 minutes length are necessary to provide a time resolution sufficient to temporally locate the water table change. Nevertheless, it can be observed that short sub-signals in the estimation of the seismic velocity variations bring to noisy results. This is particularly true if we consider the  $dV/V$  curve obtained using sub-signals of one-minute length.

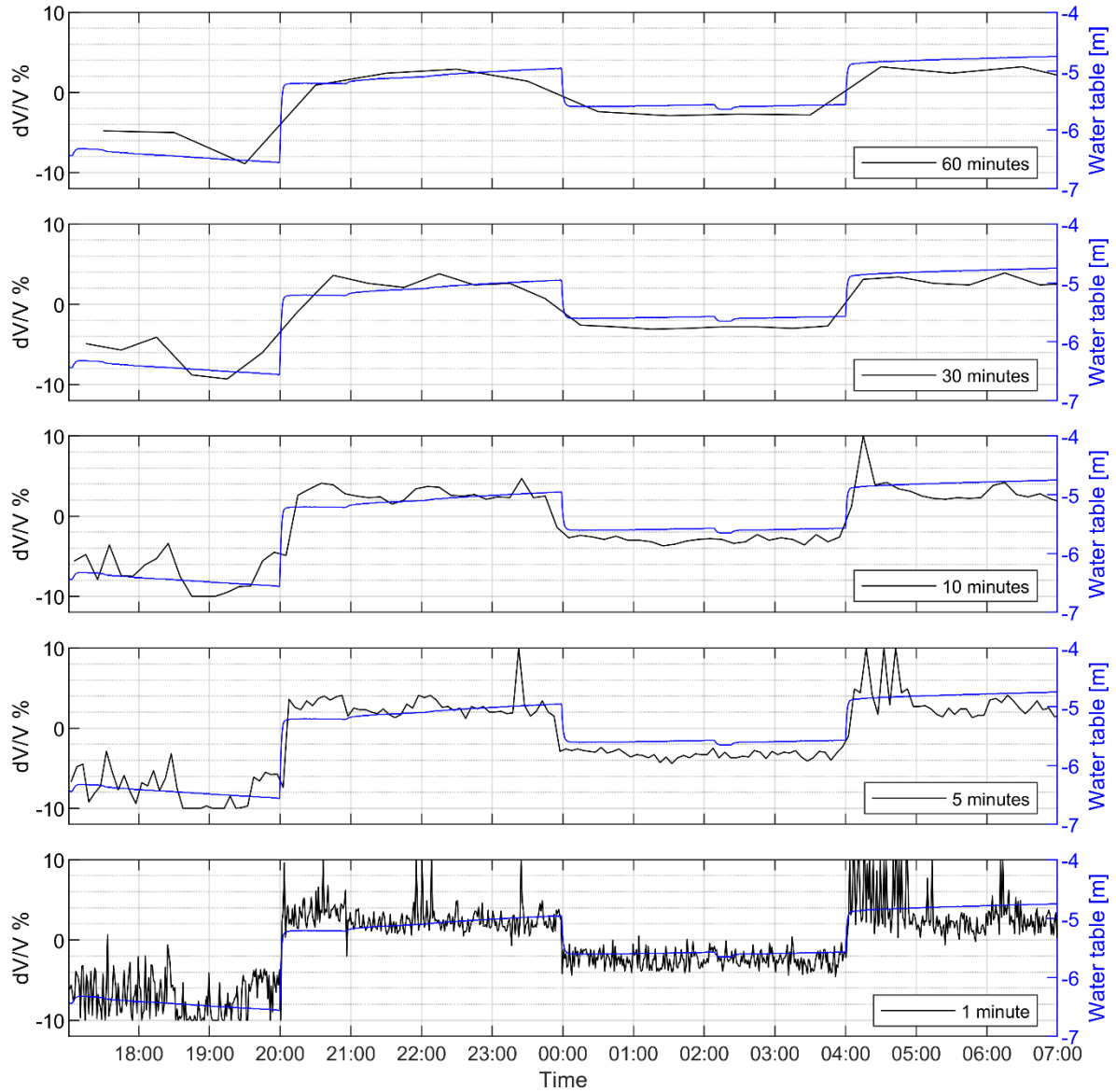


Figure 10  $dV/V$  computed in the 1-30Hz frequency range and 0-0.3s correlogram window for different sub-signals length (station pair STN13-STN14).

### 3. The experimental test in the Campastrino aquifer

#### 3.1. Site description

The second experimental test has been performed in the water catchment field located in the northern Apennines, in the so-called Campastrino aquifer, in the municipality of Ventasso (Reggio Emilia province) (Figure 11).



Figure 11 Location of the Ventasso water catchment field. The green rectangle represents the area where the test has been performed. The building is the bottling plant.

The underground water is not contained in a fluvial deposit like the Crépieux-Charmy case study, but in the Petrignacola sandstones formation which is an alternation of shale and fractured sandstone (Plesi et al, 2002). This layer is limited by the shale formations of Canetolo and San Siro, respectively at the bottom and at the top (Plesi et al, 2002), which make the aquifer confined. Such geological condition leads to a complex hydrogeological regime characterized by a secondary permeability ( $10^{-4}$  m/s) that guarantee very slow and effective water filtering action preventing any possible direct contact between surface waters, of meteoric origins, and deep waters. Moreover, the lithology of the Petrignacola formation makes the aquifer extremely heterogeneous, whose response to the extraction is extremely rapid, but with limited quantity and extremely long refilling times. The recharge of the aquifers occurs, first of all, by direct infiltration of the meteoric precipitations that fall within the drainage basin which approximately extends for 2.5 km<sup>2</sup>. Surface watercourses probably provide an additional contribution by dispersing part of their water throughout the intense rock fracture state. The water level depth varies depending on the position of the fractured sandstone layers that are difficult to be identified because of their heterogeneity. In our test, given the small distance covered by the seismic array, we assumed that, in the neighbouring area of the well used for the experiment, the geological conditions do not vary.

Since 1984, the SEM Group (Sorgenti Emiliane Modena SpA) has been exploiting the site for the bottling, production and distribution of natural mineral water. In the years, 13 wells have been built within the study area (Figure 12), however, not all of them nowadays are used to provide water to the bottling plant. In fact, the current most used well is the Lieta 1 that is supported by Cerca-Ventasso one in case the water demand is increased. For this reason, we did perform our experimental test generating water table variation with the Manutenzione well which is not used by the SEM Group and is sufficiently far from the other active pumping systems.

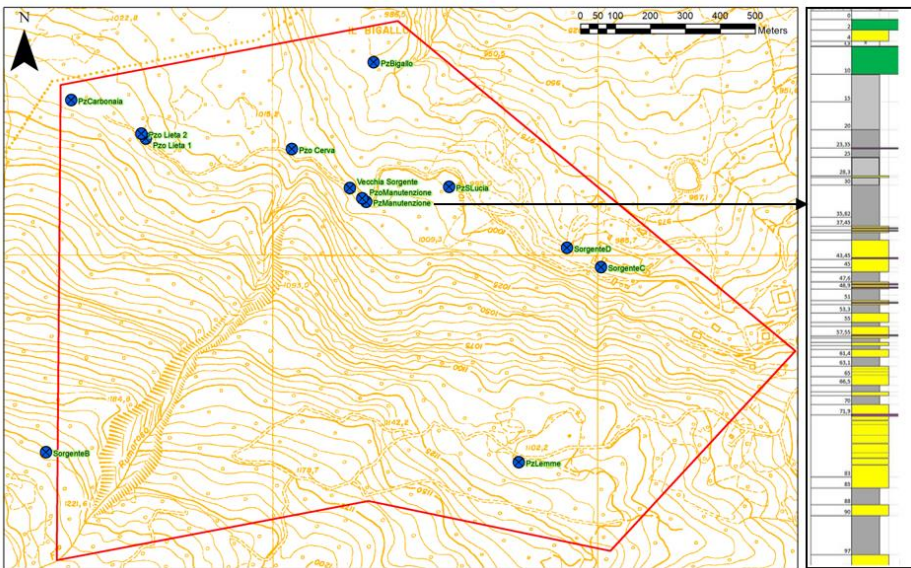


Figure 12 Left: Cartography with the location of the wells. The red polygon represents the area where the SEM Group is allowed to exploit water. Right: Stratigraphy of the Manutenzione well: green = debris deposits, yellow: Petrignacola sandstones and, grey: shale formations of Canetolo and San Siro.

### 3.2. Methods

In comparison to the Crépieux-Charmy case study, at the Ventasso site, we deployed 5 Nanometrics Trillium 3-C seismometers (0.05-100 Hz -3dB band) coupled to the Centaur data-loggers that have been recording the ambient seismic noise with a sampling frequency of 200 Hz. The digitizers were connected to a GPS antenna for time synchronization. The seismometers have been installed around the Manutenzione pumping station that has been used to produce artificial underground water variation (Figure 13Figure 4). The recordings have been processed following the same procedure mentioned for the French case study. In detail, mean and trend removal, time-domain normalization and spectral whitening have been performed (Bensen et al., 2007). As well as the previous experimental test, cross-correlations have been computed using five-minute-long sub-signals to ensure a fair reconstruction of the fast underground water level changes. Finally, the obtained dataset has been processed according to the seismic interferometry technique.

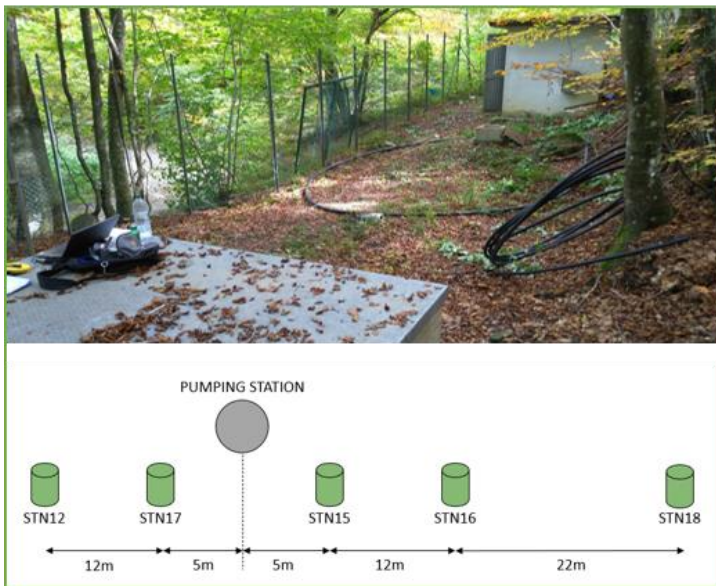


Figure 13 Photo of the water catchment field with a scheme of the installed seismic stations.

Contrary to the previous case study, in the Ventasso site, during the acquisition of the ambient vibrations, the pumping system has been activated only once at 9 am. It produced a decrease of the groundwater level from 9 to 33m depth, measured within the well itself (Figure 14). The evolution of the underground water was monitored by means of a piezometer located inside the Manutenzione well and it is shown in Figure 14.

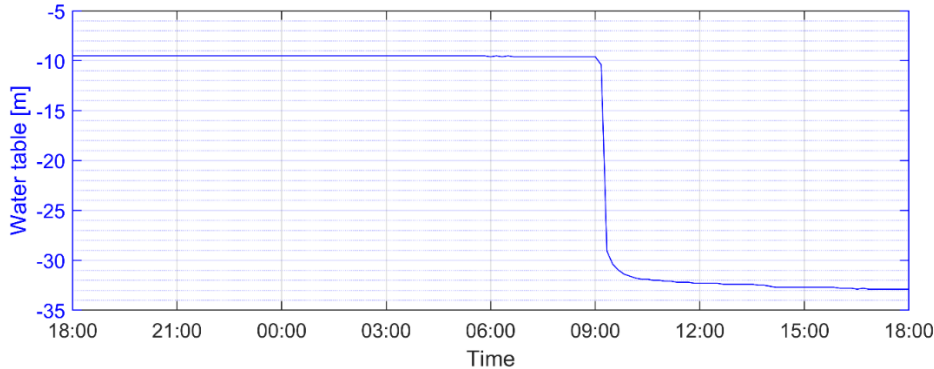


Figure 14 Water level measured at the pumping station.

### 3.3. Results and discussions

The vertical component of the collected ambient seismic noise signals exhibits a clear difference between the day and night hours. In fact, the first part of the signals does not present any time-domain peak, whereas, starting from 7:00 am the signals get noisier. This trend is linked to the operators that performed simultaneously surveys for the characterization of the aquifer (ERT and manual piezometer readings). We can notice that such disturbances hide the amplification of the signals due to the activation of the pumping system. Nevertheless, an apparent change of the waveform's amplitude is still visible (around 9.00 am) for station STN17 and STN15 which were the closest ones to the well. We verified that the noise field remained quite stable both in space and time in the 0.05-60 Hz frequency band although noises have been generated by the pumping system activation and the survey's execution.

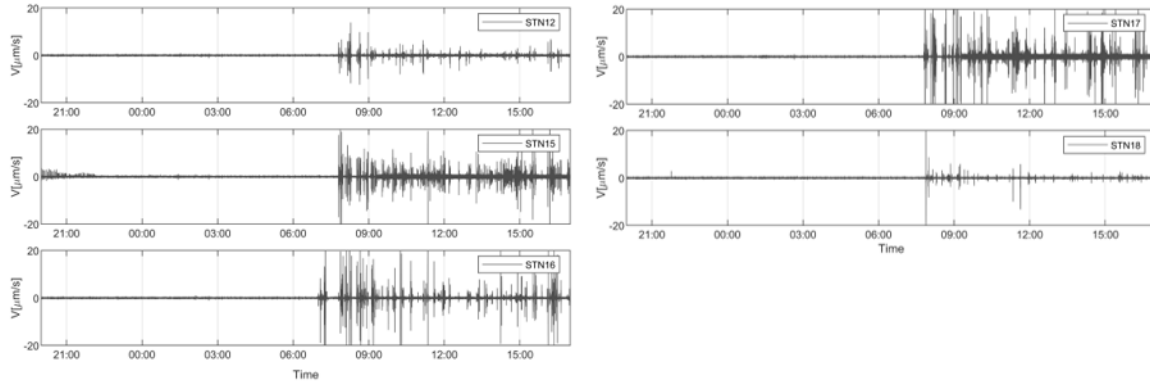


Figure 15 Vertical component of the ambient seismic noise records for each seismic station.

Figure 16 focus on the results obtained considering the stations' pairs STN15-STN16 and the STN15-STN18, which distance is 12m and 34m, respectively. Both the correlograms and dV/V curves have been obtained in the broadband frequency range (0.05-60Hz). It can be noticed that for the closest stations (STN15-STN16), the highest amplitude phases in the correlogram arrives at 0s lag meaning that the two seismometers are too close to each other to highlight a delay in the correlogram. On the contrary, for the stations with the greater inter-distance, the correlogram exhibits phase peaks occurring at 1.5s. In this case, the distance between the stations is therefore sufficient to show the propagation of the ambient seismic noise wavefield. We deem that for both station pairs, the most energetic arrivals correspond to the ballistic waves travelling from one seismometer to the other.

The dV/V curves have been estimated considering the correlogram window with the most energetic phases. For the STN15-STN16 pair, we did use the correlations in the 0-0.3 s window, whereas for the couple STN15-STN18 we did consider the 1.5-1.8 s window. The obtained results show that the computed dV/V curves are noisier during the daytime. We think that the strong fluctuations in the seismic velocity variation curves are associated with the disturbances introduced while performing the ERT survey. Despite the noisy results, considering the smoothed dV/V it is possible to obtain dV/V variations coherent with the water table level. With regard to the station pair with the lower inter-distance (STN15-STN16), the seismic velocity variations are in agreement with the underground water level measured in the well (Figure 16-top). We, therefore, believe that the wavefield in the 0-0.3 s window is dominated by P-waves since the velocity variations are in agreement with the saturation state.

On the contrary, the dV/V curve obtained for the stations that are 34 m distance from each other (STN15-STN18), exhibits an anticorrelated trend to the water table level (Figure 16– bottom). We thus hypothesize that the selected correlogram time window is dominated by surface waves. Despite the result of the couple STN15-STN16, the result obtained for the STN15-STN18 station pair shows a not noisy dV/V curve during the night-time, and without any seismic velocity variation (the curve is stable around 0% dV/V). Such behaviour has been also observed while analysing other stations pairs. Figure 17 displays the results obtained for the other four couples of stations. The dV/V curves that show an anticorrelated trend to the water table fluctuation, are the only ones that present a 0% variation of the seismic velocities during the night-time. This suggests that in a natural environment, where the ambient seismic noise does not interfere with spurious signals (i.e. people walking close to the seismometers), the passive interferometry could lead to obtained more robust dV/V estimates. All the obtained dV/V estimates share a very variable portion that occurs a few hours before the pump has been turned on (Figure 16 and Figure 17). Smoothing these strong variations (black line in the plot) generates a dV/V which seems to predict the change of the water table. However, considering the raw seismic velocity variations (dotted grey line) it is possible to observe that in the time window between 7:00 and 9:00 am the estimated dV/V shows the most variable trend. We deem that the strong dV/V variability observed few hours before the pumps were switched on is linked to the noise generated by the operators that unload the instrumentation from the car and deploy the electrical cables necessary to perform the electrical resistivity tomography. The analysis also revealed that when considering stations pairs with greater inter-distance (i.e. STN15-STN18, STN12-STN16 and, STN12-STN18) the obtained dV/V is anti-correlated to the water table level. Such behaviour may be linked to the fact that considering a bigger portion of soil between the stations there is a higher level of scattering which result in a generation of surface waves.

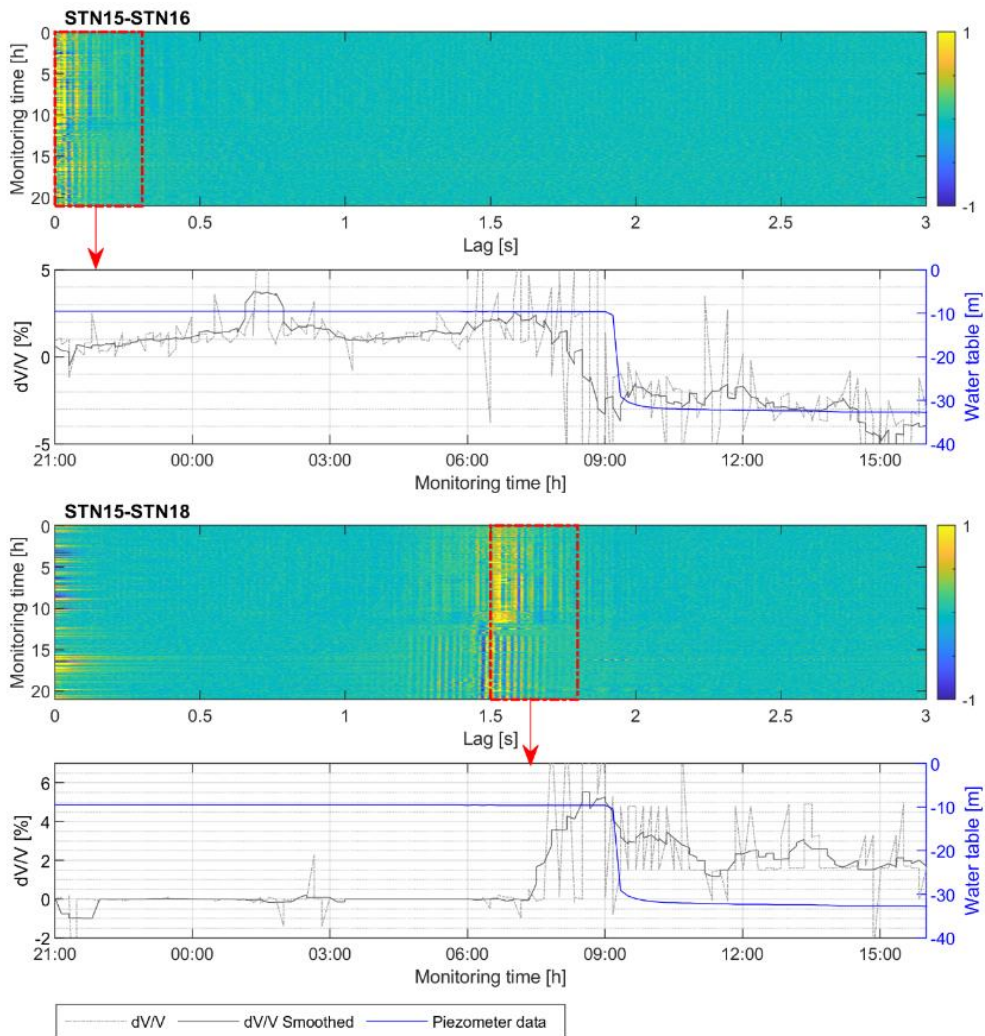


Figure 16 Results of the passive interferometry method applied to the station's pairs STN15-STN16 and STN15-STN18. In each panel, at the top the correlogram; at the bottom the computed  $dV/V$  for the selected red-framed time window. The dashed and solid grey curves represent the raw and the smoothed seismic velocity variation ( $dV/V$ ) respectively. The blue curve is the water level measured in the well during the test.

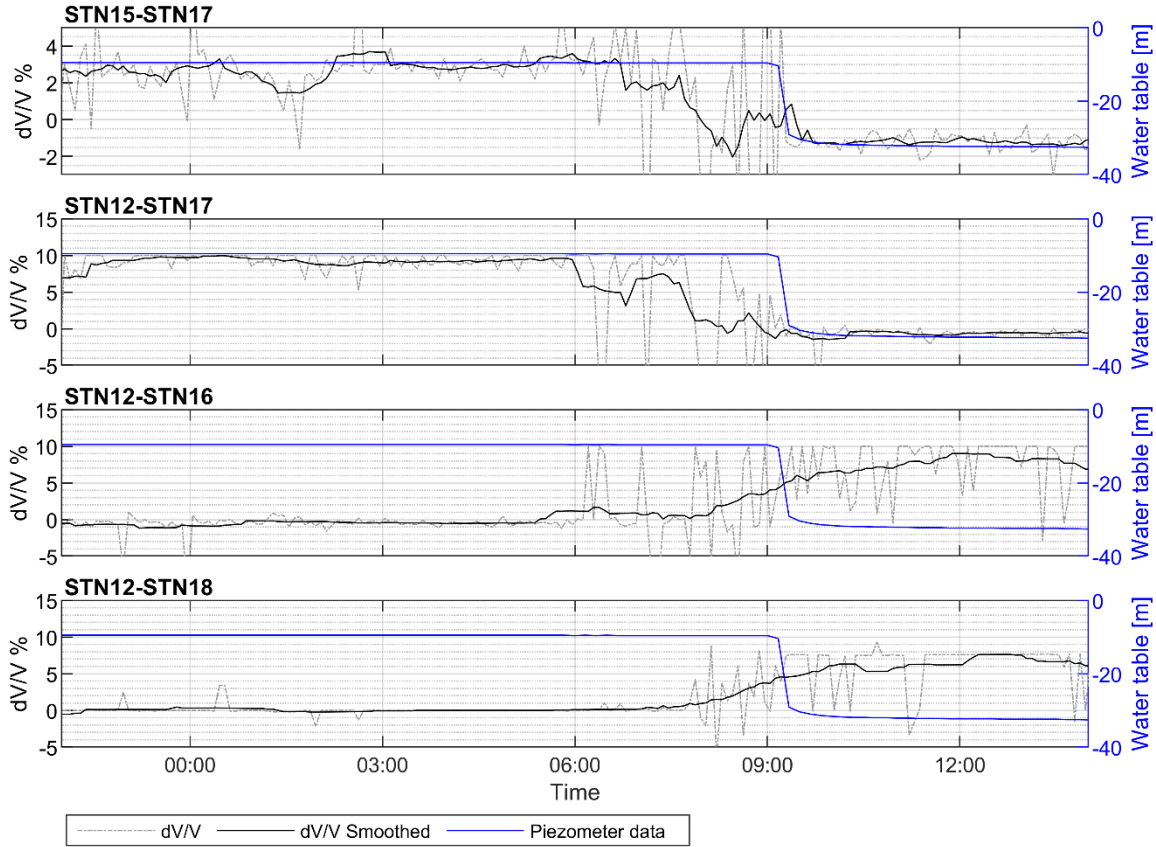


Figure 17 Seismic velocity variations estimated for different stations pairs.

#### 4. Conclusions

In this work, we applied seismic noise interferometry to assess whether this methodology can be used to monitor the water table variations occurring in different hydrogeological contexts in the future perspective of monitoring saturation state in landslides. The analysed case studies differ both in terms of aquifer type as well as in water depth. In detail, the French site concern an unconfined aquifer whose water table generally oscillates in the first ten-meter depth. On the contrary, the Italian aquifer is confined in the Petrignacola sandstone formation that, in the surrounding area where the test has been performed, is found around 40 m depth. Both experimental tests have been performed by artificially changing the groundwater level using pumping systems. The estimated seismic velocity variations showed to be strictly dependent on the water table, thus, to the soil saturation state. Depending on the selected correlogram window used to compute the  $dV/V$  changes with the Stretching technique, we retrieved seismic velocity variations that are either correlated or anti-correlated to the groundwater level. We associate this result to a different composition of the wavefield within the analysed time window of the cross-correlations. In more detail, provided the different response of seismic waves velocity to the saturation (density effect), we deem that lags correlogram windows are dominated by P-waves when the  $dV/V$  curves follow the groundwater changes; on the contrary, if the estimated seismic velocity changes are anti-correlated to the water table it is plausible to suppose that the surface waves dominate the selected time window. However, more seismic investigations and experimental tests are going on to deep understand the composition of the seismic noise wavefield and thus to assess which wave-type dominates the correlogram, according to the site, the station offset and the considered lag window (Bonnefoy-Claudet et al., 2006).

Even though there is an overall agreement between piezometric measurements and passive interferometry results, some discrepancies are present. As often mentioned in the literature, the monitoring of the water table based on seismological measurements requires a stable distribution of the sources of noise (Le Breton et al. 2021). This requirement is hardly achieved in the water catchment fields, where water pumping happens at different times and locations in the field. The nonstationary distribution of the sources of noise creates spurious artefacts that may

affect the velocity changes. We believe that the activation of such sources creates strong energetic seismic body waves that are refracted inside the medium and may arrive simultaneously with the surface waves of interest for the monitoring of the water table. This is particularly true when the stations inter-distance is too small to separate body and surface waves arrivals. This becomes an issue when trying to identify the depth dependence of the velocity change because it is difficult to clearly identify time windows mainly dominated by surface waves.

The tested sub-signals length in the French case study showed that the increase in time resolution (i.e. short sub-signals lengths) reduces the signal-to-noise ratio and thus it results in dV/V curves noisier with spurious velocity variations that may not be linked to changes in the medium. Nevertheless, in the perspective of building landslide early monitoring systems, it is extremely important to increase the time-resolution to promptly prevent the landslide occurrence.

The obtained results are promising and show the ability of the noise interferometry technique in monitoring soil saturation within complex hydrogeological conditions (i.e. in landslide bodies). However, it is necessary to perform longer monitoring tests to understand if this methodology performs well also under natural conditions. Additionally, numerical simulations are going on to investigate the effect of the involved parameters (filters, correlogram time window, seismic stations inter-distance, etc) in the dV/V estimates. In conclusion, the results of this study suggest that landslide early-warning systems could be improved using the ambient noise correlation method since it can provide in-depth knowledge of the landslides features. The use of low-cost seismic sensors could also promote the deployment of dense monitoring networks allowing for better management of the water resource. Nevertheless, estimating groundwater fluctuations using the dv/v in the natural environment might require distinguishing it from other influence factors (i.e. thermoelastic effects).

## 5. Bibliography

- Alimohammadlou, Y., Najafi, A., Yalcin, A., 2013. Landslide process and impacts: A proposed classification method. *CATENA* 104, 219–232. <https://doi.org/10.1016/j.catena.2012.11.013>.
- Bensen, G.D., Ritzwoller, M.H., Barmin, M.P., Levshin, A.L., Lin, F., Moschetti, M.P., Shapiro, N.M., et al. (2007) Processing seismic ambient noise data to obtain reliable broad-band surface wave dispersion measurements. *Geophysical Journal International*, 169, 1239–1260. doi:10.1111/j.1365-246X.2007.03374.x
- Bièvre, G., Franz, M., Larose, E., Carri`ere, S., Jongmans, D., Jaboyedoff, M., 2018. Influence of environmental parameters on the seismic velocity changes in a clayey mudflow (Pont-Bourquin Landslide, Switzerland). *Engineering Geology* 245, 248–257. <https://doi.org/10.1016/j.enggeo.2018.08.013>. Biot, M.A., 1962. Mechanics of deformation and acoustic propagation in porous media. *Journal of applied physics* 33, 1482–1498.
- Bonnefoy-Claudet, S., Cotton, F. & Bard, P.-Y. (2006) The nature of noise wavefield and its applications for site effects studies. *Earth-Science Reviews*, 79, 205–227. doi:10.1016/j.earscirev.2006.07.004
- Clements, T., Denolle, M.A., 2018. Tracking Groundwater Levels Using the Ambient Seismic Field. *Geophysical Research Letters* 45, 6459–6465. <https://doi.org/10.1029/2018GL077706.vo>
- Coussot, P., 1995. Structural Similarity and Transition from Newtonian to Non-Newtonian Behavior for Clay-Water Suspensions. *Phys. Rev. Lett.* 74, 3971–3974. <https://doi.org/10.1103/PhysRevLett.74.3971>.
- Froude, M.J., Petley, D.N., 2018. Global fatal landslide occurrence from 2004 to 2016. *Natural Hazards and Earth System Sciences* 18, 2161–2181. <https://doi.org/10.5194/nhess-18-2161-2018>.
- Garambois, S., Voisin, C., Romero Guzman, M.A., Brito, D., Guillier, B. & Réfloch, A. (2019) Analysis of ballistic waves in seismic noise monitoring of water table variations in a water field site: added value from numerical modelling to data understanding. *Geophysical Journal International*, 219, 1636–1647. doi:10.1093/gji/ggz391
- Gret, A., Snieder, R., Scales, J., 2006b. Time-lapse monitoring of rock properties with coda wave interferometry: TIME-LAPSE MONITORING OF ROCK PROPERTIES. *J. Geophys. Res.* 111 <https://doi.org/10.1029/2004JB003354> n/a-n/a.
- Huang, X., García, M.H., 1998. A Herschel–Bulkley model for mud flow down a slope. *Journal of Fluid Mechanics* 374, 305–333. <https://doi.org/10.1017/S0022112098002845>.
- Hillers, G., Campillo, M., Ma, K.-F., 2014. Seismic velocity variations at TCDP are controlled by MJO driven precipitation pattern and high fluid discharge properties. *Earth and Planetary Science Letters* 391, 121–127. <https://doi.org/10.1016/j.epsl.2014.01.040>.
- Intrieri, E., Gigli, G., Mugnai, F., Fanti, R., Casagli, N., 2012. Design and implementation of a landslide early warning system. *Engineering Geology* 147–148, 124–136. <https://doi.org/10.1016/j.enggeo.2012.07.017>.

- Jongmans, D., Garambois, S., 2007. Geophysical investigation of landslides : a review. *Bulletin de la Société Géologique de France* 178, 101–112. <https://doi.org/10.2113/gssgbull.178.2.101>.
- Le Breton, M., Bontemps, N., Guillemot, A., Baillet, L. & Larose, É. (2021) Landslide monitoring using seismic ambient noise correlation: challenges and applications. *Earth-Science Reviews*, 216, 103518. doi:10.1016/j.earscirev.2021.103518
- Meier, U., Shapiro, N.M., Brenguier, F., 2010. Detecting seasonal variations in seismic velocities within Los Angeles basin from correlations of ambient seismic noise. *Geophysical Journal International* 181, 985–996. <https://doi.org/10.1111/j.1365-246X.2010.04550.x>.
- Obermann, A., Froment, B., Campillo, M., Larose, E., Plan`es, T., Valette, B., Chen, J.H., Liu, Q.Y., 2014. Seismic noise correlations to image structural and mechanical changes associated with the Mw 7.9 2008 Wenchuan earthquake. *Journal of Geophysical Research: Solid Earth* 119, 3155–3168. <https://doi.org/10.1002/2013JB010932>.
- Plesi, G., Daniele, G., Chicchi, S., Bettelli, G., & Catanzariti, R. [2002]. Note illustrative della Carta Geologica d'Italia alla scala 1: 50.000, Foglio 235 “Pievepelago”. Serv. Geol. d’Italia-Regione Emilia Romagna, Roma Pliny Elder (77–78 AD). Hist. mundi Nat. II.
- Rivet, D., Brenguier, F., Cappa, F., 2015. Improved detection of preeruptive seismic velocity drops at the Piton de La Fournaise volcano. *Geophysical Research Letters* 42, 6332–6339. <https://doi.org/10.1002/2015GL064835>.
- Sens-Schönfelder, C. & Wegler, U. (2006) Passive image interferometry and seasonal variations of seismic velocities at Merapi Volcano, Indonesia. *Geophysical Research Letters*, 33. doi:10.1029/2006GL027797
- Shapiro, N.M., Campillo, M., 2004. Emergence of broadband Rayleigh waves from correlations of the ambient seismic noise. *Geophysical Research Letters* 31. <https://doi.org/10.1029/2004GL019491>.
- Van Asch, T.W.J., Malet, J.-P., 2009. Flow-type failures in fine-grained soils: an important aspect in landslide hazard analysis. *Natural Hazards and Earth System Sciences* 9, 1703–1711. <https://doi.org/10.5194/nhess-9-1703-2009>.
- Voisin, C., Garambois, S., Massey, C., Brossier, R., 2016. Seismic noise monitoring of the water table in a deep-seated, slow-moving landslide. *Interpretation* 4, SJ67–SJ76. <https://doi.org/10.1190/INT-2016-0010.1>.
- Voisin, C., Guzmán, M.A.R., Réfloch, A., Taruselli, M., Garambois, S., 2017. Groundwater Monitoring with Passive Seismic Interferometry. *Journal of Water Resource and Protection* 09, 1414. <https://doi.org/10.4236/jwarp.2017.912091>.

## Conclusions

In the last years, many hydrogeological events occurred all around the world resulting in loss of life as well as economic and material damages. The increase of such events is strongly conditioned by both natural and human factors and adequate prevention and mitigation measures are not provided in a timely manner. One of the current challenges is to provide monitoring techniques that allow forecasting and real-time monitor these phenomena, reducing the adverse effect of their consequences. To this perspective, researchers started to integrate geophysical techniques in multidisciplinary approaches to study slope instability processes as well as to monitor their evolution over time.

In this regard, in this PhD thesis, ambient seismic noise data were collected at different sites and analysed with different techniques to evaluate whether the natural vibration can provide precious information to support already existing technologies towards the monitoring of landslide hazard as well as the management of related risk. Among the available geophysical methods for the analysis of ambient noise recordings, three type of analysis were chosen due to their capability in observing the variation of specific effects or parameters during time: 1) spectral analysis; 2) polarization analysis; 3) monitoring of seismic wave velocity changes ( $dV/V$ ). These methodologies have been used within the scope of the PhD project to study the dynamic response of unstable rock compartments, both in terms of resonance frequencies and preferential vibrational directions, and to infer whether ambient seismic noise allows retrieving information concerning the stability and water content of landslides. These activities have enabled us to present a clearer picture of the validity of the considered methods as well as to infer whether all of them can be used for the analysis of the ambient seismic noise. In addition, to achieve the above-mentioned objective and in view of a future deployment of long-term monitoring stations, new low-cost seismometers were tested carrying out in-situ and laboratory testing.

With regards to the monitoring of unstable rock blocks, the controlled collapse test confirmed that both spectral and polarization features of seismic noise recordings are strictly dependent on the evolving constraints of the unstable rock blocks thus, with their stability. According to previous studies, we observed that rock bridges breakage leads to a drop of resonance frequencies, however, it has been additionally noticed that they can also bring to a new dynamic response if the monitored rock undergoes an abrupt change of its initial stability condition.

Different methodologies have been tested for the analysis of the seismic noise recordings. As far as the spectral analysis is concerned, the implementation of the multitaper method was proposed for the estimate of structures' vibrational modes allowing for a reduction of the bias and variability with respect to the traditional techniques used in seismic methods. In terms of polarization features, the experimented spectral Singular Value Decomposition (SVD) approach proved to be the most complete method to study 3D motion characteristics of rock structures, either to understand their vibration modes and to track their variation over time. This analysis provides more knowledge on the kinematic and dynamic conditions of unstable slopes with respect to the hodograms, the time-domain covariance matrix method and the HVSRA approach. Our work also shows that realistic numerical modelling of the dynamic behaviour of rock structures is still a challenging task especially in terms of the accurate definition of the spatial and mechanical features of the constraints. Therefore, the support of modelling to guide the processing and interpretation of seismic noise data still needs to be improved. The analysed case studies lead us to state that a proper monitoring approach should take into account both spectral and polarization features, as well as different signals processing methods, to better infer the dynamic response of the monitored structures. Seismic noise tests have provided preliminary outcomes since a rigorous investigation should involve continuous monitoring for an extended time length and through different climatic conditions. Nevertheless, these studies evidenced the capability of continuous seismic ambient noise measurements to be applied for monitoring the changes in the dynamic response of the unstable rocks, which could indicate an incoming general collapse.

Concerning water content in landslide body, the two pilot tests confirmed the potential of the ambient seismic noise cross-correlation method in retrieving water content variations in both confined and unconfined aquifers. The results highlighted the different composition of the wavefield within different correlogram time windows. In more detail, provided the different response of seismic waves velocity to the saturation, it has been possible to retrieve seismic velocity variations either correlated or anti-correlated to the groundwater level. In view of using such methodology for landslides characterization, different signals' length has been tested revealing the possibility to increase the time resolution down to one minute. This result is of crucial importance in the view of building

early monitoring systems since it allows to promptly prevent the landslide occurrence. The analysed case studies additionally highlight the importance of array design, particularly station spacing, for shallow environmental studies using seismic noise. In fact, it has been observed that interstation distances had a dominant control on cross-correlation frequency content and thus depth sensitivity. To this concern, numerical simulations are going on to investigate the effect of the involved parameters (filters, correlogram time window, seismic stations inter-distance, etc) and to deeply understand the composition of the seismic noise wavefield, thus assessing which wave-type dominates the correlogram, according to the site, the station offset and the considered lag window.

Within the preliminary test performed to monitor the landslide stability, the seismic noise measurements evidenced the different seismic response of diverse area of the slope involved in the complex landslide process. The use of polarization analysis and passive interferometry revealed that both techniques can provide useful information to characterize the dynamic conditions of the unstable slopes, thus improve our capabilities of landslides forecasting.

In view of future deployment of the long-term monitoring network, in this manuscript, we proposed the analysis of a low-cost seismometer. Both laboratory and field experimental tests demonstrated that the RaspberryShake-3D seismometers could be a valuable alternative to the high-cost broadband sensors in the evaluation of unstable rock dynamic response, provided the vibrational frequencies are within the RS flat frequency response. Moreover, their low cost combined with the limited installation and maintenance efforts as well as the possibility to send real-time data to a remote computer, make them an ideal candidate for rock-fall monitoring purposes.

Finally, in this thesis work, PassiveBarinda software for the analysis of ambient seismic noise data has been included. PassiveBarinda is a graphical user interface designed with Matlab for organising, viewing, and processing seismic signals. In the manuscript, a user guide is provided explaining how to use the available tools and thus implement the ambient seismic noise techniques discussed within the manuscript.

In conclusion, even if with different levels of results obtained for the analysed case studies, this PhD thesis evidenced as the passive seismic represents a useful tool for investigating and monitoring slope instability processes since it allows to infer spectral, polarization and seismic wave velocity features of the analysed site which give a contribution for managing the landslide risk.



## Appendix: PassiveBarinda Guide

### Index

<b>Introduction .....</b>	<b>122</b>
<b>Runnig PassiveBarinda.....</b>	<b>122</b>
<b>File.....</b>	<b>123</b>
Load signals .....	123
Save signals .....	124
Exit PassiveBarinda .....	124
<b>Processing .....</b>	<b>124</b>
<b>Basic processing.....</b>	<b>125</b>
Align signals.....	125
Resampling.....	125
Merge .....	126
Filter.....	126
Cut .....	126
Response deconvolution.....	127
<b>Advanced processing .....</b>	<b>129</b>
Spectral analysis.....	129
Polarization analysis .....	131
HVSR analysis .....	136
Cross-correlation analysis .....	139
Propagation plot .....	146
<b>Display .....</b>	<b>148</b>
Plot signals .....	148
Video CrossCorr .....	148
<b>Save.....</b>	<b>149</b>

## Introduction

This thesis section is devoted to the illustration of a Graphical User Interface (GUI) developed to process ambient seismic noise data. This appendix provides a manual that describes all the up-to-date available tools of the software. The figures used within the guide are obtained through the analysis of real seismic data collected on the field. PassiveBarinda is a graphical user interface designed with Matlab for organising, viewing, and processing seismic signals. The user needs to have Matlab installed on its personal computer to use the software. The manual documents how to use the available tools for the analysis of ambient seismic noise techniques, providing all the necessary information to apply the passive methods discussed within the manuscript.

### Runnig PassiveBarinda

PassiveBarinda is based on many functions which are contained all in the same folder. The user must set the Matlab current folder to the PassiveBarinda path. Running the *MAIN\_PassiveBarinda.m* file, figure 1 will appear. This is the main page of the software (Figure 1). On the left, the two tables will be filled with loaded signals. On the top, there are four uiMenu: File, Processing, Display and Save.

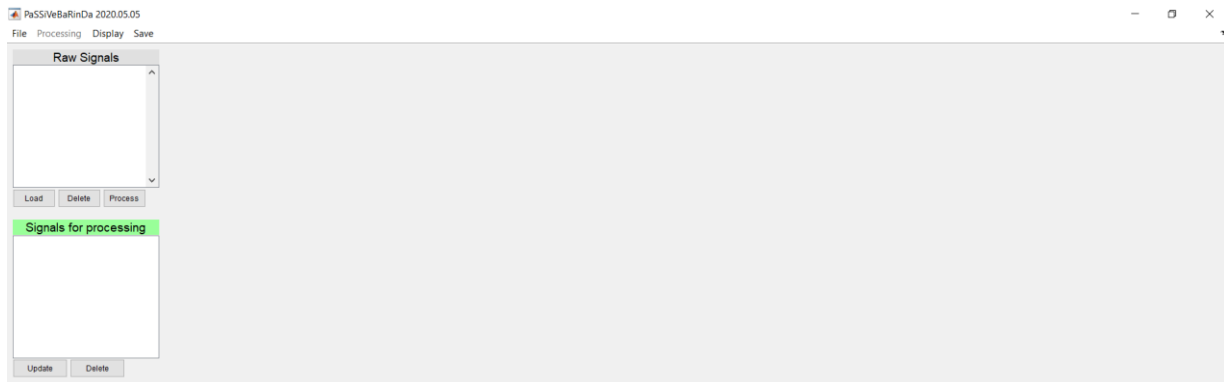


Figure 1: Main frame of PassiveBarinda.

The uiMenus contain the following tools:

- File:
  - Load signals
  - Save signals
  - Exit PassiveBarinda
- Processing:
  - Align Signals
  - Resampling
  - Merge
  - Filter
  - Cut
  - Response Deconvolution
  - Spectral Analysis
  - Polarization Analysis
  - HVSR Analysis
  - Passive Interferometry:
    - Cross-Correlation Analysis
    - Propagation plot
- Display:
  - Plot signals
  - Video CrossCorr
- Save

The next chapters navigate through each of these tools explaining how to use them and for which purpose.

## File

### Load signals

This version of the software accepts two types of files: .miniseed and .taru. The latter type of file is generated while using the *Save signals* tool (see next section).

Click on the menu "File" and select the "Load signals" item or hit the "Load" button below the first empty table (Figure 2). You get the open file dialogue box where you can select one or more files to be open. Use the SHIFT and CTRL keys to create custom selections. Click on "Open" to load the signals. All the selected files will appear in the table "Raw Signals" as shown in Figure 2-right.

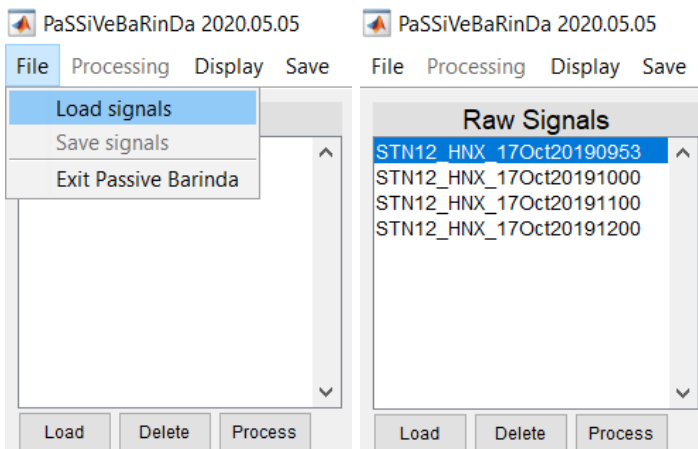
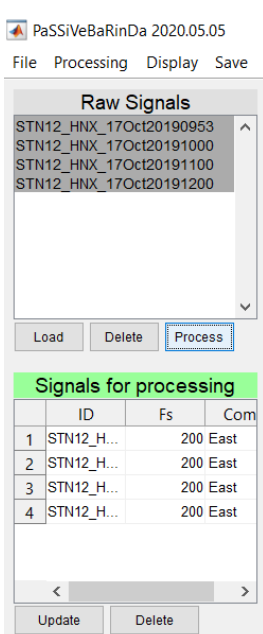


Figure 2: Left: Load Signals; Right: Loaded signals appear into Raw Signals table

Once the signals have been imported in the upper table (Raw Signals) the user can either load other files, delete some or all of them or process them. **Signals within the “Raw Signals” table will be never modified during the processing: they always remain RAW data.**

To work with the loaded data, the user must select the signals and click on the “Process” button. In such a way, the selected signals will appear also in the “Signals for processing” (SFP) table (Figure 3).



In this table, for each signal, its sampling frequency and its component will be displayed. The latter can be modified using the popup menu (choosing among East, West or Vertical options) according to the on-field setup of the sensor. If the component has been modified, the user must confirm the modifications by clicking on the “Update” button (left bottom corner). In this table, the user may also choose to delete some signals through the “Delete” button. If the user decides to add more signals in the “Signal for processing” table, the interface will ask whether to keep the already existing data or to substitute them with the new ones.

Once the signals are in the “Signals for processing” table, the user can start working on them. Indeed, the “Processing” uiMenu (on top of the main figure) will be activated only if this table is not empty.

To display the signals, after selection, use the “Display ➔ Plot signals” uiMenu (see “Plot signals” section).

Figure 3: Selected signals are moved in “Signals for processing” table using the “Process” button.

## Save signals

Using the "File ➔ Save signals" menu, all the signals within the "**Signals for processing**" table will be saved. The user will be asked to specify the directory and the name of the file. The saved file will have a .taru extension.

## Exit PassiveBarinda

Using either "File ➔ Exit PassiveBarinda" or the "X" icon on the upper-right corner of the tab, the user can close the application. Doing so the user will be asked to confirm his choice. In case of confirmation, all the open tabs will be closed, and the workspace will be emptied.

## Processing

This part of the software can be divided into two main sub-sections:

Within this guide, we will call the first one *Basic processing* (highlighted by a green square in Figure 4). These tools directly affect the signals and the results are automatically updated on the "signals for processing" data. Reverting to the original input is always possible by recalling signals from the "Raw Signals" table.

The second one, called *Advanced processing*, is highlighted by a blue square in Figure 4. These are tools developed for special purposes and thus dedicated to the analysis of the ambient vibrations as shown within the manuscript.

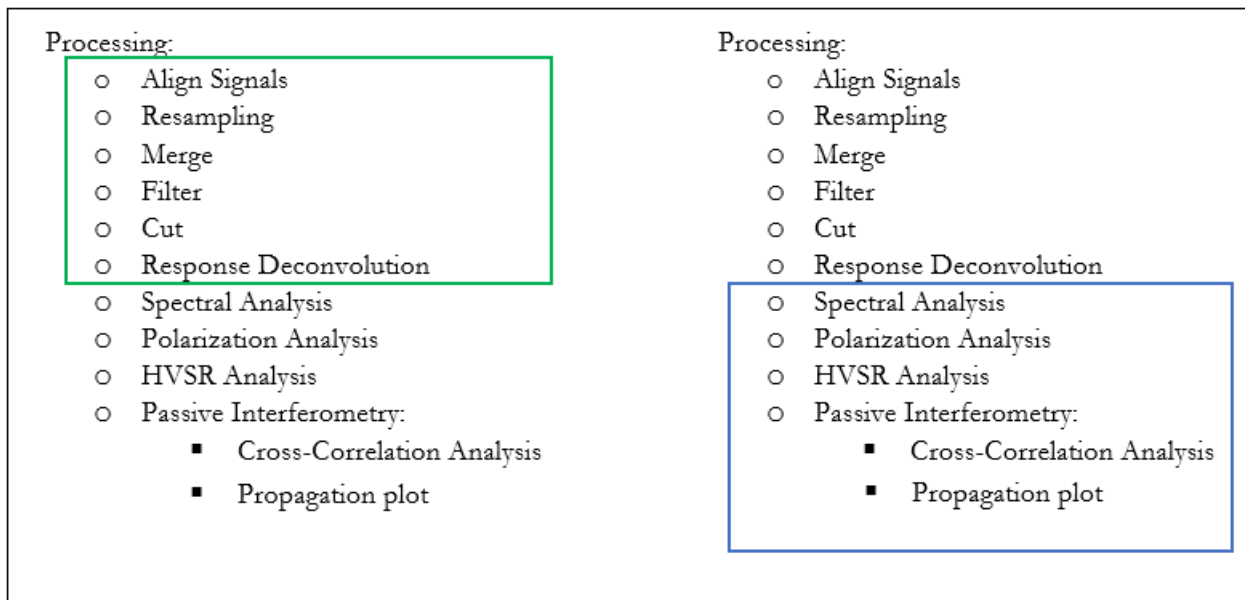


Figure 4: Subdivision of Processing uiMenu into Basic (green) and Advanced (Blue) tools.

## Basic processing

### Align signals

This tool is used to align two signals which contain a delay. To perform the alignment the user must select two signals in the SFP table, then by clicking on “*Processing*” uiMenu and thus on “*Align signals*” the tab in figure 5 will appear. The first plot shows the two signals that did not undergo any time alignment. The bottom one shows the computed alignment. Additionally, at the bottom of the tab, there is a description of the measured delay. By using the toolbar of the plot, the user can perform the zoom of the signals to visually check whether the two signals have been properly aligned. Finally, by clicking on the “*Align*” or “*Quit*” button the alignment will be confirmed or not, respectively.

N.B. Whether less or more than two signals have been selected, the Error tab will appear.

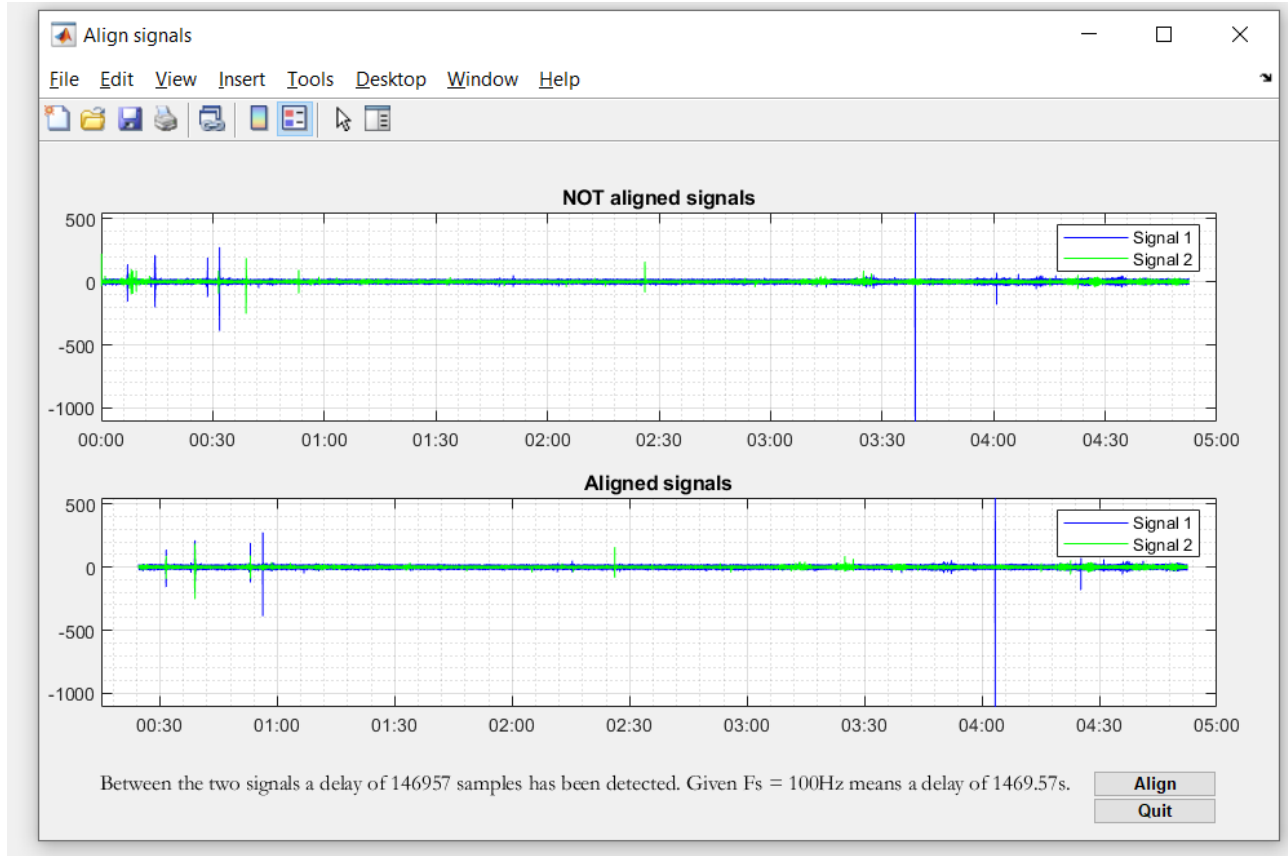


Figure 5: Alignment tab.

### Resampling

This tool resamples the input signal/s to the desired sampling frequency (Figure 6). The user can access the tool by clicking on “*Processing* ➔ Resampling”. Then, the new sampling frequency must be set and using the “Compute” button the resampling will be computed.

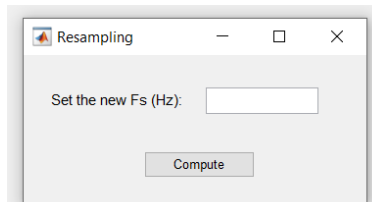


Figure 6: Resampling tab.

## Merge

This function is automatic. This means that, after signals selections, by clicking on “*Processing ➔ Merge*”, the data that belong to the same station and that have the same sampling frequency will be merged in a unique signal. Whether empty data exist they will be filled with zeros.

## Filter

Within PassiveBarinda three types of filters can be performed through the “*Processing ➔ Filter*” command:

- Low-pass: remove all frequency components above a specified frequency threshold (Fcut);
- High-pass: remove all frequency components below a specified frequency threshold (Fcut);
- Band-pass: remove all frequency components outside a specified interval (Fcut1, Fcut2) ;

Using the popup menu the user must select the type of filter and then specify Fcut for High-pass/Low-pass or Fcut1,Fcut2 for Band-pass filter (Figure 7). Using the “*Compute*” button the selected signals will be filtered.

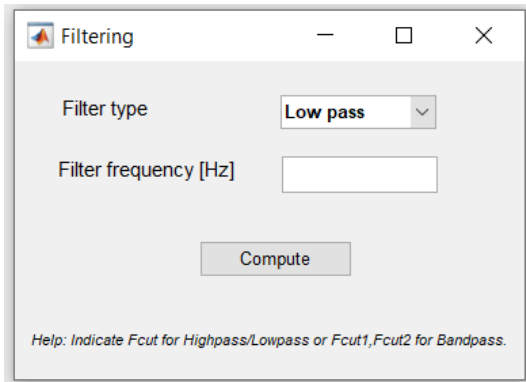


Figure 7: Filtering tab.

The software uses already existing Matlab functions which designs a minimum-order infinite impulse response (IIR) filter and uses the filtfilt function to perform zero-phase filtering and compensate for the filter delay. The width of the filter's transition region is controlled by the 'Steepness' argument that has been set to 0.95 value, meaning that the transition region is very narrow.

## Cut

This function allows cutting the signals at a specified date (*Processing ➔ Cut*). The user can select between two options (a combination of two is possible):

- *To - end* (Figure 8-left) ➔ This function is helpful when two or more signals are selected. Indeed, in this case, the PassiveBarinda automatically search the common initial and final date among the selected signals. It can be noticed that the user cannot modify the editable text field.
- *This time-This time* (Figure 8-right) ➔ When the “this time” option is selected the editable text field is enabled and the user can specify the date he wants. If the latter does not exist within the signal sampled time vector, the closest date is automatically selected.

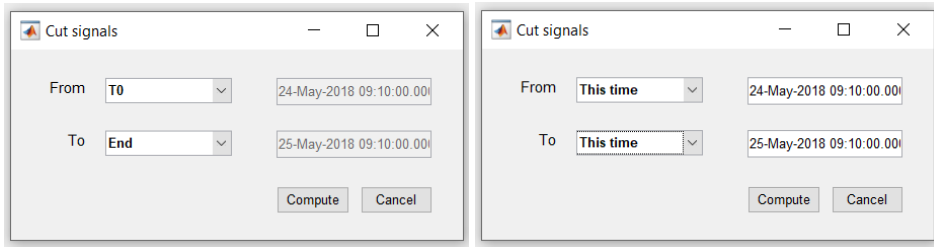


Figure 8: Cut tab with the two available options.

#### Response deconvolution

This tool performs the instrument response removal using the [JEvalResp](#) utility. The latter is a Javascript for evaluating and processing instrument response that can be downloaded through the [IRIS DMC Library](#). For more details about the instrument-response deconvolution check out this [link](#).

After the signal selection, clicking on the “*Processing → Response deconvolution*” uiMenu, the tab in Figure 9 will appear.

In this tab the user has to select:

1. The folder containing the JEvalResp utility (already within PassiveBarinda software);
2. The Sensor response;
3. The Digitizer response.

N.B. If both geophones and digitizer are in the same box enclosure, the user must upload only the sensor response because it is usually built taking into consideration the response of both sensor and digitizer.

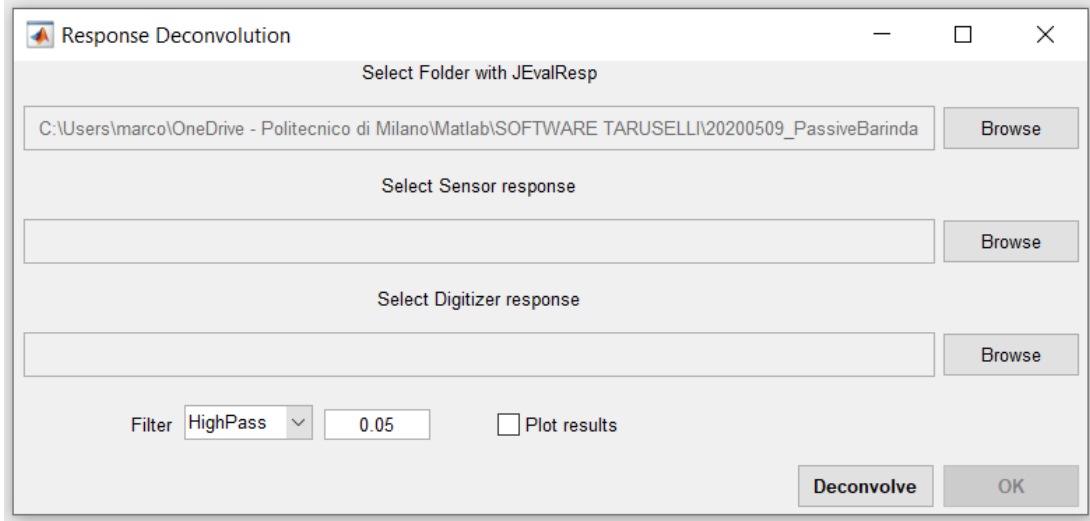


Figure 9: Response Deconvolution tab

To attenuate low-frequency components greatly amplified by the deconvolution process, the output signal needs to be high-pass filtered. It has been decided therefore to add in the response deconvolution tab the possibility to perform the filtering on the deconvolved signals. The user can furthermore decide whether to plot or not the results. To compute the deconvolution the user must click on the “*Deconvolve*” button. When the procedure is computed, if it has been checked the “*Plot results*” option, the following results will appear:

- 1) A figure showing the input signal in both time and frequency domain:

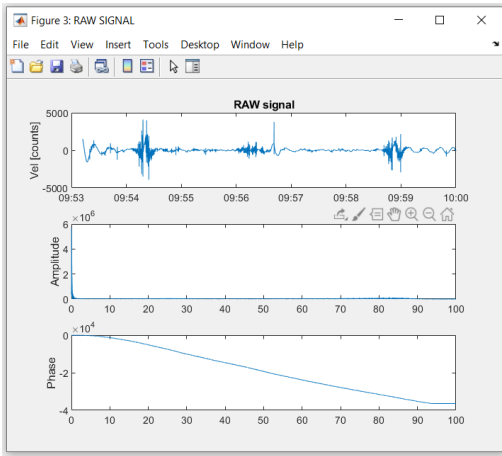


Figure 10: Raw signals characteristics

2) A figure showing the deconvolved signal in both time and frequency domain:

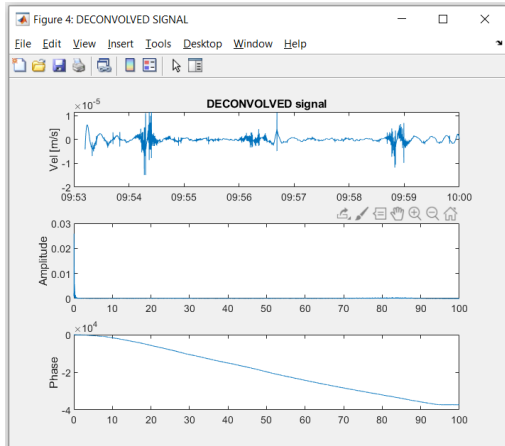


Figure 11: Deconvolved signals characteristics

3) A figure with the sensor and digitizer FRF:

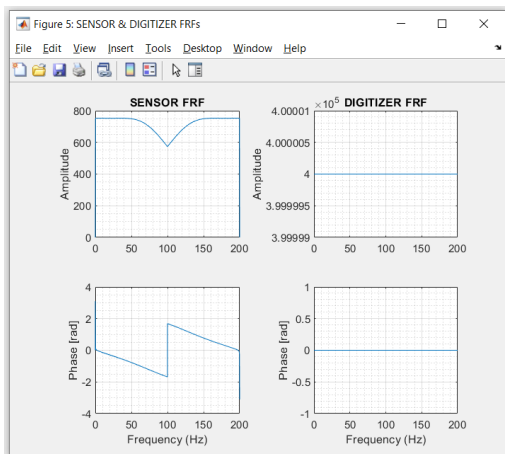


Figure 12: FRF of sensor and digitizer

N.B. This tool can be used even when more than one signal is selected. In this case, it is suggested to avoid plotting the results to save time in the processing procedure.

## Advanced processing

### Spectral analysis

This tool can be activated by selecting one signal within the *Signals for Processing* table and then clicking on *Processing* ➔ *Spectral analysis* (this analysis cannot be initiated if more than one signal is selected). The *Spectral Analysis* tab will appear as shown in figure 13.

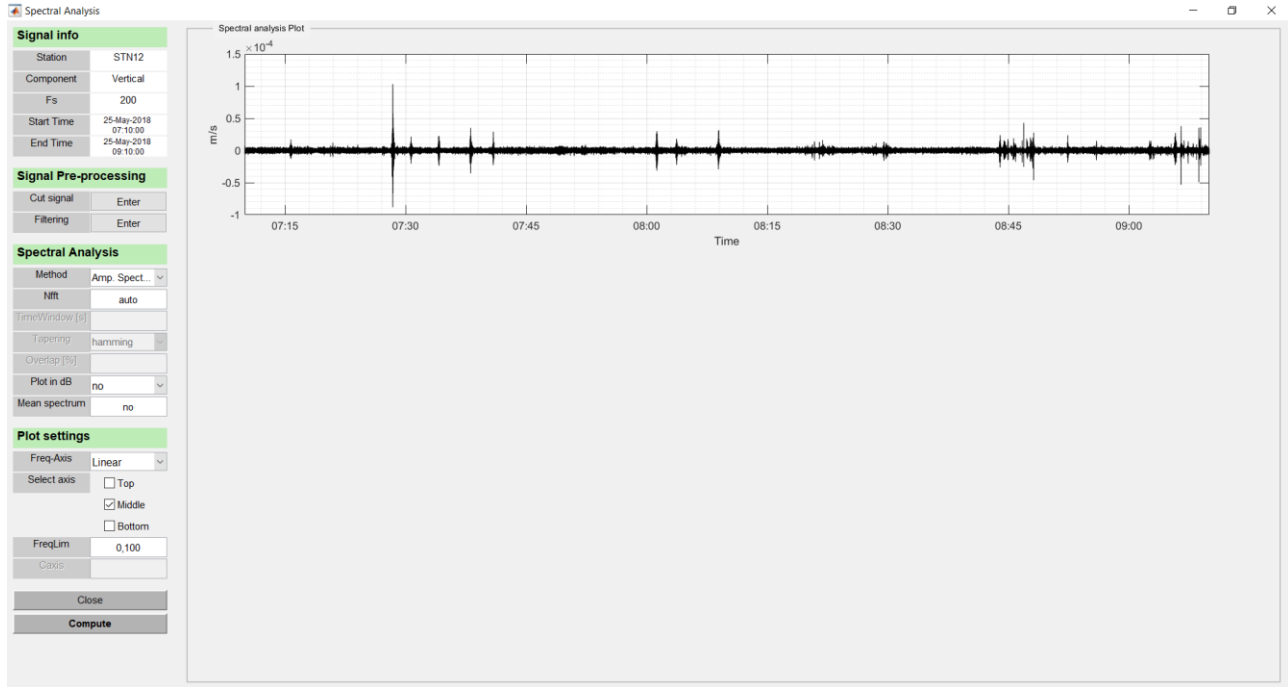


Figure 13: Spectral Analysis tab

The tab contains 4 sections:

1. Signal info: it contains all the information about the selected signal and it does not have any practical purpose.
2. Signal Pre-processing: it allows the user to cut or filter the signal (see the Basic processing section for more details about these tools).
3. Spectral analysis: it contains all the settings to perform the spectral estimate.
4. Plot settings: these parameters allow the modification of the obtained plots.

This document will focus only on the third and fourth sections of the list since the first one is just an info tab and the second tab tools have been described in the previous paragraphs.

Among the seven *Spectral Analysis* options, the user must first use the popup *method* menu to select the analysis he wants to perform:

- Amplitude spectrum: computes the amplitude spectrum of the signal using the FFT function;
- Phase spectrum: computes the phase spectrum of the signal using the FFT function;
- Periodogram: estimates the periodogram power spectral density (PSD) of the signal;
- Welch's Periodogram: returns the power spectral density (PSD) estimate of the input signal performed using Welch's overlapped segment averaging estimator;
- Multitaper: returns the Thomson's multitaper power spectral density (PSD) estimate of the signal;
- Spectrogram: returns the short-time Fourier transform of the input signal versus time;
- Stacked Spectrogram: it returns the stacked spectrogram.

Once the method is selected, the *Nfft*, *TimeWindow [s]*, *Tapering*, *Overlap[%]*, *Plot in dB* and *Mean spectrum* editable fields will be enabled or disabled depending on the required input for the chosen spectral analysis method. Here below more details about each of the input:

- *Nfft* = number of samples used to compute the Fourier transform.
- *TimeWindow [s]* = length (in seconds) of the window used to subdivide the entire signal in sub-signals.
- *Tapering* = type of window used to taper the time window.
- *Overlap [%]* = percentage of overlap among the windows.
- *Plot in dB* = it allows plotting the results either with the proper unit of measure or in decibel.
- *Mean spectrum* = for some spectral analysis, it is possible to plot the averaged spectrum.

Once all the required input has been set up, it is possible to perform the analysis by clicking on the *Compute* button. Figure 14 shows an example of a signal which underwent a spectral analysis. Into detail: the first plot shows the signal, the second one show the PSD computed with the Welch method and the last plot is the spectrogram.

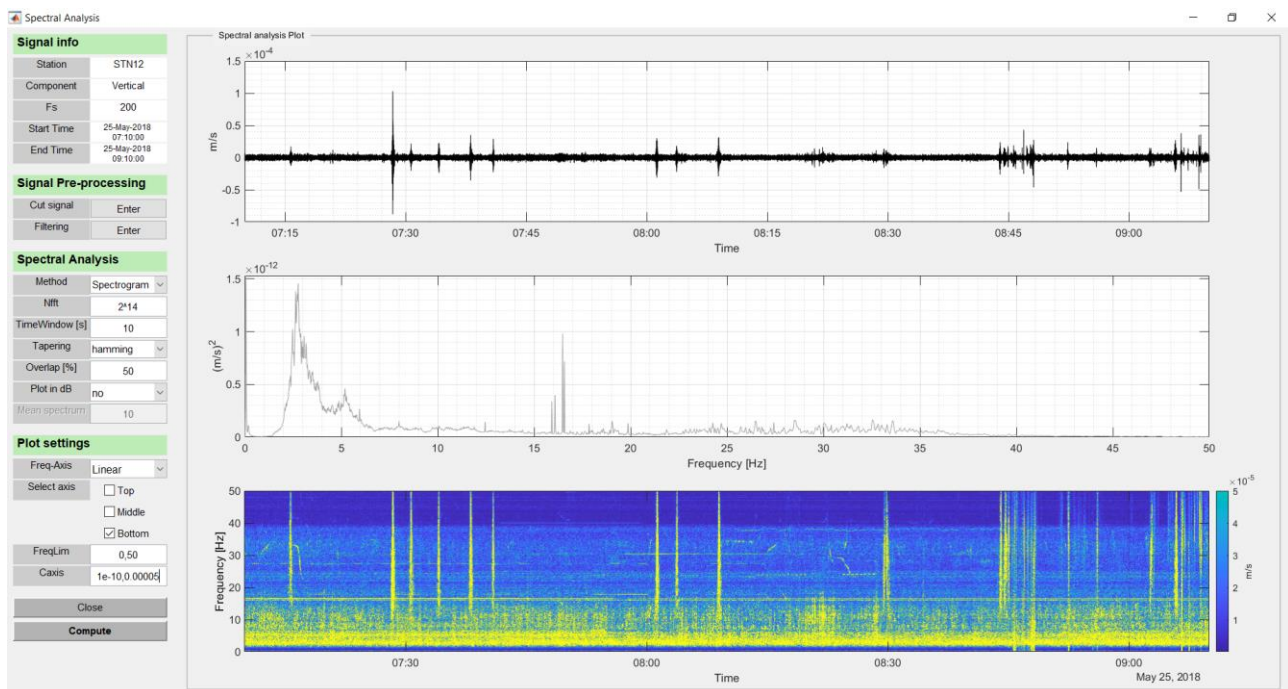


Figure 14: Spectral Analysis example: top: signal; middle: PSD with Welch method; bottom: Spectrogram.

Finally, in the *Plot settings* menu, the user can modify the plot appearance by changing the following options:

- *Freq-Axis*: it is possible to show the frequency axis either on a linear or logarithmic scale.
- *Select axis*: this option is used for two main reasons: first of all the plot settings are applied on the selected axis; secondly you can use this tool to select the axis used to plot the result of a new analysis.
- *FreqLim*: it allows to set the frequency limits.
- *Caxis*: it allows to set the colour scale of the spectrogram in case this method has been used.

Once the analysis is completed the user may choose to save the obtain plots by clicking on the specific icon that appears on the upper-right of the axes: .

## Polarization analysis

This analysis involves the four different approaches described in the manuscript to investigate the polarization features of the ambient vibrations:

1. HV rotate: the Horizontal-to-Vertical Spectral Ratio as a function of Azimuth (HVSRA);
2. H rotate: the Horizontal-to- Horizontal Spectral Ratio as a function of Azimuth (HHSRA);
3. the Principal Component Analysis (PCA) of the time-domain covariance matrix;
4. the Singular Value decomposition (SVD) of the Hermitian spectral density matrix.

The tool can be activated after selecting the three components belonging to the same sensor within the *Signals for Processing*” table and then clicking on *Processing → Polarization analysis* (an error will appear if the three components have not been selected). The *Polarization Analysis* tab will appear (figure 15) showing the user the three selected signal components.

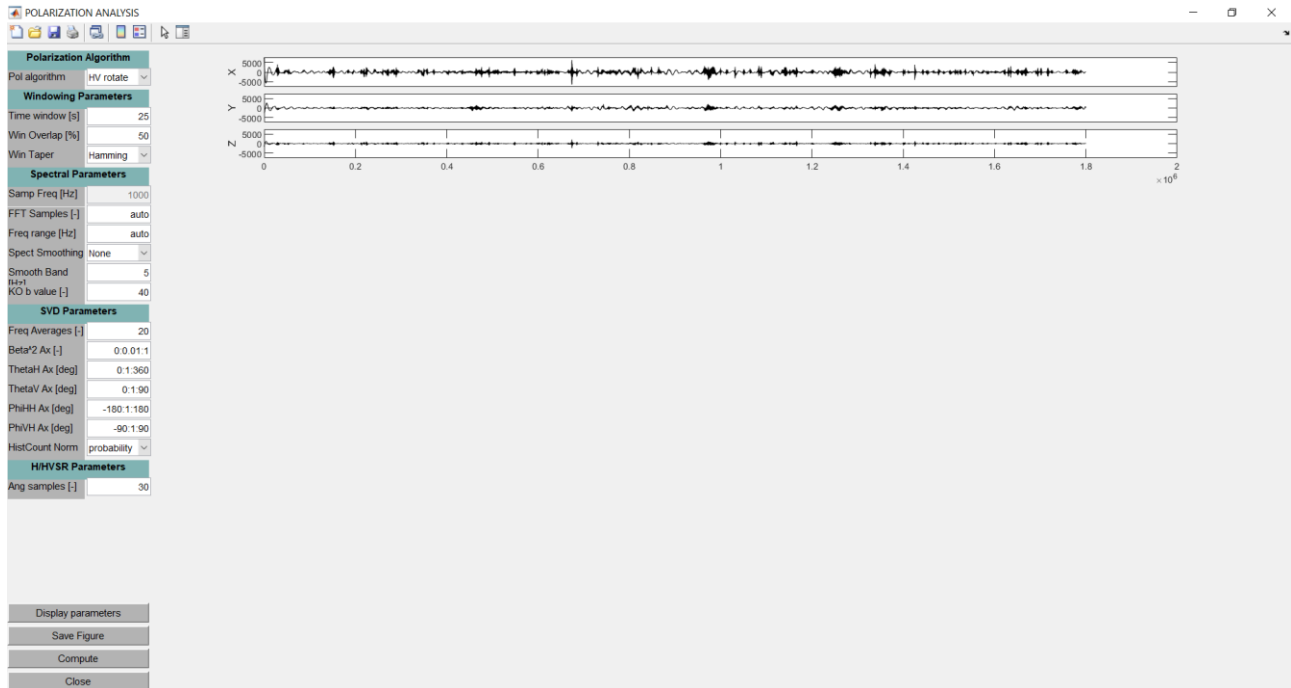


Figure 15: *Polarization Analysis* tab.

The tab contains 5 main sections:

1. Polarization Algorithm: it allows the selection of the method used to perform the polarization analysis.
2. Windowing Parameters: it allows to set the window used to perform the analysis.
3. Spectral Parameters: it contains all the spectral settings.
4. SVD Parameters: it contains the required parameters for the SVD algorithm.
5. H/HVSR Parameters: it contains the required parameters for the H/HVSR algorithms.

Hereafter, there is a description of each command listed in the five abovementioned sections.

### 1. Polarization Algorithm:

- a. *Pol algorithm*:
  - i. HV rotate
  - ii. PCA covariance matrix
  - iii. SVD spectral matrix
  - iv. H rotate

## 2. Windowing Parameters:

- a. *Time window [s]*: The longer the time window, the better the spectral resolution. The shorter the time window, the better the statistical significance. The lower frequency resolution achievable is approximately defined by  $1/(\text{time window}/10)$ .
- b. *Win Overlap [%]*: percentage of overlap among the windows.
- c. *Win Taper*: type of window used to taper the time window.
  - i. Hamming
  - ii. Tukey
  - iii. Blackmanharris
  - iv. Hann
  - v. None

## 3. Spectral Parameters:

- a. *Samp Freq [Hz]*: uneditable parameter.
- b. *FFT Samples [-]*: FFT Samples should be equal or greater than (time window\*sampling frequency). Powers of 2 give better performance of the FFT algorithm. "auto" option:  $2^{(\text{nextpow2}(\text{length}(\text{signal})))}$ .
- c. *Freq range [Hz]*: Indicate F1-F2- The lower limit should be  $\geq 1/(\text{time window}/10)$ . "auto" option: range spans from  $1/(\text{time window}/10)$  to  $F_{Nyquist}$ .
- d. *Spect Smoothing*:
  - i. None
  - ii. KonnoOhmachi
  - iii. Triangular
  - iv. Rectangular
- e. *Smooth Band [Hz]*: This parameter applies to Rectangular and Triangular smoothing. The value must be  $>$  sampling interval of the frequency axis and smaller than the Nyquist frequency.
- f. *KO b value [-]*: This parameter applies to KonnoOhmachi smoothing only. The value must be  $0 < b < 100$ .

## 4. SVD Parameters:

- a. *Freq Averages [-]*: Number of spectral matrixes to be averaged before computing polarization parameters with the spectral SVD algorithm. A value  $> 1$  is mandatory.
- b. *Beta^2 Ax [-]*: Axis of the degree-of-polarization parameter computed with the spectral SVD algorithm. Fill in as min:step:max. Values must be  $0 \leq x \leq 1$ .
- c. *ThetaH Ax [deg]*: Axis of the azimuthal polarization parameter computed with the spectral SVD algorithm. Fill in as min:step:max. Values must be  $0^\circ \leq x \leq 360^\circ$ .
- d. *ThetaV Ax [deg]*: Axis of the vertical polarization parameter computed with the spectral SVD algorithm. Fill in as min:step:max. Values must be  $0^\circ \leq x \leq 90^\circ$ .
- e. *PhiHH Ax [deg]*: Axis of the horizontal phase lag polarization parameter computed with the spectral SVD algorithm. Fill in as min:step:max. Values must be  $-180^\circ \leq x \leq 180^\circ$ .
- f. *PhiVH Ax [deg]*: Axis of the vertical-to-horizontal phase lag polarization parameter computed with the spectral SVD algorithm. Fill in as min:step:max. Values must be  $-90^\circ \leq x \leq 90^\circ$ .
- g. *HistCount Norm*:
  - i. Probability
  - ii. Pdf
  - iii. Count

## 5. H/HVSR Parameters:

- a. *Ang samples [-]*: Samples of angular axis for the HV rotate algorithm (divide pi by this number). A value  $> 1$  is mandatory.

The user can access the command description by moving the mouse indicator above each of the editable text fields in the panel. Figure 16 shows an example:

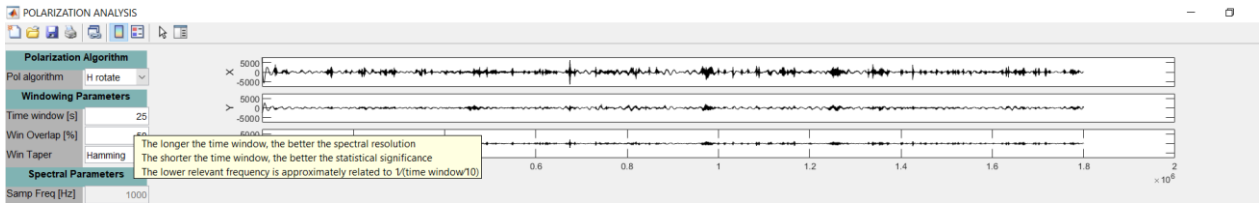


Figure 16: Tip for the Time window [s] parameter.

On the bottom left side of the *Polarization Analysis* tab, there are four buttons with the following use:

- Display parameters: it allows the user to modify the plot settings.
- Save Figure: it allows the user to save the obtained results.
- Compute: it allows the user to perform the selected polarization analysis.
- Close: it allows the user to close the polarization analysis tab.

Once all the required input has been set up, it is possible to perform the analysis by clicking on the *Compute* button. Figure 17-18-19 show the examples of the polarization analysis performed with the available algorithms.

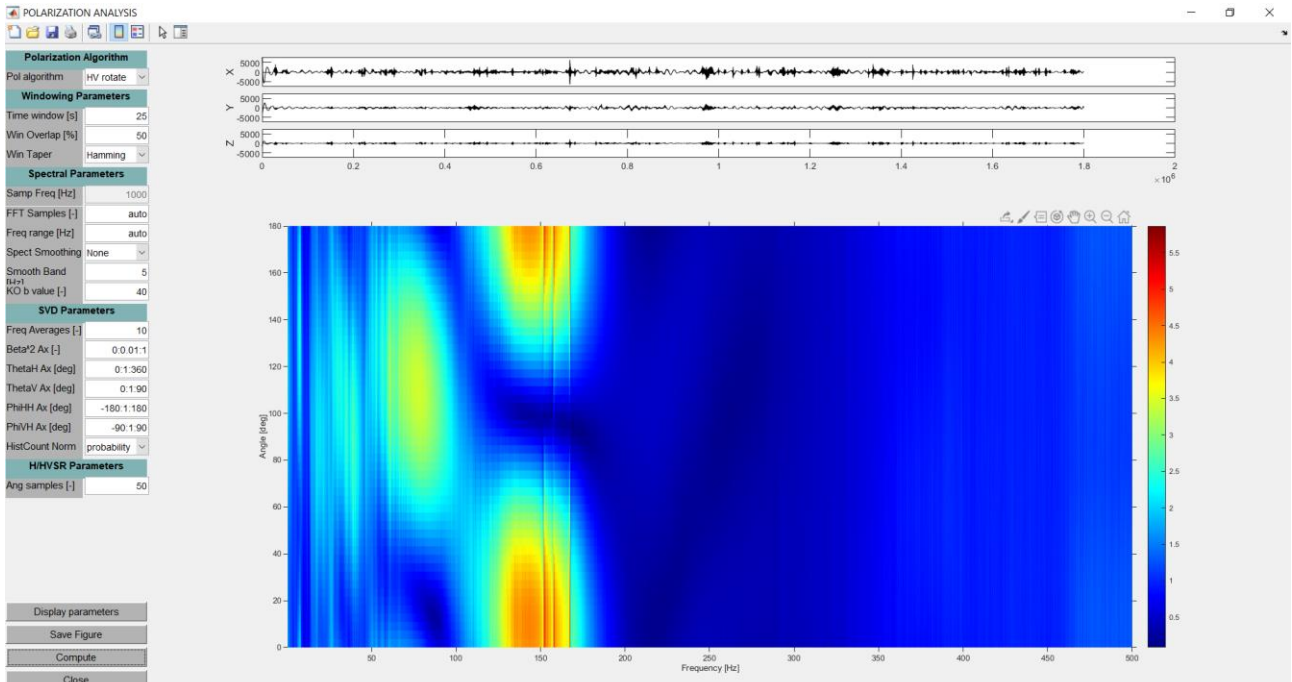


Figure 17: Example of the HV rotate algorithm.

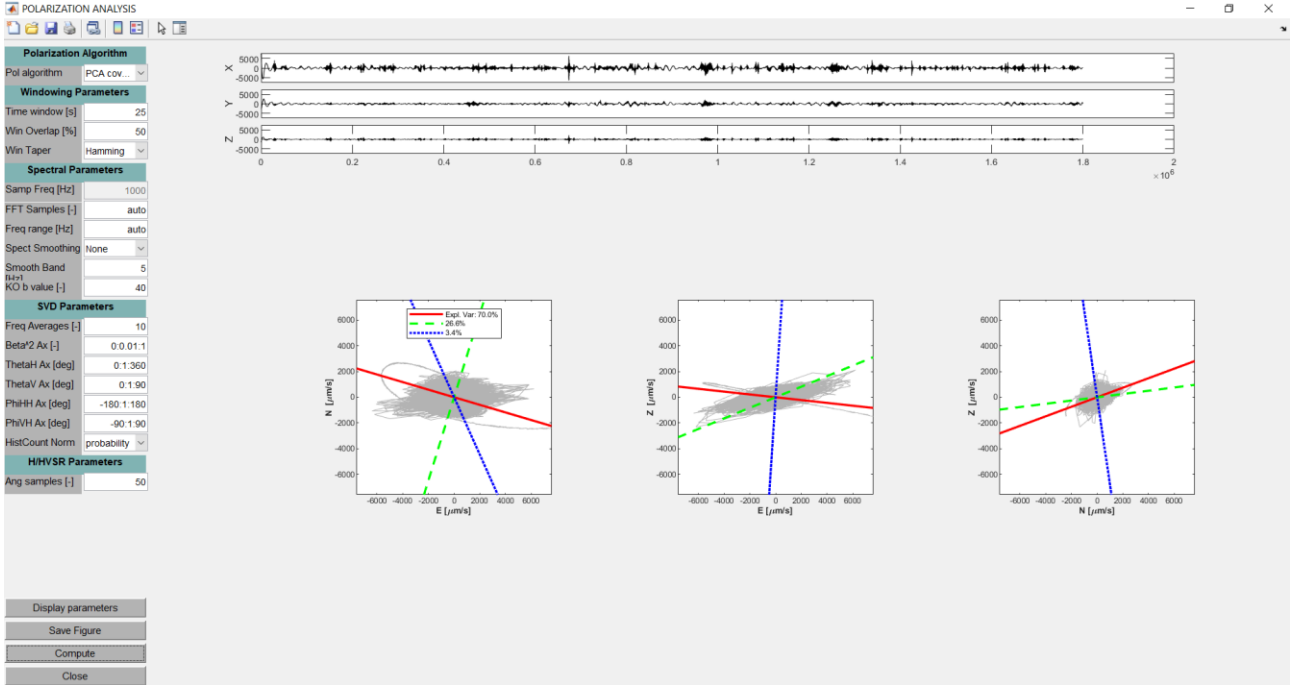


Figure 18: Example of the PCA algorithm.

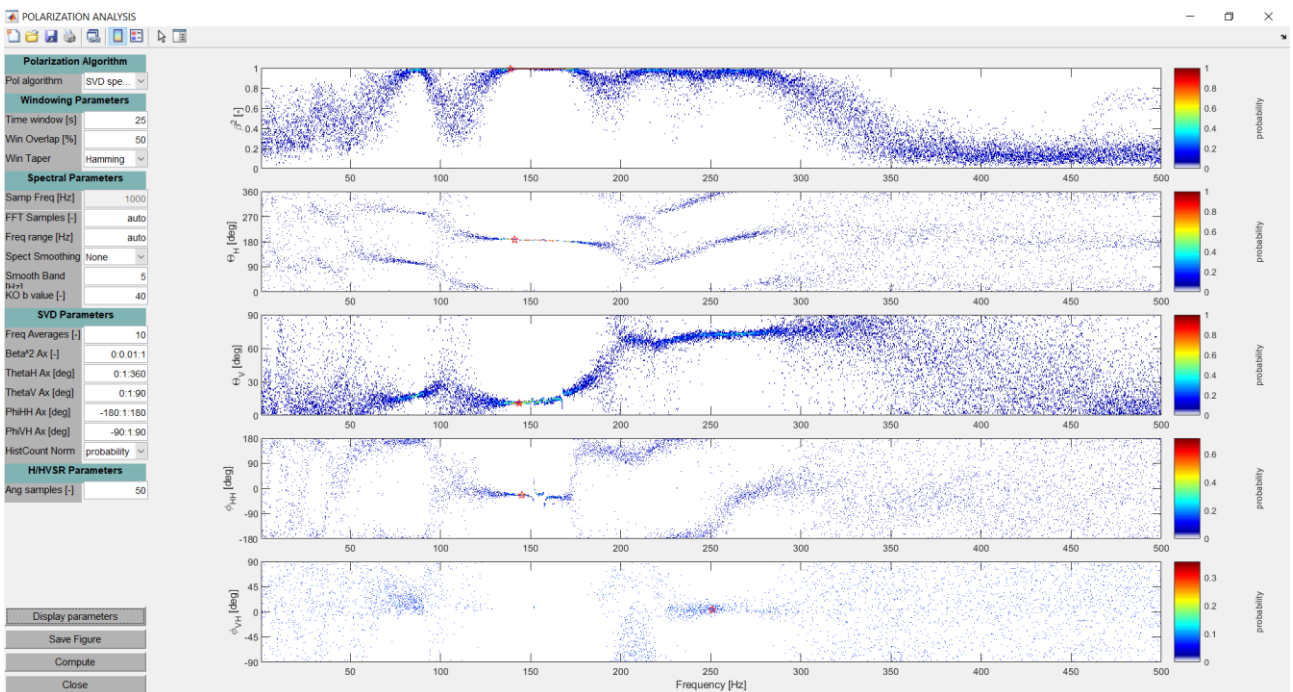


Figure 19: Example of the SVD algorithm.

Finally, by clicking on the *Display parameters* button, the user can modify the plot appearance (Figure 20) by changing the following options:

- Axes type: it is possible to show the axes either in Cartesian or Polar mode.
- Freq Axis: it is possible to show the frequency axis either on a linear or logarithmic scale.
- Freq Limits [Hz]: it allows to set the frequency limits.
- Colormap: it allows to change the colourmap.
- Colormap range: it allows to set the colourmap limits.
- H/HVSR angular rule: it allows to set the angular reference system.

- SVD ThetaH rule: it allows to set the angular reference system.
- SVD ThetaV rule: it allows to set the angular reference system.

To update the plot appearance the user must click on the *Update* button.

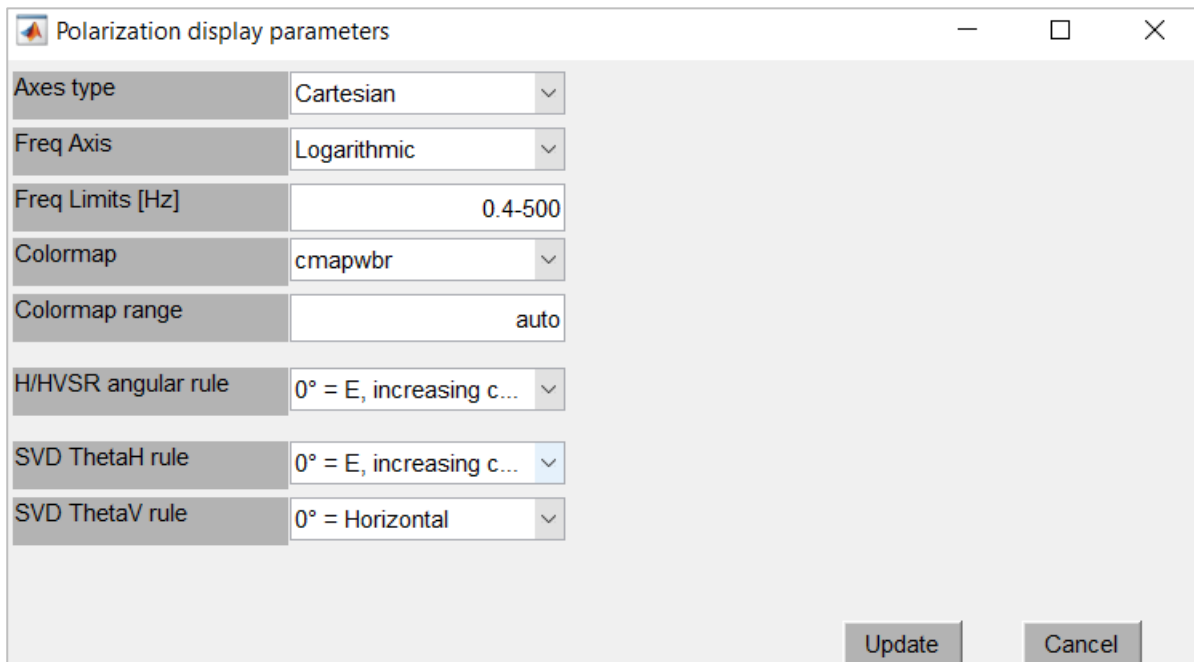


Figure 20: Plot settings for Polarization plots.

## HVSR analysis

The tool can be activated after selecting the three components belonging to the same sensor within the *Signals for Processing* table and then clicking on *Processing ➔ HVSR analysis* (an error will appear if the three components have not been selected). The *HVSR Analysis* tab will appear as shown in figure 21. More details about this methodology can be found in ‘SESAME-HV-User-Guidelines’.

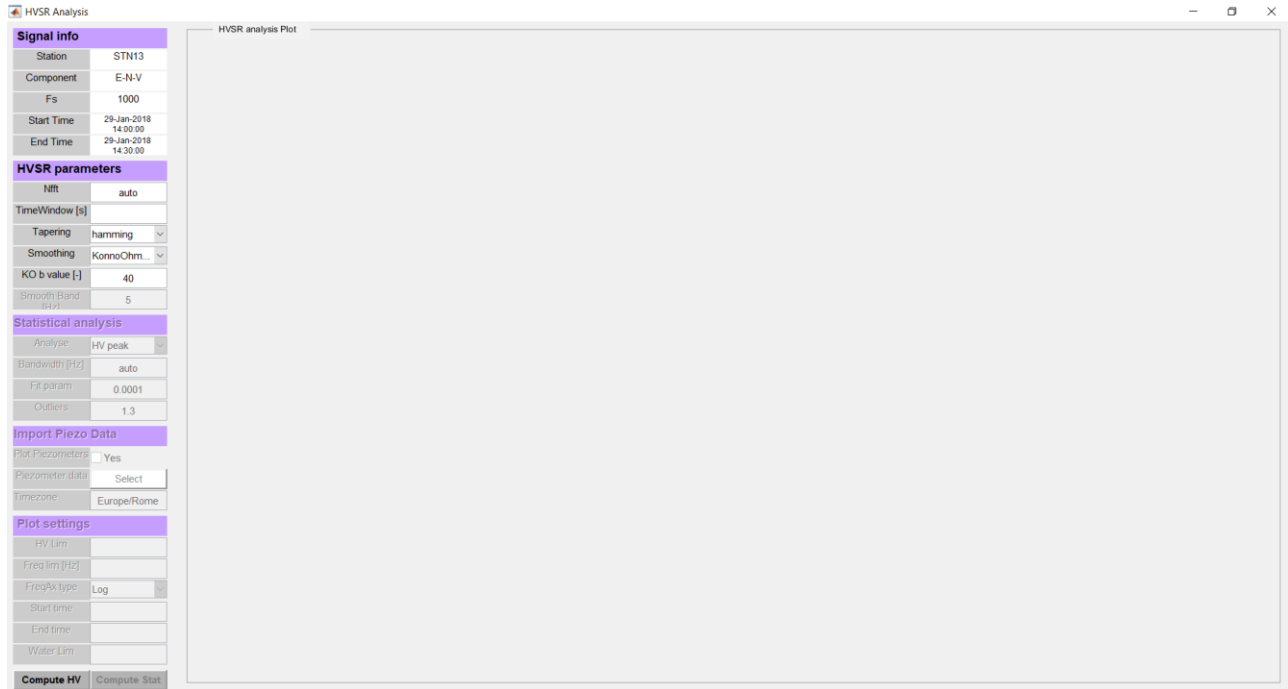


Figure 21: HVSR analysis tab

The tab contains five sections:

1. Signal info: it contains all the information about the selected signal. This section is not treated since it does not have any practical use.
2. HVSR parameters: it contains all the parameters that must be set up before performing the analysis.
3. Statistical analysis: it contains the tools to statistically analyse the HV curve computed over time.
4. Import Piezo Data: it allows to import of piezometers data to compare the HVvsTime curve with the underground water table.
5. Plot settings: these parameters allow the modification of the obtained plots.

In the HVSR parameters section the user must first set up the *Nfft*, *TimeWindow [s]*, *Tapering*, *Smoothing*, *KO b value [-]* and the *Smooth Band [Hz]* (in case triangular or rectangular smoothing type has been selected). Here below more details about each of the input:

- *Nfft* = number of samples used to compute the Fourier transform.
- *TimeWindow [s]* = length (in seconds) of the window used to subdivide the entire signal in sub-signals.
- *Tapering* = type of window used to taper the time window.
- *Smoothing* = select the smoothing type that will be used in the processing.
- *KO b value [-]* = required parameter for Konno Ohmachi smoothing type.
- *Smooth Band [Hz]* = required parameter for triangular or rectangular smoothing types.

The user can access the parameter description by moving the mouse indicator above each of the editable text fields in the panel as previously shown in figure 16.

Once all the required input has been set up, it is possible to perform the analysis by clicking on the *Compute HV* button. Figure 22 shows an example of a signal which underwent the HVSR analysis. Into detail: the first plot shows the Horizontal-to-Vertical spectral ratio curve, the second one show the HVSR curve computed over time.

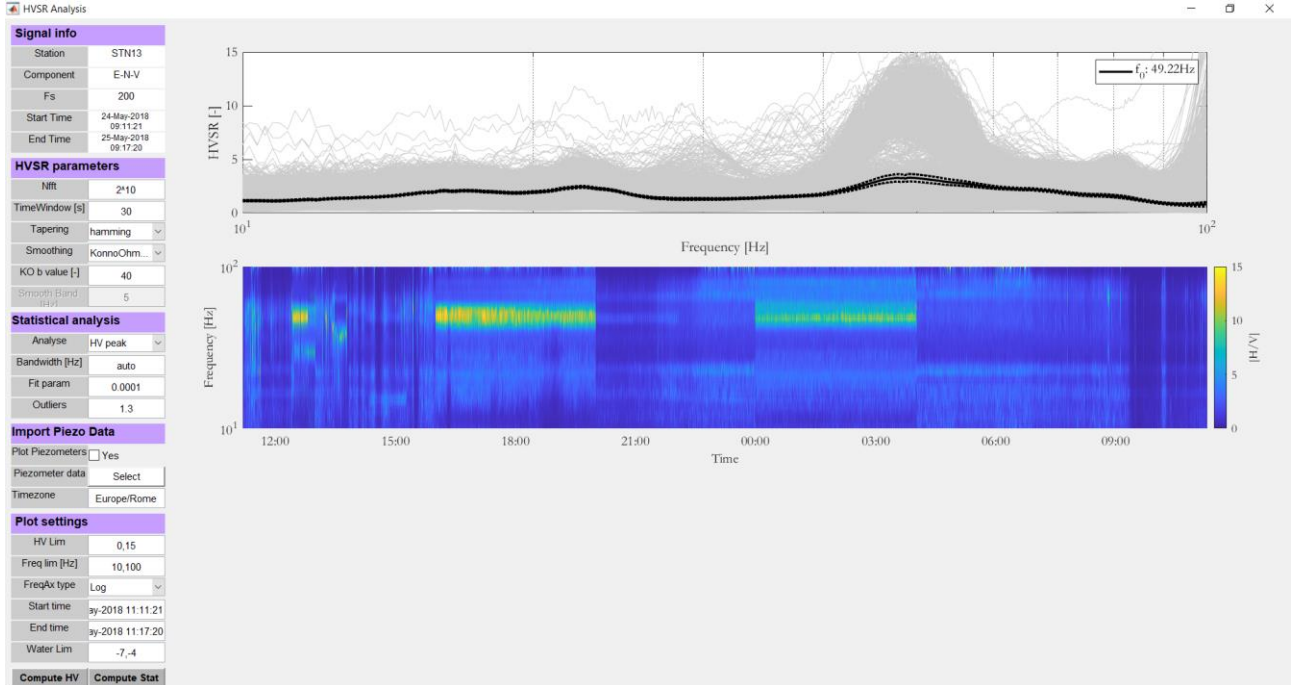


Figure 22: top plot shows the HVSR curves: in light grey, all the curves obtained for each time window; the black curve is the average; the dashed black curve is the standard deviation. The lowest plot represents the HVSR computed over time.

Once the HVSR has been computed, the user may also perform a statistical analysis to study the trend of the HV curve over time. In this perspective different parameters must be set up:

1. *Analyse*: the user can decide whether to study the:
  - a. *HV peak*: it finds the value of the highest peaks of the HVSR for each time window.
  - b. *HV frequency*: it finds the frequency corresponding to the highest peaks in the HVSR (for each time window).
2. *Bandwidth [Hz]*: the above-mentioned types of analysis can be performed in a specific frequency range.
3. *Fit param*: the points identified with the selected analysis will be then fitted using the smoothing-spline method which requires a starting coefficient. The software suggests a value of 0.0001 to start the fitting.
4. *Outliers*: This value will multiply the std of the HVSR peak curve to determine the outliers. Identify "outliers" as points at a distance greater than  $x^*$ standard deviations from the baseline model and refit the data with the outliers excluded.

Within the HVSR Analysis, it is furthermore possible to import piezometer data and plot them in comparison to the curve obtained throughout the statistical analysis (this option has been included in the software because it has been observed that the HVSRvsTime curve exhibits variations correlated to the underground water table). This option is available in the *Import Piezo Data* section that consists of the following buttons:

1. *Plot Piezometers*: if the “yes” checkbox is checked, the piezometers will be plotted.
2. *Piezometer data*: by clicking on the *Select* button the user can import the piezometer data that must be with the .xls extension.
3. *Timezone*: the user must set the time zone according to the place where the data have been collected.

To perform the statistical analysis the user must then click on *Compute Stat* button.

Figure 23 shows an example of the result obtained with the statistical analysis. It can be noticed that the lowest plot contains:

- Grey-dots that represent, in this case, the HVSR peaks found for each time window.
- Red-stars represent the outliers.
- The green curve represents the fitted HVRS peaks.
- The black curve represents the fitted HVRS peaks without outliers.
- The blue curve represents the water table.

Within the same plot, there is also a box containing the information about the goodness of the fit. In detail, it shows the value of  $R^2$  with or without considering the outliers.

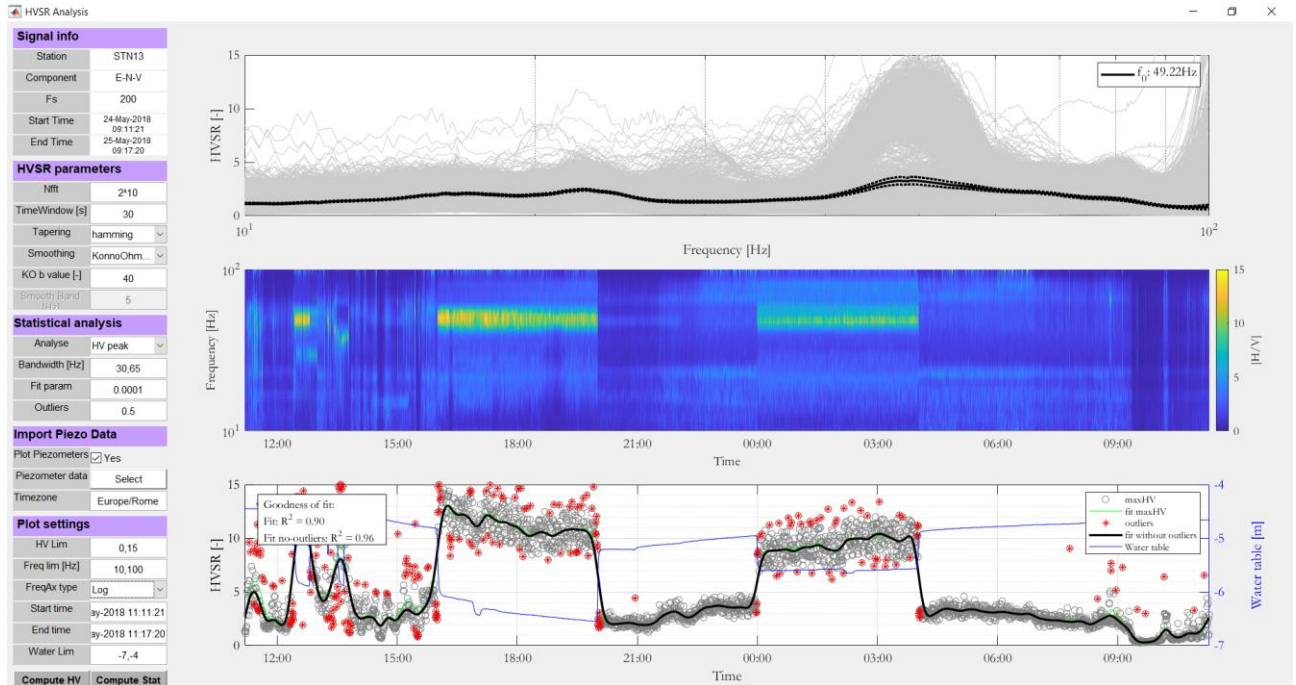


Figure 23: Same as Figure 22 but with the statistical analysis result.

Finally, in the *Plot settings* menu, the user can modify the plot appearance by changing the following options:

- *HV Lim*: it allows to set the limits of the HVSR [-] axis.
- *Freq lim [Hz]*: it allows to set the frequency limits.
- *FreqAx type*: it is possible to show the frequency axis either on a linear or logarithmic scale.
- *Start time* and *End time*: these edit fields allow modification of the time axis limits.
- *Water Lim*: it allows to set the limits of the water table axis.

The plots will be automatically updated when one of these parameters will be modified.

Once the analysis is completed the user may choose to save the obtain plots by clicking on the specific icon that appears on the upper-right of the axes:



## Cross-correlation analysis

This analysis must be performed using two signals that belong to different seismic sensors. Generally, this technique makes use of vertical components, however, this software allows to perform also the intra-correlation which involves different components (e.g. vertical and East-West components). After signals selection within the *Signals for Processing* table, the tool can be activated by clicking on *Processing* → *Passive Interferometry* → *Cross-Correlation Analysis* (an error will appear if more than two signals have been selected). The *Cross-Correlation Analysis* tab will appear as shown in figure 24.

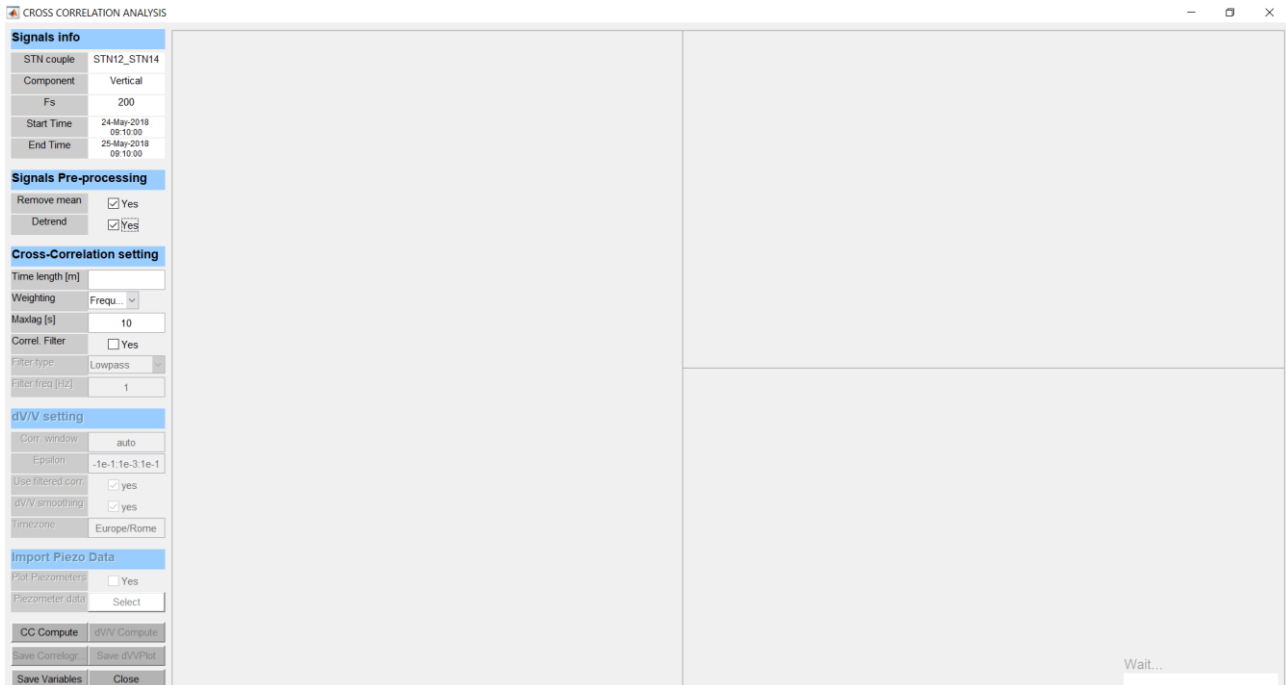


Figure 24: Cross-Correlation analysis tab

The tab contains five sections:

1. Signal info: it contains all the information about the selected signals. This section is not treated since it does not have any practical use.
2. Signals Pre-processing: it allows to detrend and remove the mean of the input signals when the checkboxes are selected.
3. Cross-Correlation setting: it contains all the parameters that must be set up to compute the correlogram.
4. dV/V setting: it contains all the parameters that must be set up to compute the dV/V curve.
5. Import Piezo Data: it allows to import of piezometers data and compare them with the dV/V curve.

In the *Cross-Correlation setting* section, the user must first set up the *Time length [m]*, *Weightining*, *Maxlag [s]* and *Correl. Filter*. Here below more details about each of the input:

- *Time length [m]* = length (in minutes) of the window used to subdivide the entire signal into sub-signals. The latter will be used to compute the cross-correlation.
- *Whitening* = it allows to “equalize” the signal avoiding that spurious data might rule the cross-correlation. The user may select to perform this in:
  - *Time-domain*
  - *Frequency domain*
  - *Both Time-Frequency domain*

- *None*
- *Maxlag [s]* = Maximum lag (in seconds), specified as an integer scalar. The returned cross-correlation sequence ranges from -maxlag to maxlag.
- *Correl. Filter* = it allows filtering the correlogram. This process is faster than filtering signals before performing cross-correlation. If this option is activated, the user must define the characteristics of the filter using *Filter type* and *Filter freq [Hz]* editable fields.

Once all the required input has been set up, it is possible to perform the cross-correlation analysis by clicking on the *CC Compute* button. Figure 25 shows an example of the obtained correlogram: the x-axis represents the time lag and the y-axis all the computed cross-correlations expressed in phase-amplitude.

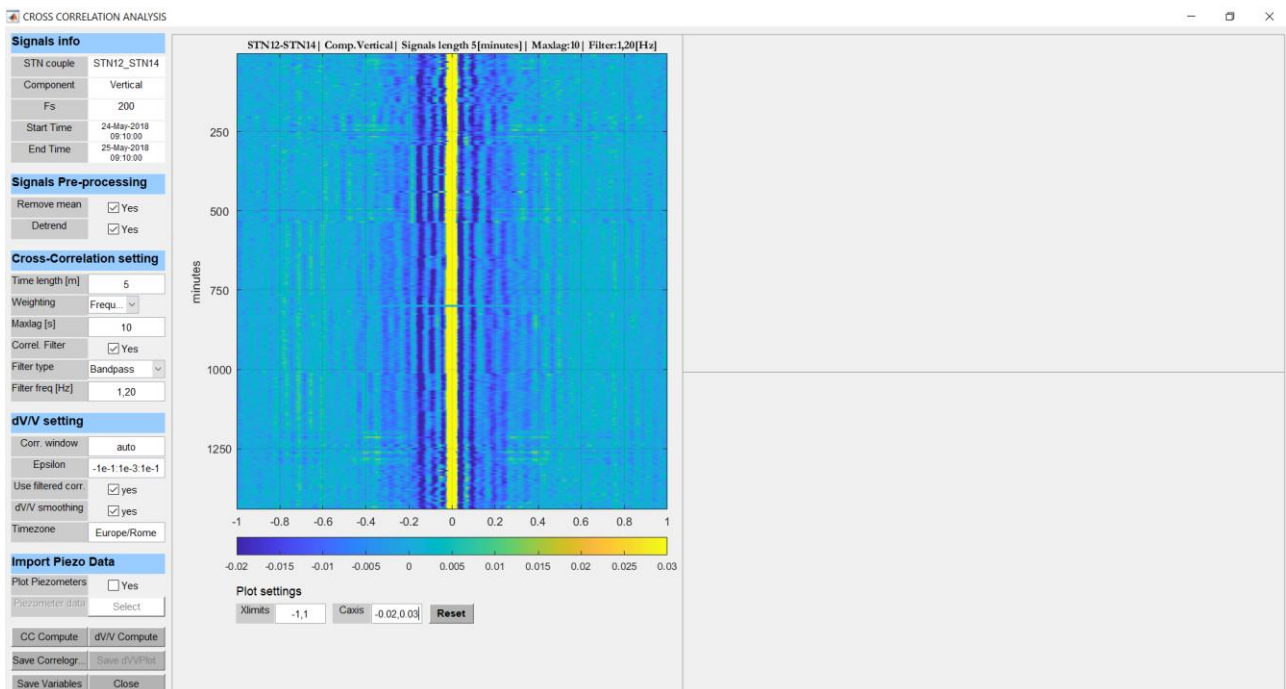


Figure 25: Correlogram obtained with signals length of 5 minutes.

The *Xlimits* and *Caxis* editable text fields in the *Plot settings* section (below the correlogram) allow the modification of the correlogram appearance. Whereas, the *Reset* button allows to go back to the initial aspect.

Once the correlogram has been obtained, the user must set up the parameters within the *dV/V setting* section:

- *Corr. Window*: The user must select a “lag” window in the correlogram that will be used to compute the velocity variation curve ( $dV/V$ ). If “auto” is specified, the code will perform the analysis considering a correlogram window that spans between -maxlag and maxlag (previously set up).
- *Epsilon*: This is a vector containing a list of values required by the Stretching technique which is used to obtain the  $dV/V$  curve. The pre-set values are generally enough for most of the case studies.
- *Use filtered corr.*: The user may select whether to perform the analysis using the filtered or the raw correlogram.
- *$dV/V$  smoothing*: The user may decide to smooth the  $dV/V$ . In the plot both the smoothed and the real  $dV/V$  curves will be shown. It is generally recommended to activate this tool.
- *Timezone*: the user must set the time zone according to the place where the data have been collected. This is necessary to align the  $dV/V$  curve with the piezometer data.

Within the *Cross-correlation Analysis* tool, it is possible to import piezometer data and plot them in comparison to the curve obtained throughout the statistical analysis. This option is available in the *Import Piezo Data* section that consists of the following buttons:

1. Plot Piezometers: if the “yes” checkbox is checked, the piezometers will be plotted.
2. Piezometer data: by clicking on the Select button the user can import the piezometer data that must be with the .xls extension.

To obtain the  $dV/V$  curve the user must click on the  *$dV/V$  Compute* button. The figure below shows an example of the obtained seismic velocity variations curve obtained for the same data used in figure 25. It can be noted that the selected *Corr. Window* is now highlighted within the correlogram using a red-dashed rectangle. On the right upper side of the panel the  $dV/V$  (dashed grey curve), the smoothed  $dV/V$  (black curve) and the water table level (blue curve) are shown (Figure 26).

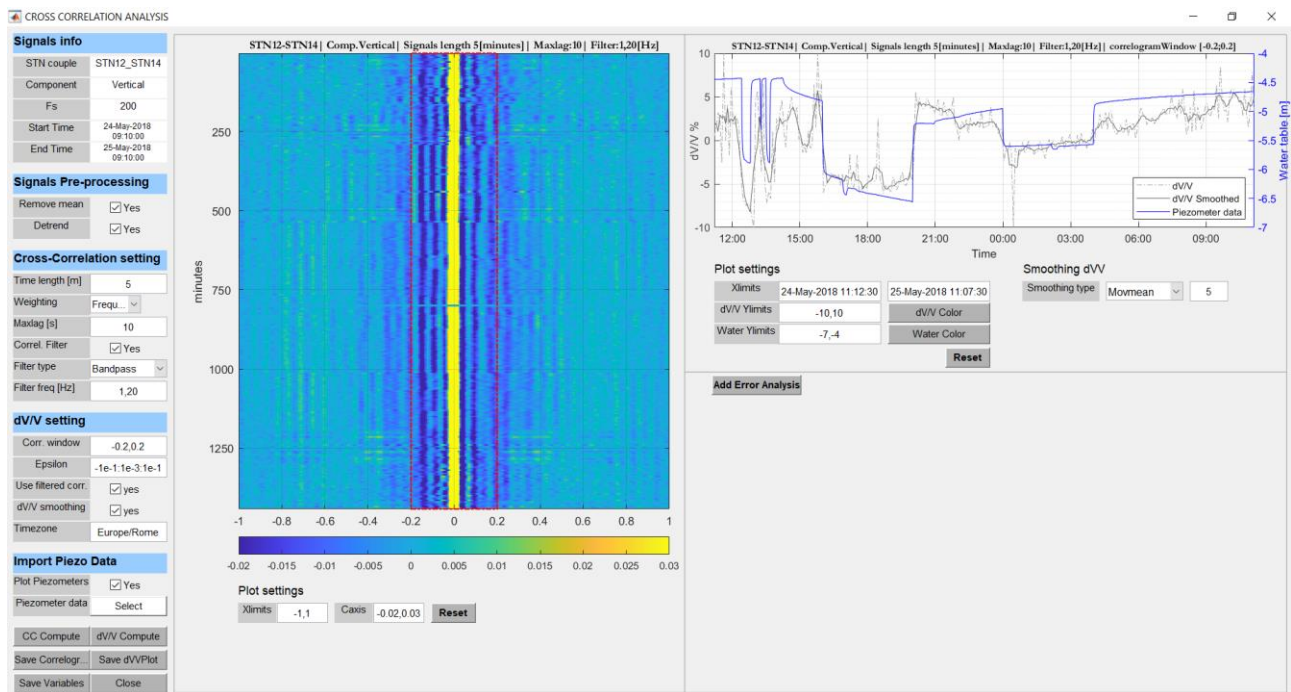


Figure 26: Example of  $dV/V$  computation.

It is now possible to modify the plot appearance also for the right-side plot. Into detail, the user may choose:

- *Xlimits*: it allows the modification of the limits of the time axis.
- *$dV/V$  Ylimits*: it allows the modification of the left-side y-axis limits.
- *$dV/V$  Colour*: it allows the modification of the colour of the  $dV/V$  curves.
- *Water Ylimits*: it allows the modification of the right-side y-axis limits.
- *Water Colour*: it allows the modification of the colour of the piezometer curve.
- *Smoothing type*: it allows to select the type of smooth to apply to the  $dV/V$  curve.
- *Reset button*: it allows to go back to the initial aspect.

Finally, it is possible to perform an error analysis to study the goodness of the  $dV/V$  estimation by clicking on the *Add Error Analysis* button. The section on the bottom-right side will appear as shown in figure 27. The user must set:

- $t2-t1$ : which is equal to the correlogram window interval.

- $Wc$ : it is the central frequency that corresponds to the most energetic peak in the CrossCorr-REF spectrum.
- *Bandwidth*: (in Hz) it will be used to compute T in the Weaver equation.

To perform the analysis, use the *Compute* button.

Figure 27 shows the performed error analysis. This example shows that the obtained dV/V is reliable. Indeed, its RMS error is very low.

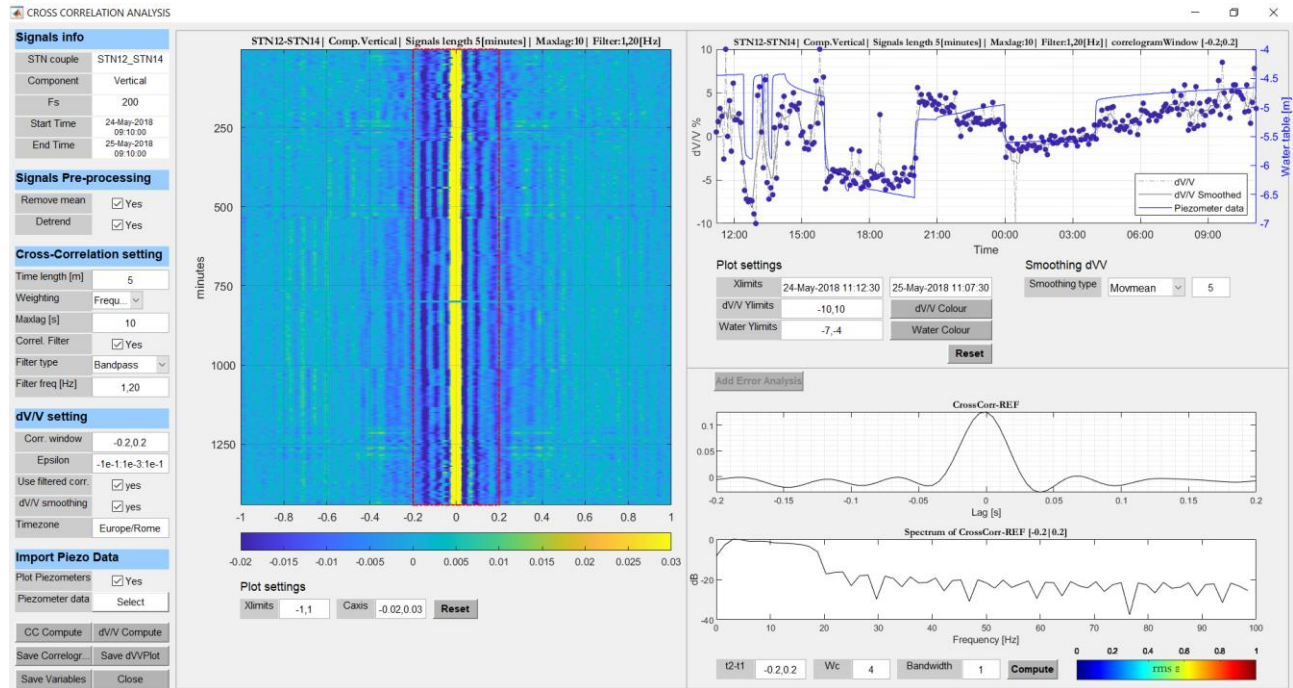


Figure 27: Example of Error Analysis computation.

It is important to notice that the titles of the correlogram and the dV/V plots contain the parameters set up for the analysis. This is useful when the user wants to export these graphs by means of the *Save Correlogram* and *Save dVVPPlot* button (on the bottom-left corner). Indeed, using one of these buttons a new figure will be created containing the corresponding plot. Without the title, it would be impossible to know the parameters used in the analysis.

## Dynamic options

The cross-correlation of ambient seismic noise is a technique strongly influenced by the chosen correlogram filter and by the selected correlogram window. For this reason, it has been decided to implement in the software the possibility to define a “dynamic” filter and corr.window (Figure 28). The main idea behind this “dynamic” option is that the software will automatically compute the analysis by changing one of these parameters.

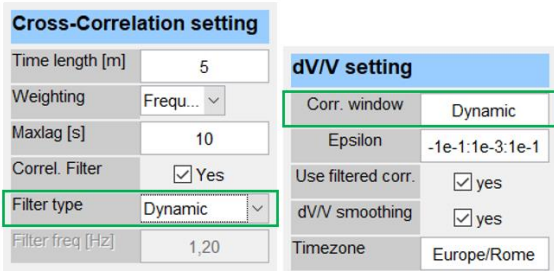


Figure 28: Dynamic option for Filter type (left) and Corr. window (right) parameters.

### 1. Dynamic Filter type:

This option allows the user to compute the dV/V for different filtered correlograms and compare all the dV/V curves to choose the correct frequency band. To use this tool it is suggested to first compute the dV/V in the broad-band frequency to determine the *corr.wind* in which the dV/V is sensitive to water table variations. Then, using the dynamic filter tool it is possible to inspect different frequency bands. NB. If you select this option you cannot use the dynamic option in *Corr. window*!

Once *Dynamic* has been selected within the drop-down *Filter type* menu, clicking on the *CC Compute* button the following tab will appear:

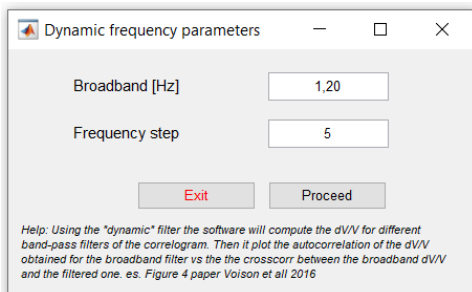


Figure 29: Dynamic filter tab.

The user must set:

- *Broadband [Hz]*: it defines the limits of the filter.
- *Frequency step*: it defines the frequency step.

I.e. According to the values set up in Figure 29, the dV/V will be computed considering the four-following filtered correlograms: 1-6 Hz, 6-11 Hz, 11-16 Hz and 16-21Hz.

Figure 30 (right-side plot) shows the result of the analysis with the dynamic filter. The plot represents the mean cross-correlation computed for the broadband (blue curve) and for each frequencies range. The latter curve will be green if the filtered mean cross-correlation is sufficiently similar (correlation coefficient >0.6) to the blue one. Otherwise, it will be grey. For this case, the correlogram filtered in the 16-21 Hz band it is linked to the mean broad-band cross-correlation. This result is useful to inspect the different depth of the analysed medium and thus partially understand the water table depth.

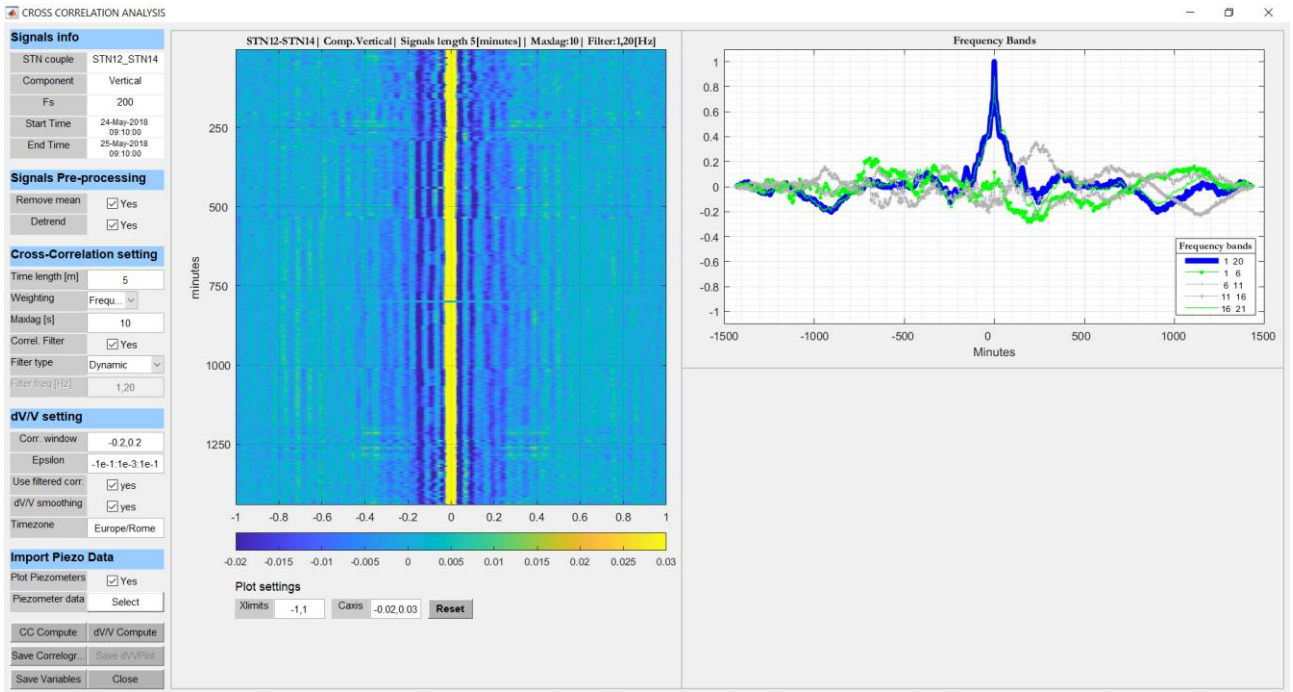


Figure 30: Result obtained using the Dynamic filter option.

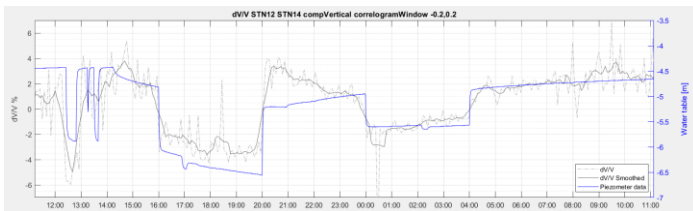


Figure 31:  $dV/V$  computed considering the correlogram filtered in the 16-21 Hz frequency band.

## 2. Dynamic Corr. window:

This option allows computing the  $dV/V$  for different correlogram windows. To use this tool the user must write “dynamic” within the *Corr. window* editable text field. Then, clicking on the  *$dV/V$  Compute* button the following tab will appear:

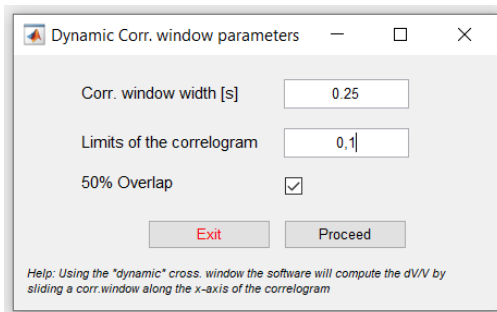


Figure 32: Dynamic Corr. window tab.

The user must set:

- *Corr. window width [s]*: it defines the width, in second, of the moving correlogram window.
- *Limits of the correlogram*: it defines the limits of the correlogram in which the window will move.
- *50% Overlap*: if selected, the moving window will move to the next one with an overlap of 50%.

I.e. According to the values set up in Figure 32, the  $dV/V$  will be computed considering the following *Corr. windows*: 0-0.25, 0.125-0.375, 0.25-0.5, 0.375-0.625, 0.5-0.75, 0.625-0.875 and 0.75-1s.

The obtained result is like what has been observed in figure 26 but with two more tools (highlighted with the green rectangle in figure 33):

- *Dynamic Corr. window* sliding bar: it allows to move among the dV/V curves computed for each correlogram window.
- *CC between dVV & Piezometer*: This color bar shows the correlation coefficient computed between the dV/V and the piezometer curves. It allows visualizing which is the correlogram window that brings the dV/V curve more similar to the water table variation.

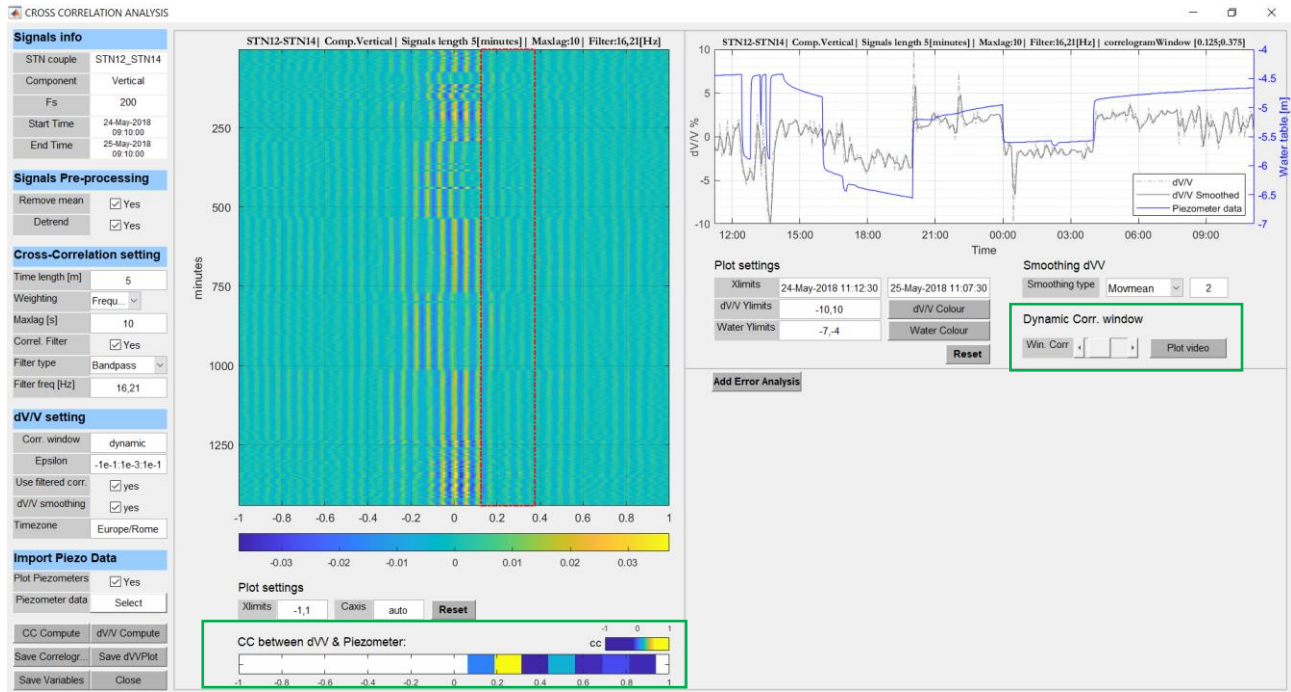


Figure 33: Result obtained using the Dynamic Corr. option.

Finally, it is possible to export the results of the analysis. Clicking on the *Save Variables* button (bottom-left corner), the following tab will appear:

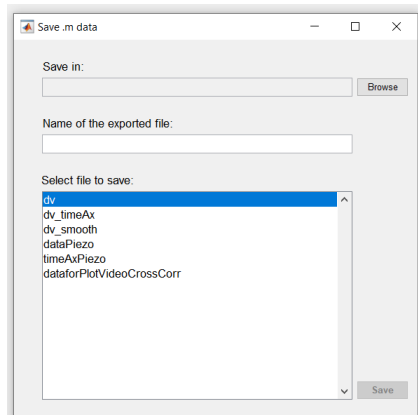


Figure 34: Save data tab

The user will be asked to:

- Select the folder to save the data.
- Give the name to the file.
- Select which data must be saved.

NB: The *dataforPlotVideoCrossCorr* file will appear only in case the *Dynamic Corr. window* has been used.

## Propagation plot

This analysis is generally performed to distinguish different seismic waves within ambient vibrations. Given data collected with a seismic array, this methodology consists of computing the cross-correlation among all the possible couple of stations and plot them versus the distance between the considered station pair.

After signals selection within the *Signals for Processing* table, the tool can be activated by clicking on *Processing ➔ Passive Interferometry ➔ Propagation plot*. The following tab will appear:



Figure 35: Propagation plot tab

The tab contains three sections:

1. Stations coordinates: it is used to define the coordinates of each seismic sensor.
2. Cross-Correlation setting: it contains all the parameters that must be set up to compute the cross-correlation.
3. Cross-Correlation filtering: it allows filtering the obtained cross-correlations.

In the *Stations coordinates* section, the user must first set up the coordinates of the sensors. In this perspective, it is possible to choose between cartesian or geographical (lat/long) coordinates. Once the table is filled, the *Save coord* button allows exporting the coordinates in a .coord file. This could be useful in case of future analysis. If this file already exists, the user can import the coordinates using the *Load coord* button.

Using the *Compute distance of station-pair* button, the permutations (without repetition) among all the sensors are performed and the second table will be automatically filled with all the possible station pairs and their relative distance. Here, it is possible to exclude some station pairs from the propagation analysis by means of the check box. Then, the user must complete the *Cross-Correlation setting* section (with the same criteria explained within the Cross-correlation Analysis paragraph) and click on *Compute cross-correlations* button.

Figure 36 shows the result of this analysis. One may notice that for the analysed signals there is not a clear propagation of the seismic wavefield among the stations. The reason is that the sensors have been installed too close to each other (5 m for this case study).

Even for this analysis, it is possible to filter the results using the *Cross-correlation filtering* section and then clicking on the *Compute filtering* button. Moreover, the graph appearance can be modified using the *Xlimits* editable text field and the *Amplitude* sliding bar.

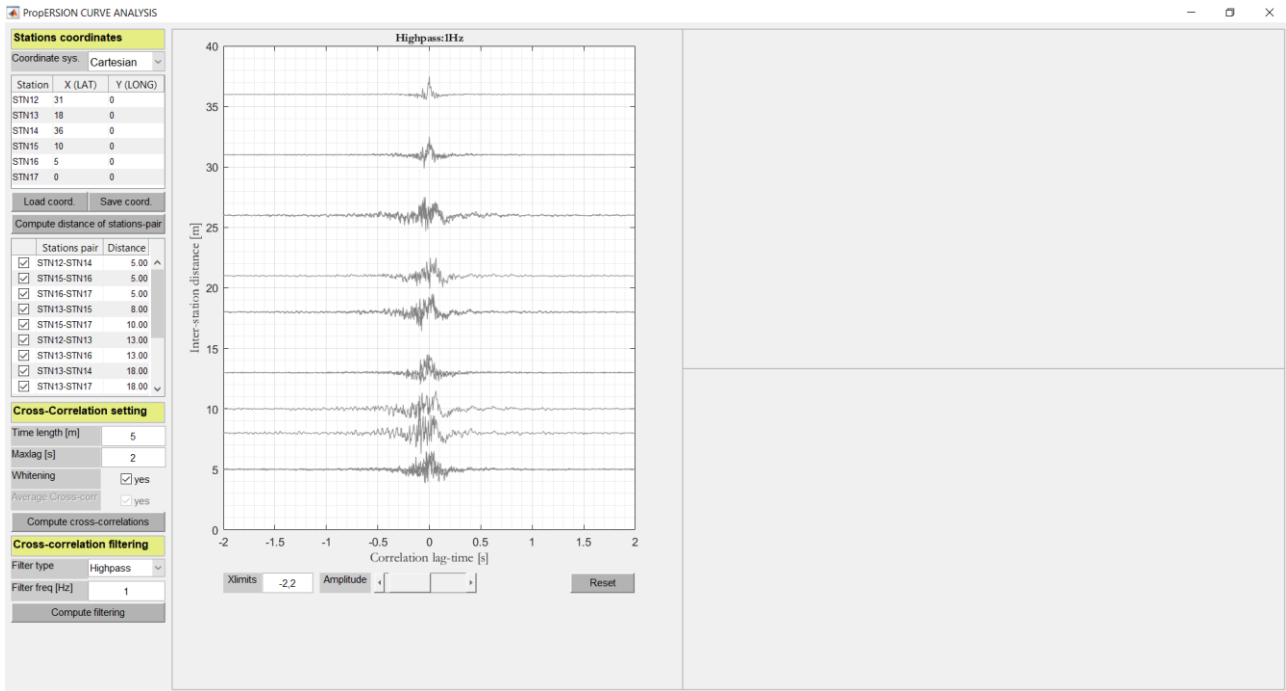


Figure 36: Result of the Propagation plot analysis

## Display

### Plot signals

This tool allows the user to visualize the imported signals. After signals selection within the *Signals for Processing* table, they will be plotted in a new tab by clicking on *Display* → *Plot signals* (Figure 37). The title of each axis will contain information about the sensor, the component, and the initial and final time of the signal. It is important to underline that if the signals did not undergo the instrument response removal, the y-axis will not have any unit of measure. This function of the software can be useful to visualize signals that underwent one of the *Basic processing* tools.

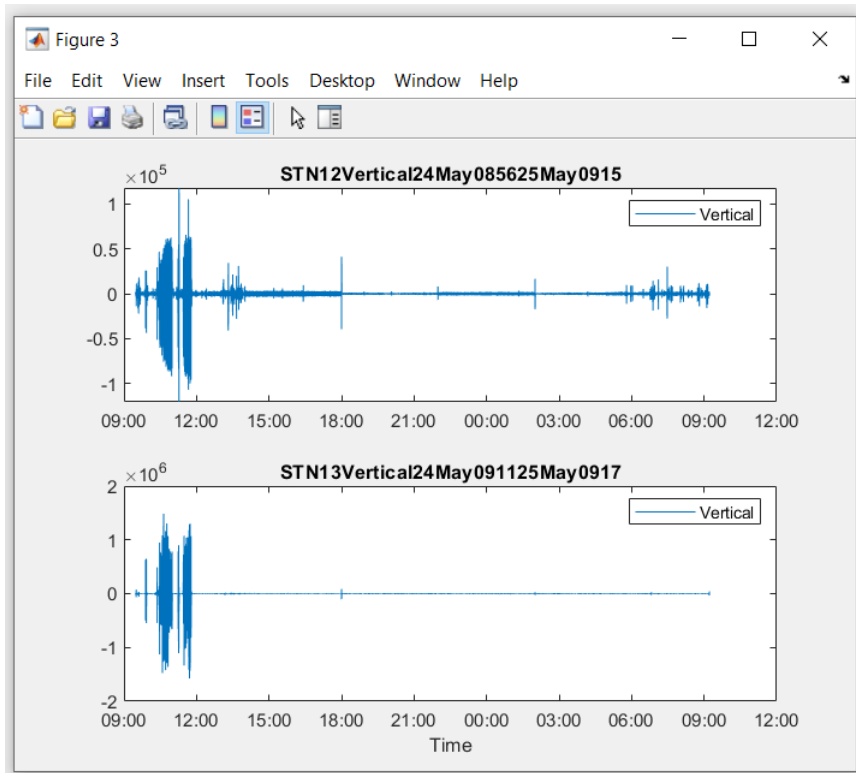


Figure 37: Visualization of signals.

### Video CrossCorr

This tool allows the user to visualize the results obtained through the *cross-correlation analysis* when the *Dynamic Corr. window* is used. By clicking on *Display* → *Video CrossCorr* the user will be asked to select the *dataforPlotVideoCrossCorr* file (for more details about this file see *Dynamic Corr. window* section in *Cross-correlation analysis* paragraph). The tab shown in figure 38 will then appear. The window is almost a replica of the *Cross-correlation analysis* one. Therefore, to have information about each available tool refer to the *Cross-correlation analysis* paragraph.

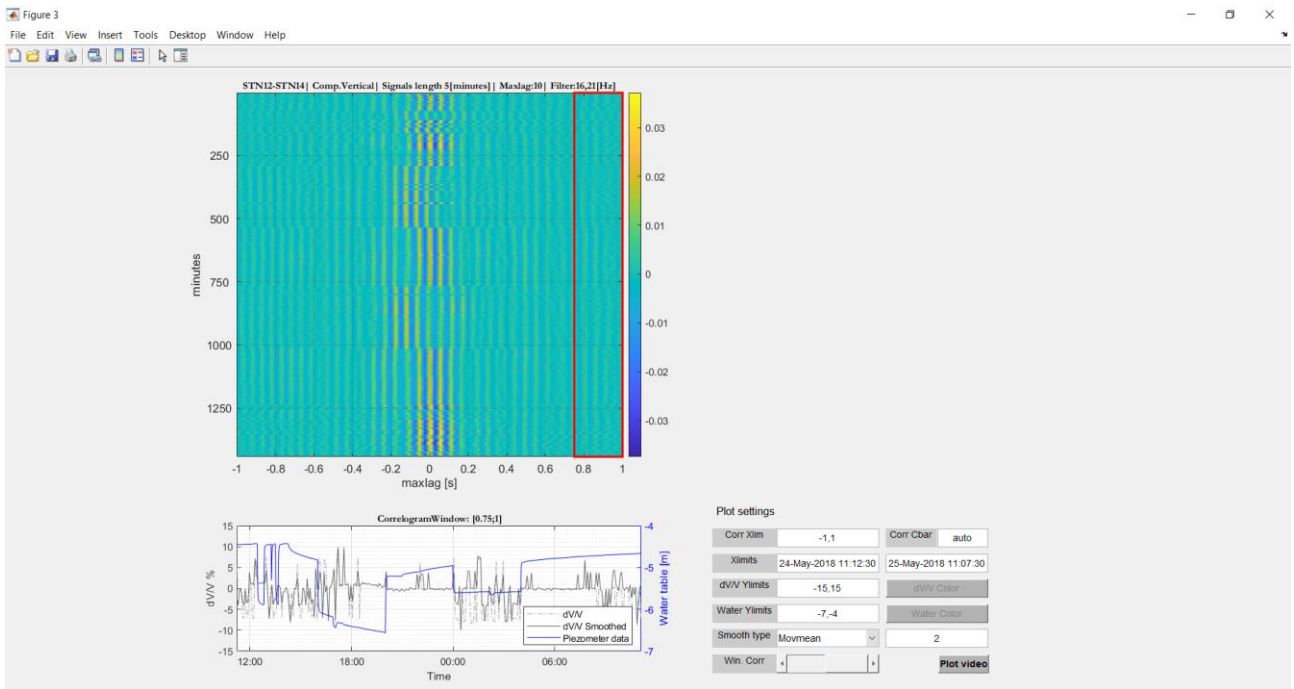


Figure 38: Video CrossCorr tab

## Save

In this software, there is also the possibility to export the results of the different analysis. Clicking on the *Save Variables* button (bottom-left corner), the following tab will appear:

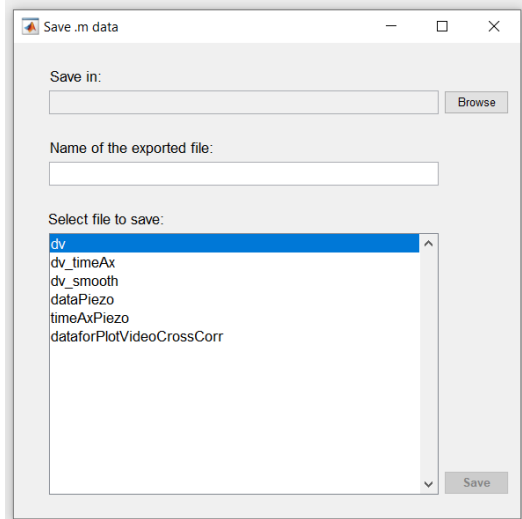


Figure 39: Save data tab

The user will be asked to:

- Select the folder to save the data.
- Give the name to the file.
- Select which data must be saved.